Electrodynamique quantique d'une jonction Josephson couplée à un environnement fortement dissipatif

Sébastien Leger

▶ **To cite this version:**

Sébastien Leger. Electrodynamique quantique d'une jonction Josephson couplée à un environnement fortement dissipatif. Systèmes mésoscopiques et effet Hall quantique [cond-mat.mes-hall]. Université Grenoble Alpes [2020-..], 2021. Français. NNT : 2021GRALY038 . tel-03517115

HAL Id: tel-03517115

https://theses.hal.science/tel-03517115v1

Submitted on 7 Jan 2022

HAL is a multi-disciplinary open access archive for the deposit and dissemination of scientific research documents, whether they are published or not. The documents may come from teaching and research institutions in France or abroad, or from public or private research centers.

L'archive ouverte pluridisciplinaire **HAL**, est destinée au dépôt et à la diffusion de documents scientifiques de niveau recherche, publiés ou non, émanant des établissements d'enseignement et de recherche français ou étrangers, des laboratoires publics ou privés.

THÈSE

Pour obtenir le grade de

DOCTEUR DE L'UNIVERSITÉ GRENOBLE ALPES

Spécialité : Physique de la Matière Condensée et du Rayonnement

Arrêté ministériel : 25 mai 2016

Présentée par

Sébastien LEGER

Thèse dirigée par **Olivier BUISSON**,chercheur, Université Grenoble Alpes
et codirigée par **Nicolas ROCH**,Chargé de recherche, Université Grenoble Alpes

préparée au sein du **Laboratoire Institut Néel**
dans **l'École Doctorale Physique**

Electrodynamique quantique dune jonction Josephson couplée à un environnement fortement dissipatif

Quantum Electrodynamics of a Josephson junction coupled to a strongly dissipative environment

Thèse soutenue publiquement le **16 juin 2021**,
devant le jury composé de :

Monsieur ZAKI LEGHTAS
MAITRE DE CONFERENCE HDR, MINES PARIS TECH, Rapporteur
Monsieur MARCO APRILI
DIRECTEUR DE RECHERCHE, CNRS DELEGATION ILE-DE-FRANCE SUD, Rapporteur
Madame ANNA MINGUZZI
DIRECTEUR DE RECHERCHE, CNRS DELEGATION ALPES, Présidente
Monsieur HAKAN TURECI
PROFESSEUR ASSOCIE, Princeton University, Examinateur
Monsieur MICHEL DEVORET
PROFESSEUR, Yale University, Examinateur

Acknowledgment

Tout d'abord, je te tiens à remercier les membres du mon jury d'avoir accepté d'évaluer le résultat de ces trois ans de thèse. Je sais combien le temps est la ressource la plus importante de tout chercheur et je suis reconnaissant que vous ayez accepté de m'en accorder. Marco Aprili et Zaki Leghtas pour la relecture attentive de mon manuscrit, mais aussi Anna Minguzzi, Hakan Türeci et Michel Devoret pour la séance de questions passionnante qui a suivi ma présentation. C'est toujours remarquable de constater que malgré trois ans de travail acharné la connaissance de mon sujet reste lacunaire.

Je remercie aussi la Fondation CFM pour la recherche qui, en plus d'avoir financé cette thèse, m'aura permis d'avoir des échanges passionnants avec des doctorants travaillant dans des domaines très variés lors des journées de la fondation. Les résultats obtenus durant ma thèse n'auraient pas été possibles sans l'environnement de travail exceptionnel au sein de l'Institut Néel. Aussi je remercie les différents pôles technologiques de l'institut : Ingénierie expérimentale, Cryogénie, Électronique, Nanofab. Ils auront été d'une grande aide pour des tâches aussi variées que la fabrication des échantillons et leur caractérisation, l'entretien des cryostats et la mise en place de nouveau système de mesures. Dans cette optique je remercie tout particulièrement Eric pour le nombre de fois où tu nous as sortis de situation délicate et pour les explications et astuces partagées, Julien pour toutes les aides apportées pendant la programmation de la RedPitaya et bien sûr Julien et Laurent pour nous avoir conçus toutes les pièces ayant permis d'augmenter la qualité de nos mesures. J'ai aussi une pensée pour l'équipe d'Administrative, et notamment Angélique, Otmane et Florence, qui a été disponible et bienveillante bien que je ne fusse pas toujours le meilleur interlocuteur.

Tant sur le point de vue scientifique qu'humain, j'ai eu beaucoup de chance de pouvoir travailler au sein de l'équipe Cohérence Quantique, puis Quanteca. Les nombreuses présentations et discussions que j'ai pu avoir avec ses membres a permis de forger une bonne partie de ma culture scientifique. Cette équipe étant maintenant très élargis j'ai naturellement interagi plus en profondeur avec les membres de l'équipe circuit supraconducteur. I would also like to thank Javier for taking me under his wing when I arrived. Your patience, your kindness and your humor are for much in the few (quantum) successes obtained. Rémy, ton calme et ta rigueur ont été une source d'inspiration importante. Luca nul besoin de préciser que sans toi ce PhD, et ma vie à Grenoble bien évidemment, n'aurait pas eu la même saveur. Ta tolérance et cette capacité à vouloir toujours être une meilleure personne m'impressionne encore. Karthik, being your office partner during these long years has been a pleasure from the beginning to the end, even though it may have been harder for you... Kazi, on top of being et very good friend and a top reseacher you teach me what it means to work as a team. Arpit and Martina (I cannot separate the TWPA team it seems) the progress you have made during my PhD was very impressive to see from the outside

! Vladimir I'm glad we met, your passion for things I had not even considered, not to mention nanofabrication, is fascinating. Jovian, I never thought I would meet someone like you in a laboratory, take it the way you want. More seriously, I wouldn't know half the people I know now in Grenoble without you, maybe I should be worried about that... Enfin, Tibo et Dorian je m'excuse d'avoir été un si mauvais "superviseur", vous n'avez pas eu la voie royale pour commencer dans la recherche. Néanmoins, quand je vois comme vous avez progressé depuis je ne me fais pas trop de soucis pour la suite. Enfin, comment parler de l'équipe circuit supraconducteur sans parler de ces membres permanents Cécile, Wiebke et surtout Olivier et Nico mes superviseurs. Olivier, c'est un honneur pour moi d'avoir pu travailler avec toi. Scientifiquement, ta profonde connaissance des débuts des circuits supraconducteurs aura été d'une grande aide pour mon projet. Humainement, j'ai pris beaucoup de plaisir à discuter avec toi de choses aussi variées que la politique, l'économie, les pays sud-américains et j'en passe. C'est rare de rencontrer quelqu'un avec une telle honnêteté intellectuelle. Nico, merci de m'avoir fait confiance dès le début de ma thèse alors que j'avais, et que j'ai encore, tout à prouver. Merci, de m'avoir aiguillé, mais aussi de m'avoir laissé libre quand il le fallait. Ton optimisme contrastait avec mon pessimisme, ce qui fait, à mon sens, que le duo a plutôt bien fonctionné. Cela m'a aussi appris qu'il y a toujours une façon de retomber sur ces pieds même, et surtout, quand rien ne marche

Comment parler de ma thèse sans parler de la formidable équipe de théoriciens avec laquelle j'ai pu travailler. Serge, le fait que tu aies pu aussi simplement nous introduire aux outils théoriques permettant d'expliquer nos expériences est formidable. Tu es définitivement le théoricien le plus pédagogue que j'ai pu rencontrer pendant cette thèse. Denis, ta réputation te précédait, mais cela ne m'a pas empêché d'être abasourdi quand tu es revenu nous voir avec un modèle expliquant les pertes de notre système seulement quelques jours après que l'on t'ait présenté notre système. Théo, tout d'abord je te remercie d'avoir passé autant de temps à m'expliquer comment calculer des diagrammes de Feynman, ou du moins les plus simples ! Ensuite, félicitation pour les derniers résultats ! Qui d'autre aurait pu passer près d'un an à analyser ces données sans perdre espoir ? Finally, thank you, Izak for accepting to calculate all kind of quantities, from the most trivial to the most complex. And more globally, thank you for all these exciting discussions. Je salue aussi Manuel, Alain Joye et Benoît Vermersch pour les nombreux échanges scientifiques que l'on a pu avoir.

Comme la thèse pousse à vouloir travailler toujours plus il était important de trouver un équilibre. Pour se faire, j'ai pu compter sur tout un tas d'individus plus ou moins respectables. Tout d'abord les membres honoraires de la coloc des Narvals : Roméo, Titiksha, Papotin et Roumzy. Mais aussi les psycho-pot (d'après Jovian): Suzy, Stef, Pierre et Margot. Ensuite, les quelques potes qu'il me reste de Phelma : Axel, Mael, Thomas, Xav et Antoine. Sans oublier la fine fleur de Cherbourg. Merci, pour toutes ces soirées, ces pétanques, ces randos et j'en passe. Si j'étais réticent en arrivant à Grenoble je vais maintenant avoir bien du mal à partir.

Enfin, je ne peux pas conclure autrement qu'en remerciant ma famille. Me supporter pendant 26 ans ce n'est pas donné à tout le monde, j'ai moi-même bien du mal. Plus particulièrement, je remercie mes parents, pour m'avoir tout donné pendant toutes ces années. D'avoir accepté très tôt de me donner beaucoup de liberté, de m'avoir fait confiance et d'avoir été exigeant avec moi. Mes grands-parents pour m'avoir transmis des valeurs et des connaissances qui me guident tous les jours dans mes décisions.

Contents

1 Introduction and summary 1
1.1 Introduction . . . 1
1.2 Summary . . . 6
1.2.1 Theoretical predictions . . . 6
1.2.2 Experiment . . . 7
1.2.3 Manuscript . . . 14
1.2.4 Author's contribution . . . 14

2 Introduction et résumé 17
2.1 Introduction . . . 17
2.2 Résumé . . . 22
2.2.1 Prédictions théoriques . . . 22
2.2.2 Expériences . . . 24
2.2.3 Organisation du manuscrit . . . 30

3 Theory 31
3.1 Circuitry . . . 32
3.1.1 The Josephson Junction . . . 32
3.1.2 The Environment . . . 37
3.2 Boundary Sine Gordon . . . 49
3.2.1 Even and odd modes circuit . . . 49
3.2.2 Boundary Sine Gordon Ground State within the Self Consistent Harmonic Approximation . . . 51
3.2.3 Normal mode decomposition . . . 54
3.2.4 Phase mode profil . . . 56
3.3 How to design a complex Hamiltonian ? . . . 58
3.3.1 Link between response function and phase fluctuations. . . . 58
3.3.2 Toy model for the phase fluctuations . . . 59
3.4 Renormalisation of the nonlinear junction. . . . 62
3.4.1 Influence of the nonlinear junction impedance. . . . 63
3.4.2 Influence of the chain impedance. . . . 63
3.4.3 Influence of the chain plasma frequency. . . . 64
3.4.4 Influence of the temperature of the system. . . . 65
3.5 Phase shift . . . 66
3.5.1 Analytical expressions . . . 66
3.5.2 Link with other quantities. . . . 68
3.5.3 An illustration of the thermodynamic limit . . . 71
3.6 Backaction on the environment modes . . . 72
3.6.1 Comparison between the SCHA and the Kerr approximation . . . 72

3.6.2 Damping induced by the nonlinear junction - Photon conversion. . . . 75

4 Experimental Setup and Fabrication 87
4.1 Thermalisation and Filtering . . . 88
4.1.1 Preamble . . . 88
4.1.2 Different kinds of attenuators . . . 88
4.1.3 The microwave setup . . . 92
4.1.4 Radiative and magnetic shielding . . . 96
4.2 Temperature regulation . . . 97
4.3 Fabrication . . . 97
4.3.1 Bridge Free fabrication technique. . . . 98
4.3.2 DC measurement on test structures . . . 99

5 Renormalization of the nonlinear junction 103
5.1 Fixed nonlinearity . . . 104
5.1.1 Sample presentation . . . 104
5.1.2 Transmission measurement . . . 105
5.1.3 Dispersion Relation . . . 107
5.1.4 Phase shifts . . . 112
5.1.5 Renormalization as a function of temperature . . . 115
5.1.6 How many modes contribute ? . . . 117
5.2 Tunable nonlinearity . . . 120
5.2.1 Sample presentation . . . 121
5.2.2 Flux tunability . . . 122
5.2.3 Dispersion relation . . . 122
5.2.4 Josephson relative phase shift . . . 124
5.2.5 Renormalization with respect to the nonlinearity . . . 127

6 Dissipation induced by the nonlinear junction 131
6.1 Dissipation with respect to various parameters . . . 132
6.1.1 Dissipation with respect to the magnetic flux . . . 132
6.1.2 Dissipation with respect to the input power . . . 132
6.1.3 Dissipation with respect to frequency . . . 135
6.2 Theory-Data agreement . . . 137
6.2.1 Photon conversion broadening . . . 138
6.2.2 Other loss mechanisms . . . 139

7 Conclusion and Perspectives 145
7.1 Conclusion . . . 145
7.2 Perspectives . . . 146
7.2.1 Conclude on the SCHA temperature problem . . . 146
7.2.2 Measuring direct evidence of photon conversion . . . 146
7.2.3 Investigating the superconductor-insulator transition . . . 147

Appendices 149

A Calculation 151
A.1 Charge offset . . . 151

A.2 SCHA for the nonlinear oscillator . . . 153
A.3 Mode Envelope Normalization . . . 154
A.4 Self Consistent Harmonic Approximation . . . 155
A.5 Response function and noise spectral density . . . 156
A.6 Response function and toy model . . . 157
A.7 Link between the total impedance and the response function 158
A.8 Link between $\mathrm{Im}\, G_{\phi_0}(\omega)$ and $\chi''_{\phi_0}(\omega)$ . . . 158
A.9 Derivation of $\Sigma^{(2)}$ . . . 159
A.10 $G^{(0)}_{\phi_0}$ in the vicinity of a mode . . . 163
A.11 Fourier transform of the approximate formula for $\Sigma^{(2)}$ . . . 163

B Fabrications 165
B.1 Recipe . . . 166
B.2 Different designs of junction . . . 166

C Spectroscopy 169
C.1 Spectroscopy of a resonator . . . 169
C.1.1 In line resonator . . . 169
C.1.2 Hanging resonator . . . 171
C.2 Calibration of the background for the hanging resonator. . . . 172

D Microwave simulation - Capacitance estimation 173
D.1 Circuit modeling . . . 173
D.2 Microwave simulation . . . 173

E SQUID chain 177

F Supplementary information for the Renormalization 179
F.1 Does the capacitive pads affect the relative phase shifts ? . . . 179
F.2 Even and odd modes fits . . . 180
F.3 Splitting fits . . . 181
F.4 Effective Temperature . . . 181
F.5 Response function for the second circuit design . . . 184

G Supplementary information for the mode damping 187
G.1 Toy model for the losses induced by the junction γ_J . . . 187
G.2 Internal broadening versus the photon number. . . . 188

Bibliography 190

Introduction and summary 1

The work done during this PhD focused on dissipation phenomenon in quantum mechanics. Dissipation occurs when a quantum system couples to an environment. The most striking effect of this dissipation is the loss of coherence induced on the system. Because of this loss of coherence a quantum system can lose its quantum character and behaves as a classical object. In this sense, dissipation can be seen as the mechanism at the interface between classical and quantum physics. If these questions have fundamental implications they also have practical ones. We can think about the realization of quantum computers where coherence loss is a major problem. During this PhD we focused on the interaction between a quantum degree of freedom, a nonlinear oscillator, coupled to a strongly dissipative environment. Although this problem seems simplistic, it is at the heart of a very rich but poorly understood physics ranging from the non-perturbative renormalization of the oscillator parameters, to the generation of dissipation via non-trivial photon conversion phenomena, passing by the physics of quantum phase transition. The investigation of this new physics is made possible by the particular nature of the engineered environment, at the interface between a continuum and a discrete one, allowing us to question how does an environment induce dissipation. In this section we will first review the state of the art on the use of Josephson junctions to address quantum dissipative systems. This will allow us to introduce the key concepts of such problems. A summary of the work done during this PhD will then be provided.

1.1 Introduction

Since the pioneering work of B.D. Josephson [1, 2], the superconducting tunnel junction, also called *Josephson junction*, has become of fundamental importance for testing different hypotheses in quantum mechanics. Such success is based on two properties, simple at first glance, but with important consequences. The first comes from the use of superconducting materials, allowing these junctions to be relatively well decoupled from any source of dissipation. The second, comes from the nonlinearity of such junctions, allowing to make predictions that could not be obtained from a classical model. This is the so-called *correspondence limit*. This last assertion can be verified by using Ehrenfest theorem on a degree of freedom $\hat{x}$ of momentum $\hat{p}$ in a potential V. It states that:

$$\frac{d}{dt}\langle\hat{p}\rangle = -\langle\frac{d}{dx}V\left(\hat{x}\right)\rangle \tag{1.1}$$

On the other hand, using Newton's second law, which is its classical counterpart, we obtain:

$$\frac{d}{dt}\langle\hat{p}\rangle = -\frac{d}{dx}V\left(\langle\hat{x}\rangle\right) \tag{1.2}$$

Hence, since $\frac{d}{dx}V\left(\langle\hat{x}\rangle\right)$ and $\langle\frac{d}{dx}V\left(\hat{x}\right)\rangle$ are equal for a quadratic potential, or equivalently a linear system, we do not expect to see a difference between the quantum and the classical prediction. It is not the case if the potential is nonlinear.

Now that we have seen why the fundamental properties of Josephson junctions make them so attractive for the study of quantum problems we will discuss the variables and parameters governing their dynamics with the help of the seminal work on Macroscopic Quantum Tunneling (MQT). A Josephson junction is described by two conjugate variables: the number $\hat{n}$ of Cooper pairs transferred across the junction and the superconducting phase difference $\hat{\phi}$ between the two superconducting leads. The observation of the MQT of $\hat{\phi}$ is probably the first experimental demonstration [3, 4][a] showing the potential of Josephson junctions to test the quantum theory, validating that despite its macroscopic nature $\hat{\phi}$ could be treated as a quantum degree of freedom. Hence, these junctions could be used as full-fledged quantum objects, paving the way towards circuit QED [6]. In addition, this pioneering work also studied the influence of dissipation on the quantum tunneling and therefore proved that Josephson junction was a good platform to study *quantum dissipative systems*. Indeed, even though a junction is naturally protected against dissipation, it is not entirely immune to it. In a good approximation, this dissipation can be modeled as a shunt resistor R. That resistance has to be compared to the junction impedance. Despite being an anharmonic oscillator, a Josephson junction with Josephson energy E_J and charging energy E_c, can be associated to an impedance $Z_\mathrm{J} = Z_\mathrm{q}/(2\pi)\sqrt{E_\mathrm{c}/E_\mathrm{J}}$ where $Z_\mathrm{q} = h/(2e)^2 \simeq 6.5\,\mathrm{k\Omega}$ is the superconducting quantum of resistance. If $R \gg Z_\mathrm{J}$ the junction is said to be underdamped while in the opposite situation the junction is overdamped. A. O. Caldeira and A. J. Leggett, using a their famous effective model, predicted that, in both regime, the shunt resistance will reduce the phase fluctuations and hence the quantum tunneling rate [7]. A. I. Larkin and Yu. N. Ovchinnikov were able to reproduce these findings from a microscopic modeling of the junction [8], using previous results from Ambegaokar and coworkers [9]. Such a model was latter improved by A. D. Zaikin and S. V. Panyukov [10]. Experiments presented in [3] and [4] confirmed these predictions respectively in the deep underdamped and overdamped regimes by measuring the tunneling rate of $\hat{\phi}$ as a function of the temperature.

Nevertheless, until then, dissipation was treated as a perturbation. Later on, the use of renormalization group allowed to free this constraint and predicted that a Josephson junction coupled to its environment should undergo a *superconductor-isolator transition*, also called Schmid-Bulgadaev transition [11, 12]. A Josephson junction can indeed be seen as a particle of position $\hat{\phi}$ and momentum $\hat{n}$, trapped in a nonlinear periodic potential $E_\mathrm{J}\cos\hat{\phi}$. Depending on the dissipation strength, this particle might then tunnel between the potential energy minima thanks to its *zero point energy*, even at T=0. According to the renormalization group theory, the introduction of dissipation has two opposite consequences. If $R < Z_\mathrm{q}$ the phase fluctuations

[a] These are not really the first experiments measuring macroscopic quantum tunneling, see for example [5]. However, these are the first experiments where the extraction of all the parameters of the circuit was possible. Allowing a quantitative description of the MQT with respect to various parameters.

$\langle\hat{\phi}^2\rangle$ are damped and finite. Therefore, the amplitude of the potential E_J is lowered, or conversely *renormalized*, to $E_J^\star$ signaling that the particle position fluctuates and therefore has a finite zero point energy, contrary to a classical one. However, the phase fluctuations are not large enough for the particle wavefunction to tunnel between the potential minima. The particle is said to be *localized* in the phase space. In such regime the junction resistance is zero at zero current bias[b] and is therefore superconducting. On the other hand, if $R > Z_q$ the theory predicts that the potential is renormalized to zero, signaling that the particle is *delocalized*. Therefore, the junction acts as a non-superconducting tunnel barrier and a finite resistance is expected at zero current bias because of Coulomb blockade[c]. Taking advantage of the particle analogy, the superconductor-isolator transistion is also called *localized-delocalized transistion*. Attempts were made to reproduce the phase diagram foreseen by the theory [14, 15] but were plagued by either heating effect or by the finite accuracy of the measurement setup. Closely related researches were carried out by D. B. Haviland and coworkers who measured Bloch oscillations of Cooper pairs [16], that were expected to be another consequence of the particle model of a Josephson junction [17]. However, because of the difficulty of unambiguously measuring the predicted phase diagram, modeling the effect of dissipation on a junction, and thus the resulting phase transition, remains subject to debate [18].

Despite both theoretical and experimental advances made possible by the study of Josephson junctions, a more direct proof that its dynamics is governed by the laws of quantum mechanics was missing. This clear-cut evidence was provided by the measurement of the coherent tunneling of wavefunctions in the charge space in NEC laboratories [19][d]. This device consisted in a junction in the $Z_J \gg Z_q$ regime wired to a capacitance such that the two form a superconducting island. By setting the offset charge of the island to half the one of a Cooper pair, two states, corresponding to combinations of the two neighboring charge configurations, can be manipulated. Therefore, the coherent manipulation was made possible because of the strong nonlinearity of the junction where two levels could be isolated from the others. Because of that such systems can be seen as a *qubits*. After that, an ever-increasing number of qubits were invented and measured. Some of them being based on coherent tunneling between two minima in the charge space, the Cooper pair box previously introduced or the Quantronium [22]. Or in the phase space, the flux qubit [23–26] or the fluxonium [27]. While others are based on the manipulation of two isolated intrawell states such as the phase qubit [28, 29] and the Transmon qubit [30].

Inspired by the Cavity QED field [31, 32], this new devices were coupled to a resonator enabling their non destructive and efficient readout [33–37]. This was made possible because the strong coupling regime, where the coupling g between the qubit and the resonator is larger than the losses γ at the qubit level, can be reached easily. In circuits the coupling is done via the charge or the phase. This coupling is proportional to the square root of the fluctuations of the corresponding variable [38, 39] that

[b] It is coming from the fact that if the particle is localized then the phase is constant over time and therefore no voltage can build up across the junction. Here we neglected other source of dissipation, such that quasiparticles for the sake of clarity

[c] It is interesting to note that the predicted transition does not depend on the junction impedance, or conversely its E_J/E_C ratio while the calculations where made for $Z_J \gg Z_q$ or $Z_J \ll Z_q$ where the transition lies on different physical interpretations [13]

[d] The first fabrication of such a device was done in Saclay [20], inspired by a proposal of M. Buttiker [21]

itself depends on respectively $1/Z_r$ or $1/Z_r$, where Z_r is the characteristic impedance of the resonator. Hence, the coupling in these circuits is nothing but a matter of design. The ultrastrong coupling, where the coupling g is between 0.1 and 1 time the qubit frequency ω_q, leading to a rotating wave approximation breakdown, was then reached [40, 41]. Finally, the deep strong coupling regime, where g is larger than ω_q, leading to a strong renormalization of the qubit parameters was observed [42]. This renormalization is closely related to the previously introduced localized-delocalized transition where the localization in one potential minima is replaced by the suppression of quantum tunneling between the two qubit states and the resistance is replaced by the resonator impedance.

In parallel, the coupling between a flux qubit and an open $50\,\Omega$ transmission line (and hence to a broadband environment) was implemented [43, 44], opening new perspectives for the study of quantum dissipative systems. Indeed a qubit coupled to a broadband environment can be used to study a class of quantum dissipative system called *quantum impurity problems*, such as the spin-boson [45, 46] and the Kondo problem. The first experiments were in a coupling regime such as the techniques used to describe their properties were borrowed from quantum optics [47–49]. However, a breakthrough was made when such circuits reached the deep strong coupling regime [50, 51][e]. In these experiments a non perturbative renormalization of ω_q was observed, signaling that the circuit could no longer be described using quantum optics tools. The circuits described so far were based on a flux qubit coupled to a low impedance environment in order to reach coupling such that the circuit was highly non trivial and belongs to the quantum impurity class. This was the most straightforward approach since the design of $50\,\Omega$ transmission lines has been mastered for a long time. Another option to study quantum impurity problems is to use a charge qubit coupled to a broadband environment [54–56]. The first implementation of these ideas relied on a Transmon qubit coupled to a $50\,\Omega$ line [57, 58], and later to a long resonator [59]. Contrary to a $50\,\Omega$ line, a resonator has boundaries that lead to the formation of resonant modes. The frequency spacing between these modes, called free spectral range $\Delta\omega_{FSR}$, is inversely proportional to the resonator length. For the experiment previously cited it was about 100 MHz since the resonator was more than half-a-meter long. It is known, according to the Jaynes-Cummings model [60], that the coupling between a qubit and a multimode environment increases with the mode index. However, because the characteristic impedance of the resonator was low, and since the coupling is proportional to that latter for a charge coupling, no ultrastrong coupling effects could be observed. Nevertheless, using a multimode resonator instead of a transmission line represents an interesting paradigm shift for the study of dissipative systems: not only the influence of the environment on the nonlinear system, formed by a nonlinear oscillator or a qubit, can be studied but the opposite is also possible. In other words, the dissipative element can be coupled to a nonlinearity and both being weakly coupled to the measurement apparatus, making a coherent manipulation of the complete system possible.[f]

Ultrastrong coupling between a Transmon qubit and a few modes resonator could

[e] Two goods reviews can be found on this different coupling regimes [52, 53]

[f] Recently a group implemented the coupling between a Transmon qubit and a multimode 3D cavity [61] which should make the coherent manipulation of such system easier because such modes are strongly decoupled from any source of dissipation, however the system is slightly below the super strong coupling (defined in the following) and the nonlinearity is weak because of the use of a Transmon qubit.

be reached by a careful design of the coupling element [62]. However, increasing further the coupling requires high impedance environment. It took a long time to design and build high impedance environments because of the given values of the relative permittivity and permeability of vacuum [38]. To circumvent this, *Josephson junction chains* were used. A junction used in the linear regime, where $Z_\mathrm{J} << Z_\mathrm{q}$, can be seen as a harmonic oscillator with an inductance $L_\mathrm{J} \propto 1/E_\mathrm{J}$. Since the junctions have a small footprint they can be compactly cascaded to form a meta-material were the inductance per meter is orders of magnitude higher than the one obtained using conventional material. Since their characteristic impedance is proportional to this inductance the resulting chains will constitute a high impedance material. Finally, because of its high impedance, such a chain will be impedance mismatched with the measurement setup, which is $50\,\Omega$ matched. This chain therefore forms a resonator. The free spectral range $\Delta\omega_\mathrm{FSR}$ depends then on the number of junction that can be cascaded. The first implementation of these chains were fabricated with junction in the nonlinear regime to study quantum phase slips [63–65]. They were then used in the linear regime [49, 66]. Our team was the first to couple a Transmon and these chains [67]. We used a chain of SQUID instead of simple junctions to tune in situ the coupling between the two parts of the circuit. In this experiment, the coupling g had the same order of magnitude than $\Delta\omega_\mathrm{FSR}$ but was still one order of magnitude lower that the qubit frequency ω_q. Shortly after, a coupling such that $g > \Delta\omega_\mathrm{FSR}$, called superstrong coupling, was reported thanks to the use of a longer chain and to a different coupling scheme [68]. In this regime, the qubit mediates interactions between the resonator modes such that the circuit can be considered as a complex many body problem [69].

Nevertheless, even if reaching the deep strong coupling was technically possible, it turns out that the nonlinearity of the Transmon was diluted in the modes. To put it another way, at higher coupling the number of coupled modes would increase and hence the Transmon would have to share its nonlinearity with even more modes, resulting in a linear problem. Because of that, it was recently shown that the localized-delocalized phase transition expected for the spin boson model [46] can not be observed with a Transmon circuit with realistic parameters [70]. According to this paper, a possible strategy to circumvent this problem is to directly wire a Josephson junction to the high impedance medium and therefore to get ride of the coupling capacitance[g]. However, by doing so the system under study no longer implements the spin-boson model but the Boundary Sine Gordon (BSG) one [71]. As a conclusion, by doing so, we shall study a nonlinear junction wired to a dissipative element that mimics an impedance, coming back to were the introduction started. The main difference being that the dissipative element is no longer an actual resistance but a multimode resonator, forming a quasi-continuum. This quasi-continuum imitates perfectly a continuum if the broadening of its modes γ_r is larger to its free spectral range $\Delta\omega_\mathrm{FSR}$, or, in the time domain, if the round-trip time of an excitation in the multimode resonator is longer than the time required for this excitation to decay out of the system[h]. However, this would amount to measuring a nonlinearity coupled to an open system and we lose the possibility to study the backaction of the nonlinearity on its environment. Hence, γ_r has to be kept below $\Delta\omega_\mathrm{FSR}$ and if $\gamma_\mathrm{r} \ll \Delta\omega_\mathrm{FSR}$ even coherent manipulations become possible. Because of its frequency distribution, a quasi-continuum seems to be a more

[g] That is how the charge coupling was implemented in such circuits

[h] γ_r can either come from the measurement setup or from uncontrolled losses channels

complex problem to study than a continuum. Nevertheless, as we shall see, if the characteristic time of the studied phenomena, that can be the damping time induced by the environment on the nonlinearity[i], is short compared to the round-trip time of a photon then the quasi-continuum behaves like a continuum.

1.2 Summary

This work aimed at measuring the interaction between a nonlinear Josephson junction and a quasi-continuum formed by a Josephson junction chain. In particular, we studied the influence of different parameters, such as the nonlinearity of the junction and the circuit temperature, on the nonlinear junction Josephson energy. In a second time, we also studied the backaction of the nonlinear junction on the discrete modes of the quasi-continuum.

1.2.1 Theoretical predictions

In the first chapter we prove that the main properties of our circuit are related to the dissipative part of the nonlinear junction phase response function χ''_{ϕ_0}. We show that in the thermodynamic limit, meaning when the number of junctions in the chain goes to infinity, the response function is given by (see Section 3.3.1):

$$\chi''_{\phi_0}(\omega) = \frac{\pi}{2\hbar\Delta\omega_{\mathrm{FSR}}(\omega)}\xi_0(\omega)^2 \tag{1.3}$$

where ξ_0^2 are the phase zero point fluctuations (ZPF) induced by the chain across the nonlinear junction as a function of the frequency and $\Delta\omega_{\mathrm{FSR}}$ is the free spectral range of the chain modes, which can also depend on the frequency. This quantity is maximal at the damped renormalized frequency of the nonlinear junction $\omega_{\mathrm{d}}^\star = \sqrt{\omega_{\mathrm{J}}^{\star 2} - (\gamma_{\mathrm{RC}}/2)^2}$ in the underdamped regime (see Section 3.3.2). Where $\omega_{\mathrm{J}}^\star$ is the renormalized junction frequency, because of the junction nonlinearity, and γ_{RC} is the damping induced by the quasi-continuum[j]. The full-width at half maximum (FWHM) of the response function is given by this damping.

Influence of the environment on the nonlinear junction

When coupling the nonlinear junction to the chain, phase fluctuations are induced over the environment bandwidth. These fluctuations lead to a renormalization of the Josephson energy. This renormalization can be estimated using the Self-Consistent Harmonic Approximation (SCHA, see Section 3.2.2):

$$E_{\mathrm{J}}^\star = E_{\mathrm{J}} e^{-\langle\hat{\phi}_0^2\rangle_{\mathrm{t}}/2} = E_{\mathrm{J}}\exp\left[-\sum_{k=0}^{N}\frac{\xi_{0,k}^2}{2}(n_k+\tfrac{1}{2})\right] \tag{1.4}$$

where E_{J} is the bare Josephson energy, $\xi_{0,k}^2$ are the phase fluctuations induced by a chain mode of frequency ω_k and n_k is the thermal occupation of this mode. This

[i] In the frequency domain it means that the damping rate γ_{d} has to be much larger than $\Delta\omega_{\mathrm{FSR}}$.

[j] γ_{RC} is not frequency dependant only if we neglect the plasma frequency of the chain (see Section 3.3.2 and Appendix A.6)

equation is self-consistent since ω_k, and therefore $\xi^2_{0,k}$, depends on the values of $E^\star_\mathrm{J}$ via the phase shift it induces (see Section 3.2.3). From this equation, we see that the renormalization is linked to the response function via the phase fluctuations. We can also see that is the renormalization increases, or conversely that the Josephson energy decreases, when the ZPF of phase are increased. It is also the case if the thermal occupation of the modes is increased via heating, since the thermal part of the fluctuations increases. From the renormalized Josephson energy we can define the nonlinear junction frequency as $\omega^\star_\mathrm{J} = \sqrt{2E^\star_\mathrm{J}E_\mathrm{C}}$ (see Section 3.1.1) where E_C is the charging energy of the junction[k]. This expression is valid only for $E_\mathrm{J} \gtrsim E_\mathrm{C}$.

Backaction of the nonlinear junction on the modes: the photon conversion processes

In addition to the renormalization of E_J coming from the interaction between the nonlinear junction and the chain we studied the backaction of the junction on the modes. More specifically, we show that the nonlinear junction induces dissipation in the chain modes (see Section 3.6.2). This dissipation translates in a mode broadening in the frequency space, given by:

$$\gamma_k = \Sigma^{''}(\omega_k)\xi^2_{0,k} \tag{1.5}$$

where γ_k is the broadening of the mode k and $\Sigma^{''}(\omega_k)$ is the complex part of the self-energy. The self-energy comes from the junction nonlinearity. It couples single-photon-states to multi-photon-states. Because of that these single-photon states can decay into multi-photon states and hence are called photon conversion processes. Because of these processes the single-photon states acquire a finite lifetime and the modes broaden in the frequency space.

1.2.2 Experiment

The samples

To study the effects previously introduced we implemented two kinds of circuits. The first one consists in a nonlinear Josephson junction of characteristic impedance on the order of Z_q ($E_\mathrm{J}/E_\mathrm{C} \lesssim 1$), embedded in the middle of two SQUID chains, each consisting of 1500 unit cells (Figure 2.1). Nevertheless, the magnetic flux control of these SQUIDs has not been used. Therefore, they will be considered as junctions. The chains are capacitively coupled to the measurement setup to suppress DC noise which could affect the nonlinear junction. Because of its symmetry the circuit can be decomposed into two sub-circuits (see Section 3.2.1). The first one contains the nonlinear junction galvanically connected to a chain of characteristic impedance $2Z_\mathrm{C}$, where $Z_\mathrm{C} = \sqrt{L/C_\mathrm{g}}$. This sub-circuit corresponds to the BSG model. The second one consists in a bare chain of characteristic impedance $2Z_\mathrm{C}$. These sub-circuits sustain modes called respectively odd and even. From the measurement of these modes we were able to measure the nonlinear junction frequency $\omega^\star_\mathrm{J}$ for three samples corresponding to different nonlinearity regimes and various temperature (see Section 5.1.2) as it will be shown in the next section.

[k] Where $E_\mathrm{C} = (2e)^2/(2C_\mathrm{J})$, C_J being the junction capacitance

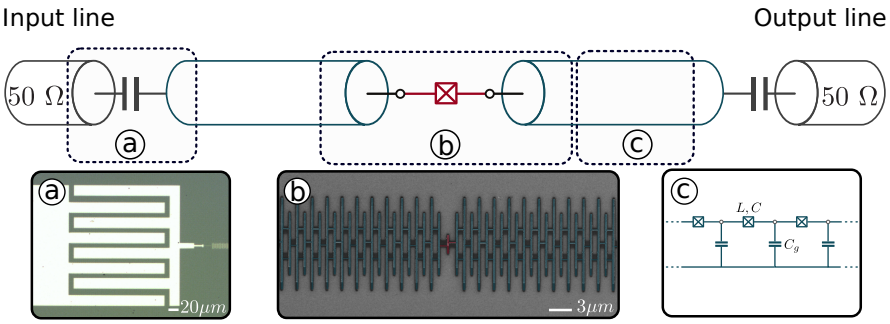

Figure 1.1 – Schematic of the first designed circuits. The SQUID chains, depicted as blue transmission lines, are capacitively coupled to the input and output 50 Ω coaxial cables and galvanically coupled to the nonlinear Josephson junction (in red). **a** Optical picture of the input and output capacitive coupling pads. **b** SEM picture of a few of the SQUIDs (1500 in total for each chain) that are coupled to the nonlinear Josephson junction (in red). **c** Equivalence between the transmission line effective picture and the SQUID chain characterized by three microscopic parameters L and C the inductance and capacitance per SQUID respectively and C_g the ground capacitance.

The second designed circuit is a nonlinear SQUID galvanically coupled to a junction chain, made of 4250 cells. The chain is galvanically coupled at its left to a 50 Ω micro-strip feed-line while the nonlinear SQUID is grounded at its right. Because of that, the circuit can be seen as a hanging resonator. That geometry is more convenient for a quantitative study of the mode damping (see Appendix C.1.2). In addition, the use of a SQUID allowed us to tune in situ the SQUID nonlinearity by applying a magnetic flux. This circuit is a direct implementation of the BSG Hamiltonian since there are no more Odd and Even modes. This design choice was made so that the mode damping (or equivalently the quality factor) was easier to extract because only one family of modes is kept (see Section 5.2) while the number of junctions in the chain is increased by a factor 4. Therefore, the quasi-continuum formed by the chain is closer to the thermodynamic limit compared to the previous design.

Temperature dependence

From the spectroscopy of the first designed circuit we could measure the nonlinear junction frequency for three samples, denoted A, B and C, corresponding to three nonlinearities (from the largest to the smallest), as a function of the circuit temperature (see Section 5.1.5). The results are reported in the left panel of Fig.2.3. The experimental data correspond to the dots, their error bars are given by the shaded areas. The black curves correspond to the SCHA estimation. The dashed lines are the estimated junctions frequency when discarding the quantum part of the phase fluctuation, meaning by using:

$$\langle \hat{\phi}_0^2 \rangle (T)_{\text{no ZPF}} = \sum_{k=0}^{N} \frac{|\xi_{0,k}|^2}{2} n_k \tag{1.6}$$

in Eq.2.4. By comparing this two quantities we can see the relative contribution of the thermal and quantum fluctuations. For the three samples the frequency decreases

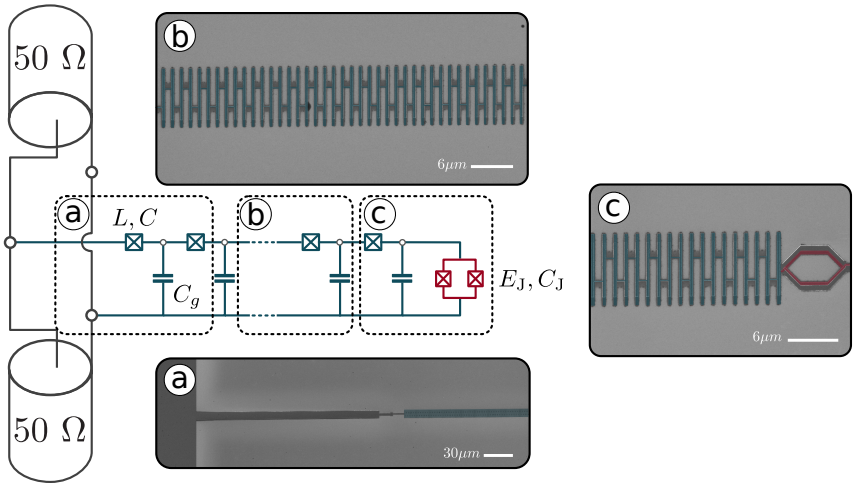

Figure 1.2 – Schematic of the second designed circuit. The chain, depicted in blue, is characterized by its three parameters L, C and C_g. The chain is terminated by a nonlinear SQUID, depicted in red and characterized by its two parameters E_J and E_C. **a** SEM picture of the galvanic coupling between the chain and the 50 Ω microstrip feed-line. The two are coupled such that the circuit forms a hanging resonator. **b** SEM picture of the chain composed of 4250 sites. **c** SEM picture of the galvanic coupling between the chain and the nonlinear SQUID. The junction is grounded at its right.

when the temperature increases. This is expected since the thermal fluctuations increase with the temperature (see Eq.2.4). Therefore, the renormalization increases and the junction frequency decreases. This downward renormalization with respect to the temperature is more important for sample A and is less and less pronounced from sample A to C. This is because the junction frequency of sample A is lower than sample B which is itself lower than sample C. Hence, the nonlinear junction in sample A is more coupled to the lowest modes, which are more sensitive to the temperature (see Section 3.4.4 and especially Figure 3.18).

This explanation is confirmed by the study of the dissipative part of the phase response function of the nonlinear junction in the frequency domain. The result of this study is shown in the right panel of Fig.2.3. The plain lines are the response functions in the thermodynamic limit resulting from the use of $\xi^2_{0,k}$, using both from the nonlinear junction frequency and the chain parameters estimation, in Eq.2.3. The vertical lines correspond to the value of $\omega_J^\star$ estimated from the previous study. Both the damped frequency of the nonlinear junction $\omega_d^\star$ and the FWHM γ_{RC} can be extracted form the response function. The shift between the renormalized frequency estimated from the SCHA $\omega_J^\star$ and the damped frequency $\omega_d^\star$ (maximum of the response function) increases from sample C to A. This can be explain from the fact that the damping increases from sample C to A (see Tab.5.3). Hence, from our formalism we can distinguish the renormalization coming from the ZPF, given by $\omega_J - \omega_J^\star$, and the one coming from the coupling to a thermodynamic bath, given by $\omega_d^\star - \omega_J^\star$.

From these two studies we see that the designed circuits constitute a complex many body problem displaying a non perturbative renormalization of the Josephson energy of the nonlinear junction, and therefore of its resonant frequency. The maximal renormalization was obtained for sample A for which the $E_J^\star/E_J$ ratio was about 0.5.

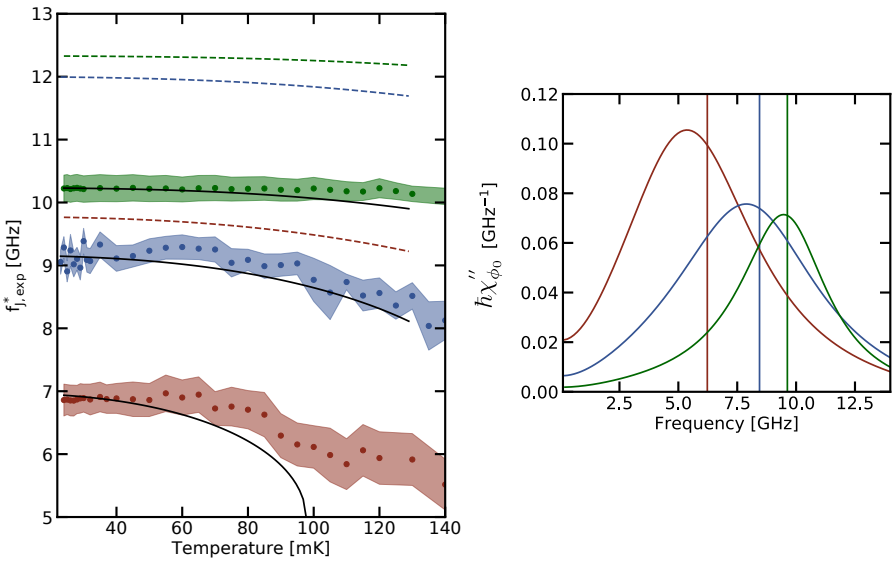

Figure 1.3 – **Left.**Renormalized frequency of the nonlinear junction as a function of the temperature for sample A (red), B (blue) and C (green). The dots are the values extracted from the spectroscopy measurements, the shaded areas are the corresponding error bars. The black lines are the result from the fit using the SCHA while the dashed lines represent what would be the temperature evolution of these frequencies if the ZPF were omitted from $\langle\phi_0^2\rangle$. **Right.** Dissipative phase response function of the nonlinear junction with respect to frequency. The plain lines are the response functions given from Eq.2.3 in the thermodynamic limit. The vertical line denote the position of $\omega_{\mathrm{J}}^{\star}$. The shift of the damped frequency $\omega_{\mathrm{d}}^{\star}$ with respect to $\omega_{\mathrm{J}}^{\star}$ increases from almost zero to 1 GHz from sample C to A.

To reproduce such a result from our model at least 30 chain modes had to be taken into account. This is due to the fact that the damping induced by the environment has the same order of magnitude than the junction frequency and that the free spectral range of the chain mode is one order of magnitude smaller that these two. From the value of γ_{RC} and $\omega_{\mathrm{d}}^{\star}$ extracted we can see that the nonlinear junctions are in the so-called deep strong coupling regime since the ratio between the two is about one [52, 53] for the three samples. Note that this regime has been defined in the context of the Spin Boson model and very little is known about such a regime for the BSG model. Nevertheless, a recent paper shows that a mapping exists between the two systems [70]. Therefore, we can safely say than reaching such a regime is an important step toward the observation of phenomena analoguous to the predictions made in such a regime for the Spin Boson Hamiltonian [55, 72–75]

Nonlinearity influence

The spectroscopy of the second circuit design was used to study more systematically the influence of the junction nonlinearity on the renormalization. The renormalized Josephson energy as a function of the bare one is shown in the left panel of Fig.2.4. The dots corresponds to the experimental data, the grey line is the estimation form the SCHA. The dashed line is a guide to the eyes corresponding to the bare value of the Josephson energy. From this, we can see that the renormalization increases

when the bare Josephson energy decreases. That can be understood from the fact that when the potential barrier is lowered the phase fluctuations increase, leading to a larger renormalization. We see that for the smallest values of E_J the ratio $E_J^\star/E_J$ is between 0.2 and 0.1 (for exemple at $E_J = 1\,\text{GHz}$ we have $E_J^\star = 0.2\,\text{GHz}$). Hence, the renormalization is strong enough to almost suppress the Cooper pair tunneling across the nonlinear SQUID. This interpretation is confirmed in the right panel of Fig.2.4. This panel shows the nonlinear junction phase fluctuations as a function of $Z_J^\star/Z_C$, where $Z_J^\star$ is the renormalized SQUID impedance, defined as $Z_J^\star = Z_q/2\pi\sqrt{2E_C/E_J^\star}$ and Z_C is the chain impedance. The phase fluctuations are obtained from the SCHA, using:

$$\langle\hat{\phi}_0^2\rangle = 2\ln\left(\frac{E_J}{E_J^\star}\right) \tag{1.7}$$

where $E_J^\star$ corresponds to experimental data and E_J is the bare Josephson energy estimated from the previous fit. This panel confirms that the phase fluctuations increase with the nonlinear SQUID impedance, or equivalently with the SQUID nonlinearity.

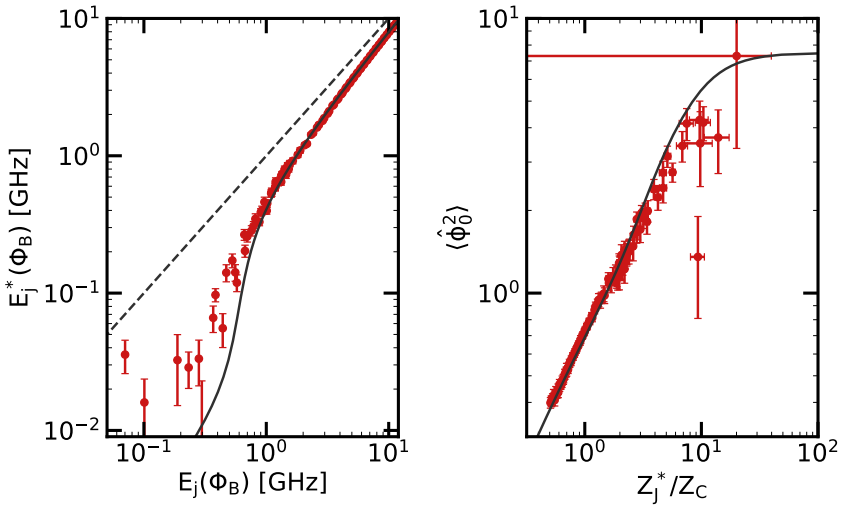

Figure 1.4 – **Left.** Renormalized Josephson energy $E_J^\star$ as a function of the bare Josephson Energy obtained from the fit of the nonlinear SQUID frequency. The red dots are the data extracted from the phase shifts. The dashed line indicate the bare Josephson energy. The plain line is the renormalized one given by the SCHA. **Right.** Phase fluctuations of the junction as a function of the ratio of its renormalized characteristic impedance and the one of the chain. Red dots are the data. The plain line is the estimation from the SCHA.

Thus, this circuit is a very good platform to study the BSG problem both in trivial regimes, where the nonlinearity is weak, and in highly non-trivial regimes where the nonlinearity is such that phase fluctuations induce measurable effects such as a nonperturbative renormalization of its resonant frequency. In what follows we will take advantage of the fact that the nonlinearity is coupled to a quasi-continuum (and not to a true continuum) to study the impact that the latter has on its environment.

Damping in the modes

From the second designed circuit we could also study losses that can be attributed to the nonlinearity, labeled $\gamma_{\mathrm{J},k}$. To do so, we measured their dependence on input power, magnetic flux and frequency. We observed that these losses are maximum at $\omega_{\mathrm{d}}^{\star}$ indicating that they are compatible with the photon conversion processes previously introduced. The results of this study is given for six magnetic fluxes $\Phi_{\mathrm{B}}/\Phi_{\mathrm{q}}$ between 0.35 and 0.5 and for four circuit temperatures between 0 and 120 mK in Fig.2.5. We see that for a circuit temperature equal to zero, the photon conversion processes are negligible and hence cannot explain losses induced by the SQUID. However, when increasing the circuit temperature up to 120 mK we see that the photon conversion processes can fairly reproduce the observed losses with respect to both the frequency and magnetic fluxes lower that 0.46 since the perturbative treatment breaks down at higher fluxes (see the last panel of 2.5).

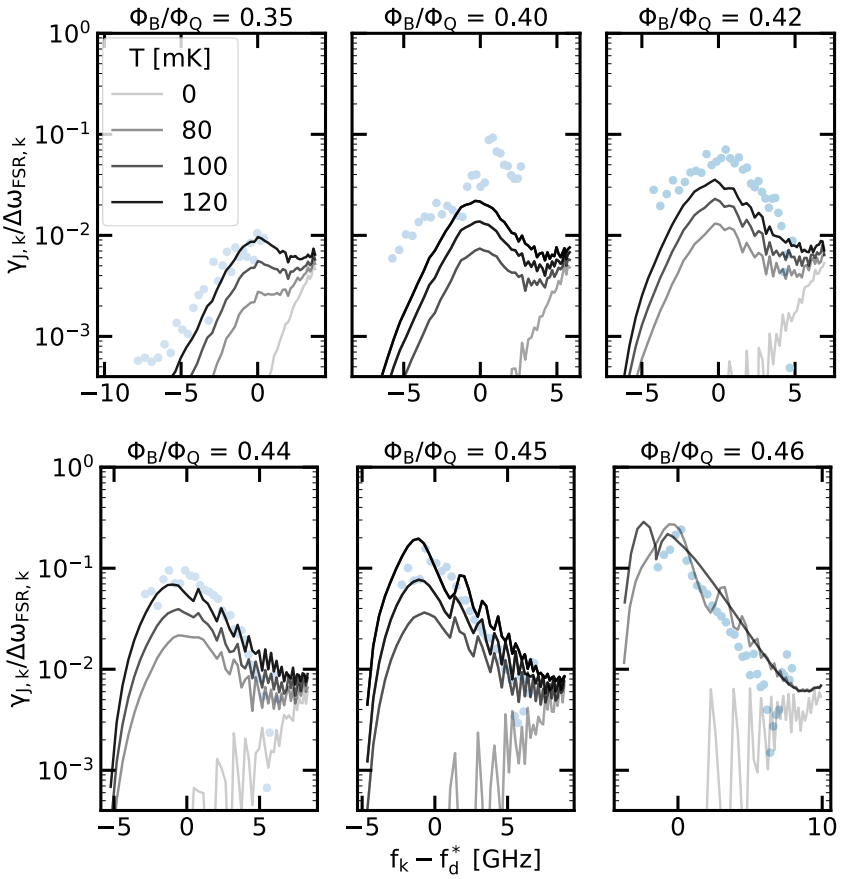

Figure 1.5 – The decay probability per round trip $\gamma_{\mathrm{J},k}/\Delta\omega_{\mathrm{FSR},k}$ as a function of $f_k - f_{\mathrm{d}}^{\star}$ for six magnetic fluxes $\Phi_{\mathrm{B}}/\Phi_{\mathrm{q}}$ between 0.35 and 0.46. The dots corresponds to the experimental data while the plain line result from the fit using four circuit temperature ranging from 0 mK (light grey) to 120 mK (black).

The drastic increase of the photon conversion losses can be understood since at $T = 0$ only the processes involving the decay of a probing photon into an odd number of photons can generate losses. However, at higher temperature the mode population increases and is no longer equal to zero. Hence, processes where one photon inserted

in the circuit interacts with, for example, a thermal photon and both are converted at different frequencies can occurs (in other words Σ'' connects more states). Moreover, when the temperature increases the phase fluctuations also increase and the processes involving 5,7,... photons become more likely. Therefore, the number of processes involving a photon conversion, and hence the associated losses, explode while warming up.

1.2.3 Manuscript

The manuscript is divided in three chapters. The first chapter gives the theoretical background necessary to understand the experiment. The second one presents the measurement setup and the experimental results are discussed in the third chapter. The first chapter is divided in six sections the first one discusses the basics of a Josephson junction and of a JJ chain separately. In the two next sections the BSG physics is introduced and a simple toy model is used to explain the key ingredients needed to design a complex many body system. The fourth sections is used to present different parameters influencing the Josephson energy renormalization. Then, the different phase shifts used to characterize our circuits are presented. Finally, the backaction of the nonlinearity on the chain modes is discussed. The experimental chapter is divided in two sections. In the first one the junction nonlinearity is fixed and the temperature influence is studied. In the second one, the use of a SQUID allows us to tune the nonlinearity. We also, discuss the damping induced by the nonlinearity in the modes. Finally, I made the choice to include only the main results of my PhD in these chapters. Therefore, the appendices are used as supplementary materials.

1.2.4 Author's contribution

The work presented in this manuscript is of course a collective effort. However, in this section I will present what part can, and cannot, be fairly attributed to myself since it is an evaluation criteria.

Theoretical contribution

The main theoretical tools used in this work, meaning the SCHA, the photon conversion losses mechanism, the phase shift formalism and the Hamiltonian diagonalization, were developed by Izak Snyman, Serge Florens, Denis Basko and Theo Sepulcre. My contribution to this part was to adapt it to our circuit when needed. On the other hand, the connection between the phase fluctuations in the modes $\xi^2_{0,k}$, the nonlinearity response function and the phase shift was derived by myself and inspired from what Izak and Serge derived for slightly different circuits. In addition, I derived most of the formula coming from the toy models and the formulas derived to give hand-waving arguments about the physics of our circuits.

Setup contribution

On the setup part, my main contribution was to improve the setup installed by Nicolas Roch and Javier Puertas-Martínez. To do so, I added the distributed attenuators on the input and output lines after a study on the type of material and cable length best suited to our dilution fridge. I also implemented a PID allowing us to control the base temperature of our fridge. As a side project that is not discussed in this manuscript I programmed a virtual instrument for a FPGA card coupled to high-end ADCs from Redpitaya which enabled us to measure the T_1 and T_2 of the V shape qubit fabricated by Remy Dassoneville and measured now by Vladimir Milchakov. The measured T_1 and T_2 were as good as the one obtained with a more conventional setup (see [76] for more information), therefore proving that these simple cards could be used for basic qubit measurement.

Experimental contribution

On the experimental side I designed, fabricated and characterized the samples presented in this work. I also performed the data analysis and compared the data with our theoretical models. The only exception was for the nonlinearity induced losses where we compared the experimental data and the model together with Theo.

Introduction et résumé 2

Les travaux réalisés au cours de ce doctorat ont porté sur le phénomène de dissipation en mécanique quantique. La dissipation se produit lorsqu'un système quantique se couple à un environnement. L'effet le plus frappant de cette dissipation est la perte de cohérence induite sur le système. En raison de cette perte de cohérence, un système quantique peut perdre son caractère quantique et se comporter comme un objet classique. En ce sens, la dissipation peut être considérée comme le mécanisme à l'interface entre la physique classique et la physique quantique. Si ces questions ont des implications fondamentales, elles ont également des implications pratiques. Notamment dans la réalisation d'ordinateurs quantiques où la perte de cohérence est un problème majeur. Au cours de cette thèse, nous nous sommes concentrés sur l'interaction entre un degré de liberté quantique, un oscillateur non linéaire, couplé à un environnement fortement dissipatif. Bien que ce problème semble simpliste, il est au cœur d'une physique très riche mais mal comprise allant de la renormalisation non-perturbative des paramètres de l'oscillateur, à la génération de dissipation via des phénomènes non-triviaux de conversion de photons, en passant par la physique de la transition de phase quantique. L'étude de cette nouvelle physique est rendue possible par la nature particulière de l'environnement artificiel, à l'interface entre un continuum et un environement discret, ce qui nous a permis de nous demander comment un environnement induit de la dissipation. Dans cette section, nous allons d'abord passer en revue l'état de l'art sur l'utilisation des jonctions Josephson pour aborder les systèmes dissipatifs quantiques. Cela nous permettra d'introduire les concepts clés de tels problèmes. Un résumé du travail effectué au cours de cette thèse sera ensuite fourni.

2.1 Introduction

Depuis les travaux pionniers de B.D. Josephson [1, 2], la jonction tunnel supraconductrice, également appelée *jonction Josephson*, est devenue d'une importance fondamentale pour tester différentes hypothèses en mécanique quantique. Un tel succès repose sur deux propriétés, simples à première vue, mais aux conséquences importantes. La première provient de l'utilisation de matériaux supraconducteurs, permettant à ces jonctions d'être relativement bien découplées de toute source de dissipation. La seconde, provient de la non-linéarité de ces jonctions, permettant de faire des prédictions qui ne pourraient pas être obtenues à partir d'un modèle classique. C'est ce que l'on appelle la "limite classique". Cette dernière affirmation peut être vérifiée en utilisant le théorème d'Ehrenfest sur un degré de liberté $\hat{x}$ de d'impulsion $\hat{p}$ dans un potentiel V. Il stipule que :

$$\frac{d}{dt}\langle\hat{p}\rangle = -\langle\frac{d}{dx}V\left(\hat{x}\right)\rangle \tag{2.1}$$

D'autre part, en utilisant la deuxième loi de Newton, qui est sa contrepartie classique, nous obtenons :

$$\frac{d}{dt}\langle\hat{p}\rangle = -\frac{d}{dx}V\left(\langle\hat{x}\rangle\right) \tag{2.2}$$

Par conséquent, puisque $\frac{d}{dx}V\left(\langle\hat{x}\rangle\right)$ et $\langle\frac{d}{dx}V\left(\hat{x}\right)\rangle$ sont égaux pour un potentiel quadratique, ou de manière équivalente un système linéaire, nous ne nous attendons pas à voir de différence entre la prédiction quantique et classique. Ce n'est pas le cas si le potentiel est non linéaire. Maintenant que nous avons vu pourquoi les propriétés fondamentales des jonctions Josephson les rendent si attrayantes pour l'étude des problèmes quantiques, nous allons introduire les variables et les paramètres qui régissent leur dynamique à l'aide des travaux précurseurs sur l'effet tunnel quantique macroscopique (MQT). Une jonction Josephson est décrite par deux variables conjuguées : le nombre de paires de Cooper transférées à travers la jonction $\hat{n}$ et la différence de phase supraconductrice $\hat{\phi}$ entre les deux conducteurs supraconducteurs. L'observation du tunneling de $\hat{\phi}$ est probablement la première démonstration expérimentale [3, 4][a] montrant le potentiel des jonctions Josephson pour tester la théorie quantique, validant que malgré sa nature macroscopique $\hat{\phi}$ pouvait être traité comme un degré de liberté quantique. Par conséquent, ces jonctions pouvaient être utilisées comme des objets quantiques à part entière, ouvrant la voie à la l'électrodynamique quantique en circuit [6].

De plus, ces travaux pionniers ont également étudié l'influence de la dissipation sur l'effet tunnel quantique et a donc prouvé que la jonction Josephson était un bon outil pour étudier les *systèmes dissipatifs quantiques*. En effet, bien qu'une jonction soit naturellement protégée contre la dissipation, elle n'en n'est pas entièrement immunisée. Une bonne approximation est de modéliser cette dissipation comme une résistance en parallèle R. Cette résistance doit être comparée à l'impédance de la jonction. Bien qu'il s'agisse d'un oscillateur anharmonique, une jonction Josephson avec une énergie Josephson E_J et une énergie de charge E_c, l'impédance de la junction est bien approximée par $Z_\mathrm{J} = Z_\mathrm{q}/(2\pi)\sqrt{E_\mathrm{c}/E_\mathrm{J}}$ où $Z_\mathrm{q} = h/(2e)^2 \simeq 6.5\,\mathrm{k\Omega}$ est le quantum de résistance supraconducteur. Si $R \gg Z_\mathrm{J}$, la jonction est dite sous-amortie alors que dans la situation inverse la jonction est suramortie. A. O. Caldeira et A. J. Leggett, à l'aide de leur célèbre modèle effectif, ont prédit que, dans ces deux régimes, la résistance réduira les fluctuations de phase et donc le taux de tunneling [7]. A. I. Larkin et Yu. N. Ovchinnikov ont pu reproduire ces résultats à partir d'une modélisation microscopique de la jonction [8], en utilisant les résultats précédents d'Ambegaokar et de ses collègues [9]. Un tel modèle a ensuite été amélioré par A. D. Zaikin et S. V. Panyukov [10]. Les expériences présentées dans [3] et [4] ont confirmé ces prédictions respectivement dans les régimes de sous-amortissement et de suramortissement fort en mesurant le taux de tunnelling de $\hat{\phi}$ en fonction de la température.

[a] Ce ne sont pas vraiment les premières expériences mesurant l'effet tunnel quantique macroscopique, voir par exemple [5]. Cependant, ce sont les premières expériences où l'extraction de tous les paramètres du circuit a été possible. Permettant une description quantitative du tunneling par rapport à différents paramètres.

Néanmoins, jusqu'alors, la dissipation était traitée comme une perturbation. Par la suite, l'utilisation du groupe de renormalisation a permis de s'affranchir de cette contrainte et de prédire qu'une jonction Josephson couplée à son environnement devait subir une *transition supraconducteur-isolant*, aussi appelée transition de Schmid-Bulgadaev [11, 12]. Une jonction Josephson peut en effet être vue comme une particule de position $\hat{\phi}$ et d'impulsion $\hat{n}$, piégée dans un potentiel périodique non linéaire $E_\mathrm{J}\cos\hat{\phi}$. En fonction de la force de la dissipation, cette particule peut alors tunneler entre les minima du potentiel grâce à son *énergie du point zéro*, même à T=0. Selon la théorie du groupe de renormalisation, l'introduction de la dissipation a deux conséquences opposées. Si $R < Z_\mathrm{q}$ les fluctuations de phase $\langle\hat{\phi}^2\rangle$ sont amorties et finies. Par conséquent, l'amplitude du potentiel E_J est abaissée, ou *renormalisée*, à $E_\mathrm{J}^\star$ signalant que la position de la particule fluctue et a donc une énergie au point zéro finie, contrairement à une particle classique. Cependant, les fluctuations de phase ne sont pas assez importantes pour que la fonction d'onde de la particule puisse tunneler entre les minima de potentiel. On dit que la particule est *localisée* dans l'espace des phases. Dans un tel régime, la résistance de la jonction est nulle pour un courant nul [b] et est donc supraconductrice. Au contraire, si $R > Z_\mathrm{q}$ la théorie prédit que le potentiel est renormalisé à zéro, signalant que la particule est *delocalisée*. Par conséquent, la jonction agit comme une barrière tunnel non supraconductrice et une résistance finie est attendue à une polarisation de courant nulle en raison du blocage de Coulomb. Il est intéressant de noter que la transition prédite ne dépend pas de l'impédance de la jonction, ou de manière équivalente, de son rapport $E_\mathrm{J}/E_\mathrm{C}$ alors que les calculs ont été effectués pour $Z_\mathrm{J} \gg Z_\mathrm{q}$ ou $Z_\mathrm{J} \ll Z_\mathrm{q}$ où la transition est due à des phénomènes physiques différents [13]. Profitant de l'analogie avec la particule, la transistion supraconducteur-isolant est également appelée *transistion localisée-délocalisée*. Des tentatives ont été faites pour reproduire le diagramme de phase prévu par la théorie [14, 15] mais elles ont été contrariées par soit par des effet de température soit par la précision limitée du dispositif de mesure. Des recherches très proches ont été menées par D. B. Haviland et ses collègues qui ont mesuré les oscillations de Bloch des paires de Cooper [16], celle-ci étant une autre conséquence du modèle précédemment introduit [17]. Cependant, en raison des difficultés à mesurer sans ambiguïté le diagramme de phase prédit, la modélisation de l'effet de la dissipation sur une jonction, et donc de la transition de phase qui en résulte, reste sujette à débat [18].

Malgré les avancées théoriques et expérimentales rendues possibles par l'étude des jonctions Josephson, il manquait une preuve plus directe montrant que sa dynamique est régie par les lois de la mécanique quantique. Cette dernière a été fournie par la mesure de l'effet tunnel cohérent de fonctions d'onde dans l'espace de charge dans les laboratoires du NEC [19][c]. Ce dispositif consistait en une jonction dans le régime $Z_\mathrm{J} \gg Z_\mathrm{q}$ reliée à une capacité tel que les deux forment un îlot supraconducteur. En fixant la charge de décalage de l'îlot à la moitié de celle d'une paire de Cooper, deux états, correspondant à des combinaisons des deux configurations de charge voisines, peuvent être manipulés. La manipulation cohérente a donc été rendue possible grâce à la forte non-linéarité de la jonction où deux niveaux peuvent être isolés des autres.

[b] Cela vient du fait que si la particule est localisée, la phase est constante dans le temps et donc aucune tension ne peut s'accumuler aux bornes de la jonction. Nous avons négligé ici d'autres sources de dissipation, telles que les quasi-particules pour des raisons de clarté

[c] La première fabrication d'un tel dispositif a été réalisée à Saclay [20], inspirée par une proposition de M. Buttiker [21]

Pour cette raison, de tels systèmes peuvent être considérés comme des *qubits*. Par la suite, un nombre toujours plus grand de qubits a été inventé et mesuré. Certains d'entre eux sont basés sur l'effet tunnel cohérent entre deux minima dans l'espace des charges, la boîte à paires de Cooper présentée précédemment ou le Quantronium [22]. Ou dans l'espace des phases, le qubit de flux [23–26] ou le fluxonium [27]. Tandis que d'autres sont basés sur la manipulation de deux états isolés intra-puits comme le qubit de phase [28**?**] et le qubit Transmon [30].

Inspirés par les expériences d'électrodynamique en cavité [31, 32], ces nouveaux dispositifs ont été couplés à un résonateur permettant leur lecture non destructive et efficace [33–37]. Cela a été rendu possible car le régime de couplage fort, où le couplage g entre le qubit et le résonateur est plus grand que les pertes γ au niveau du qubit, peut être atteint facilement. Dans les circuits, le couplage se fait via la charge ou la phase. Ce couplage est proportionnel à la racine carrée des fluctuations de la variable correspondante [38, 39] qui elle-même dépend respectivement de $1/Z_\mathrm{r}$ ou $1/Z_\mathrm{r}$, où Z_r est l'impédance caractéristique du résonateur. Par conséquent, le couplage dans ces circuits n'est rien d'autre qu'une question de conception. Le couplage ultra fort, où le couplage g est compris entre 0,1 et 1 fois la fréquence du qubit ω_q, conduisant à une rupture de l'approximation des ondes tournantes, a ensuite été atteint [40, 41]. Enfin, le régime de couplage fort profond, où g est plus grand que ω_q, conduisant à une forte renormalisation des paramètres du qubit a été observé [42]. Cette renormalisation est étroitement liée à la transition localisée-délocalisée introduite précédemment où la localisation dans un minimum de potentiel est remplacée par la suppression de l'effet tunnel quantique entre les deux états du qubit et la résistance est remplacée par l'impédance du résonateur.

En parallèle, le couplage entre un qubit de flux et une ligne de transmission $50\,\Omega$ (et donc à un environnement large bande) a été mis en œuvre [43, 44], ouvrant de nouvelles perspectives pour l'étude des systèmes dissipatifs quantiques. En effet, un qubit couplé à un environnement à large bande peut être utilisé pour étudier une classe de systèmes dissipatifs quantiques appelés *problèmes d'impuretés quantiques*, tels que le modèle spin-boson [45, 46] et le problème de Kondo. Les premières expériences se situaient dans un régime de couplage tel que les techniques utilisées pour décrire leurs propriétés étaient empruntées à l'optique quantique [47–49]. Cependant, une percée a été réalisée lorsque ces circuits ont atteint le régime de couplage fort profond [50, 51][d]. Dans ces expériences, une renormalisation non perturbative de ω_q a été observée, signalant que le circuit ne pouvait plus être décrit avec les outils de l'optique quantique. Les circuits décrits jusqu'à présent étaient basés sur un qubit de flux couplé à un environnement à faible impédance afin d'atteindre un couplage tel que le circuit était hautement non trivial et appartenait ainsi à la classe des impuretés quantiques. Il s'agissait de l'approche la plus simple puisque la conception de lignes de transmission $50\,\Omega$ est maîtrisée depuis longtemps. Une autre option pour étudier les problèmes d'impuretés quantiques consiste à utiliser un qubit de charge couplé à un environnement à large bande [54–56]. La première mise en œuvre de ces idées reposait sur un qubit Transmon couplé à une ligne $50\,\Omega$ [57, 58], puis à un long résonateur [59]. Contrairement à une ligne $50\,\Omega$, un résonateur possède des conditions aux limites qui conduisent à la formation de modes résonants. L'écart de fréquence entre ces modes, appelé plage spectrale libre $\Delta\omega_\mathrm{FSR}$, est inversement proportionnel à la longueur du résonateur. Pour l'expérience précédemment citée, il était

[d] Deux bonnes revues peuvent être trouvées sur ces différents régimes de couplage [52, 53]

d'environ 100 MHz puisque le résonateur faisait plus d'un demi-mètre de long. On sait, d'après le modèle de Jaynes-Cummings [60], que le couplage entre un qubit et un environnement multimode augmente avec l'indice de mode. Cependant, comme l'impédance caractéristique du résonateur était faible, et que le couplage est proportionnel à cette dernière pour un couplage de charge, aucun effet de couplage ultra fort n'a pu être observé. Néanmoins, l'utilisation d'un résonateur multimode au lieu d'une ligne de transmission représente un changement de paradigme intéressant pour l'étude des systèmes dissipatifs : non seulement l'influence de l'environnement sur le système non linéaire, formé par un oscillateur non linéaire ou un qubit, peut être étudiée mais l'inverse est également possible. En d'autres termes, l'élément dissipatif peut être couplé à une non-linéarité, les deux étant faiblement couplés à l'appareil de mesure, ce qui rend possible une manipulation cohérente du système complet. [e]

Un couplage ultra fort entre un qubit Transmon et un résonateur à quelques modes a pu être atteint par une conception soignée de l'élément de couplage [62]. Cependant, pour augmenter encore le couplage, il faut un environnement à haute impédance. Il a fallu beaucoup de temps pour concevoir et construire des environnements à haute impédance en raison des valeurs données par la nature à la permittivité et la perméabilité relatives du vide [38]. Pour contourner ce problème, des *chaînes de jonctions Josephson* ont été utilisées. Une jonction utilisée dans le régime linéaire, où $Z_\mathrm{J} << Z_\mathrm{q}$, peut être vue comme un oscillateur harmonique avec une inductance $L_\mathrm{J} \propto 1/E_\mathrm{J}$. Ces jonctions peuvent être mises en cascade de manière compacte pour former un métamatériau dont l'inductance par mètre est supérieure de plusieurs ordres de grandeur à celle obtenue avec un matériau conventionnel. Comme leur impédance caractéristique est proportionnelle à la racine carrée de l'inductance, les chaînes résultantes constituent un matériau à haute impédance. Enfin, du fait de sa haute impédance, une telle chaîne aura une impédence très différente de celle du système de mesure, qui vaut elle $50\,\Omega$. Cette chaîne forme ainsi un résonateur. La plage spectrale libre $\Delta\omega_\mathrm{FSR}$ dépend alors du nombre de jonctions pouvant être mises en cascade. La première implémentation de ces chaînes a été fabriquée avec des jonctions dans le régime non linéaire pour étudier les sauts de phase quantiques [63–65]. Ils ont ensuite été utilisés dans le régime linéaire [49, 66]. Notre équipe a été la première à coupler un Transmon et ces chaînes [67]. Nous avons utilisé une chaîne de SQUID au lieu de simples jonctions pour pouvoire régler in situ le couplage entre les deux parties du circuit. Dans cette expérience, le couplage g avait le même ordre de grandeur que $\Delta\omega_\mathrm{FSR}$ mais était toujours inférieur d'un ordre de grandeur à la fréquence du qubit ω_q. Peu après, un couplage tel que $g > \Delta\omega_\mathrm{FSR}$, appelé couplage super fort, a été rapporté grâce à l'utilisation d'une chaîne plus longue et à un schéma de couplage différent [68]. Dans ce régime, le qubit est le médiateur des interactions entre les modes du résonateur, de sorte que le circuit peut être considéré comme un problème complexe à plusieurs corps [69].

Néanmoins, quand bien le régime de couplage fort fut atteint, il s'est avéré que la non-linéarité du Transmon était diluée dans les modes. En d'autres termes, à un couplage plus élevé, le nombre de modes couplés augmente et, par conséquent, le

[e] Récemment, un groupe a mis en œuvre le couplage entre un qubit Transmon et une cavité 3D multimode [61], ce qui devrait faciliter la manipulation cohérente d'un tel système car ces modes sont fortement découplés de toute source de dissipation, cependant le système est légèrement en dessous du couplage super fort (défini dans la suite) et la non-linéarité est faible en raison de l'utilisation d'un qubit Transmon.

Transmon doit partager sa non-linéarité avec encore plus de modes, ce qui rend le système quasi-linéaire. Pour cette raison, il a été récemment démontré que la transition de phase localisé-délocalisé prédite pour le modèle du boson de spin [46] ne pouvait pas être observée avec un circuit utilisant un Transmon [70]. Selon cet article, une stratégie possible pour contourner ce problème est de brancher directement une jonction Josephson au milieu à haute impédance et donc de s'affranchir de la capacité de couplage. Cependant, en procédant ainsi, le système étudié n'implémente plus le modèle spin-boson mais le modèle Boundary Sine Gordon (BSG) [71]. En conclusion, nous étudierons une jonction non linéaire reliée à un élément dissipatif qui mime une impédance, revenant ainsi au point de départ de l'introduction. La principale différence étant que l'élément dissipatif n'est plus une résistance réelle mais un résonateur multimode, formant un quasi-continuum. Ce quasi-continuum imite parfaitement un continuum si l'élargissement de ses modes γ_r est plus grand que sa plage spectral libre $\Delta\omega_{FSR}$, ou, dans le domaine temporel, si le temps d'aller-retour d'une excitation dans le résonateur multimode est plus long que le temps nécessaire à cette excitation pour s'échapper du système[f]. Cependant, si ce régime était atteint reviendrait à mesurer une non-linéarité couplée à un système ouvert et nous perdrions la possibilité d'étudier la rétroaction de la non-linéarité sur son environnement. Par conséquent, γ_r doit être maintenu en dessous de $\Delta\omega_{FSR}$ et si $\gamma_r \ll \Delta\omega_{FSR}$ même les manipulations cohérentes deviennent possibles. En raison de sa distribution de fréquence, un quasi-continuum semble être un problème plus complexe à étudier qu'un continuum. Néanmoins, comme nous le verrons, si le temps caractéristique des phénomènes étudiés, qui peut être le temps d'amortissement induit par l'environnement sur la non-linéarité[g], est court comparé au temps d'aller-retour d'un photon alors le quasi-continuum se comporte comme un continuum.

2.2 Résumé

Le travail présenté dans ce manuscrit visait à mesurer l'interaction entre une jonction Josephson non linéaire et un quasi-continuum formé par une chaîne de jonctions Josephson. En particulier, nous avons étudié l'influence de différents paramètres, tels que la non-linéarité de la jonction et la température du circuit, sur l'énergie Josephson de la jonction non linéaire. Dans un deuxième temps, nous avons également étudié la rétroaction de la jonction non linéaire sur les modes discrets du quasi-continuum.

2.2.1 Prédictions théoriques

Dans le premier chapitre, nous montrons que les principales propriétés de notre circuit sont liées à la partie dissipative de la fonction de réponse de phase de la jonction non linéaire χ''_{ϕ_0}. Nous montrons que dans la limite thermodynamique, c'est-à-dire lorsque le nombre de jonctions dans la chaîne tend vers l'infini, la fonction de réponse est donnée par (voir Section 3.3.1) :

$$\chi''_{\phi_0}(\omega) = \frac{\pi}{2\hbar\Delta\omega_{FSR}(\omega)}\xi_0(\omega)^2 \tag{2.3}$$

[f] γ_r peut provenir soit du système de mesure, soit de canaux de pertes non contrôlés

[g] Dans le domaine fréquentiel cela signifie que le taux d'amortissement γ_d doit être beaucoup plus grand que $\Delta\omega_{FSR}$.

où ξ_0^2 sont les fluctuations du point zéro (ZPF) de phase induites par la chaîne à travers la jonction non linéaire en fonction de la fréquence et $\Delta\omega_{\mathrm{FSR}}$ est la plage spectrale libre des modes de la chaîne, qui peut également dépendre de la fréquence. Cette quantité est maximale à la fréquence amortie renormalisée de la jonction non linéaire $\omega_{\mathrm{d}}^\star = \sqrt{\omega_{\mathrm{J}}^{\star 2} - (\gamma_{\mathrm{RC}}/2)^2}$, dans le régime sous amorti (voir la section 3.3.2). Où $\omega_{\mathrm{J}}^\star$ est la fréquence de jonction renormalisée, venant de la non-linéarité de la jonction, et γ_{RC} est l'amortissement induit par le quasi-continuum[h]. La largeur totale à mi-hauteur (FWHM) de la fonction de réponse est donnée par cet amortissement.

Influence de l'environement sur la jonction non lineaire

En couplant la jonction non linéaire à la chaîne, des fluctuations de phase sont induites sur toute la bande passante de l'environnement. Ces fluctuations conduisent à une renormalisation de l'énergie Josephson. Cette renormalisation peut être estimée en utilisant l'approximation harmonique autoconsistante (SCHA, voir la section 3.2.2) :

$$E_{\mathrm{J}}^\star = E_{\mathrm{J}} e^{-\langle \hat{\phi}_0^2 \rangle_{\mathrm{t}}/2} = E_{\mathrm{J}} \exp\left[-\sum_{k=0}^{N} \frac{\xi_{0,k}^2}{2} (n_k + \tfrac{1}{2}) \right] \tag{2.4}$$

où E_{J} est l'énergie Josephson, $\xi_{0,k}^2$ sont les fluctuations de phase induites par un mode de chaîne de fréquence ω_k et n_k est l'occupation thermique de ce mode. Cette équation est auto-consistante puisque ω_k, et donc $\xi_{0,k}^2$, dépend des valeurs de $E_{\mathrm{J}}^\star$ via le déphasage qu'il induit (voir Section 3.2.3). A partir de cette équation, nous voyons que la renormalisation est liée à la fonction de réponse via les fluctuations de phase. Nous pouvons également voir que la renormalisation augmente, ou inversement que l'énergie Josephson diminue, lorsque les ZPF de phase augmentent. C'est également le cas si l'occupation thermique des modes augmente via la température, puisque la partie thermique des fluctuations augmente. À partir de l'énergie Josephson renormalisée, nous pouvons définir la fréquence de la jonction non linéaire comme $\omega_{\mathrm{J}}^\star = \sqrt{2E_{\mathrm{J}}^\star E_{\mathrm{C}}}$ (voir Section **??**) où E_{C} est l'énergie de charge de la jonction[i]. Cette expression n'est valable que pour $E_{\mathrm{J}} \gtrsim E_{\mathrm{C}}$.

Rétroaction de la jonction non lineaire sur les modes : les processus de conversion de photons

En plus de la renormalisation de E_{J} provenant de l'interaction entre la jonction non linéaire et la chaîne, nous avons étudié la rétroaction de la jonction sur les modes. Plus précisément, nous montrons que la jonction non linéaire induit une dissipation dans les modes de la chaîne (voir Section 3.6.2). Cette dissipation se traduit par un élargissement des modes dans l'espace des fréquences, donné par :

$$\gamma_k = \Sigma''(\omega_k) \xi_{0,k}^2 \tag{2.5}$$

où γ_k est l'élargissement du mode k et $\Sigma''(\omega_k)$ est la partie complexe de la self-énergie. La self-énergie provient de la non-linéarité de la jonction. Elle couple les

[h] γ_{RC} ne dépend pas de la fréquence seulement lorsque l'on néglige la fréquence plasma de la chaîne (voir Section 3.3.2 et Annexe A.6)

[i] où $E_{\mathrm{C}} = (2e)^2/(2C_{\mathrm{J}})$, C_{J} étant la capacité de la jonction

états à photons uniques aux états à photons multiples. Pour cette raison, ces états à photons uniques peuvent se désintégrer en états à photons multiples. La non linearité déclanchant donc des processus de conversion de photons. Grâce à ces processus, les états monophotoniques acquièrent une durée de vie limitée et les modes s'élargissent dans l'espace des fréquences.

2.2.2 Expériences

Présentation des échantillons

Pour étudier les effets précédemment introduits, nous avons mis en œuvre deux types de circuits. Le premier consiste en une jonction Josephson non linéaire d'une impédance caractéristique de l'ordre de Z_q ($E_\mathrm{J}/E_\mathrm{C} \lesssim 1$), intégrée entre deux chaînes de SQUIDs, chacune constituée de 1500 cellules (Figure 2.1). Néanmoins, aucun flux magnétique n'a été appliqué à ces SQUIDs. Par conséquent, ils seront considérés par la suite comme des jonctions. Les chaînes sont couplées capacitivement au système de mesure pour supprimer le bruit DC qui pourrait affecter la jonction non linéaire. En raison de sa symétrie, le circuit peut être décomposé en deux sous-circuits (voir Section 3.2.1). Le premier contient la jonction non linéaire connectée galvaniquement à une chaîne d'impédance caractéristique $2Z_\mathrm{C}$, où $Z_\mathrm{C} = \sqrt{L/C_\mathrm{g}}$. Ce sous-circuit correspond au modèle BSG. Le second consiste en une chaîne nue d'impédance caractéristique $2Z_\mathrm{C}$. Ces sous-circuits contiennent des modes appelés respectivement impairs et pairs. A partir de la mesure de ces modes, nous avons pu mesurer la fréquence de la jonction non linéaire $\omega_\mathrm{J}^\star$ pour trois échantillons correspondant à différents régimes de non-linéarité et à diverses températures (voir Section 5.1.2).

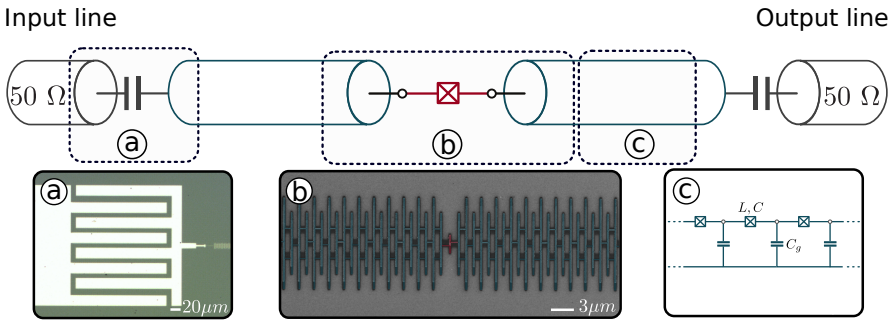

Figure 2.1 – Schéma des premiers circuits conçus. Les chaînes de SQUIDs, représentées par des lignes de transmission bleues, sont couplées capacitivement aux câbles coaxiaux d'entrée et de sortie $50\,\Omega$ et couplées galvaniquement à la jonction Josephson non linéaire (en rouge). **a** Image optique des capacités de couplage d'entrée et de sortie. **b** Image MEB de quelques-uns des SQUIDs (1500 au total pour chaque chaque chaîne) qui sont couplés à la jonction Josephson non linéaire (en rouge). **c** Equivalence entre l'image effective de la ligne de transmission et la chaîne de SQUIDs caractérisée par trois paramètres microscopiques L et C respectivement l'inductance et la capacité par SQUID et C_g la capacité à la masse.

Le deuxième circuit conçu est un SQUID non linéaire couplé galvaniquement à une chaîne de 4250 jonctions. La chaîne est couplée galvaniquement à sa gauche à une ligne microruban $50\,\Omega$ tandis que le SQUID non linéaire est mis à la masse à sa

droite. De ce fait, le circuit peut être vu comme un résonateur de type hanging. Cette géométrie est plus pratique pour une étude quantitative de l'amortissement des modes (voir Annexe C.1.2). De plus, l'utilisation d'un SQUID nous a permis de régler in situ la non-linéarité du SQUID en appliquant via l'application d'un flux magnétique. Ce circuit est une implémentation directe de l'hamiltonien BSG puisqu'il n'y a plus de modes impairs et pairs. Ce choix de conception a été fait pour que l'amortissement des modes (ou de manière équivalente leur facteur de qualité) soit plus facile à extraire car une seule famille de modes est conservée (voir Section 5.2). De plus, le nombre de jonctions dans la chaîne est augmenté d'un facteur 4. Par conséquent, le quasi-continuum formé par la chaîne est plus proche de la limite thermodynamique par rapport au design précédente.

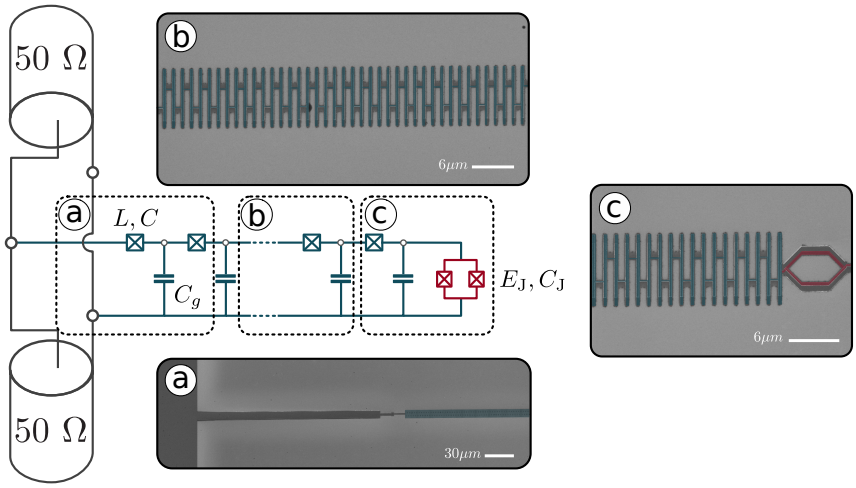

Figure 2.2 – Schéma du second circuit conçu. La chaîne, représentée en bleu, est caractérisée par ses trois paramètres L, C et C_g. La chaîne se termine par un SQUID non linéaire, représenté en rouge et caractérisé par ses deux paramètres E_J et E_C. **a** Image MEB du couplage galvanique entre la chaîne et la ligne d'alimentation microruban 50 Ω. Les deux sont couplés de telle sorte que le circuit forme un résonateur suspendu. **b** Image MEB de la chaîne composée de 4250 sites. **c** Image MEB du couplage galvanique entre la chaîne et le SQUID non linéaire. La jonction est mise à la masse à sa droite.

Etude en température

À partir de la spectroscopie du premier circuit conçu, nous avons pu mesurer la fréquence de jonction non linéaire pour trois échantillons, notés A, B et C, correspondant à trois non-linéarités (de la plus grande à la plus petite), en fonction de la température du circuit (voir section 5.1.5). Les résultats sont reportés dans le panneau gauche de la Fig.2.3. Les données expérimentales correspondent aux points, leurs barres d'erreur sont indiquées par les zones ombrées. Les courbes noires correspondent à l'estimation SCHA. Les lignes en pointillés sont la fréquence des jonctions estimée en écartant la partie quantique de la fluctuation de phase, c'est-à-dire en utilisant :

$$\langle \hat{\phi}_0^2 \rangle (T)_{\text{no ZPF}} = \sum_{k=0}^{N} \frac{|\xi_{0,k}|^2}{2} n_k \tag{2.6}$$

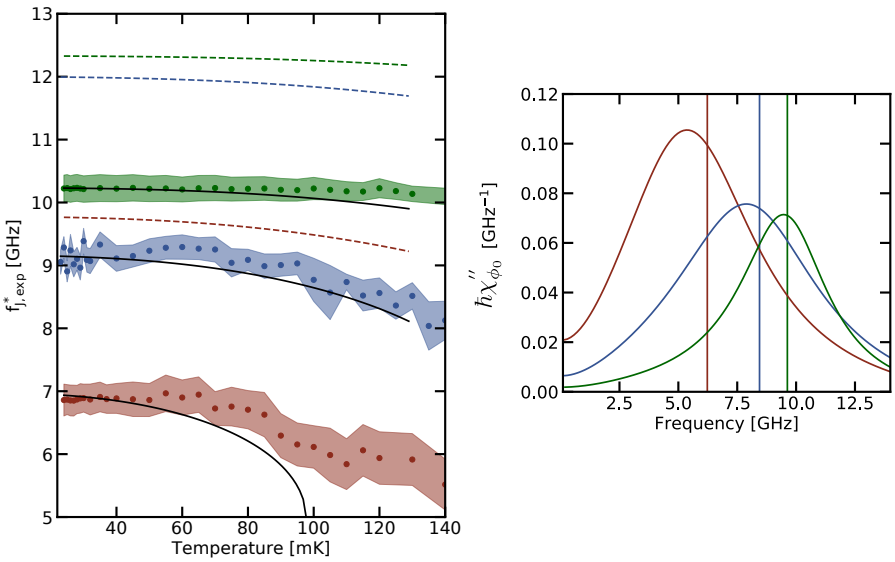

Figure 2.3 – **Left.** Fréquence renormalisée de la jonction non linéaire en fonction de la température pour les échantillons A (rouge), B (bleu) et C (vert). Les points sont les valeurs extraites des mesures spectroscopiques, les zones ombrées sont les barres d'erreur correspondantes. Les lignes noires sont le résultat de l'ajustement utilisant la SCHA tandis que les lignes pointillées représentent ce que serait l'évolution de ces fréquences en fonction de la température si les ZPF était omis de $\langle\phi_0^2\rangle$. **Right.** Partie dissipative de la fonction de réponse de la jonction non linéaire en fonction de la fréquence. Les lignes continues sont les fonctions de réponse données par l'équation 2.3 dans la limite thermodynamique. La ligne verticale dénote la position de $\omega_{\mathrm{J}}^{\star}$. Le décalage de la fréquence amortie $\omega_{\mathrm{d}}^{\star}$ par rapport à $\omega_{\mathrm{J}}^{\star}$ passe de presque zéro à 1 GHz de l'échantillon C à A.

dans l'équation 2.4. En comparant ces deux quantités, nous pouvons voir la contribution relative des fluctuations thermiques et quantiques. Pour les trois échantillons, la fréquence diminue lorsque la température augmente. Ceci est attendu puisque les fluctuations thermiques augmentent avec la température (voir Eq.2.4). Par conséquent, la renormalisation augmente et la fréquence de la jonction diminue. Cette renormalisation en fonction de la température est plus importante pour l'échantillon A et est de moins en moins prononcée de l'échantillon A à C. Ceci est dû au fait que la fréquence de la jonction de l'échantillon A est plus basse que celle de l'échantillon B qui est elle-même plus basse que celle de l'échantillon C. Par conséquent, la jonction non linéaire de l'échantillon A est plus couplée aux moded basse fréquence, qui sont plus sensibles à la température (voir Section 3.4.4 et surtout Figure 3.18).

Cette explication est confirmée par l'étude de la partie dissipative de la fonction de réponse de phase de la jonction non linéaire dans le domaine fréquentiel. Le résultat de cette étude est présenté dans le panneau de droite de la Fig.2.3. Les lignes pleines sont les fonctions de réponse dans la limite thermodynamique en utilisant à la fois la fréquence de la jonction non linéaire et l'estimation des paramètres de la chaîne, dans l'Eq.2.3. Les lignes verticales correspondent à la valeur de $\omega_{\mathrm{J}}^{\star}$ estimée à partir de l'étude précédente. La fréquence amortie de la jonction non linéaire $\omega_{\mathrm{d}}^{\star}$ et la FWHM γ_{RC} peuvent être extraites de la fonction de réponse. Le décalage entre la fréquence renormalisée estimée à partir du SCHA $\omega_{\mathrm{J}}^{\star}$ et la fréquence amortie $\omega_{\mathrm{d}}^{\star}$ (maximum de

la fonction de réponse) augmente de l'échantillon C à A. Cela peut s'expliquer par le fait que l'amortissement augmente de l'échantillon C vers A (voir Tab.5.3). Ainsi, à partir de notre formalisme, nous pouvons distinguer la renormalisation provenant du ZPF, donnée par $\omega_J - \omega_J^\star$, et celle provenant du couplage à un bain thermodynamique, donnée par $\omega_d^\star - \omega_J^\star$.

Ces deux figures montrent que les circuits conçus constituent un problème complexe à N corps présentant une renormalisation non perturbative de l'énergie Josephson de la jonction non linéaire, et donc de sa fréquence de résonance. La renormalisation maximale a été obtenue pour l'échantillon A pour lequel le rapport $E_J^\star / E_J$ était d'environ 0,5. Pour reproduire un tel résultat à partir de notre modèle, au moins 30 modes de chaîne ont dû être pris en compte. Ceci est dû au fait que l'amortissement induit par l'environnement a le même ordre de grandeur que la fréquence de jonction et que la plage spectral libre des modes de la chaîne est d'un ordre de grandeur plus petit que ces deux-derniers. D'après la valeur de γ_{RC} et de $\omega_d^\star$ extraite, nous pouvons voir que les jonctions non linéaires sont dans le régime dit de couplage fort profond puisque le rapport entre les deux est d'environ un [52, 53] pour les trois échantillons. Notez que ce régime a été défini dans le contexte du modèle Spin Boson et que l'on sait très peu de choses sur un tel régime pour le modèle BSG. Néanmoins, un article récent montre qu'une correspondance existe entre les deux systèmes [70]. Par conséquent, nous pouvons affirmer que l'atteinte d'un tel régime est un pas important vers l'observation de phénomènes analogues aux prédictions faites dans un tel régime pour le hamiltonien du Spin Boson [55, 72–75].

Etude de la nonlinéarité

La spectroscopie du deuxième type de circuit conçu a été utilisée pour étudier plus systématiquement l'influence de la non-linéarité de la jonction sur la renormalisation. L'énergie Josephson renormalisée en fonction de celle non renormalisée est présentée dans le panneau de gauche de la Fig.2.4. Les points correspondent aux données expérimentales, la ligne grise est l'estimation donnée par la SCHA. La ligne en pointillés est un guide pour les yeux correspondant à la valeur non remormalisée de l'énergie Josephson. Nous pouvons constater que la renormalisation augmente lorsque l'énergie Josephson diminue. Cela peut être compris par le fait que lorsque la barrière de potentiel est abaissée, les fluctuations de phase augmentent, ce qui conduit à une renormalisation plus importante. Nous voyons que pour les plus petites valeurs de E_J, le rapport $E_J^\star / E_J$ est compris entre 0,2 et 0,1 (par exemple à $E_J = 1\,\mathrm{GHz}$, nous avons $E_J^\star = 0.2\,\mathrm{GHz}$). Par conséquent, la renormalisation est suffisamment forte pour presque supprimer l'effet tunnel des paires de Cooper à travers le SQUID non linéaire. Cette interprétation est confirmée dans le panneau de droite de la Fig.2.4. Ce panneau montre les fluctuations de phase de la jonction non linéaire en fonction de $Z_J^\star / Z_C$, où $Z_J^\star$ est l'impédance renormalisée du SQUID, définie comme $Z_J^\star = Z_q / 2\pi\sqrt{2E_C / E_J^\star}$ et Z_C est l'impédance de la chaîne. Les fluctuations de phase sont obtenues à partir du SCHA, en utilisant :

$$\langle \hat{\phi}_0^2 \rangle = 2 \ln\left(\frac{E_J}{E_J^\star}\right) \tag{2.7}$$

où $E_J^\star$ correspond aux données expérimentales et E_J est l'énergie Josephson estimée à partir de l'ajustement précédent. Ce panneau confirme que les fluctuations de phase

augmentent avec l'impédance du SQUID non lineaire, ou de manière équivalente avec sa non-linéarité.

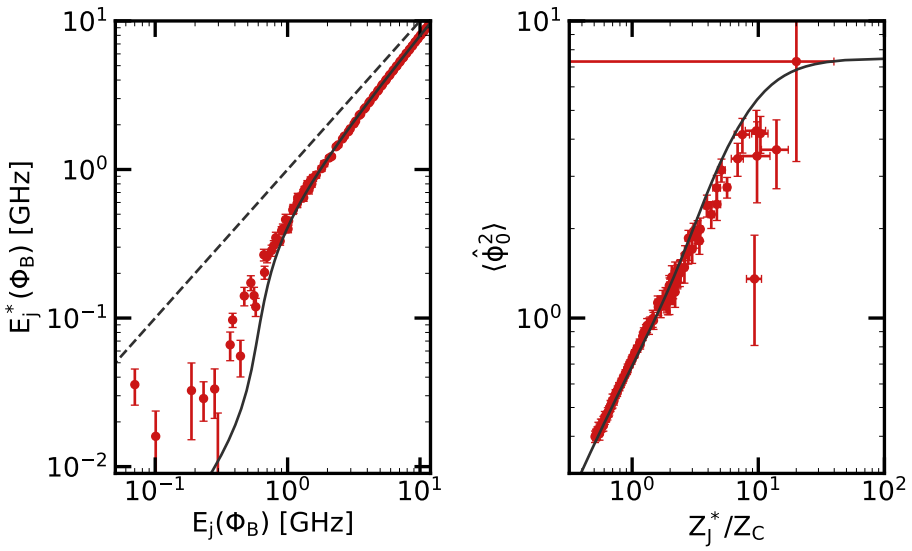

Figure 2.4 – **Left.** Énergie Josephson renormalisée $E_J^\star$ en fonction de l'énergie Josephson non renormalisée obtenue à partir de l'ajustement de la fréquence du SQUID non lineaire. Les points rouges sont les données extraites de la spectroscopie. La ligne pointillée indique l'énergie Josephson non renormalisée. La ligne pleine est l'estimation donnée par la SCHA.**Right.** Fluctuations de phase de la jonction en fonction du rapport entre son impédance caractéristique renormalisée et celle de la chaîne. Les points rouges représentent les données. La ligne unie est l'estimation du SCHA.

Ainsi, ce circuit est une très bonne plateforme pour étudier le problème BSG à la fois dans des régimes triviaux, où la non-linéarité est faible, et dans des régimes hautement non triviaux où la non-linéarité est telle que les fluctuations de phase induisent des effets mesurables tels qu'une renormalisation non-perturbative de sa fréquence de résonance. Dans ce qui suit, nous profiterons du fait que la non-linéarité est couplée à un quasi-continuum (et non à un vrai continuum) pour étudier l'impact que cette dernière a sur son environnement.

Amortissement des modes

À partir du deuxième type de circuit conçu, nous avons également pu étudier les pertes qui peuvent être attribuées à la non-linéarité, nommées $\gamma_{J,k}$. Pour ce faire, nous avons mesuré leur dépendance à la puissance d'entrée, au flux magnétique et à la fréquence. Nous avons observé que ces pertes sont maximales à $\omega_d^\star$ indiquant qu'elles sont compatibles avec les processus de conversion de photons introduits précédemment. Les résultats de cette étude sont donnés pour six flux magnétiques Φ_B/Φ_q entre 0,35 et 0,5 et pour quatre températures de circuit entre 0 et 120 mK dans la Fig.2.5. Nous voyons que pour une température de circuit égale à zéro, les processus de conversion des photons sont négligeables et ne peuvent donc pas expliquer les pertes induites par le SQUID. Cependant, en augmentant la température du circuit jusqu'à 120 mK, nous voyons que les processus de conversion de photons peuvent assez bien reproduire

les pertes observées à la fois pour la fréquence et les flux magnétiques inférieurs à 0,46 puisque le traitement perturbatif s'effondre à des flux plus élevés (voir le dernier panneau de 2.5).

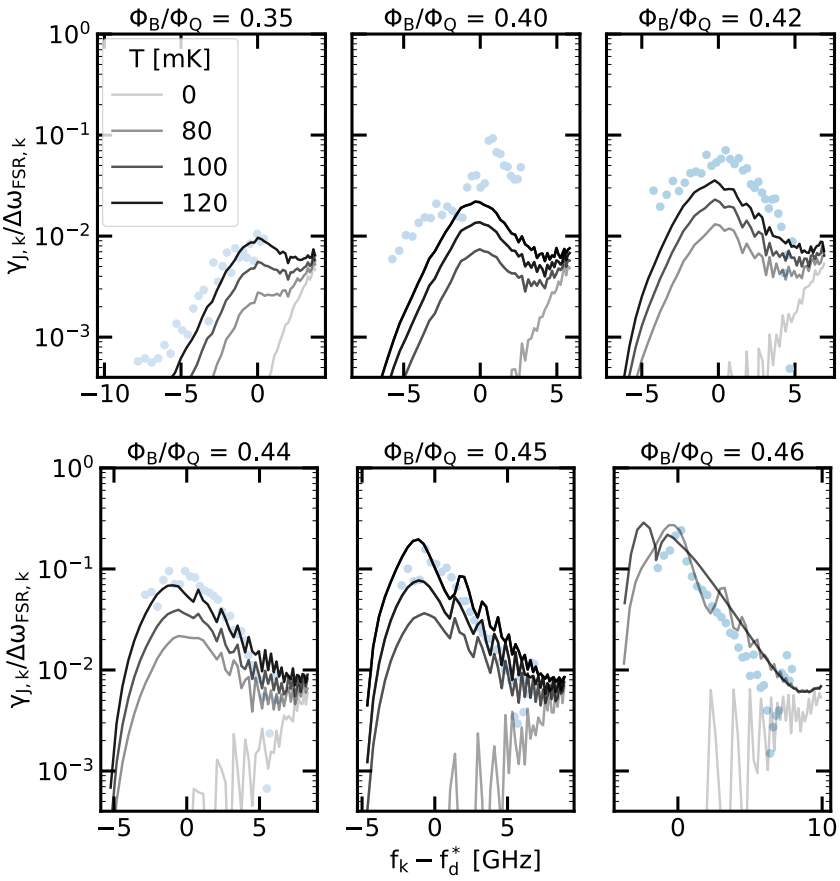

Figure 2.5 – La probabilité de désintégration par aller-retour $\gamma_{J,k}/\Delta\omega_{FSR,k}$ en fonction de $f_k - f_d^\star$ pour six flux magnétiques Φ_B/Φ_q entre 0,35 et 0,46. Les points correspondent aux données expérimentales tandis que les lignes pleines résultent de l'ajustement utilisant quatre températures de circuit allant de 0 mK (gris clair) 120 mK (noir).

L'augmentation drastique des pertes par conversion de photons peut être comprise car à $T = 0$, seuls les processus impliquant la désintégration d'un photon en un nombre impair de photons peuvent générer des pertes. Cependant, à une température plus élevée, la population des modes augmente et n'est plus égale à zéro. Par conséquent, des processus où un photon inséré dans le circuit interagit avec, par exemple, un photon thermique et les deux sont convertis à des fréquences différentes peuvent se produire (en d'autres termes, Σ'' relie plus d'états). De plus, lorsque la température augmente, les fluctuations de phase augmentent également et les processus impliquant 5,7,... photons deviennent aussi non négligeables. Par conséquent, le nombre de processus impliquant une conversion de photons, et donc les pertes associées, explosent lorsque la température augmente.

2.2.3 Organisation du manuscrit

Le manuscrit est divisé en trois chapitres. Le premier chapitre donne le contexte théorique nécessaire à la compréhension des l'expériences. Le deuxième chapitre présente le dispositif de mesure et les résultats expérimentaux sont discutés dans le troisième chapitre. Le premier chapitre est divisé en six sections : la première introduit les concepts permettant de décrire la physique d'un jonction Josephson et d'une chaîne de jonction. Dans les deux sections suivantes, la physique du BSG est introduite et un modèle simplifié est utilisé pour expliquer les ingrédients clés nécessaires à la conception d'un système complexe à plusieurs corps. La quatrième section est utilisée pour présenter différents paramètres influençant la renormalisation de l'énergie Josephson. Ensuite, les différents déphasages utilisés pour caractériser nos circuits sont présentés. Enfin, la rétroaction de la non-linéarité sur les modes de la chaîne est discutée. Le chapitre expérimental est divisé en deux sections. Dans la première, la non-linéarité de la jonction est fixée et l'influence de la température est étudiée. Dans la seconde, l'utilisation d'un SQUID nous permet de faire varier la non-linéarité. Nous discutons également de l'amortissement induit par la non-linéarité dans les modes. Enfin, j'ai fait le choix de n'inclure dans ces chapitres que les principaux résultats de ma thèse. Par conséquent, les annexes sont utilisées comme matériel supplémentaire.

Theory 3

Contents

3.1 Circuitry 32
3.1.1 The Josephson Junction 32
3.1.2 The Environment 37
3.2 Boundary Sine Gordon 49
3.2.1 Even and odd modes circuit 49
3.2.2 Boundary Sine Gordon Ground State within the Self Consistent Harmonic Approximation 51
3.2.3 Normal mode decomposition 54
3.2.4 Phase mode profil 56
3.3 How to design a complex Hamiltonian ? 58
3.3.1 Link between response function and phase fluctuations. . 58
3.3.2 Toy model for the phase fluctuations 59
3.4 Renormalisation of the nonlinear junction. 62
3.4.1 Influence of the nonlinear junction impedance. 63
3.4.2 Influence of the chain impedance. 63
3.4.3 Influence of the chain plasma frequency. 64
3.4.4 Influence of the temperature of the system. 65
3.5 Phase shift 66
3.5.1 Analytical expressions 66
3.5.2 Link with other quantities. 68
3.5.3 An illustration of the thermodynamic limit 71
3.6 Backaction on the environment modes 72
3.6.1 Comparison between the SCHA and the Kerr approximation 72
3.6.2 Damping induced by the nonlinear junction - Photon conversion. 75

3.1 Circuitry

In this section the building blocks of circuit Quantum Electrodynamics (c-QED) are explained. We start by introducing the ground state properties of a Josephson Junction in different regimes of nonlinearity. After that, the concept of chain of Josephson junctions will be developed. Finally we will see how to combine these two to design a Boundary Sine Gordon Hamiltonian.

3.1.1 The Josephson Junction

Linear Regime

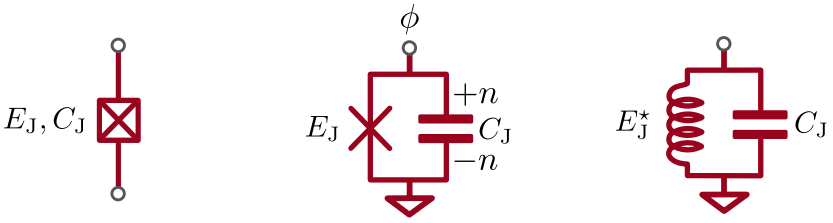

Figure 3.1 – Circuit representation of a Josephson junction. From left to right: an embedded representation encompassing the Josephson energy and its capacitance, a representation separating the Josephson and capacitive terms, an effective representation within the Self Consistance Harmonic Approximation (SCHA, explained below). E_J, $E_J^\star$ and C_J are respectively the Josephson Energy, renormalized Josephson energy and Josephson capacitance. ϕ and n are the phase and number of Cooper pairs differences across the junction.

A Josephson Junction consists in a superconductor interrupted by a non superconducting layer. That last should be thin enough so that tunneling can take place. In our case the junctions are made of two aluminum layers sandwiching an aluminium oxyde barrier. The different circuit representations are displayed in Fig.3.1. In c-QED it is convenient to define two variables [77]:

$$\phi(t) = \frac{1}{\phi_q}\int_{-\infty}^{t} dt' v\left(t'\right) \tag{3.1}$$

$$n(t) = \frac{1}{2e}\int_{-\infty}^{t} dt' i\left(t'\right) \tag{3.2}$$

where i and v are the classical current and voltage while $\phi_q = \hbar/2e$ is the reduced flux quantum. Therefore, ϕ and n are defined as a superconducting phase and a number of Cooper pairs. They are quantized by imposing $\left[\hat{\phi}, \hat{n}\right] = i$. The Hamiltonian of such a junction is then:

$$\hat{H} = E_C\left(\hat{n} - n_g\right)^2 + E_J\left(1 - \cos\hat{\phi}\right) \tag{3.3}$$

where $E_C = \frac{(2e)^2}{2C_J}$ is the charging energy coming from the fact that there are two metallic parts interrupted by an oxide and E_J is due to the fact that these metals are

superconducting. n_g is a static charge offset coming from the junction environment. Thereafter, we set it to zero because the junctions that will be used will either be in a regime in which this offset will have no effect on the Hamiltonian properties (the linear regime) or will be screened (see Appendix A.1).

If E_J is way larger than E_C phase fluctuations will be negligible. Consequently, the cosine part of the Josephson Energy can be developed to second order (This is justified a posteriori by Eq.3.9):

$$\hat{H} = E_C \hat{n}^2 + \frac{E_J}{2}\hat{\phi}^2 \tag{3.4}$$

This Hamiltonian is quadratic. Hence it is convenient to define creation and annihilation operators such that:

$$\hat{\phi} = \sqrt{2\pi \frac{Z_J}{Z_q}} \frac{\left(\hat{a} + \hat{a}^\dagger\right)}{\sqrt{2}} \tag{3.5}$$

$$\hat{n} = \sqrt{\frac{1}{2\pi}\frac{Z_q}{Z_J}} \frac{\left(\hat{a} - \hat{a}^\dagger\right)}{\sqrt{2}i} \tag{3.6}$$

with $\left[\hat{a}, \hat{a}^\dagger\right] = 1$ and $Z_q = h/(2e)^2$ is the superconducting quantum of impedance. The characteristic impedance of the junction is defined as:

$$Z_J = \frac{Z_q}{2\pi}\sqrt{\frac{2E_C}{E_J}} \tag{3.7}$$

The Hamiltonian can be expressed with the creation and annihilation operators:

$$\hat{H} = \hbar\omega_J \left(\hat{a}^\dagger \hat{a} + \frac{1}{2}\right) \tag{3.8}$$

with $\omega_J = \sqrt{2E_J E_C}/\hbar$ the plasma, or equivalently resonant, frequency of the junction. From Eq.3.5 and 3.6 we can compute the fluctuations of the phase and of the charge number:

$$\langle \hat{\phi}^2 \rangle = \pi \frac{Z_J}{Z_q}\left(2\langle \hat{a}^\dagger \hat{a}\rangle + 1\right) = \phi_{ZPF}^2 \left(2n_B + 1\right) \tag{3.9}$$

$$\langle \hat{n}^2 \rangle = \frac{1}{4\pi}\frac{Z_q}{Z_J}\left(2\langle \hat{a}^\dagger \hat{a}\rangle + 1\right) = n_{ZPF}^2 \left(2n_B + 1\right) \tag{3.10}$$

where ϕ_{ZPF} and n_{ZPF} are respectively the Zero Point Fluctuation (ZPF) amplitude in phase and charge number coming from the Heisenberg uncertainty principle. Here, we have made the hypothesis that the system is at thermal equilibrium with its environment. Therefore, n_B is the occupation number of the junction given by the Bose factor at frequency ω_J and temperature T:

$$n_B = \frac{1}{e^{\hbar\omega_J/k_B T} - 1} \tag{3.11}$$

The chemical potential has been ignored because the circuit excitations can be considered as microwave photons. From Eq.3.9 we see that phase fluctuations depend

linearly on the junction impedance. This is confirming the assumption that when $E_C \ll E_J$ the cosine can be developed to second order.

We now introduce a quantity that will be very important for the next sections, the time correlator of the phase defined as:

$$S_\phi(t) = \langle \hat{\phi}(t)\, \hat{\phi} \rangle \tag{3.12}$$

First thing to notice is that the phase fluctuations are given by $S_\phi(t=0)$. More information can be extracted from that correlator by taking its Fourier transform, called noise spectral density, given by:

$$S_\phi(\omega) = \int_{\mathbb{R}} dt S_\phi(t)\, e^{i\omega t} \tag{3.13}$$

For our junction it reads[a]:

$$S_\phi(\omega) = 2\pi\phi_{\mathrm{ZPF}}^2 \left[n_B \delta(\omega + \omega_J) + (n_B + 1)\, \delta(\omega - \omega_J) \right] \tag{3.14}$$

Where we used $\hat{a}(t) = \hat{a} e^{-i\omega_J t}$. The noise spectral density is not a symmetric function of the frequency (contrary to the classical case) due to the +1 factor in the positive part of the spectrum. This expression can be understood in the following way: phase fluctuations can be thermal or quantum. According to the fluctuation-dissipation theorem [78, 79], these fluctuations can only come from the absorption ($\omega < 0$) or emission ($\omega > 0$) of excitations[b]. The thermal part of the fluctuations give the symmetric part of the noise spectral density. In other words, it gives the part depending on the occupation number. In addition, the quantum part of the fluctuations (ZPF) of the environment trigger spontaneous emission of excitations. Hence, quantum fluctuations are responsible for the asymmetry in the noise spectrum. This interpretatoin is supported by the fact the at $T = 0$, $S_\phi(\omega = -\omega_J)$ is equal to zero since no energy can be absorbed from the ZPF while $S_\phi(\omega = \omega_J)$ is nonzero since the resonator can always absorb excitations.

We see that having a linear Hamiltonian enables us to compute easily the properties of a junction. In the following we will see a way to make the $E_J \gg E_C$ condition less stringent.

The Self-Consistent Harmonic Approximation

From now on, we will only consider the Ground State (GS) of the junction. In this section we consider the system at T=0. A more general study can be found in Section 3.2.2. We have seen that having a harmonic Hamiltonian is quite convenient so it will be interesting to find a way to release the $E_J \gg E_C$ condition. This is possible within the Self-Consistent Harmonic Approximation (SCHA). This approximation is based on the search for the harmonic Hamiltonian which mimics the most accurately the GS of our junction. That trial Hamiltonian reads:

$$\hat{H}_t = E_C \hat{n}^2 + \frac{E_J^\star}{2} \hat{\phi}^2 \tag{3.15}$$

[a] Using the definition of the delta function $2\pi\delta(\omega - \omega_k) = \int_{\mathbb{R}} dt e^{i(\omega-\omega_k)t}$

[b] we can also say that $\omega < 0$ measure the energy that can be absorbed from the resonator while $\omega > 0$ measure the one that can be absorbed by the latter, see [80] for a detailled discussion

where $E_J^\star$ is a free parameter that will be optimized. Eq.3.15 gives:

$$\hat{H} = \hat{H}_t + 1 - E_J \cos\hat{\phi} - \frac{E_J^\star}{2}\hat{\phi}^2 \tag{3.16}$$

Applying variational principle yields (see [81] Complement E-XI):

$$\partial_{E_J^\star} \langle\psi_t| \hat{H} |\psi_t\rangle = 0 \tag{3.17}$$

where $|\psi_t\rangle$ is the ground state of the trial Hamiltonian. A detailed calculation is given in Appendix A.2. The resulting expression for the renormalized Josephson Energy is:

$$E_J^\star = E_J e^{-\langle\hat{\phi}^2\rangle_t/2} = E_J \exp\left(-\frac{1}{2}\sqrt{\frac{E_C}{2E_J^\star}}\right) \tag{3.18}$$

where we used Eq.3.9 and 3.7 to express $\langle\hat{\phi}^2\rangle_t$. We see that when phase fluctuations increase the renormalized Josephson energy decreases. This is due to the fact that when the fluctuations increase a bigger part of the cosine potential is explored. Hence, the effective energy barrier is reduced. Since the best harmonic approximation has been found we can define the resonant frequency of that Hamiltonian as:

$$\omega_J^\star = \frac{1}{\hbar}\sqrt{2E_J^\star E_C} \tag{3.19}$$

$$= \sqrt{2E_J E_C} e^{-\langle\hat{\phi}^2\rangle_t/4} \tag{3.20}$$

$$= \sqrt{2E_J E_C} \exp\left(-\frac{E_C}{4\hbar\omega_J^\star}\right) \tag{3.21}$$

Eq.3.18 and 3.21 are self-consistent because the resonance frequency and respectively the Josephson energy depend on themselves. These equations can be solved by looking for the zero of $E_J^\star|\omega_J^\star - f(E_J^\star|\omega_J^\star)$ where f stands for the right-hand side of Eq.3.18 or Eq.3.21 respectively. However, if the junction is weakly nonlinear we can treat the effect of phase fluctuations perturbatively and develop the exponential up to the second order:

$$\omega_J^\star = \omega_J - \frac{E_C}{4\hbar} \tag{3.22}$$

which is nothing less than the well known formula for the ground to first excited state transition frequency of the Transmon qubit [30]. Hence, the SCHA seems to gives an accurate description of a weakly-nonlinear oscillator ground state. Its limitations can now be studied. To do so, the first transition frequency given either by the SCHA or by the numerical diagonalization of the junction Hamiltonian will be compared in different regime of nonlinearity. In the charge basis the matrix elements of the Hamiltonian are (see [82] Chapter 3):

$$\langle n| \hat{H} |m\rangle = E_C \delta_{n,m} n^2 + \frac{E_J}{2}\left(\delta_{n,m+1} + \delta_{n,m-1}\right) \tag{3.23}$$

Therefore, the first transition frequency of the junction can easily be found by numerical diagonalization.

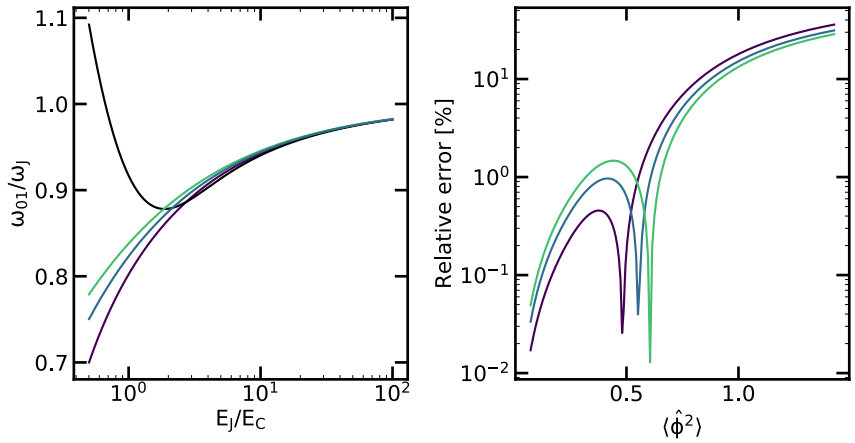

Figure 3.2 – **Left.** First transition frequency given by numerical diagonalization (black), first order perturbative treatment (green), first iteration of the SCHA (blue) and the SCHA (violet) as a function of E_J/E_C. All of theses quantities are normalized to the plasma frequency expected in the linear regime. **Right.** Relative error between these last three quantities and the numerical diagonalization as a function of the phase fluctuations.

To understand a bit more quantitatively the SCHA we distinguish four scenarios for the first transition frequency:

1. $\omega_{01} = (E_1 - E_0)/\hbar$ given by the numerical diagonalization previously explained. This can be taken as an exact solution when the Hamiltonian matrix size is large enough compared to the amplitude of charge number fluctuations.
2. $\omega_{01} = \omega_J - \frac{E_C}{4\hbar}$ resulting from a first order perturbative treatment of the phase fluctuation.
3. $\omega_{01} = \omega_J e^{-E_C/4\hbar\omega_J}$ resulting from the first iteration of the SCHA.
4. $\omega_{01} = \omega_J e^{-E_C/4\hbar\omega_{J^\star}}$ given by the SCHA.

These four quantities are plotted on the left panel of Fig.3.2. At low nonlinearity, or conversely high E_J/E_C ratio, the four quantities are in close agreement all together and do not deviate much from the linear behavior. At $E_J/E_C \gtrsim 1$ they all follow the same trend but some quantitative errors appears. At $E_J/E_C < 1$ the first transition frequency given by numerical diagonalisation starts to increase while the others continue to decrease. In this regime of nonlinearity the phase fluctuations start to be on the order of unity as the right panel of Fig.3.2 shows. The qualitative disagreement between the SCHA and the numerical diagonalization comes from the replacement of the cosine by a quadratic term. This approximation is justified when E_J/E_C is large enough so that the tunneling probability between two minima of the Josephson potential in phase space is negligible. To estimate a limit on the SCHA accuracy we recall that the ground state of a quadratic Hamiltonian is a Gaussian state [82]:

$$\psi(\phi) = \langle\phi|\psi\rangle = \left(\frac{1}{2\pi\langle\hat{\phi}^2\rangle}\right)^{1/4} \exp\left(-\frac{\phi^2}{4\langle\hat{\phi}^2\rangle}\right) \tag{3.24}$$

where the t index has been drop for the phase fluctuations and wavefunction. Therefore the overlap between two minima is given by[c]:

$$\int_{\mathbb{R}} d\phi \psi\left(\phi\right) \psi\left(\phi + 2\pi\right) = \exp\left(-\frac{\pi^2}{2\langle\hat{\phi}^2\rangle}\right) \tag{3.25}$$

As long as $\langle\hat{\phi}^2\rangle \lesssim 1$ the overlap between two minima is below 10^{-2} explaining why the first transition frequency is well estimated (the relative error is of the order on 1%) in this regime. Fig.3.3 illustrate the wave function overlap for different $E_{\mathrm{J}}^{\star}/E_{\mathrm{C}}$ ratio.

When $\langle\hat{\phi}^2\rangle \gtrsim 1$ the wave function is not really confined in phase space but in charge. Therefore, it is more convenient to see the junction as a particle in Bloch bands in the charge representation. In this regime the barrier potential depends on the charge number fluctuations. Eq.3.10 tells us that these fluctuations vary inversely to the phase ones. Moreover, in the limit $E_{\mathrm{C}} \gg E_{\mathrm{J}}$ the transition frequency is given by E_{C}. Thus, $E_{\mathrm{C}}/\omega_{\mathrm{J}} = \sqrt{E_{\mathrm{C}}/2E_{\mathrm{J}}}$ is rapidly growing. This is a hand waving explanation of why the first transition frequency start to increases when $E_{\mathrm{J}}/E_{\mathrm{C}}$ goes below 1.

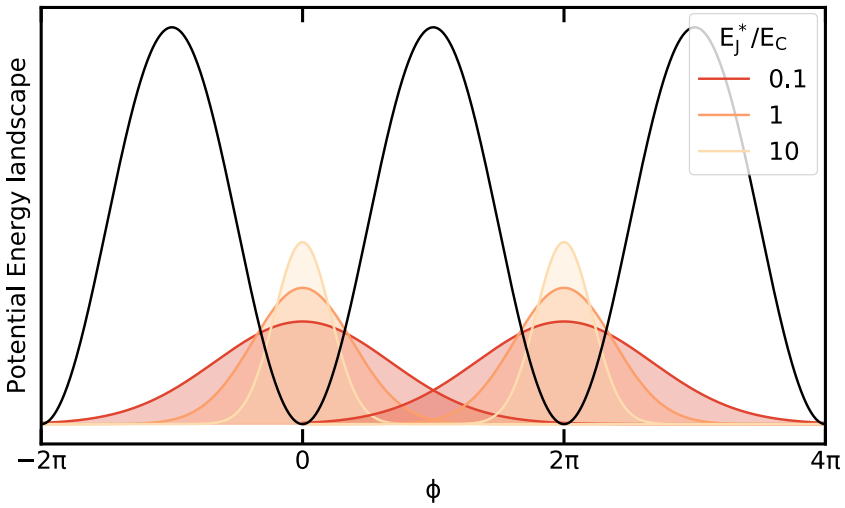

Figure 3.3 – Ground state wavefunction in the phase space for different regimes of nonlinearity. The black line is the classical representation of the Josephson Energy.

3.1.2 The Environment

High Impedance transmission line

To design a circuit that mimics the one of a Boundary Sine Gordon we need to couple a Josephson junction to a 1D free massless scalar field. In the vocabulary of statistical physics this means that it must be coupled to an environment. The coupling to an environment in a classical electrical circuit is described via the introduction of a resistor. Because of the irreversible nature of the dissipation induced by an environment,

[c]Note that the integration is performed over the entire real branch because by approximating the junction as a harmonic oscillator, the phase variable loses its compact nature.

its modeling within the quantum framework, which is based on Analytical Mechanics, is not straightforward since the latter is composed of time reversible equations. However, a transmission line of infinite length can be used to reproduce the behavior of a resistor [77]. This is due to the fact that any excitation emitted in such a transmission line will take an infinite amount of time to return according to the Poincaré recurrence theorem [83].

For the system resulting from the coupling between this transmission line and the junction to show complex nonlinear behaviour, we need the junction phase fluctuations to be as large as possible, for reasons similar to the isolated junction case we've discussed in the previous section. Hence, as we will prove in Section 3.3.2, the characteristic impedance of the latter, given by $Z_\mathrm{C} = \sqrt{L/C}$ (where L and C are respectively the inductance and ground capacitance per unit length), needs to be comparable to the quantum of resistance (see Eq. 3.9).

The characteristic impedance of a transmission line is given by (up to a prefactor depending on the geometry, see Section 4.1.2):

$$Z_\mathrm{C} \sim \frac{1}{2\pi}\sqrt{\frac{\mu_0}{\epsilon_\mathrm{r}\epsilon_0}} \simeq \frac{60}{\sqrt{\epsilon_\mathrm{r}}} \tag{3.26}$$

Where ϵ_r is the relative permittivity of the oxide between the two metallic parts of a transmission line. From that formula we see that the maximal impedance is reached if the oxide is the vacuum. Nevertheless, even in this case the characteristic impedance is far from the quantum of resistance. A possible strategy is then to play on the inductive part of the characteristic impedance. Geometrical inductance per meter is given by $L_\mathrm{geo} = \mu_0/2\pi \sim 0.2\,\mu\mathrm{H\,m^{-1}}$. That last is quite low but can be replaced by the kinetic inductance offered by disordered superconductors such as GrAl [84, 85], NbN [86], NbTiN [87] and TiN [88], etc. A detailed presentation of these materials is beyond the scope of this manuscript but the key concept can be understood from the Drude model. In that model the conductivity is given by:

$$\sigma = \sigma_\mathrm{m} - i\omega\tau\sigma_\mathrm{m} \tag{3.27}$$

where τ is a damping time corresponding to the loss induced by scattering with electron, phonon... In normal metals τ is so short that the complex part of the conductivity can be discarded. Nonetheless, in superconductors we can take $\tau \to \infty$. Therefore, the inductance per meter in this model is given by:

$$L_\mathrm{kin} = \frac{m}{n_\mathrm{c} q^2 A} \tag{3.28}$$

where m and n_C are the mass and density of Cooper pairs while A is a cross section. From this formula we see that the inductance per meter is inversely proportional to the density of Cooper pair. In disordered superconductor the latter is low enough to allow the design of high impedance transmission lines. Despite being promising, a lot of things remains to be understood with these materials and a different, yet close, approach has been chosen for our circuit. The key idea is to make use of the kinetic inductance generated by a Josephson junction [89–91]. The current going through such a junction is given by:

$$i = \frac{1}{\phi_\mathrm{q}}\frac{\partial H}{\partial \phi} = I_\mathrm{c}\sin\phi \tag{3.29}$$

Then from the definition of the inductance:

$$v = L_{\mathrm{J}}(\phi)\frac{\partial i}{\partial t} \tag{3.30}$$

we end up with the following expression for the Josephson inductance:

$$L_{\mathrm{J}}(\phi) = \frac{\phi_{\mathrm{q}}}{I_{\mathrm{c}}\cos\phi} \tag{3.31}$$

This inductance is nonlinear because of the nonlinear nature of the JJ. Since we want to design a linear environment we will use the junctions forming our environment in the high $E_{\mathrm{J}}/E_{\mathrm{C}}$ regime. Hence, the Josephson inductance will be given by $\phi_{\mathrm{q}}/I_{\mathrm{C}}$. The critical current density obtained in our nano-fabrication process is about $15\,\mathrm{Acm}^{-2}$. A typical area for the junctions we use is 0.2x10 $\mu\mathrm{m}^2$ (see Section 4.3). Consequently, the inductance of one junction is around 1 nH.

Now that we know how to fabricate large inductances with a rather small footprint the idea is to cascade them in the fashion of Fig.3.4 so that we create a quasicontinuum made of JJ. That medium is very similar to a disordered supraconductor where the tunnel barrier of the junctions is the analogue to the low Cooper pairs density. For these reasons such chains of junctions are often called a metameterial. Since we are able to design arrays with at least one junction per micrometer it gives an inductance per meter of $1\,\mathrm{mHm}^{-1}$. This is three orders of magnitude larger than the geometrical one. Thanks to that, transmission lines with a characteristic impedance on the order of the superconducting resistance quantum can be obtained [68, 92–94].

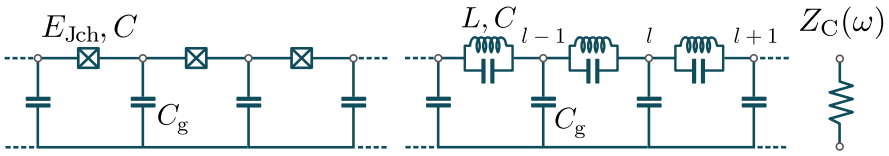

Figure 3.4 – **Left.** A chain of Josephson junction with a Josephson energy E_{Jch} and capacitance C. Each node is grounded via a capacitance C_{g}. **Middle.** Equivalent representation when the junctions are in the linear regime with $L = \phi_{\mathrm{q}}^2/E_{\mathrm{Jch}}$. **Right.** When the chain is infinite it can be seen as an impedance $Z_{\mathrm{C}}(\omega)$.

Dispersion Relation

The circuit resulting from cascading an infinite number of junctions is not exactly the same than the one of a transmission line because of the capacitance in parallel to the inductance. To understand what this means for our environment we will study its different properties starting with the dispersion relation.

Because the chain is infinite, phase and charge waves can propagate inside. The relation between the frequency and wave vector of the latter is called a dispersion relation. Most of the properties of a chain are linked to this relation. Thus it is crucial to understand it properly. Current conservation at a node l gives (see Fig.3.4):

$$\left[1-\omega^2 LC\right]\left[\xi_{l+1}(\kappa)+\xi_{l-1}(\kappa)-2\xi_l(\kappa)\right]+\omega^2 LC_g\xi_l(\kappa)=0 \tag{3.32}$$

Where ξ_l is the phase wave amplitude at site l. Since the system is invariant per translation we take a left moving plane wave Ansatz[d]:

$$\xi_l(\kappa)=A_\phi e^{i(\kappa la-\omega t)} \tag{3.33}$$

Where a is the size of an unit cell and κ, ω and A_ϕ are respectively the wavevector, frequency and amplitude of the wave. Inserting this Ansatz in Eq.3.32 gives:

$$\omega(\kappa)=v_\varphi\sqrt{\frac{2\left(1-\cos\kappa a\right)}{1+2\left(1-\cos\kappa a\right)l_c^2}} \tag{3.34}$$

where $v_\varphi=1/\sqrt{LC_g}$ and $l_c=\sqrt{C/C_g}$. To understand the meaning of the these two parameters we will take the continuum limit $\kappa \ll 1/a$:

$$\omega(\kappa)=\frac{\left(v_\varphi a\right)\kappa}{\sqrt{1+\left(al_c\right)^2\kappa^2}} \tag{3.35}$$

Three regimes can be distinguished:

— when $\kappa \ll 1/al_c$ the dispersion relation is linear. Hence, $v_\varphi a$ is the phase velocity of the TEM waves propagating in the transmission line.

— when $\kappa \sim 1/al_c$ the in-line capacitance starts to bend the dispersion relation. Because of that al_c can be interpreted as the length for which the inter site Coulomb screening starts to be efficient [95].

— when $\kappa \gg 1/al_c$ the wave frequency reaches its maximal value $\omega_p=1/\sqrt{LC}$. The latter is called plasma frequency since it is the resonant frequency of the junctions forming the transmission line. At this frequency all the junctions are self oscillating and no wave can propagate.

If the $\kappa \ll 1/a$ limit is not taken the previous discussion is still valid. The only difference is that the finite size of the chain unit cells introduces a wavevector cut-off. The smallest wavelength that can be reached is $2a$. Therefore, the largest wavevector is $\kappa=\pi/a$. Because of that, the actual plasma frequency of the chain is slightly different than in the $\kappa \ll 1/a$ limit. To find it we compute Eq.3.34 with the cut off wavevector and we find:

$$\omega_p=\frac{1}{\sqrt{L\left(C+C_g/4\right)}} \tag{3.36}$$

In the following we will work with dimensionless wavevectors and define $k=\kappa a$. The different dispersion relation behavior are displayed in Fig.3.5.

[d]From now until the end discrete variables will be indexed and continuous variables in brackets. For exemple the site number l is indexed while the wavector for an infinite transmission line κ is in brackets

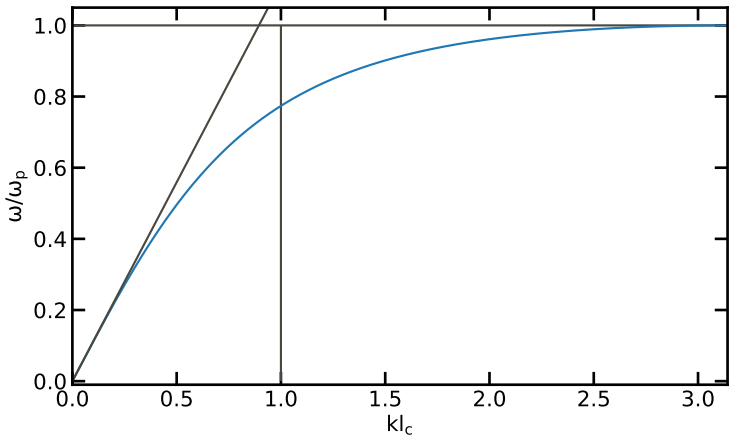

Figure 3.5 – Dispersion relation of the Josephson junction chain (blue line). The vertical grey line indicates the regime in which Coulomb screening is predominant. The linear function shows the region for which waves are mostly TEM. The horizontal line indicates the plasma frequency of the chain.

Characteristic impedance

An infinite transmission line can be seen as a real impedance $Z_C = \sqrt{L/C_g}$, called its characteristic impedance. Because of its inline capacitance the JJ chain characteristic impedance will be a bit more complicated.

Let us consider an infinite ladder with an inline impedance Z_1 and an impedance to ground Z_2. Using the recipe introduced in Feynman lectures [96] (Chapter 23) we find the characteristic impedance of such a ladder to be:

$$Z_C(\omega) = \sqrt{\frac{Z_1^2}{4} + Z_1 Z_2} \tag{3.37}$$

For our chain $Z_1 = i\omega L/(1-\omega^2 LC)$ and $Z_2 = 1/i\omega C_g$. If we were using a real continuum we could use the limit $a \to 0$. Because $Z_1 \propto a$ and $Z_2 \propto 1/a$, Z_1 would go to zero with $Z_1 Z_2$ fixed. But since we are using a chain made out of lumped elements that approximation is not realistic. However, since Z_1/Z_2 is on the order of C_g/C we can consider that Eq.3.37 is given by $\sqrt{Z_1 Z_2}$ up to a C_g/C factor. This is not a strong approximation since in our experiments C is always four orders of magnitude bigger than C_g. Therefore, the characteristic impedance can be approximated by:

$$Z_C(\omega) = \frac{Z_C}{\sqrt{1-\omega^2 LC}} \tag{3.38}$$

Which is equivalent to what is found in the continuum limit. Thus, at low frequency with respect to the plasma frequency the characteristic impedance is the one expected for a transmission line. On the other hand, when the frequency approaches the plasma frequency the impedance diverges and becomes complex above the latter. This is another way to see that no wave can propagate above the plasma frequency. Note that because we made the approximation $C_g \gg C$, the plasma frequency is given by $1/\sqrt{LC}$.

Boundary conditions and Thermodynamic limit

From the beginning the chain has been considered infinite. In fact this is not possible: it will be connected to a nonlinear junction and therefore must be at least semi-infinite. Moreover, when it will be fabricated, a finite number of sites will have to be chosen. Because of that, we have to consider the influence of these boundaries on the chain physics. For now we will only consider the two limit cases:

— The last (first) site is an open. Thus, the voltage is maximum (so does the phase) and we have:

$$\partial_l \xi_l \Big|_{l=0(N)} = 0 \tag{3.39}$$

— The last (first) site is grounded. Thus, the voltage is equal to zero and we have:

$$\xi_{0(N)} = 0 \tag{3.40}$$

Because these boundary conditions do not contain any dissipative elements the waves propagating in the transmission line will be reflected without loss of energy. Left-moving and right-moving waves will therefore interfere with each other. These interferences will be either constructive or destructive depending on the wavelength. Thus, certain frequency ranges will be forbidden while others will not, leading to the formation of resonant modes. A general Ansatz fo these modes is[e]:

$$\xi_{l,k} = A_k \cos(kl - \theta_k) \tag{3.41}$$

To understand how does the boundary condition affect the system we will consider two cases:

— First and last sites are grounded.

— First site is an open, last site is grounded.

In the first case we have $\xi_{0,k} = 0$ and $\xi_{N,k} = 0$. The first condition imposes $\theta_k = \pi/2$ while the second sets $k_n = \pi n/N$. Hence, the phase mode envelop is given by $\xi_{l,k} = A_k \sin(k_n l)$.

In the second case the boundary conditions are $\partial_l \xi_l \Big|_{l=0} = \xi_{1,k} - \xi_{0,k} = 0$ and $\xi_{N,k} = 0$. The first condition gives $\theta_k = k/2$ while the second imposes $k_n = \pi(n + 1/2)/(N - 1/2)$. Thus the phase mode envelop is $\xi_{l,k} = A_k \cos(k_n [l - 1/2])$

Note that more general boundary conditions can be considered within these formalism (see Section 3.2.3). In any case the minimal interval between two wavevectors is given by $\Delta k = \pi/N$ (we consider $N \gg 1$). Therefore the frequency interval between two modes, called Free Spectral Range (FSR), is given by:

$$\Delta\omega_{\mathrm{FSR}}(\omega) = \frac{\pi}{N} \frac{\partial\omega}{\partial k_n} \tag{3.42}$$

[e]The wavevector k is now indexed since the transmission line is no longer infinite. Hence, k is a discrete variable.

From the dispersion relation expression (Eq.3.34):

$$\Delta\omega_{\mathrm{FSR}}(\omega) = \frac{\pi}{N} v_\varphi \left(1 - \omega^2 LC\right) \sqrt{1 - \left(\frac{\omega}{\omega_{\mathrm{p}}}\right)^2} \tag{3.43}$$

A simple interpretation of the free spectral range can be given in the limit $\omega \ll \omega_{\mathrm{p}}$:

$$\Delta\omega_{\mathrm{FSR}} = \frac{\pi}{N} v_\varphi = \frac{2\pi}{T_{\mathrm{r}}} \tag{3.44}$$

Where T_{r} is the round trip time, the time it takes for an excitation emitted in the chain to come back. This simple observation allows us to understand why an infinite set of non dissipative elements can be seen as a dissipative element of characteristic impedance $Z_{\mathrm{C}}(\omega)$. If we take the chain as semi infinite (meaning $N \to \infty$) the FSR goes to zero and both the dispersion relation and the impedance are continuous functions of the frequency. Moreover, the round trip time goes to infinity. Hence, any emitted photon in such a chain will be lost.

We have seen that in practice no chain is (semi) infinite. Nevertheless, if the round trip time is way longer than all the characteristic times of the system (for example the damping time of an oscillator connected to it). Then, it can be taken as infinite at the scale of the experiment. In the frequency domain it means that the FSR has to be much smaller than all other characteristic frequencies. We will refer to this as the thermodynamic limit. This limit is different from the continuum limit corresponding to $a \to 0$.

Mode quantization

We have seen how boundary conditions in the chain lead to the formation of resonant modes. Moreover, the phase mode profiles depend strongly on these boundaries. Now we will discuss a very generic framework allowing to find the amplitude of these modes for arbitrary non dissipative boundary conditions, which is often the case in realistic circuits. The Hamiltonian of a chain is:

$$\hat{H} = \frac{(2e)^2}{2} \sum_{l,m=0}^{N} \hat{n}_l [C]^{-1}_{l,m} \hat{n}_m + \frac{\phi_{\mathrm{q}}^2}{2} \sum_{l,m=0}^{N} \hat{\phi}_l [L^{-1}]_{l,m} \hat{\phi}_m \tag{3.45}$$

Where $[C]$ and $[L^{-1}]$ are matrices containing the capacitances and inductances of the chain. An explicit expression of these two will be given later. The phase and charge number operators are defined as:

$$\hat{n}_l = \sum_{k=0}^{N} \nu_{l,k} \frac{\hat{a}_k - \hat{a}_k^\dagger}{\sqrt{2}i} \tag{3.46}$$

$$\hat{\phi}_m = \sum_{k=0}^{N} \xi_{m,k} \frac{\hat{a}_k + \hat{a}_k^\dagger}{\sqrt{2}} \tag{3.47}$$

and conversely:

$$\hat{a}_k^\dagger = \frac{1}{\sqrt{2}} \sum_{m=0}^{N} \xi_{m,k} \hat{n}_m + i\nu_{m,k} \hat{\phi}_m \tag{3.48}$$

$$\hat{a}_k = \frac{1}{\sqrt{2}} \sum_{m=0}^{N} \xi_{m,k} \hat{n}_m - i\nu_{m,k} \hat{\phi}_m \tag{3.49}$$

with $[\nu]$ and $[\xi]$ the matrices containing the mode envelopes of the charge and phase modes. By imposing the canonical commutation relations $[\hat{\phi}_m, \hat{n}_l] = i\delta_{lm}$ and $[\hat{a}_k, \hat{a}_{k'}^\dagger] = \delta_{kk'}$ we find:

$$\sum_{k=0}^{N} \nu_{l,k} \xi_{m,k} = \delta_{lm} \tag{3.50}$$

$$\sum_{m=0}^{N} \nu_{m,k} \xi_{m,k'} = \delta_{kk'} \tag{3.51}$$

By inserting Eq. 3.46 and 3.47 in Eq. 3.45 and imposing:

$$\hat{H} = \sum_{k=0}^{N} \hbar\omega_k \left(\hat{a}_k^\dagger \hat{a}_k + \frac{1}{2} \right) \tag{3.52}$$

we find:

$$\phi_{\mathrm{q}}^2 \sum_{l,m}^{N} [L^{-1}]_{l,m} \xi_{m,k} \xi_{l,k'} + (2e)^2 \sum_{l,m}^{N} [C]_{l,m}^{-1} \nu_{m,k} \nu_{l,k'} = 2\hbar\omega_k \delta_{kk'} \tag{3.53}$$

$$\phi_{\mathrm{q}}^2 \sum_{l,m}^{N} [L^{-1}]_{l,m} \xi_{m,k} \xi_{l,k'} - (2e)^2 \sum_{l,m}^{N} [C]_{l,m}^{-1} \nu_{m,k} \nu_{l,k'} = 0 \tag{3.54}$$

The sum and difference of the two equations give the following conditions for the mode amplitude normalization:

$$\vec{\xi_{k'}}^{\mathrm{T}} [L^{-1}] \vec{\xi_k} = \frac{\hbar\omega_k}{\phi_{\mathrm{q}}^2} \delta_{kk'} \tag{3.55}$$

$$\vec{\nu_{k'}}^{\mathrm{T}} [C]^{-1} \vec{\nu_k} = \frac{\hbar\omega_k}{(2e)^2} \delta_{kk'} \tag{3.56}$$

with $\vec{\xi_k}^{\mathrm{T}} = (\xi_{0,k} ... \xi_{N,k})^{\mathrm{T}}$ and equivalently for $\vec{\nu_k}$. Then by multiplying the two equations respectively by $\vec{\nu_k}$ and $\vec{\xi_k}$ and using Eq. 3.51:

$$[L^{-1}] \vec{\xi_k} = \frac{\hbar\omega_k}{\phi_{\mathrm{q}}^2} \vec{\nu_k} \tag{3.57}$$

$$[C]^{-1} \vec{\nu_k} = \frac{\hbar\omega_k}{(2e)^2} \vec{\xi_k} \tag{3.58}$$

Finally, by inserting Eq. 3.57 in 3.58 we have:

$$[L^{-1}]\vec{\xi_k} = \omega_k^2[C]\vec{\xi_k} \tag{3.59}$$

which is the well known wave equation for a 1D medium [55, 67]. From this equation we can find the dispersion relation and the phase shift when the boundary conditions are more complex than an open or a short. However, as a starter, we will focus on the situation in which the first site is open and the last one is connected to the ground. To compute the mode amplitude we need to know the capacitance and inductance matrices. The latter are given by:

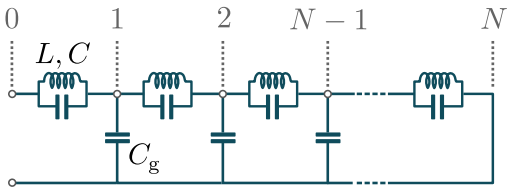

Figure 3.6 – Lumped element representation of the JJ chain. The first site is an open while the last is shorted to ground.

$$[C] = \begin{bmatrix} C & -C & 0 & 0 & \dots & 0 \\ -C & 2C + C_g & -C & 0 & \dots & 0 \\ 0 & -C & 2C + C_g & -C & \dots & 0 \\ \vdots & \vdots & \ddots & \ddots & \ddots & \vdots \\ 0 & 0 & 0 & -C & 2C + C_g & -C \\ 0 & 0 & 0 & 0 & -C & C \end{bmatrix}$$

$$[L^{-1}] = \begin{bmatrix} 1/L & -1/L & 0 & 0 & 0 & \dots & 0 \\ -1/L & 2/L & -1/L & 0 & 0 & \dots & 0 \\ 0 & -1/L & 2/L & -1/L & 0 & \dots & 0 \\ \vdots & \vdots & \ddots & \ddots & \ddots & \dots & 0 \\ 0 & 0 & 0 & -1/L & 2/L & -1/L & 0 \\ 0 & 0 & 0 & 0 & -1/L & 2/L & -1/L \\ 0 & 0 & 0 & 0 & 0 & -1/L & 1/L \end{bmatrix}.$$

We can now compute the phase mode amplitude using the fact that the phase mode profile for an open at first site and a grounded last site is given by (that was studied

in Section 3.1.2):

$$\xi_{l,k} = A_k \cos(k_n \left[l - 1/2\right]) \tag{3.60}$$

$$k_n = \pi \frac{n + \frac{1}{2}}{N - \frac{1}{2}} \tag{3.61}$$

Using it in Eq.3.55 we find:

$$2A_k^2 \left(1 - \cos k\right) \sum_{l=1}^{N} {\xi_{l,k}}^2 = \frac{L}{\phi_{\mathrm{q}}^2} \hbar\omega_k \tag{3.62}$$

A detailed calculation of the sum is provided in Appendix A.3. Hence, the phase mode amplitude reads:

$$A_k = \sqrt{\frac{\hbar\omega_k L}{\phi_{\mathrm{q}}^2 \left(1 - \cos k\right)\left(N - 1/2\right)}} \tag{3.63}$$

That formalism will be applied to more complex boundary conditions in Section 3.2.3.

Noise spectral density and phase fluctuations of a Josephson junction chain

Now that we have found an expression for the phase modes amplitude we can compute the noise spectral density of the JJ chain at site 0. For that we need to compute:

$$S_{\phi_0}\left(t\right) = \langle \hat{\phi}_0\left(t\right) \hat{\phi}_0 \rangle \tag{3.64}$$

By inserting Eq.3.47 in the correlator:

$$S_{\phi_0}\left(t\right) = \sum_{k,k'} \frac{\xi_{0,k}\xi_{0,k'}}{2} \langle \left(\hat{a}_k e^{-i\omega_k t} + \hat{a}_k^\dagger e^{i\omega_k t}\right)\left(\hat{a}_{k'} + \hat{a}_{k'}^\dagger\right) \rangle \tag{3.65}$$

$$= \sum_{k,k'} \frac{\xi_{0,k}\xi_{0,k'}}{2} \langle \hat{a}_k \hat{a}_{k'}^\dagger \rangle e^{-i\omega_k t} + \langle \hat{a}_k^\dagger \hat{a}_{k'} \rangle e^{-i\omega_k t} \tag{3.66}$$

We consider that the system is at thermal equilibrium:

$$S_{\phi_0}\left(t\right) = \sum_{k} \frac{\xi_{0,k}^2}{2} \left[n_k e^{i\omega_k t} + \left(n_k + 1\right) e^{-i\omega_k t}\right] \tag{3.67}$$

Where n_k stands for the number of excitation in mode k. Then the noise spectral density reads[f]:

$$S_{\phi_0}\left(\omega\right) = \pi \sum_{k} \xi_{0,k}^2 \left[n_k \delta\left(\omega + \omega_k\right) + \left(n_k + 1\right) \delta\left(\omega - \omega_k\right)\right] \tag{3.68}$$

The latter shows that the chain can be seen as an assembly of harmonic oscillators, as expected from the Hamiltonian form (see the similarities with Eq.3.14). Then $\xi_{0,k}^2/2$ is

[f] Using again $2\pi\delta\left(\omega - \omega_k\right) = \int_{\mathbb{R}} dt e^{i(\omega - \omega_k)t}$

nothing but the phase fluctuations amplitude of mode k. It appears even more clearly if we set $t = 0$ in Eq.3.67.

From now on, we will consider the system to be in the thermodynamic limit. Hence, taking $N \to \infty$ and converting the sums to integrals yields [g]:

$$S_{\phi_0}(\omega) = \pi \int dk \frac{N}{\pi} \xi_0(k)^2 \left[n(k)\, \delta(\omega + \omega_k) + (n(k)+1)\, \delta(\omega - \omega_k) \right] \tag{3.69}$$

$$= N \int_0^{\omega_{\mathrm{P}}} d\omega_k \partial_{\omega_k} k \xi_0(\omega_k)^2 \left[n(\omega_k)\, \delta(\omega + \omega_k) + (n(\omega_k)+1)\, \delta(\omega - \omega_k) \right] \tag{3.70}$$

$$= N\Theta(-\omega)\, \xi_0(-\omega)^2\, n(-\omega)\, \partial_{\omega_k} k \Big|_{\omega_k = -\omega}$$

$$+ N\Theta(\omega)\, \xi_0(\omega)^2\, n(\omega)\, \partial_{\omega_k} k \Big|_{\omega_k = \omega} \tag{3.71}$$

Where Θ is the Heavyside step function. Finally using $\xi_0(-\omega)^2 = -\xi_0(\omega)^2$ and the free spectral range expression (Eq.3.43) we obtain:

$$S_{\phi_0}(\omega) = \frac{\pi}{\Delta\omega_{\mathrm{FSR}}(\omega)} \frac{1}{1 - e^{-\hbar\omega/k_{\mathrm{B}}T}} \xi_0(\omega)^2 \tag{3.72}$$

Because $\hat{\phi}_0(t)$ does not generally commute with $\hat{\phi}_0$ it is convenient to define two other correlators corresponding respectively to the symmetric and antisymmetric part of the correlator:

$$\bar{S}_{\phi_0}(t) = \frac{\langle \{\hat{\phi}_0(t), \hat{\phi}_0\} \rangle}{2} \tag{3.73}$$

$$\tilde{S}_{\phi_0}(t) = \frac{\langle \left[\hat{\phi}_0(t), \hat{\phi}_0\right] \rangle}{2} \tag{3.74}$$

where $\{A, B\} = AB + BA$. The Fourier transforms of these correlators are then:

$$\bar{S}_{\phi_0}(\omega) = \frac{S_{\phi_0}(\omega) + S_{\phi_0}(-\omega)}{2} \tag{3.75}$$

$$\tilde{S}_{\phi_0}(\omega) = \frac{S_{\phi_0}(\omega) - S_{\phi_0}(-\omega)}{2} \tag{3.76}$$

Hence $\bar{S}_{\phi_0}$ is the symmetric in frequency part of the noise spectral density while $\tilde{S}_{\phi_0}$ is the anti-symmetric one. Because of that, the first is the noise spectral density that a classical apparatus will measure (see Section II of [80] for more details) while the second is linked to the dissipative part of the response function of the chain (see Section 3.3.1).

[g] Where we used $\sum_k \xrightarrow[N\to\infty]{} \int dk \frac{N}{\pi}$ since we saw in Section 3.1.2 that the interval between two consecutive wavevector is π/N

To understand that more deeply let us consider the case where we plug a classical apparatus on the first site. Since we want to measure the voltage, or phase, this apparatus can be modeled as an ideal component of infinite input impedance. Therefore, the first site can be modeled as an open and we can use Eq.3.72 and the fact that ξ_0^2 is an odd function of the frequency to compute the spectral noise density measured by the latter, given by $\bar{S}_{\phi_0}$:

$$\bar{S}_{\phi_0}(\omega) = \frac{\pi}{\Delta\omega_{\mathrm{FSR}}(\omega)} \xi_0(\omega)^2 \left[n(\omega) + \frac{1}{2} \right] \tag{3.77}$$

Where n is the excitation number. The amplitude of ξ_0 in the continuum limit is obtained from Eq.3.63. We can express it as a function of the frequency by using the dispersion relation expression (Eq.3.34):

$$A(\omega) = \sqrt{\frac{2\hbar\left(1 - LC\omega^2\right)}{\phi_{\mathrm{q}}^2 \omega C_{\mathrm{g}} N}} \tag{3.78}$$

Therefore the symmetric noise spectral density is:

$$\bar{S}_{\phi_0}(\omega) = \frac{2\hbar Z_{\mathrm{C}}(\omega)}{\omega\phi_{\mathrm{q}}^2} \left[n(\omega) + \frac{1}{2} \right] \cos\left(\frac{k(\omega)}{2} \right)^2 \tag{3.79}$$

where Z_{C} is given by Eq.3.38 .We derived an expression for the symmetric part of the spectral noise density for the junction chain in the thermodynamic limit. We can now take the continuum limit to end up with a more familiar result. We have seen that the continuum limit correspond to $a \to 0$ therefore $k = \kappa a$ goes to zero and the cosine term is equal to one. So that finally the voltage noise spectral density is given by:

$$\bar{S}_{\mathrm{V}}(\omega) = \bar{S}_{\phi_0}(\omega)\,\omega^2\phi_{\mathrm{q}}^2 = 2\hbar\omega Z_{\mathrm{C}}(\omega) \left[n(\omega) + \frac{1}{2} \right] \tag{3.80}$$

which is nothing but a slightly modified version of the Johnson-Nyquist formula [97] for an impedance $Z_{\mathrm{C}}(\omega)$. The additional 1/2 factor being there to handle the quantum part of the fluctuations. In most electrical engineering textbook we find:

$$\bar{S}_{\mathrm{V}}(\omega) = 4\hbar\omega Z_{\mathrm{C}}(\omega) \left[n(\omega) + \frac{1}{2} \right] \tag{3.81}$$

The factor 2 discrepancy comes from the fact that we consider a two sided spectral noise density while the convention is to consider one-sided noise. This proves that in the continuum and thermodynamic limit the JJ chain can be considered as an impedance $Z_{\mathrm{C}}(\omega)$.

A comparison between the voltage noise of a transmission line and our chain of JJ is provided in Fig.3.7[h]. Both of them are computed at $T = 0$. As expected, the spectral noise density is zero for $\omega < 0$ since the apparatus has no excitation to absorb from the transmission line (T=0). At $\omega > 0$ the noise increases linearly with the frequency because the energy of the emitted photon is given by $\hbar\omega$. Finally, the JJ chain noise starts to deviate from the one of a transmission line when the frequency gets close to

[h] Note that we plot the voltage noise and not its symmetric part

the plasma frequency. It is simply explained by Eq.3.38: the characteristic impedance increases with the frequency, so does the voltage noise.

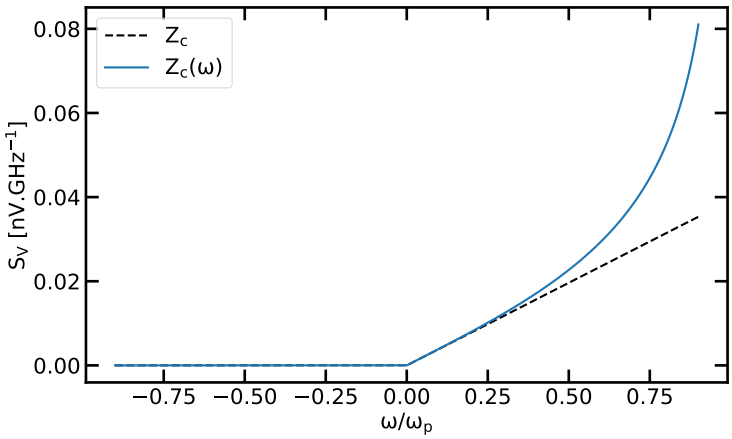

Figure 3.7 – Voltage noise spectral density for the chain (blue line) and a transmission line (black dashed line). At negative frequency the noise is zero while it is linearly increasing in the positive part of the plot. Near the plasma frequency, the chain noise starts to deviate from the linear behavior since the impedance diverges.

3.2 Boundary Sine Gordon

We have seen the basic properties of both a nonlinear Josephson Junction and a chain of linear ones. We are now going to consider how these two can come together to obtain a Boundary Sine Gordon Hamiltonian.

3.2.1 Even and odd modes circuit

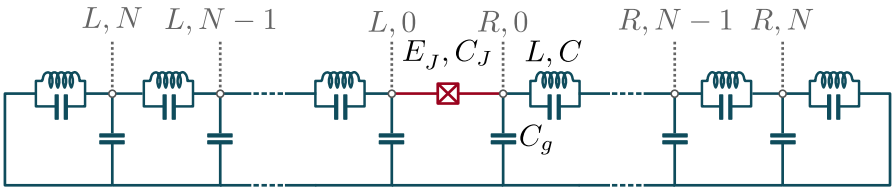

Figure 3.8 – Lumped element representation of a nonlinear junction (red) embedded in two linear Josephson chains (blue)

In this thesis, I have investigated two types of circuit I will now describe. The first studied circuit consists of two long Josephson chains of N sites tailored to be in the linear regime interconnected via a nonlinear Josephson junction. Its lumped element

circuit is displayed in Fig. 3.8. The equivalent Hamiltonian is the following:

$$\hat{H} = \frac{(2e)^2}{2} \sum_{i,j=0}^{N} \sum_{\sigma,\sigma' \in L,R} \hat{n}_{i\sigma} [C]^{-1}_{i,\sigma,j,\sigma'} \hat{n}_{j,\sigma'} + \frac{\phi_q^2}{2L} \sum_{i=0}^{N-1} \sum_{\sigma \in L,R} \left(\hat{\phi}_{i,\sigma} - \hat{\phi}_{i+1,\sigma}\right)^2 - E_J \left[1 - \cos\left(\hat{\phi}_{0,L} - \hat{\phi}_{0,R}\right)\right] \tag{3.82}$$

with $\hat{n}_{i,\sigma}$ and $\hat{\phi}_{i,\sigma}$ the charge number and phase operators on site $i \in [1..N]$ and in chain $\sigma = L, R$. The capacitance matrices can be decomposed into an intra-chain part $[C_0] = [C]_{LL} = [C]_{RR}$ and an interchain part intra-chain part $[C_1] = [C]_{LR} = [C]_{RL}$, which read explicitly:

$$[C_0] = \begin{bmatrix} C_\Sigma & -C & 0 & 0 & \dots & 0 \\ -C & 2C + C_g & -C & 0 & \dots & 0 \\ 0 & -C & 2C + C_g & -C & \dots & 0 \\ \vdots & \vdots & \ddots & \ddots & \ddots & \vdots \\ 0 & 0 & 0 & -C & 2C + C_g & -C \\ 0 & 0 & 0 & 0 & -C & 2C + C_g \end{bmatrix},$$

and $[C_1]_{i,j} = -\delta_{0,i}\delta_{j,0} C_J$ with $(i,j) \in [0,N]^2$. The total capacitance at the first site of the chain amounts to $C_\Sigma = C_J + C + C_g$. Because of the symmetry of the circuit, it is useful to define respectively *even* and *odd* modes:

$$\hat{n}_{j,\pm} = \frac{1}{2}\left(\hat{n}_{j,R} \pm \hat{n}_{j,L}\right), \tag{3.83}$$

$$\hat{\phi}_{j,\pm} = \left(\hat{\phi_{j,R}} \pm \hat{\phi_{j,L}}\right). \tag{3.84}$$

In this basis, the Hamiltonian decomposes in two uncoupled subsystems: $\hat{H} = \hat{H}_+ + \hat{H}_-$, where:

$$\hat{H}_+ = \frac{(2e)^2}{2} \sum_{i,j=0}^{N} \hat{n}_{i,+} \left[\frac{C_0 + C_1}{2}\right]^{-1}_{i,j} \hat{n}_{j,+} + \frac{\phi_q^2}{2\tilde{L}} \sum_{i=0}^{N-1} \left(\hat{\phi}_{i,+} - \hat{\phi}_{i+1,+}\right)^2 \tag{3.85}$$

$$\hat{H}_- = \frac{(2e)^2}{2} \sum_{i,j=0}^{N} \hat{n}_{i,-} \left[\frac{C_0 - C_1}{2}\right]^{-1}_{i,j} \hat{n}_{j,-} + \frac{\phi_q^2}{2\tilde{L}} \sum_{i=0}^{N-1} \left(\hat{\phi}_{i,-} - \hat{\phi}_{i+1,-}\right)^2 + E_J \left(1 - \cos\hat{\phi}_{0,-}\right). \tag{3.86}$$

The tilde means that the inductances are multiplied by two. The new capacitance matrices of the odd and even modes are then:

$$[C_+] = \frac{[C_0]+[C_1]}{2} = \begin{bmatrix} \tilde{C}+\tilde{C}_\mathrm{g} & -\tilde{C} & 0 & 0 & \dots & 0 \\ -\tilde{C} & 2\tilde{C}+\tilde{C}_\mathrm{g} & -\tilde{C} & 0 & \dots & 0 \\ 0 & -\tilde{C} & 2\tilde{C}+\tilde{C}_\mathrm{g} & -\tilde{C} & \dots & 0 \\ \vdots & \vdots & \ddots & \ddots & \ddots & \vdots \\ 0 & 0 & 0 & -\tilde{C} & 2\tilde{C}+\tilde{C}_\mathrm{g} & -\tilde{C} \\ 0 & 0 & 0 & 0 & -\tilde{C} & 2\tilde{C}+\tilde{C}_\mathrm{g} \end{bmatrix},$$

$$[C_-] = \frac{[C_0]-[C_1]}{2} = \begin{bmatrix} C_\mathrm{J}+\tilde{C}+\tilde{C}_\mathrm{g} & -\tilde{C} & 0 & 0 & \dots & 0 \\ -\tilde{C} & 2\tilde{C}+\tilde{C}_\mathrm{g} & -\tilde{C} & 0 & \dots & 0 \\ 0 & -\tilde{C} & 2\tilde{C}+\tilde{C}_\mathrm{g} & -\tilde{C} & \dots & 0 \\ \vdots & \vdots & \ddots & \ddots & \ddots & \vdots \\ 0 & 0 & 0 & -\tilde{C} & 2\tilde{C}+\tilde{C}_\mathrm{g} & -\tilde{C} \\ 0 & 0 & 0 & 0 & -\tilde{C} & 2\tilde{C}+\tilde{C}_\mathrm{g} \end{bmatrix}$$

The tilde means the capacitances are divided by two. $\hat{H}_+$ reduces to the Hamiltonian of a linear chain, while $\hat{H}_-$ takes the form of a boundary Sine-Gordon model where the capacitances and inductances of the chain are respectively divided and multiplied by two. Therefore, the characteristic impedance of the chains is doubled with respect to the original circuit. Equivalent odd and even circuits are represented in Fig. 3.9.

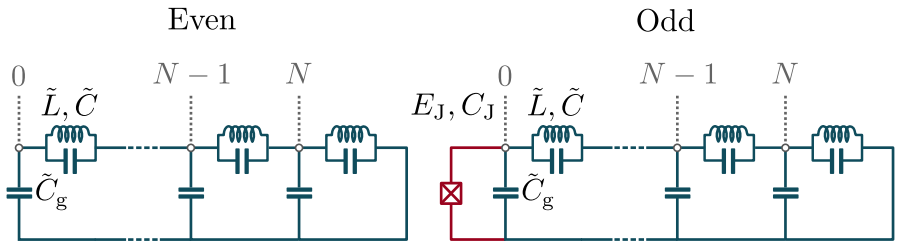

Figure 3.9 – Circuit equivalent for the odd and even Hamiltonian.

The second studied circuit is a direct implementation of the BSG circuit similar to the odd circuit described on Fig.3.9. The only difference is that the nonlinear JJ is replaced by a SQUID, enabling in situ flux tuning of its nonlinearity.

3.2.2 Boundary Sine Gordon Ground State within the Self Consistent Harmonic Approximation

From now on we will focus on the BSG circuit presented before. Consequently, the tildes and odd mode subscripts are dropped. The Hamiltonian then reads:

$$\hat{H} = \frac{1}{2}(2e)^2 \sum_{l,m=0}^{N} \hat{n}_l [C]^{-1}_{l,m} \hat{n}_m + \frac{\phi_q^2}{2L} \sum_{l=0}^{N-1} \left(\hat{\phi}_{l+1} - \hat{\phi}_l\right)^2 + E_J \left(1 - \cos\hat{\phi}_0\right) \tag{3.87}$$

$\hat{H}$ describes a quantum many-body problem that cannot be solved analytically. We therefore develop here an approximate yet microscopic approach to the problem. It consists in the generalization of the self consistent harmonic approximation with the complete Hamiltonian [93, 94, 98]. Moreover, the thermal fluctuations will be included in this derivation . To do so, we need to find the best trial harmonic Hamiltonian $\hat{H}_t$ which satisfies the Gibbs-Bogoliubov inequality [99] $F \leq F_t + \langle \hat{H} - \hat{H}_t \rangle_t$, where F is the free energy of the system and F_t is the one of the trial Hamiltonian. It is defined as:

$$F_t = -k_B T \ln Z_t \tag{3.88}$$

$$Z_t = \mathrm{tr}\left(e^{-\hat{H}_t/k_B T}\right) \tag{3.89}$$

And the mean value is defined a:

$$\langle \hat{H} - \hat{H}_t \rangle_t = \mathrm{tr}\left((\hat{H} - \hat{H}_t)\hat{\rho}_t\right), \tag{3.90}$$

$$\hat{\rho}_t = \frac{1}{Z_t} e^{-\hat{H}_t/k_B T}. \tag{3.91}$$

The trial Hamiltonian $\hat{H}_t$ is defined by replacing in $\hat{H}$ the nonlinear tunneling term $-E_J \cos\hat{\phi}_0$ by a renormalized potential $E_J^\star \hat{\phi}_0^2/2$ [13]. Explicitly, the trial Hamiltonian reads:

$$\hat{H}_t = \frac{(2e)^2}{2} \sum_{l,m=0}^{N} \hat{n}_l [C]^{-1}_{l,m} \hat{n}_m + \frac{1}{2} \frac{\hbar^2}{(2e)^2} \sum_{l,m=0}^{N} \hat{\phi}_l [L^{-1}]_{l,m} \hat{\phi}_m \tag{3.92}$$

with the capacitance matrix:

$$[C] = \begin{bmatrix} C_\Sigma & -C & 0 & 0 & 0 & \dots & 0 \\ -C & 2C + C_g & -C & 0 & 0 & \dots & 0 \\ 0 & -C & 2C + C_g & -C & 0 & \dots & 0 \\ \vdots & \vdots & \ddots & \ddots & \ddots & \dots & 0 \\ 0 & 0 & 0 & -C & 2C + C_g & -C & 0 \\ 0 & 0 & 0 & 0 & -C & 2C + C_g & -C \end{bmatrix},$$

where $C_\Sigma = C_\mathrm{J} + C + C_\mathrm{g}$, and the inductance matrix:

$$[L^{-1}] = \begin{bmatrix} 1/L_\mathrm{J}^\star + 1/L & -1/L & 0 & 0 & 0 & \dots & 0 \\ -1/L & 2/L & -1/L & 0 & 0 & \dots & 0 \\ 0 & -1/L & 2/L & -1/L & 0 & \dots & 0 \\ \vdots & \vdots & \ddots & \ddots & \ddots & \dots & 0 \\ 0 & 0 & 0 & -1/L & 2/L & -1/L & 0 \\ 0 & 0 & 0 & 0 & -1/L & 2/L & -1/L \\ 0 & 0 & 0 & 0 & 0 & -1/L & 1/L \end{bmatrix}.$$

Here $L_\mathrm{J}^\star = \phi_\mathrm{q}^2/E_\mathrm{J}^\star$ is the effective inductance associated to the nonlinear junction. Let us define by $E_k = \hbar\omega_k$ the eigenvalues of $\hat{H}_\mathrm{t}$ and $\hat{a}_k^\dagger$ the corresponding creation operators associated to its normal modes. Since $\hat{H}_\mathrm{t}$ is harmonic, one can write:

$$\hat{H}_\mathrm{t} = \sum_{k=0}^{N} \hbar\omega_k \left(\hat{a}_k^\dagger \hat{a}_k + \frac{1}{2}\right), \tag{3.93}$$

$$\hat{\phi}_0 = \sum_{k=0}^{N} \xi_{0,k} \frac{\hat{a}_k^\dagger + \hat{a}_k}{\sqrt{2}}. \tag{3.94}$$

The renormalized Josephson energy $E_\mathrm{J}^\star$ is obtained by minimizing the variational free energy:

$$\frac{d}{dE_\mathrm{J}^\star}(F_\mathrm{t} + \langle \hat{H} - \hat{H}_\mathrm{t} \rangle_\mathrm{t}) = 0. \tag{3.95}$$

The first term is evaluated as follow:

$$\frac{dF_\mathrm{t}}{dE_\mathrm{J}^\star} = -\frac{k_\mathrm{B}T}{Z_\mathrm{t}} \frac{dZ_\mathrm{t}}{dE_\mathrm{J}^\star} \tag{3.96}$$

$$= -\frac{k_\mathrm{B}T}{Z_\mathrm{t}} \sum_k \frac{d}{dE_\mathrm{J}^\star} \left(e^{-E_k/k_\mathrm{B}T}\right) \tag{3.97}$$

$$= \frac{1}{Z_\mathrm{t}} \sum_k \langle k| \frac{d\hat{H}_\mathrm{t}}{dE_\mathrm{J}^\star} |k\rangle \, e^{-E_k/k_\mathrm{B}T} \tag{3.98}$$

$$= \frac{1}{Z_\mathrm{t}} \sum_k \langle k| \frac{\hat{\phi}_0^2}{2} |k\rangle \, e^{-E_k/k_\mathrm{B}T} \tag{3.99}$$

$$= \frac{\langle \hat{\phi}_0^2 \rangle_\mathrm{t}}{2} \tag{3.100}$$

where we used the fact that $\langle k|\,\hat{H}_{\mathrm{t}}\frac{d}{dE_{\mathrm{J}}^{\star}}\,|k\rangle = 0$, since $|k\rangle$ is a normalized eigenstate of $\hat{H}_{\mathrm{t}}$ and $\frac{d}{dE_{\mathrm{J}}^{\star}}\,|k\rangle$ is orthogonal to $|k\rangle$. The second term in the variational free energy is

$$\frac{d}{dE_{\mathrm{J}}^{\star}}\langle \hat{H}-\hat{H}_{\mathrm{t}}\rangle_{\mathrm{t}} = -\frac{E_{\mathrm{J}}}{2}\frac{d}{dE_{\mathrm{J}}^{\star}}\langle e^{i\hat{\phi}_0}+e^{-i\hat{\phi}_0}\rangle_{\mathrm{t}} - \frac{\langle\hat{\phi}_0^2\rangle_{\mathrm{t}}}{2} - \frac{E_{\mathrm{J}}^{\star}}{2}\frac{d}{dE_{\mathrm{J}}^{\star}}\langle\hat{\phi}_0^2\rangle_{\mathrm{t}}. \tag{3.101}$$

Inserting Eq. (3.100) and Eq. (3.101) in Eq. (3.95), one finds the following condition on $E_{\mathrm{J}}^{\star}$:

$$E_{\mathrm{J}}^{\star} = -E_{\mathrm{J}}\frac{\frac{d}{dE_{\mathrm{J}}^{\star}}(\langle e^{i\hat{\phi}_0}+e^{-i\hat{\phi}_0}\rangle_{\mathrm{t}})}{\frac{d}{dE_{\mathrm{J}}^{\star}}\langle\hat{\phi}_0^2\rangle_{\mathrm{t}}}. \tag{3.102}$$

Where $\langle e^{i\hat{\phi}_0}\rangle_{\mathrm{t}}$ is given by :

$$\langle e^{i\hat{\phi}_0}\rangle_{\mathrm{t}} = \exp\left(-\frac{1}{2}\sum_{k=0}^{N}(n_k+\frac{1}{2})\xi_{0,k}^2\right) \tag{3.103}$$

$$= \exp\Big(-\langle\hat{\phi}_0^2\rangle_{\mathrm{t}}/2\Big). \tag{3.104}$$

Where n_k is the Bose factor. One verifies easily that $\langle e^{-i\hat{\phi}_0}\rangle_{\mathrm{t}} = \langle e^{i\hat{\phi}_0}\rangle_{\mathrm{t}}$, a detailed calculation can be found in Appendix A.4. We can finally simplify the term appearing in Eq. (3.102):

$$\frac{d}{dE_{\mathrm{J}}^{\star}}\langle e^{i\hat{\phi}_0}+e^{-i\hat{\phi}_0}\rangle_{\mathrm{t}} = -e^{-\langle\hat{\phi}_0^2\rangle_{\mathrm{t}}}\frac{d}{dE_{\mathrm{J}}^{\star}}(\langle\hat{\phi}_0^2\rangle_{\mathrm{t}}) \tag{3.105}$$

so that $E_{\mathrm{J}}^{\star}$ obeys the simple self-consistency relation:

$$\boxed{E_{\mathrm{J}}^{\star} = E_{\mathrm{J}}e^{-\langle\hat{\phi}_0^2\rangle_{\mathrm{t}}/2} = E_{\mathrm{J}}\exp\left[-\sum_{k=0}^{N}\frac{\xi_{0,k}^2}{2}(n_k+\tfrac{1}{2})\right]} \tag{3.106}$$

where the self-consistency comes from the fact that the phase $\xi_{0,k}$ depends on $E_{\mathrm{J}}^{\star}$ as we will see in the following.

3.2.3 Normal mode decomposition

Now that we have an expression for $E_{\mathrm{J}}^{\star}$ we need to compute the normal modes of the trial Hamiltonian. The method will be the same than in Section 3.1.2. Nevertheless, the nonlinear junction on the first site will induce a more complex boundary condition. In order to solve the system we will use the wave equation previously derived:

$$[L^{-1}]\vec{\xi_k} = \omega_k^2[C]\vec{\xi_k} \tag{3.107}$$

Applied to our system this gives the following set of equations:

$$\xi_{1,k} = \lambda_k \xi_{0,k} \tag{3.108}$$

$$(2C + C_\mathrm{g})\,\omega_k^2 \xi_{l,k} - C\omega_k^2\,(\xi_{l-1,k} + \xi_{l+1,k}) = \frac{1}{L}\,(2\xi_{l,k} - \xi_{l-1,k} - \xi_{l+1,k}) \;\text{ for } l \in [1, N] \tag{3.109}$$

Where λ_k is defined as:

$$\lambda_k = 1 + \frac{L}{L_\mathrm{J}^\star}\frac{1 - \omega_k^2 L_\mathrm{J}^\star\,(C_\mathrm{J} + C_\mathrm{g})}{1 - \omega_k^2 LC} \tag{3.110}$$

We use a slightly modified version of the standing wave Ansatz:

$$\xi_{l,k} = A_k \cos\!\left(k\left[l - \frac{1}{2}\right] - \theta_k\right) \tag{3.111}$$

By inserting the latter in Eq. 3.109 we find the dispersion relation previously derived (Eq.3.34) while in Eq.3.108 it gives:

$$\theta_k = \arctan\!\left(\frac{\lambda_k - 1}{\lambda_k + 1}\mathrm{cotan}\left(\frac{k}{2}\right)\right) \tag{3.112}$$

$$= \arctan\!\left(\frac{\lambda_k - 1}{\lambda_k + 1}\sqrt{\left[\frac{4C}{C_g} + 1\right]\left[\left(\frac{\omega_\mathrm{p}}{\omega_k}\right)^2 - 1\right]}\right) \tag{3.113}$$

We see that the phase shift is a function of the wavevector, or conversely of the frequency. It can be understood from the fact that the nonlinear junction has a frequency dependent impedance. Hence, the boundary condition is also frequency dependent. The mode normalization constrain is given by using Eq.3.55:

$$\begin{aligned}\frac{\hbar\omega_k}{E_{\mathrm{J,ch}} A_k^2} = &\left(\frac{E_\mathrm{J}^\star}{E_{\mathrm{J,ch}}} + 1\right)\cos\!\left(\frac{k}{2} + \theta_k\right)^2 - \cos\!\left(\frac{k}{2} + \theta_k\right)\cos\!\left(\frac{k}{2} - \theta_k\right) \\ &+ 2\,(1 - \cos k)\sum_{l=1}^{N}\cos\left(k\left[l - \frac{1}{2}\right] - \theta_k\right)^2\end{aligned} \tag{3.114}$$

The sum is computed using again the result of Appendix A.3:

$$\sum_{l=1}^{N}\cos\left(k\left[l - \frac{1}{2}\right] - \theta_k\right)^2 = \frac{N}{2} + \frac{1}{2\sin k}\cos\!\left(\frac{k}{2} + \theta_k\right)\sin\!\left(\theta_k - \frac{k}{2}\right) \tag{3.115}$$

Where we used the grounded boundary condition at site N:

$$k_n\left(N - \frac{1}{2}\right) - \theta_k = \pi\left(n + \frac{1}{2}\right) \tag{3.116}$$

We replaced k by k_n to emphasize that the wavevector is a discrete function of the mode index n. Finally, by using trigonometric formulas we obtain:

$$A_k = \sqrt{\frac{\hbar\omega_k}{E_{\mathrm{J,ch}} D_k}} \tag{3.117}$$

$$\begin{aligned} D_k = N\left(1-\cos k_n\right) + \frac{E_{\mathrm{J}}^{\star}}{E_{\mathrm{J,ch}}}\cos\left(\frac{k_n}{2}+\theta_k\right)^2 \\ - \sin\frac{k_n}{2}\cos\theta_k\cos\left(\frac{k_n}{2}+\theta_k\right)\left(\tan\frac{k_n}{2}+\tan\theta_k\right) \end{aligned} \tag{3.118}$$

Now that we have an expression for θ_k, ω_k, k_n and A_k (respectively Eq.3.113, 3.34, 3.116 ,and 3.118) the phase mode profiles can be computed. However, k_n depends on θ_k which depends on ω_k. Therefore, this set of equation is self consistent. They can be solved using numerical algorithm as describe in Fig.3.10.

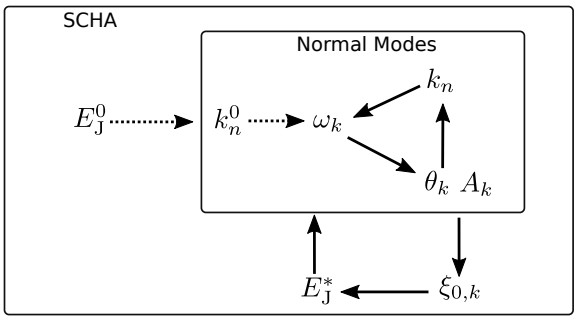

Figure 3.10 – Conceptual representation of the algorithm used to solve the SCHA for the manybody problem (Eq.3.106). An initial guess E_{J}^0 is provided to compute the normal modes (all the other circuit parameters are fixed). From that guess and a guess for the wavevector k_n^0 both ω_k, θ_k, A_k and k_n can be calculated recursively until they reach a convergence criterion. From this the phase at site 0, $\xi_{0,k}$ can be computed (we do not need the other sites for the SCHA but they can also be calculated). Using Eq.3.106 the renormalized Josephson energy $E_{\mathrm{J}}^{\star}$ is extracted and can be used to compute again the normal modes until the convergence criterion is reached.

3.2.4 Phase mode profil

In the previous part, we found an analytical formula for the resonant modes of the system. We will now compare it with the result of a numerical diagonalization. The numerical diagonalization is done by finding the eigenvectors solving:

$$[C^{-1/2}][L^{-1}][C^{-1/2}]\vec{v_k} = \omega_k^2\vec{v_k} \tag{3.119}$$

$$\vec{\xi_k} = 2e\sqrt{\frac{1}{\hbar\omega_k}}[C^{-1/2}]\vec{v_k} \tag{3.120}$$

where $[C^{-1/2}][C^{-1/2}] = [C^{-1}]$ and $\vec{v_k}$ is an unitary vector. The choice of solving Eq.3.119 instead of 3.59 is done because the matrix to diagonalise is symmetric. Therefore, numerical algorithms are more efficient. The norm chosen in Eq. 3.120 is derived in Section 6 of [100]. The chosen parameters are displayed in table 3.1. They are typical values used during my PhD.

Table 3.1 – Parameters of the system used to compare numerical diagonalization and analytical formulas for the resonant phase modes.

weak-link		Chain	
E_C [GHz]	3.6	C [fF]	144
$E_J^\star$[GHz]	5	C_g [fF]	0.1
$f_J^\star$[GHz]	6	L [nH]	0.5

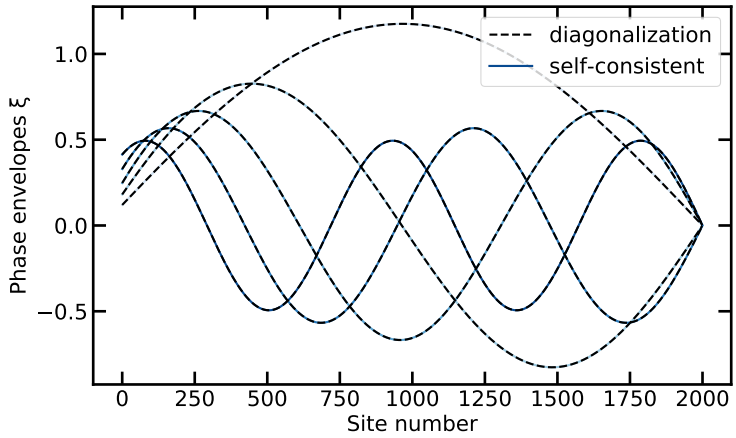

Figure 3.11 – Resonant phase modes as a function of the site position. The nonlinear junction is at first site. Shades of blue lines are the result from the self-consistent algorithm, dashed black lines result from the numerical diagonalization. Only the 5 first modes are represented.

The result of the self-consistent algorithm and numerical diagonalization comparison is given in Fig.3.11 for 2000 sites. From this result we can see the two phase envelops perfectly match each others. Consequently, both the phase shift, wavevector, dispersion relation and norm are fairly reproduced by the self-consistent solution. Nevertheless, the self-consistent algorithm is way more efficient since it relies on the computation of vector of size N while the numerical diagonalization is inverting N^2 matrices. This will prove to be important since the circuits measured have up to 4250 sites.

3.3 How to design a complex Hamiltonian ?

From now on we consider that the BSG Hamiltonian properties will be given by the optimized trial Hamiltonian. Since, it is an Ansatz not all the properties of BSG will be reproduced. But this approach will be accurate enough to understand what are the relevant parameters to design a complex Hamiltonian. In Section 3.1.1 we saw that the nonlinearity of the junction is an important parameter for the system to be complex. In addition, to observe many body effects the junction needs also to hybridize with as many modes as possible. To understand how it is possible, the link between the phase response function and the phase fluctuations of the nonlinear junction will be derived.

3.3.1 Link between response function and phase fluctuations.

To find the link between the dissipative part of the response function and the phase fluctuations of the nonlinear junction we need to go back to the definition of the antisymmetric part of the noise spectral density:

$$\tilde{S}_{\phi_0}(\omega) = \frac{S_{\phi_0}(\omega) - S_{\phi_0}(-\omega)}{2} \tag{3.121}$$

According to the Kubo formula [79] the response function of the nonlinear junction is:

$$\chi_{\phi_0}(t) = \frac{i}{\hbar}\Theta(t)\left\langle[\hat{\phi}_0(t), \hat{\phi}_0]\right\rangle \tag{3.122}$$

Where Θ is the Heaviside step function ensuring causality of the response function. As shown in Appendix A.5 the latter is linked to the antisymmetric part of the noise spectral density via:

$$\tilde{S}_{\phi_0}(\omega) = \hbar\chi''_{\phi_0}(\omega) \tag{3.123}$$

Where χ''_{ϕ_0} is the dissipative part of the response function. Using the noise spectral density of the chain (Eq.3.72) and Eq.3.121 we obtain:

$$\chi''_{\phi_0}(\omega) = \frac{\pi}{2\hbar\Delta\omega_{\mathrm{FSR}}(\omega)}\xi_0(\omega)^2 \tag{3.124}$$

The main difference between the isolated chain and the one connected to a nonlinear junction is that ξ_0 shows a frequency dependent phase shift. We have also seen that the phase fluctuations are given by:

$$\langle\hat{\phi}_0^2\rangle = \sum_k \xi_{0,k}^2 \left(n_k + \frac{1}{2}\right) \tag{3.125}$$

$$= \frac{N}{\pi}\int dk \xi_0(k)^2 \left[n(k) + \frac{1}{2}\right] \tag{3.126}$$

$$= \int_0^{\omega_\mathrm{P}} \frac{d\omega}{\Delta\omega_\mathrm{FSR}(\omega)} \xi_0(\omega)^2 \left[n(\omega) + \frac{1}{2}\right] \tag{3.127}$$

Inserting 3.124 in 3.127 yields:

$$\langle\hat{\phi}_0^2\rangle = \frac{2\hbar}{\pi}\int_0^{\omega_\mathrm{P}} \left[n(\omega) + \frac{1}{2}\right] \chi''_{\phi_0}(\omega) \tag{3.128}$$

Hence, Eq.3.124 and 3.128 show that both the relative contribution of the modes to the total fluctuation and the total fluctuations themselves can be obtained from the study of the phase response function of the nonlinear junction.

3.3.2 Toy model for the phase fluctuations

Both the mode contributions and the total phase fluctuations at the level of the nonlinear junction are given by its phase response function. Therefore, we will compute this quantity using the following assumptions: the nonlinear junction is considered as a linear oscillator once the SCHA has been applied, the JJ chain is in the thermodynamic and continuous limit and its plasma frequency is infinite. Because of that, the JJ chain will be modeled as a resistor of impedance $Z_\mathrm{C} = \sqrt{L/C_\mathrm{g}}$. As shown on Fig.3.12.

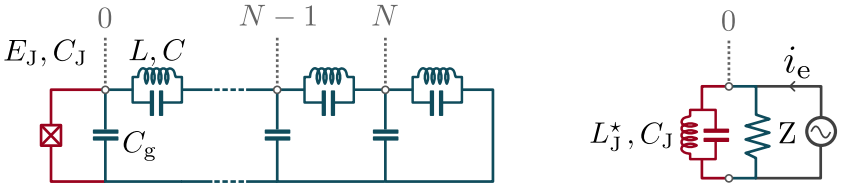

Figure 3.12 – **Left.** Boundary Sine Gordon circuit. **Right.** Toy model used to compute the phase response function of the nonlinear junction.

Since we are interested in the phase response function we can plug an external current source in parallel (because the charge $q = 2en$ and the flux $\varphi = \Phi_\mathrm{q}\phi$ are conjugate variables). Then Kirchhoff laws give:

$$\frac{i_\mathrm{e}}{C_\mathrm{J}} = \ddot{\varphi}_0 + \gamma_\mathrm{RC}\dot{\varphi}_0 + \omega_\mathrm{J}^{\star 2}\varphi_0 \tag{3.129}$$

With $\gamma_\mathrm{RC} = 1/Z_\mathrm{C}C_\mathrm{J}$ the RC cutoff and $\omega_\mathrm{J}^\star$ the nonlinear junction resonant frequency. From that equation the response function can be defined as [i]:

[i] This response function is obviously related to the impedance of the RLC circuit. See Appendix A.7 to see how.

$$\chi_{\phi_0}(\omega) = \frac{1}{\phi_q^2}\frac{\varphi(\omega)}{i_e(\omega)} = -\frac{1}{\phi_q^2 C_J}\frac{1}{\omega^2 - \omega_J^{\star 2} + i\gamma_{RC}\omega} \tag{3.130}$$

Depending on the values of γ_{RC} and $\omega_J^{\star 2}$ different regimes have to be considered. By defining the caracteristic impedance of the nonlinear junction as $Z_J^\star = \sqrt{L_J^\star / C_J}$ we can identify three regimes:

1. $2Z_C > Z_J^\star$ the response function has two poles $\omega^\pm = -i\frac{\gamma_{RC}}{2} \pm \omega_d^\star$ with $\omega_d^\star = \omega_J^\star\sqrt{1 - \left(\frac{Z_J^\star}{2Z_C}\right)^2} = \omega_J^\star r_u$. In that regime the natural oscillations of the nonlinear junction are slightly damped by the impedance, resulting in a classical renormalization of its characteristic frequency and a damping time of $2/\gamma_{RC}$. However, that renormalization has nothing to do with the nonlinearity of the junction since the SCHA has already been performed. Such a renormalization is only the counter part of the damping induced by the environment. Contrary to the renormalization predicted by the SCHA, this one happens in classical system (our toy model is purely classical) and therefore does not need ZPF. Nevertheless, they will both lower the junction frequency and a careful analysis will be needed to distinguish these two contributions(see Section 3.5). In this underdamped regime, the imaginary part of the response function is then:

$$\chi''_{\phi_0}(\omega) = \frac{\pi}{\hbar}\frac{Z_J^\star}{Z_q r_u}\left[\frac{\gamma_{RC}/2}{(\omega - \omega_d^\star)^2 + (\gamma_{RC}/2)^2} - \frac{\gamma_{RC}/2}{(\omega + \omega_d^\star)^2 + (\gamma_{RC}/2)^2}\right] \tag{3.131}$$

2. $2Z_C < Z_J^\star$ the response function has two purely imaginary poles $i\gamma_t^\pm = i\frac{\gamma_{RC}}{2}(-1 \pm r_o)$ with $r_o = \sqrt{1 - \left(\frac{2Z_C}{Z_J^\star}\right)^2}$. In that regime the impedance entirely damps the nonlinear junction oscillations, resulting in a purely damped response of characteristic time $1/\gamma_t^\pm$. This is the overdamped regime, with the imaginary part of the response function given by:

$$\chi''_{\phi_0}(\omega) = \frac{2\pi}{\hbar}\frac{Z_C}{Z_q r_o}\left[\frac{\omega}{\omega^2 + \gamma_t^{+2}} - \frac{\omega}{\omega^2 + \gamma_t^{-2}}\right] \tag{3.132}$$

3. $2Z_C = Z_J^\star$ the response function has a double pole at $-i\frac{\gamma_{RC}}{2}$, resulting in a damped characteristic time of $2/\gamma_{RC}$. This is the critical regime, where the imaginary part of the response function is:

$$\chi''_{\phi_0}(\omega) = \frac{\gamma_{RC}}{C_J\phi_q^2}\frac{\omega}{\left[\omega^2 + (\gamma_{RC}/2)^2\right]^2} \tag{3.133}$$

Equations 3.131-3.133 show that the response function is mainly a function of the nonlinear junction and chain impedance after having approximated ω_p to be infinite. Examples of response functions are plotted on Fig.3.13.

The upper part displays the response function for the three regimes by varying Z_C at $Z_J^\star$ fixed. When the chain impedance increases the response function switches

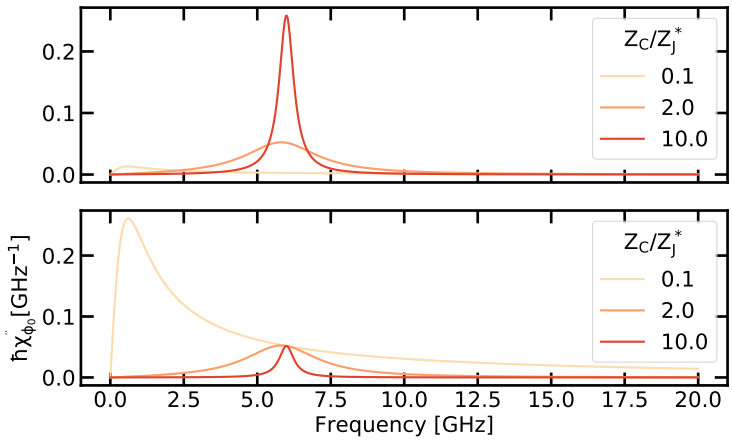

Figure 3.13 – **Upper part**. Response function for the overdamped, critical and underdamped regimes. They were obtained by varying Z_C at $Z_J^\star$ fixed. **Lower part**. Same but by varying $Z_J^\star$ at Z_C fixed.

from the overdamped to the underdamped regime. Therefore the full-width at half maximum of the response function decreases. On the other hand, the maximum of the response function increases with the impedance. That is expected since the phase fluctuations grow with the impedance. Consequently, in order to achieve a highly nonlinear regime Z_C has to be as high as possible.

The lower part displays the same quantity but by varying $Z_J^\star$ at Z_C fixed. We clearly see that the best way to have both many coupled modes and strong phase fluctuation (and hence highly nonlinear effects) is for $Z_J^\star$ much larger than Z_C. This is again expected because when the nonlinear junction impedance increases the ratio $E_J^\star/E_C$ decreases. Thus, it is more sensitive to phase fluctuations. In addition, when $Z_J^\star$ is increased at Z_C fixed the system switches from underdamped to overdamped, resulting in a broadening of the response function.

As a consequence, that simple model shows that increasing the complexity of the system implies Z_C as large as possible and $Z_J^\star$ being much larger than Z_C. Finally, from the response function we can compute the phase fluctuation by using 3.128, at $T = 0$ we have:

$$\langle\hat{\phi}_0^2\rangle = \frac{\hbar}{\pi}\lim_{\omega_p\to\infty}\int_0^{\omega_p} d\omega\chi''_{\phi_0}(\omega) \tag{3.134}$$

Therefore, phase fluctuations for the three regimes are given by:

$$\begin{aligned}
&\text{for } 2Z_C > Z_J^\star : \langle\hat{\phi}_0^2\rangle = \frac{2}{r_u}\frac{Z_J^\star}{Z_q}\arctan\left(2r_u\frac{Z_C}{Z_J^\star}\right)\\
&\text{for } 2Z_C < Z_J^\star : \langle\hat{\phi}_0^2\rangle = \frac{2}{r_o}\frac{Z_C}{Z_q}\ln\left(\frac{1+r_o}{1-r_o}\right)\\
&\text{for } 2Z_C = Z_J^\star : \langle\hat{\phi}_0^2\rangle = 2\frac{Z_J^\star}{Z_q}
\end{aligned} \tag{3.135}$$

At $Z_C \gg Z_J^\star$ equation 3.135 gives us $\langle\hat{\phi}_0^2\rangle = \pi Z_J^\star / Z_q$. This is expected since in this regime the impedance can be seen as an open. Consequently, the nonlinear junction is behaving as if there were no environment and we recover the phase fluctuations of a bare LC circuit (see Section 3.1.1). This is another way to see that maximizing only the environment impedance is not enough to design a complex Hamiltonian.

On the other hand, if $Z_J^\star \gg Z_C$ equation 3.135 tells us that $\langle\hat{\phi}_0^2\rangle = 4Z_C/Z_q \ln(Z_J^\star/Z_C)$. It means that if the ratio of impedance is kept fixed the fluctuation is a growing function of the chain impedance. These two observations are summarized in the plot of $\langle\hat{\phi}_0^2\rangle$ versus Z_C and $Z_J^\star$ (Fig.3.14).

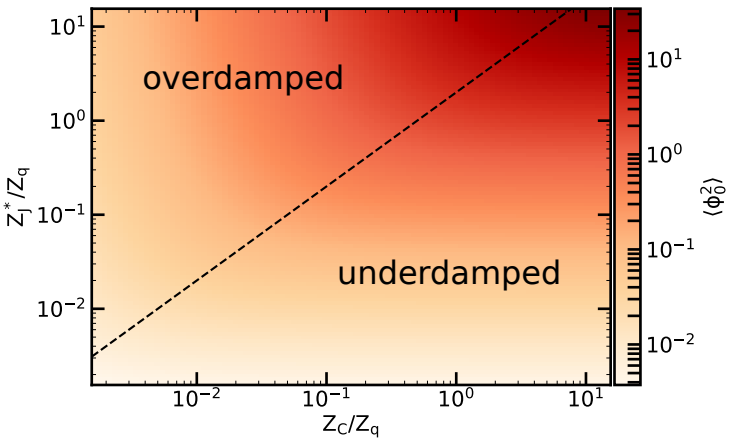

Figure 3.14 – Amplitude of fluctuations as a function of the impedance of the nonlinear junction and the chain impedance. In order to maximize the fluctuations, they should be as high as possible.

We used a toy model to show that fluctuations can be maximized when taking Z_J and Z_C as high as possible. In addition, we also need the nonlinear junction impedance to be larger or on the same order of magnitude than the one of the chain so that a large number of modes contributes to the total fluctuations.

3.4 Renormalisation of the nonlinear junction.

In this section the renormalization of the nonlinear junction Josephson energy, or conversely phase fluctuations across it, will be studied with respect to its impedance and to the one of the chain. In addition, we will see what is the influence of the chain plasma frequency and the temperature of the circuit on the renormalization.

From now on and until the end of this section the number of sites will be taken such that the chain is deep inside the thermodynamic regime. This limit is hard to reach in the highly underdamped regime. where the nonlinear junction response function is almost a delta-function since we have seen that it is a Lorentzian of width $1/Z_C C_J$. Consequently, the free spectral range should be small enough for the response function to be well defined in this regime. That implies a number of sites between 10^5 and 10^6. All the results that will be discussed in this section relies on the self-consistent algorithm explained in Fig.3.10.

3.4.1 Influence of the nonlinear junction impedance.

The first studied parameter is the nonlinear junction impedance, or equivalently the ratio E_J/E_C. The chain parameters are the same than in section 3.2.4. The result is displayed on Fig.3.15. The left panel shows that the $E_J^\star$ deviation from its bare value increases when E_J/E_C decreases. That can be understood from Eq.3.21 and 3.9. When E_J/E_C decreases the phase fluctuations increase, resulting in an increased renormalization.

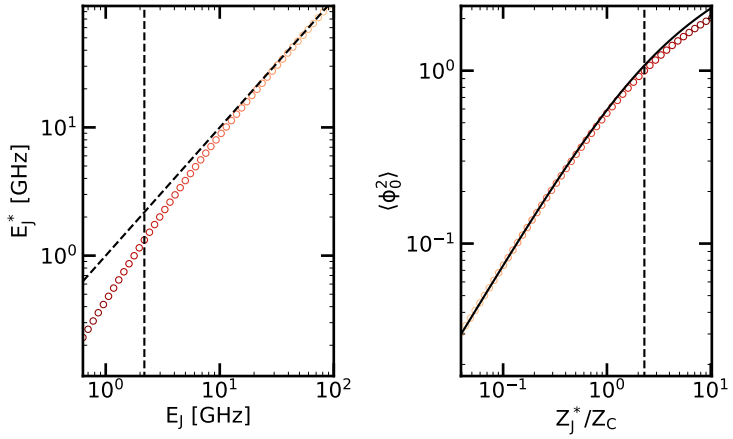

Figure 3.15 – **Left.** Renormalized Josephson energy as a function of the bare one. The vertical dashed black line indicates where the SCHA may breakdown. The other line is a guide to the eyes indicating where is the bare Josephson energy. **Right.** Phase fluctuations as a function of the ratio between the nonlinear junction impedance and the one of the chain. Vertical line indicates the same thing that for the left panel. The plain line is the result given by Eq.3.135 in the different damping regimes.

The right panel illustrates the previous explanation. As expected from the previous toy model, fluctuations increase with the nonlinear junction impedance. The main difference here is that because of its nonlinearity the nonlinear junction impedance is renormalized to $Z_J^\star = \sqrt{L_J^\star/C_J}$. The black plain line indicates the result of Eq.3.135 using the renormalized impedance. We see a deviation when $Z_J^\star$ becomes bigger that Z_C, this is because in this regime the nonlinear junction starts to couple to modes close to the plasma frequency so that the simple toy model no longer constitutes a good approximation for our system. The two panels display a vertical dashed line indicating that fluctuations are on the order of one. Hence, above these lines the SCHA may breakdown.

3.4.2 Influence of the chain impedance.

According to the toy model previously developed, phase fluctuations across the nonlinear junction should be a growing function of the chain impedance. That is confirmed by applying the SCHA for two E_J/E_C ratios at different impedance values. The result of this study is presented in Figure 3.16. It is obtained with the nonlinear junction frequency $f_J = 6\,\text{GHz}$ and the chain plasma frequency $f_p = 18.8\,\text{GHz}$ fixed.

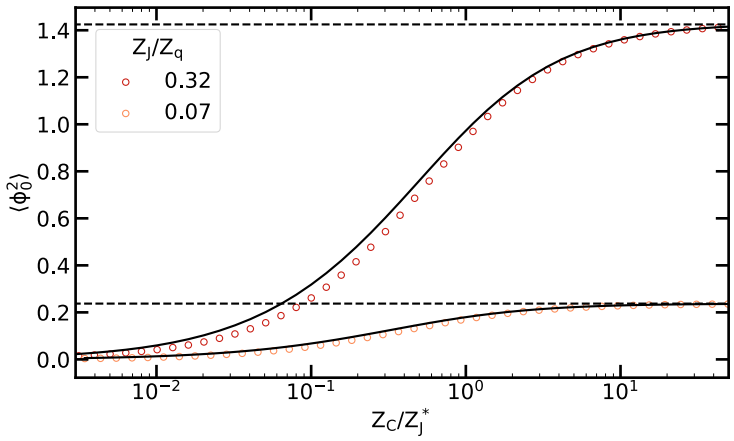

Figure 3.16 – Phase fluctuation as a function of the ratio between the chain impedance and the renormalized nonlinear junction impedance for two bare nonlinear junction impedances. The black line is the the result of the analytical formula. Horizontal dashed lines indicate the phase fluctuation expected for an isolated junction.

For the two ratios, phase fluctuations increase with the chain impedance. At $Z_C/Z_J^\star$ much larger than unity fluctuations saturate. The saturation value is the fluctuations expected for an isolated junction as indicated by the horizontal dashed lines. It should be noted that the fluctuations are higher when the nonlinear junction impedance is larger, confirming previous results. The plain black lines are the result of Equation 3.135. Even if it may seem too simplistic, this model is again in good agreement with the full Hamiltonian.

3.4.3 Influence of the chain plasma frequency.

The phase fluctuation estimated by the SCHA as a function of the nonlinear junction and chain impedance could be explained from the toy model. Nonetheless, the plasma frequency of the chain is not far enough from the nonlinear junction frequency to be completely neglected.

According to the SCHA the renormalized nonlinear junction plasma frequency is $f_J^\star = \sqrt{2E_J^\star E_C}/h$. A simple way to understand the influence of the chain plasma frequency is to look how $f_J^\star$ varies as a function of this latter. The result is given in Figure 3.17 for $f_J = 6\,\mathrm{GHz}$, $E_J/E_C = 1, Z_C = 1.6\,\mathrm{k\Omega}$ fixed.

Left panel shows that the renormalization increases, or conversely the nonlinear junction plasma frequency decreases, with the plasma frequency of the chain. When these two frequencies are equal the nonlinear junction frequency jumps to a much higher frequency. We can also see that the renormalization does not change much when the plasma frequency is larger than 15 GHz.

All these observations can be explained from the right panel. It displays ξ_0^2 as a function of the frequency for different plasma frequency. As a reminder this quantity gives the contribution of the modes to the total phase fluctuations (Eq.3.128). When the plasma function is decreased from 20 to 15 GHz the renormalization is little to not affected by that since the modes in this region does not contribute much to the total phase fluctuations. It is no longer the case when the plasma frequency gets

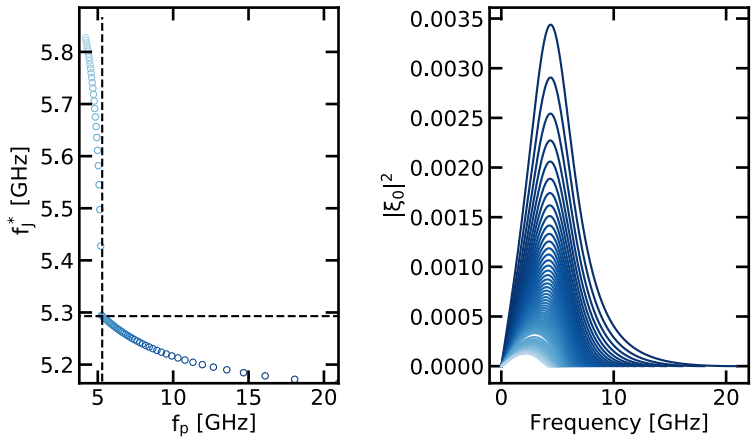

Figure 3.17 – **Left.** Nonlinear junction frequency as a function of the plasma frequency of the chain. The crossing point of the two dashed lines indicate when the two frequencies are equal. **Right.** Zero point fluctuations induced by the modes on the nonlinear junction as a function of the frequency. The color code is such that the plasma frequency of the chain increases as the blue becomes darker and vice versa.

closer to $f_J^\star$ since these modes have a large contribution. Therefore the total phase fluctuations start to drop and $f_J^\star$ increases. Finally, when the plasma frequency crosses the nonlinear junction frequency the latter has no mode in its vicinity, the remaining contributions are therefore small. Because of that it undergoes a jump as seen on the left panel.

3.4.4 Influence of the temperature of the system.

The last parameter to be studied is the temperature of the modes. Until now we only discussed the quantum aspect of the fluctuations but Equation 3.125 shows that temperature can also play a role if thermal occupation numbers become on the same order than $1/2$. That gives the following order of magnitude for a given mode k to be populated:

$$T \sim \frac{\hbar\omega_k}{k_B} \tag{3.136}$$

This equation says that the warmer the system is the more modes will be populated. To verify this simple explanation we ran the SCHA with $E_J/E_C = 1$, $Z_C = 1.6\,\mathrm{k\Omega}$ and $f_p = 18.8\,\mathrm{GHz}$, the result is given in Figure 3.18.

The right panel shows $\xi_0^2(\omega, T) = \xi_0^2(n(\omega, T) + 1/2)$ as a function of the frequency and the temperature. As expected the low frequency modes start to be populated when the system gets warmer. This increase in population gives rise to stronger fluctuations in these modes.

This phenomenon explains the temperature dependence of the nonlinear junction phase fluctuations. At low temperature only the very first modes start to be populated. However, ξ_0^2 is proportional to the nonlinear junction response function and the first mode are far from its resonant frequency. Therefore, the contribution of these modes to the total fluctuations is small. Hence, the total fluctuations are almost constant

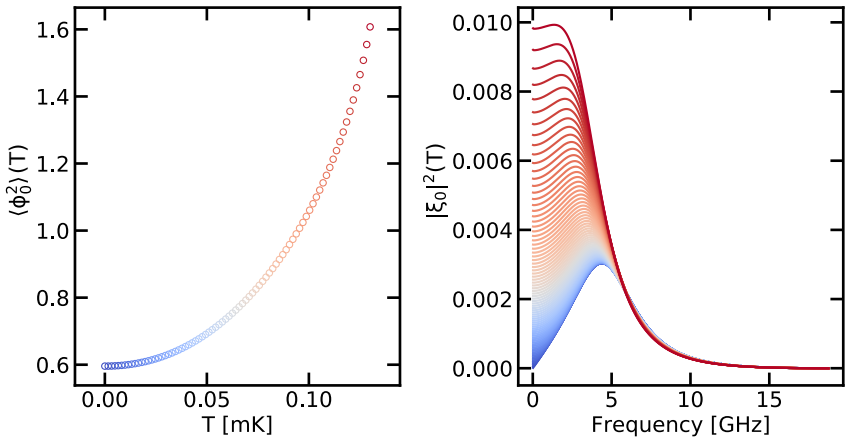

Figure 3.18 – **Left.** Total phase fluctuations versus temperature. **Right.** Phase fluctuations of the phase modes as a function of the frequency for the corresponding temperatures

in the low temperature regime. When the system is heated up the population of the low frequency modes increases linearly and the modes close to the junction also start to be thermally occupied. These two phenomena convert in a drastic increase of the nonlinear junction fluctuations.

3.5 Phase shift

In the last Section four parameters have been found to control the phase fluctuations of the nonlinear junction: the nonlinear junction impedance, the chain impedance and its plasma frequency and the temperature. We will now see how to access this information via spectroscopy measurements. With this in mind we will introduce the relative phase shift $\delta\theta$ and try to relate it to a measurable quantity. Finally the link between the latter and previously defined quantities will be derived.

3.5.1 Analytical expressions

We have seen that introducing a defect at the chain first site induces a phase shift θ_k with respect to a bare chain. This shift converts in a frequency shift via the dispersion relation (Eq. 3.34). In this section we will prove that using this quantity is a good way to get information about the nonlinear junction.

In the following several cases will be described:

1. A junction is at the first site, inducing a phase shift labeled θ_k^{JC}. It corresponds to the BSG Hamiltonian.

2. A capacitance C_{J} is at the first site, inducing a phase shift labeled θ_k^{C}. It corresponds to the BSG Hamiltonian in the limit where E_{J}, or $E_{\mathrm{J}}^{\star}$ are equal to zero. This situation happens when the weak link is a SQUID set at half flux quantum.

3. Only a capacitance C_{g} to the ground is at first site, inducing a phase shift labeled θ_k^{bare}. It corresponds to the even modes circuit of Fig. 3.9.

In these three cases only the expression of λ_k (Eq.3.110) is changed. From these phase shifts we can define three quantities that were probed in our devices: the phase difference between the odd and even modes, the phase difference between the BSG with and without E_J at first site and the phase difference between the BSG without E_J at first site and the even modes. The first ones will be called Even-Odd relative phase shift, labeled $\delta\theta^{\mathrm{e/o}}$, the second Josephson relative phase shift, labeled $\delta\theta^{\mathrm{J}}$ and the third capacitance relative phase shift labeled $\delta\theta^{\mathrm{C}}$:

$$\delta\theta_k^{\mathrm{e/o}} = \theta_k^{\mathrm{JC}} - \theta_k^{\mathrm{bare}} \tag{3.137}$$

$$\delta\theta_k^{\mathrm{J}} = \theta_k^{\mathrm{JC}} - \theta_k^{\mathrm{C}} \tag{3.138}$$

$$\delta\theta_k^{\mathrm{C}} = \theta_k^{\mathrm{C}} - \theta_k^{\mathrm{bare}} \tag{3.139}$$

However, these quantities cannot be easily measured by spectroscopy. What can be easily measured are the mode frequencies of our samples. Because of the phase shift introduced by the defect, the frequency of a mode n is given by:

$$\omega_n = \omega\left(k_n^0 + \theta_n/N\right) = \omega_n^0 + \frac{\theta\left(k_n\right)}{N}\partial_k\omega\left(k\right)\Big|_{k=k_n^0} + O(N^{-2}) \tag{3.140}$$

Here we used the fact that $N >> 1$ so that we consider ω as a continuous, differentiable, function. For the mode n+1:

$$\omega_{n+1} = \omega\left(k_{n+1}^0 + \theta_{n+1}/N\right) = \omega_n^0 + \frac{\theta\left(k_n\right)+\pi}{N}\partial_k\omega\left(k\right)\Big|_{k=k_n^0} + O(N^{-2}) \tag{3.141}$$

since from Eq. 3.113 we have $\theta\left(k_{n+1}\right) = \theta\left(k_n\right) + O(N^{-2})$. These two equations give:

$$\delta\theta_n^{\mathrm{e/o}} = \pi\frac{\omega_n^{\mathrm{o}} - \omega_n^{\mathrm{e}}}{\omega_{n+1}^{\mathrm{e}} - \omega_n^{\mathrm{e}}} \tag{3.142}$$

$$\delta\theta_n^{\mathrm{JC}} = \pi\frac{\omega_n^{\mathrm{JC}} - \omega_n^{\mathrm{C}}}{\omega_{n+1}^{\mathrm{C}} - \omega_n^{\mathrm{C}}} \tag{3.143}$$

$$\delta\theta_n^{\mathrm{C}} = \pi\frac{\omega_n^{\mathrm{C}} - \omega_n^{\mathrm{e}}}{\omega_{n+1}^{\mathrm{e}} - \omega_n^{\mathrm{e}}} \tag{3.144}$$

where ω_n^{e}, ω_n^{o} are respectively the n mode of the even and odd families while ω_n^{JC} and ω_n^{C} are the ones of the BSG Hamiltonian with $E_\mathrm{J}^\star$ different or equal to zero.

Finally we can simplify $\delta\theta^{\mathrm{e/o}}$ and $\delta\theta^{\mathrm{C}}$ since:

$$\lambda_k^{\mathrm{bare}} = \frac{1 - \omega_k^2 L\left(C + C_\mathrm{g}\right)}{1 - \omega_k^2 LC} \tag{3.145}$$

For realistic circuit $C \gg C_\mathrm{g}$, consequently $\lambda_k^{\mathrm{bare}} \simeq 1$ and using Eq.3.113 we find $\theta_k^{\mathrm{bare}} = 0$. Physically, it comes from the fact that if $C \gg C_\mathrm{g}$ the first site can be considered as an open. For the phase shift it implies $\delta\theta_n^{\mathrm{e/o}} = \theta_n^{\mathrm{JC}}$ and $\delta\theta_n^{\mathrm{C}} = \theta_n^{\mathrm{C}}$. The

different phase shifts and their relation with the frequency shifts of the mode chain are summarized in Tab.3.2.

Table 3.2 – The three relative phase shifts associated to the different boundary conditions introduced in this section. θ_n^{JC}, θ_n^{C} and θ_n^{bare} are the phase shift induced by respectively a Josephson junction, a capacitance C_{J} or a capacitance to the ground C_{g}. ω_n^{e}, ω_n^{o} are respectively the n mode of the even and odd families while ω_n^{JC} and ω_n^{C} are the ones of the BSG Hamiltonian with $E_{\mathrm{J}}^{\star}$ different or equal to zero

Name	Definition	Frequency shift
Even-Odd $\delta\theta_n^{\mathrm{e/o}}$	$\theta_n^{\mathrm{JC}} - \theta_n^{\mathrm{bare}} \simeq \theta_n^{\mathrm{JC}}$	$\pi\left(\omega_n^{\mathrm{o}} - \omega_n^{\mathrm{e}}\right) / \left(\omega_{n+1}^{\mathrm{e}} - \omega_n^{\mathrm{e}}\right)$
Josephson $\delta\theta_n^{\mathrm{J}}$	$\theta_n^{\mathrm{JC}} - \theta_n^{\mathrm{C}}$	$\pi\left(\omega_n^{\mathrm{JC}} - \omega_n^{\mathrm{C}}\right) / \left(\omega_{n+1}^{\mathrm{C}} - \omega_n^{\mathrm{C}}\right)$
Capacitance $\delta\theta_n^{\mathrm{C}}$	$\theta_k^{\mathrm{C}} - \theta_n^{\mathrm{bare}} \simeq \theta_n^{\mathrm{C}}$	$\pi\left(\omega_n^{\mathrm{C}} - \omega_n^{\mathrm{e}}\right) / \left(\omega_{n+1}^{\mathrm{e}} - \omega_n^{\mathrm{e}}\right)$

3.5.2 Link with other quantities.

Now that we have linked different phase shifts to measurable quantities we can see how they are related to the response function of the nonlinear junction. For that we will focus on the Odd-Even relative phase shift .

Phase shifts at different $E_{\mathrm{J}}/E_{\mathrm{C}}$ are plotted in the upper panel of Figure 3.19. The dots are the results of Eq.3.142 where the mode frequency is computed from the self-consistent algorithm explained in Section 3.2.3 while the lines are given by the analytic expression for the phase shift (Eq.3.113) where the frequency is considered as a continuous variable. The two agree well since a large number of mode has been taken (5000 sites) and therefore the system is in the thermodynamic limit. This will be discussed with more detail in Section 3.5.3. For the four different ratio, the phase shift goes to zero at 6 GHz corresponding to the renormalized frequency $\omega_{\mathrm{J}}^{\star}$. It can bee easily seen from Eq.3.110 and 3.113 since at $\omega_{\mathrm{J}}^{\star}$, λ_k is equal to one and therefore the phase shift goes to zero. Hence, the phase shift measurement gives access to $\omega_{\mathrm{J}}^{\star}$.

In addition, we also computed the phase shift derivatives with respect to frequency in the lower panel of Fig.3.19. Interestingly, this quantity seems to have the same behavior than the response function. At $E_{\mathrm{J}}/E_{\mathrm{C}}$ much larger than 1, or equivalently in the underdamped regime, the phase shift is peaked at a frequency close to $\omega_{\mathrm{d,\,th}}^{\star}$, the analytical damped resonant frequency defined in Section 3.3.2. Moreover, its FWHM is also close to $\gamma_{\mathrm{RC,\,th}}$. The comparison between the theoretical expression and the estimation from the phase shift derivatives, denoted respectively $\omega_{\mathrm{d},\delta\theta}^{\star}$ and $\gamma_{\mathrm{RC},\delta\theta}$, are reported in table 3.3.

From these examples we can conclude that the estimation of these two quantities improves when $Z_{\mathrm{J}}^{\star}/Z_{\mathrm{C}}$ decreases. Nevertheless, the resonant frequency is estimated more precisely than the width. In order to understand how the phase shift derivative and the response function are linked we will derive an analytic expression for these two. We already derived an analytical expression for the response function in the case of a junction coupled to an impedance Z_{C} in Section 3.3.2. Now that we understand our system a bit more we can do it in the general case. For that we use Eq.3.124 where

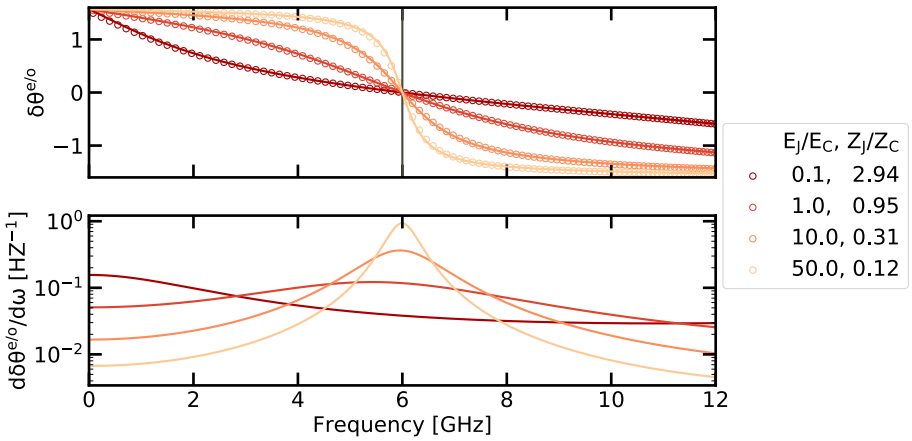

Figure 3.19 – **Upper part.**Even-Odd phase shifts for different regimes of damping. The plain line is the result of Eq.3.113 with the dots come from the use of 3.142. **Lower part.** The corresponding phase shifts derivative with respect to the frequency.

Table 3.3 – Relative error of the resonant frequency and FWHM estimation obtained from the phase shift derivative. The fist line is empty since the junction is in the overdamped regime ($Z_{\mathrm{J}}^{\star}/Z_{\mathrm{C}}$ is larger than 2). Therefore, the junction does not have a resonant frequency.

$Z_{\mathrm{J}}^{\star}/Z_{\mathrm{C}}$	$\lvert\gamma_{\mathrm{RC,\,th}}-\gamma_{\mathrm{RC},\delta\theta}\rvert/\gamma_{\mathrm{RC,\,th}}$ [%]	$\lvert\omega_{\mathrm{d,\,th}}^{\star}-\omega_{\mathrm{d},\delta\theta}^{\star}\rvert/\omega_{\mathrm{d,\,th}}^{\star}$ [%]
2.94	/	/
0.95	13.4	2.9
0.31	4.0	0.5
0.12	5.3	0.1

the only assumption was the thermodynamic limit.The phase mode envelop can be expressed as function of the frequency:

$$\xi_0(\omega) = A(\omega)\cos\left(\frac{k(\omega)}{2}+\theta(\omega)\right) \tag{3.146}$$

$$= A(\omega)\cos\left(\arctan\left(\frac{1}{X(\omega)}\right)+\arctan(X(\omega)f(\omega))\right) \tag{3.147}$$

with:

$$X(\omega) = \sqrt{\left[\frac{4C}{C_g} + 1\right]\left[\left(\frac{\omega_\mathrm{p}}{\omega}\right)^2 - 1\right]} \tag{3.148}$$

$$f(\omega) = \frac{\lambda(\omega) - 1}{\lambda(\omega) + 1} \tag{3.149}$$

$$\tag{3.150}$$

where λ is the function defined by Eq.3.110. Consequently:

$$\xi_0(\omega) = A(\omega) \frac{1}{\sqrt{1 + (X(\omega) f(\omega))^2}} \frac{(1 - f(\omega)) X(\omega)}{\sqrt{1 + X(\omega)^2}} \tag{3.151}$$

$$= 2A(\omega)\sqrt{L(\omega)} \frac{X(\omega)}{1 + X(\omega)} \tag{3.152}$$

$$\tag{3.153}$$

where:

$$L(\omega) = \frac{1}{(\lambda(\omega) + 1)^2} \frac{1}{1 + (X(\omega) f(\omega))^2} \tag{3.154}$$

Now that we have an exact solution for the phase mode envelop, and consequently for the response function, we will will use an approximation to link it to the phase shift derivative. In the following, we consider the plasma frequency of the chain to be infinite by taking $C = 0$. Thus, we have:

$$X(\omega) \simeq \frac{2}{\omega\sqrt{LC_\mathrm{g}}} \gg 1 \tag{3.155}$$

$$A(\omega) \simeq \sqrt{\frac{\hbar\omega_k}{E_{\mathrm{J,ch}} N (1 - \cos k(\omega))}} \simeq 2e\sqrt{\frac{2}{\hbar\omega C_\mathrm{g} N}} \tag{3.156}$$

Therefore the response function reads:

$$\chi''_{\phi_0}(\omega) = \frac{2\pi}{\hbar} \frac{A(\omega)^2}{\Delta\omega_{\mathrm{FSR}}(\omega)} L(\omega) \tag{3.157}$$

$$= \frac{8\pi}{\hbar\omega} \frac{Z_\mathrm{C}}{Z_\mathrm{q}} L(\omega) \tag{3.158}$$

In Appendix A.6 we prove that we can recover the response function derived from the toy model (Eq.3.131) under some assumptions. We can now derive an expression for

the phase shift derivative. That last is directly given by the derivative of $\theta(\omega)$:

$$\frac{d\theta(\omega)}{d\omega} = \frac{d}{d\omega}\arctan(f(\omega)X(\omega)) \tag{3.159}$$

$$= \frac{X(\omega)}{\sqrt{1+(X(\omega)f(\omega))^2}}\left(\frac{2\frac{d\lambda}{d\omega}}{(\lambda(\omega)+1)^2} - \frac{1}{\omega}\frac{\lambda(\omega)-1}{\lambda(\omega)+1}\right) \tag{3.160}$$

$$= -X(\omega)L(\omega)\left(\frac{4\omega L}{\omega_J^2 L_\mathrm{J}} + \frac{\lambda(\omega)^2-1}{\omega}\right) \tag{3.161}$$

For the measured circuits L/L_J is at least an order of magnitude below unity. At first order in the latter:

$$\frac{\lambda(\omega)^2-1}{\omega} = \frac{2L}{\omega L_\mathrm{J}}\left(1-\left[\frac{\omega}{\omega_\mathrm{J}}\right]^2\right) \tag{3.162}$$

the theta derivative reads:

$$\frac{d\theta}{d\omega} = -\frac{4}{\gamma_\mathrm{RC}}\left(1+\left[\frac{\omega_\mathrm{J}}{\omega}\right]^2\right)L(\omega) \tag{3.163}$$

As a consequence, the link between the phase shift and the response function is:

$$\frac{d\theta}{d\omega}(\omega) = T(\omega)\,\chi''_{\phi_0}(\omega) \tag{3.164}$$

with:

$$T(\omega) = -\frac{\hbar\omega Z_\mathrm{q} C_\mathrm{J}}{2\pi}\left(1+\left[\frac{\omega_\mathrm{J}}{\omega}\right]^2\right) \tag{3.165}$$

Finally, by developing the latter around $\omega = \omega_\mathrm{J} + \delta\omega$ we find that it is a constant up to the second order in $\delta\omega/\omega_\mathrm{J}$. Therefore, the derivative of theta and the response function are proportional around the nonlinear junction plasma frequency. It explains why the FWHM and the frequency maximum are similar when $Z_\mathrm{J}/Z_\mathrm{C}$ is low enough.

As a conclusion we have seen that the phase shift induced by the nonlinear junction is the key quantity to get information about the properties of our system since it is equal to zero at $\omega_\mathrm{J}^\star$ and its derivative can be used to estimate $\omega_\mathrm{d}^\star$ and γ_RC when the junction is underdamped.

3.5.3 An illustration of the thermodynamic limit

We proved that the phase shift is linked to the response function of the nonlinear junction. In this section we will illustrate the concept of thermodynamic limit on the phase shift. We recall that in this limit the phase shift can be expressed as a continuous function of the frequency (Eq.3.147). We also saw that in this limit it should be a function of a frequency shift (Eq.3.142). Using the parameters reported in table 3.1 we plot these two quantities in Fig.3.20 for different number of sites in the Josephson chain. We see that the curves start to collapse when the number of sites is large enough. From that last we can also estimate N to be at least 1000 for the thermodynamic limit to be a good approximation.

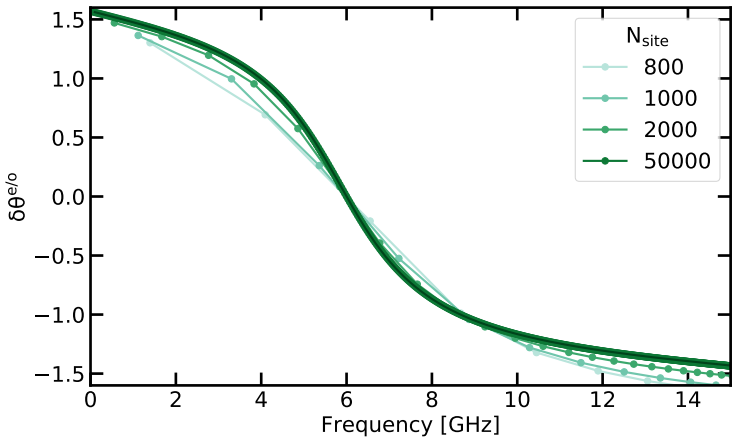

Figure 3.20 – Comparison between the analytical formula for the phase shift θ^{JC} in the thermodynamic limit (green line) and the Even-Odd Splitting $\delta\theta^{\mathrm{e/o}}$ as a function of the number of sites in the Josephson chain (green dots).

Given the parameters used for the simulation the junction is underdamped since $Z_{\mathrm{J}}^{\star}/2Z_{\mathrm{C}} = 0.28$. In the previous section we have seen that the width of the phase shift had the same order of magnitude than the one of the response function. This width is given by the damping rate of the nonlinear junction. A simple criterion can then be given for the system to be in the thermodynamic limit. To reach the latter we need the free spectral range to be way smaller than the damping rate. In this case the damping rate is equal to 3.3 GHz while the free spectral range far from the plasma frequency is 2.8, 2.2, 1.1 and 0.05 GHz for the different number of sites.

3.6 Backaction on the environment modes

So far, only the influence of the chain on the nonlinear junction has been considered.We will now discuss the backaction of the nonlinear junction on the chain modes. First, we will see how the resonance frequencies of these modes are shifted in frequency because of the nonlinearity of the junction. To do so, the predictions given by the SCHA will be compared with the one given by the Kerr approximation which is commonly used in circuit QED. Then, we will see that the nonlinear junction also induces dissipation in the modes. To understand the origin of these losses the response function concepts developed above will be generalized. By doing so, we will see that the SCHA, as it has been applied so far, is not sufficient to explain these losses. Therefore, a finer modeling of our circuit will have to be used.

3.6.1 Comparison between the SCHA and the Kerr approximation

To understand what is the effect of the nonlinear junction on the chain modes we can diagonalize the BSG Hamiltonian apart from the cosine term[j]:

[j]From now on we do not include the $\frac{1}{2}$ term in the quadratic part of the Hamiltonian since it only leads to a shift of the energy reference and can bring confusions in the following calculations.

$$\hat{H} = \frac{1}{2}(2e)^2 \sum_{l,m=0}^{N} \hat{n}_l [C]^{-1}_{l,m} \hat{n}_m + \frac{\phi_q^2}{2L} \sum_{l=0}^{N-1} \left(\hat{\phi}_{l+1} - \hat{\phi}_l\right)^2 + E_J \left(1 - \cos \hat{\phi}_0\right) \tag{3.166}$$

$$= \sum_{k=0}^{N} \hbar \tilde{\omega}_k \hat{a}_k^\dagger \hat{a}_k + E_J \left(1 - \cos \hat{\phi}_0\right) \tag{3.167}$$

As before, the junction phase can be decomposed onto the eigenmodes:

$$\hat{\phi}_0 = \sum_{k=0}^{N} g_{0,k} \frac{\hat{a}_k^\dagger + \hat{a}_k}{\sqrt{2}} \tag{3.168}$$

Where $g_{0,k}$ is different from $\xi_{0,k}$ since the junction Josephson energy is not included in the diagonalization. By inserting Eq.3.168 in 3.167 and using the series expansion of the cosine we generate an infinite number of terms. Those will be responsible for a wide range of interactions either between different modes or within the same mode. To get some intuition on what are the kind of interactions generated, the BSG Hamiltonian ground state will be studied within the Kerr approximation.

The Kerr approximation

The Kerr approximation consists in developing the cosine up to fourth order:

$$\hat{H} \simeq \sum_{k=0}^{N} \hbar \tilde{\omega}_k \hat{a}_k^\dagger \hat{a}_k + \frac{E_J}{2} \hat{\phi}_0^2 - \frac{E_J}{24} \hat{\phi}_0^4 \tag{3.169}$$

$\hat{\phi}_0^2$ can then be included in the mode decomposition. The resulting Hamiltonian is:

$$\hat{H} = \sum_{k=0}^{N} \hbar \omega_k^{\text{lin}} \hat{a}_k^\dagger \hat{a}_k - \frac{E_J}{24} \hat{\phi}_0^4 \tag{3.170}$$

$$\hat{H} = \hat{H}_0 - \frac{E_J}{24} \hat{\phi}_0^4 \tag{3.171}$$

where ω_k^{lin} is the frequency of mode k when the junction nonlinearity is neglected[k]. The mode frequencies are found using Eq.3.113, 3.116 , 3.34 and 3.118[l]. Once the linear part of the Hamiltonian has been diagonalized we can decompose $\hat{\phi}_0^4$ onto the eigenmodes:

[k] Therefore $\frac{E_J}{2}\hat{\phi}^2$ is included to compute ω_k^{lin}, not for $\tilde{\omega}_k$.

[l] By replacing $L_J^\star$ by L_J since no renormalization has been included here.

$$\hat{\phi}_0^4 = \sum_{k,l,m,n} \frac{\xi_{0,k}\xi_{0,l}\xi_{0,m}\xi_{0,n}}{4} \left(\hat{a}_k^\dagger + \hat{a}_k\right)\left(\hat{a}_l^\dagger + \hat{a}_l\right)\left(\hat{a}_m^\dagger + \hat{a}_m\right)\left(\hat{a}_n^\dagger + \hat{a}_n\right) \tag{3.172}$$

$$= \frac{1}{4}\sum_k \xi_{0,k}^4 \left(\hat{a}_k^\dagger + \hat{a}_k\right)^4 \tag{3.173}$$

$$+ \sum_k \xi_{0,k}\left(\hat{a}_k^\dagger + \hat{a}_k\right) \sum_{l\neq k} \xi_{0,l}^3 \left(\hat{a}_l^\dagger + \hat{a}_l\right)^3 \tag{3.174}$$

$$+ \frac{3}{4}\sum_k \xi_{0,k}^2 \left(\hat{a}_k^\dagger + \hat{a}_k\right)^2 \sum_{l\neq k} \xi_{0,l}^2 \left(\hat{a}_l^\dagger + \hat{a}_l\right)^2 \tag{3.175}$$

$$+ \frac{3}{2}\sum_k \xi_{0,k}^2 \left(\hat{a}_k^\dagger + \hat{a}_k\right)^2 \sum_{l\neq m\neq k} \xi_{0,l}\xi_{0,m}\left(\hat{a}_l^\dagger + \hat{a}_l\right)\left(\hat{a}_m^\dagger + \hat{a}_m\right) \tag{3.176}$$

$$+ \frac{1}{4}\sum_{k\neq l\neq m\neq n} \xi_{0,k}\xi_{0,l}\xi_{0,m}\xi_{0,n}\left(\hat{a}_k^\dagger + \hat{a}_k\right)\left(\hat{a}_l^\dagger + \hat{a}_l\right)\left(\hat{a}_m^\dagger + \hat{a}_m\right)\left(\hat{a}_n^\dagger + \hat{a}_n\right) \tag{3.177}$$

We only keep the contributions conserving the excitation number in each mode since we want to study their effects on $|0\rangle$, the ground state of $\hat{H}_0$. Therefore, only Eq.3.173 and 3.175 will be considered:

$$\left(\hat{a}_k^\dagger + \hat{a}_k\right)^4 = 6\hat{a}_k^\dagger\hat{a}_k\hat{a}_k^\dagger\hat{a}_k + 6\hat{a}_k^\dagger\hat{a}_k + 3 \tag{3.178}$$

$$= 6\left[\left(\hat{a}_k^\dagger\hat{a}_k - \langle\hat{a}_k^\dagger\hat{a}_k\rangle\right) + \langle\hat{a}_k^\dagger\hat{a}_k\rangle\right]^2 + 6\hat{a}_k^\dagger\hat{a}_k + 3 \tag{3.179}$$

$$\simeq 6\left(2\langle\hat{a}_k^\dagger\hat{a}_k\rangle + 1\right)\hat{a}_k^\dagger\hat{a}_k + 6\hat{a}_k^\dagger\hat{a}_k + 3 \tag{3.180}$$

$$\left(\hat{a}_k^\dagger + \hat{a}_k\right)^2\left(\hat{a}_l^\dagger + \hat{a}_l\right)^2 = 4\hat{a}_l^\dagger\hat{a}_l\hat{a}_k^\dagger\hat{a}_k + 2\hat{a}_k^\dagger\hat{a}_k + 2\hat{a}_l^\dagger\hat{a}_l \tag{3.181}$$

$$\simeq 2\left(2\langle\hat{a}_l^\dagger\hat{a}_l\rangle + 1\right)\hat{a}_k^\dagger\hat{a}_k + 2\left(2\langle\hat{a}_k^\dagger\hat{a}_k\rangle + 1\right)\hat{a}_l^\dagger\hat{a}_l \tag{3.182}$$

where we performed perturbative expansion of $\hat{a}_k^\dagger\hat{a}_k$ and $\hat{a}_l^\dagger\hat{a}_l$ around their mean values for the terms containing 4 operators. The constant terms and the ones depending on the square of the operators minus their mean values are dropped. The remaining terms are responsible for the photon number dependent Kerr shift [49]. To simplify the discussion we consider the mode population to be zero (we will not discuss thermal effects). Moreover, the constant term only shifts the energy origin. Therefore, only the two-operators contributions will be considered. These terms are responsible for the frequency shifts induced by the ZPF of the modes. Inserting Eq.3.180 and 3.182 in

3.170 yields:

$$\hat{H} = \sum_{k=0}^{N} \hbar\omega_k^\star \hat{a}_k^\dagger \hat{a}_k \tag{3.183}$$

with:

$$\omega_k^\star = \omega_k^{\text{lin}} - \frac{E_\text{J}}{16}\xi_{0,k}^4 - \sum_{l\neq k} \frac{E_\text{J}}{8}\xi_{0,k}^2\xi_{0,l}^2 \tag{3.184}$$

Eq.3.184 can be easily interpreted: the first term is the frequency the mode k would have if the junction was linear, the second term is the renormalization coming from the ZPF in the same mode while the last term is the renormalization coming from the ZPF in all the other modes. They are often referred as the *self-Kerr* and the *cross-Kerr* shifts [49]. From that simple expression we see that the junction nonlinearity induces interactions between the normal modes of the chain. The consequence of such interactions will be more deeply investigated in Section 3.6.2.

Comparison with the SCHA

We have seen that the nonlinearity of the junction induces a frequency shift in the chain modes. To understand the limitation of the formula obtained within the Kerr approximation we can compare it to the SCHA once again. For that we compute the modes frequencies within the SCHA and the Kerr approximation and compare them to the ones obtained when we discard the junction nonlinearity (labeled ω_k^{lin}). The resulting shifts are shown in Fig.3.21 for three values of E_J/E_C with the same circuit parameters than before for the chain (see Table 3.1), 5000 sites and $f_\text{J} = 10\,\text{GHz}$. First, the Kerr approximation underestimates the chain modes frequency shifts induced by the junction nonlinearity when compared to the SCHA (see table 3.4). Second, the nonlinearity maximum is reached at the damped nonlinear junction frequency $\omega_\text{d}^\star$ since it is where the ZPF are maximal (see Eq.3.184 and Section 3.3.1 and 3.3.2). Both the SCHA and the Kerr approximation predict a downward renormalization of $\omega_\text{d}^\star$ when the nonlinearity increases. Nevertheless, the Kerr approximation underestimates again the latter (see table 3.4). Hence, the Kerr approximation can qualitatively capture the effect of the nonlinearity but fails to give an accurate estimation for the frequency shifts induced either on the chain modes or on the junction renormalized damped frequency when the nonlinearity increases.

3.6.2 Damping induced by the nonlinear junction - Photon conversion.

In the previous section we have seen that the nonlinear junction induces interactions between the chains modes. So far, only the modes frequency shifts, or conversely renormalization, was discussed. However, interactions between these modes should also give them a finite lifetime. In other words the chain modes should broaden because of the junction nonlinearity. This broadening will be discussed in this Section.

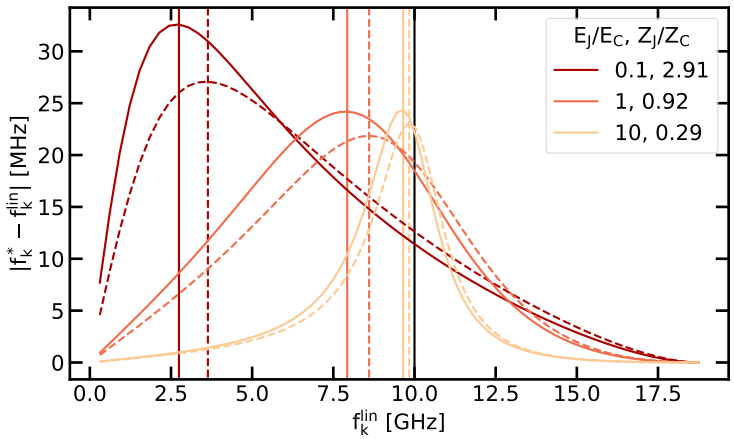

Figure 3.21 – Frequency shift between the renormalized modes $f_k^\star$ and the linear ones f_k^{lin} versus f_k^{lin} for three values of nonlinearity. The dashed lines represent the shift estimated by the Kerr approximation while the plain lines are given by the SCHA. The black vertical line is the junction frequency within the linear approximation. The plain vertical lines are the position of the damped renormalized frequency $f_{\text{r}}^\star$ given by the SCHA while the dashed lines correspond to the ones estimated by the Kerr approximation.

Table 3.4 – Relative difference of the damped renormalized frequency and the average of the relative difference for the modes k between the Kerr approximation and the SCHA. The first is defined as $\delta\omega_{\text{d}}^\star/\omega_{\text{d, SCHA}}^\star$, where $\delta\omega_{\text{d}} = |\omega_{\text{d, SCHA}}^\star - \omega_{\text{d, Kerr}}^\star|$, with $\omega_{\text{d, SCHA/Kerr}}^\star$ the renormalized damped frequency with the SCHA and Kerr approximation. The same convention is used for the modes k.

$E_{\text{J}}/E_{\text{C}}$	$\delta\omega_{\text{d}}^\star/\omega_{\text{d, SCHA}}^\star$ [%]	Average of $\delta\omega_{\text{k}}^\star/\omega_{k,\text{SCHA}}^\star$ [%]
0.1	32.5	28.9
1	8.5	12.2
10	1.9	4.49

Preamble

In Section 3.2.2 we saw that the SCHA consists in approximating the BSG Hamiltonian by a harmonic one. Therefore the phase correlator at $T = 0$ was given by:

$$S_{\phi_0}(\omega) = \pi \sum_k \xi_{0,k}^2 \delta(\omega - \omega_k) \tag{3.185}$$

Therefore, using 3.123 and 3.121 we find that the dissipative part of the response function is:

$$\chi''_{\phi_0}(\omega) = \frac{1}{\hbar}\tilde{S}_{\phi_0}(\omega) = \frac{\pi}{\hbar}\sum_k \xi_{0,k}^2 \left[\delta(\omega - \omega_k) - \delta(\omega + \omega_k)\right] \tag{3.186}$$

Hence, the response function is a sum of delta functions. We recall that any of these modes can be seen as a harmonic oscillator. Therefore, for a given mode the response function is a delta function. Using the results of Section 3.3.2 it means that the modes are not damped. Consequently, our formalism cannot describe losses induced by the nonlinear junction.

Perturbative treatment

Since, we cannot explain losses generated by the junction we will need to generalize the concepts previously developed. To do so, we will study the SCHA within the perturbative theory and see whether pushing the theory towards higher orders can account for the junction induced losses. Similarly to the previous section, the BSG Hamiltonian can be diagonalized without the cosine. To go one step further, we can add and subtract a quadratic terms with $E_{\mathrm{J}}^{\star}$ as a free parameter. We then consider that the positive quadratic terms of the Hamiltonian form the unperturbed Hamiltonian $\hat{H}_0$ while the perturbation is the sum of the cosine and the negative quadratic term:

$$\hat{H} = \hat{H}_0 + \hat{H}_{\mathrm{int}} \tag{3.187}$$

$$\hat{H}_0 = \sum_{k=0}^{N} \hbar\tilde{\omega}_k \hat{a}_k^{\dagger}\hat{a}_k + \frac{E_{\mathrm{J}}^{\star}}{2}\hat{\phi}_0^2 \tag{3.188}$$

$$\hat{H}_{\mathrm{int}} = -\left(\frac{E_{\mathrm{J}}^{\star}}{2}\hat{\phi}_0^2 + E_{\mathrm{J}}\cos\hat{\phi}_0\right) \tag{3.189}$$

Since we want to study losses induced by the junction we will look at the response function of the phase at the junction site. To do so it is convenient to introduce a new correlator :

$$G_{\phi_0}(t-t') = -i\left\langle GS\right| T\hat{\phi}_0\left(t\right)\hat{\phi}_0(t')\left|GS\right\rangle \tag{3.190}$$

Where $|GS\rangle$ is the ground state of the BSG Hamiltonian $\hat{H}$ and T is used to ensure the causality of the correlator and is defined as[m]:

$$TA(t)B(t') = \Theta(t-t')A(t)B(t') + \Theta(t'-t)B(t')A(t) \tag{3.191}$$

Because of that this correlator is often called the *causal Green function*. It is related to the response function via (see Appendix A.8):

$$\hbar\chi_{\phi_0}^{''}\left(\omega\right) = -\mathrm{sign}(\omega)\,\mathrm{Im}\,G_{\phi_0}\left(\omega\right) \tag{3.192}$$

Using the Gell-Mann and Low theorem (a demonstration can be found in Chapter 7.3 of [101]) we can express the correlator in the interaction representation:

$$G_{\phi_0}(t-t') = -i\frac{\left\langle 0\right| T\hat{\phi}_0^{\mathrm{I}}\left(t\right)\hat{\phi}_0^{\mathrm{I}}\left(t'\right)\hat{U}\left|0\right\rangle}{\left\langle 0\right| U\left|0\right\rangle} \tag{3.193}$$

[m] The plus sign in front of the second term is here since we are dealing with bosonic operators, it would be replaced by a minus sign for fermionic operators.

where $\hat{\phi}_0^{\mathrm{I}}$ is $\hat{\phi}_0$ in the interaction picture[n] and $\hat{U}$ is defined as [o]:

$$\hat{U} = T\exp\left\{\frac{1}{i\hbar}\int_{\mathbb{R}} d\tau \hat{H}_{\mathrm{int}}^{\mathrm{I}}(\tau)\right\} \tag{3.194}$$

Moreover,$|0\rangle$ is the GS of $\hat{H}_0$. Since $\hat{H}_0$ is a quadratic Hamiltonian the evaluation of the correlator on its GS will be easier as we will see in Section 3.6.2. In the following we will drop the I superscript and replace $\langle 0|\ldots|0\rangle$ by $\langle\ldots\rangle$. Then, G_{ϕ_0} can be expressed as:

$$G_{\phi_0}(t-t') = \sum_n G_{\phi_0}^{(\mathrm{n})}(t-t') \tag{3.195}$$

where $G_{\phi_0}^{(\mathrm{n})}$ corresponds to the series expansion of $\hat{U}$ at order n. For exemple if we develop it up to the first order we get:

$$G_{\phi_0}(t-t') = G_{\phi_0}^{(0)}(t-t') + G_{\phi_0}^{(1)}(t-t') \tag{3.196}$$

$$G_{\phi_0}(t-t') = -i\langle T\hat{\phi}_0(t)\,\hat{\phi}_0(t')\rangle - \frac{1}{\hbar}\int_{\mathbb{R}} dt_1 \langle T\hat{\phi}_0(t)\,\hat{\phi}_0(t')\hat{H}_{\mathrm{int}}(t_1)\rangle \tag{3.197}$$

Therefore, a hand-waving explanation can be given for this series expansion: the full expression of the correlator is given by the sum over an infinite number of "stories". At zeroth order the phase $\hat{\phi}_0$ propagates between t and t' freely, at first order it propagates with an interaction at t_1 between t and t', at second order it interacts at t_1 and t_2, ...

First order perturbation and the SCHA

The basics of the perturbative treatment being known we will now compute the causal Green function for the BSG Hamiltonian and see how it is linked to the SCHA. To do so we will start with the first order expansion of G_{ϕ_0}. Because of that we need to compute:

$$\begin{aligned}\langle T\hat{\phi}_0(t)\,\hat{\phi}_0(t')\hat{H}_{\mathrm{int}}(t_1)\rangle = &-\frac{E_{\mathrm{J}}^\star}{2}\langle T\hat{\phi}_0(t)\,\hat{\phi}_0(t')\hat{\phi}_0^2(t_1)\rangle \\ &- E_{\mathrm{J}}\langle T\hat{\phi}_0(t)\,\hat{\phi}_0(t')\cos\hat{\phi}_0(t_1)\rangle\end{aligned} \tag{3.198}$$

We saw that the corralators are evaluated on $|0\rangle$ which is the GS of $\hat{H}_0$. Since this Hamiltonian is quadratic we can use Wick's theorem (see Chapter 10.6 of [102]) to

[n] We recall that the transformation from an operator $\hat{A}(t)$ in the Heisenberg representation to the interaction picture is given by $\hat{A}^{\mathrm{I}}(t) = e^{-i\hat{H}_{\mathrm{int}}t/\hbar}\hat{A}(t)e^{i\hat{H}_{\mathrm{int}}t/\hbar}$

[o] The definition of T should be generalized since there is more than two operators. However, since we will not evaluate the correlators with more than two operators this will not be necessary.

evaluate Eq.3.198. For the first term of the right hand side we obtain:

$$\langle T\hat{\phi}_0(t)\,\hat{\phi}_0(t')\hat{\phi}_0^2(t_1)\rangle = \langle T\hat{\phi}_0(t)\,\hat{\phi}_0(t')\rangle\langle\hat{\phi}_0^2(t_1)\rangle \tag{3.199}$$

$$+ 2\langle T\hat{\phi}_0(t)\,\hat{\phi}_0(t_1)\rangle\langle T\hat{\phi}_0(t_1)\,\hat{\phi}_0(t')\rangle \tag{3.200}$$

$$= G^{(0)}_{\phi_0}(t-t')G^{(0)}_{\phi_0}(t_1) + 2G^{(0)}_{\phi_0}(t-t_1)G^{(0)}_{\phi_0}(t_1-t') \tag{3.201}$$

We managed to express this interaction term as a function of $G^{(0)}_{\phi_0}$. This Green function can easily be calculated since:

$$iG^{(0)}_{\phi_0}(t-t') = \Theta(t-t')\langle\hat{\phi}_0(t)\hat{\phi}_0(t')\rangle + \Theta(t'-t)\langle\hat{\phi}_0(t')\hat{\phi}_0(t)\rangle \tag{3.202}$$

$$= \Theta(t-t')\langle\hat{\phi}_0(t-t')\hat{\phi}_0\rangle + \Theta(t'-t)\langle\hat{\phi}_0(t'-t)\hat{\phi}_0\rangle \tag{3.203}$$

Thus, setting $\tau = t-t'$ yields:

$$iG^{(0)}_{\phi_0}(\tau) = \Theta(\tau)S_{\phi_0}(\tau) + \Theta(-\tau)S_{\phi_0}(-\tau) \tag{3.204}$$

$$= S_{\phi_0}(|\tau|) \tag{3.205}$$

Therefore the interaction terms can be expressed as a function of S_{ϕ_0} which was already calculated (see Section 3.1.2). Moreover, it can be proven that all the terms containing correlators evaluated on dummy variables[p] and on t and t' separately can be neglected since they cancel with the denominator of Eq.3.193 (see Chapter 8 of [101]). For example, the first term at the right hand side of Eq.3.201 is equal to $G^{(0)}_{\phi_0}(t-t')G^{(0)}_{\phi_0}(t_1)$ and can hence be neglected. With this in mind we can calculate the second term of Eq.3.198:

$$\langle\hat{\phi}_0(t)\,\hat{\phi}_0(t')\cos\hat{\phi}_0(t_1)\rangle = \sum_{n\geq 0}\frac{(-1)^n}{2n!}\langle\hat{\phi}_0(t)\,\hat{\phi}_0(t')\hat{\phi}_0^{2n}(t_1)\rangle \tag{3.206}$$

$$= \sum_{n\geq 0}\frac{(-1)^n}{2n!}\frac{2n(2n-1)}{2}\frac{(2n-1)!}{2^{n-2}(n-1)!}$$

$$\times G^{(0)}_{\phi_0}(t-t_1)G^{(0)}_{\phi_0}(t_1-t')\frac{G^{(0)}_{\phi_0}(t_1)^{n-1}}{2^{n-1}} \tag{3.207}$$

where $2n(2n-1)/2$ counts the number of ways there are to extract $G^{(0)}_{\phi_0}(t-t_1)G^{(0)}_{\phi_0}(t_1-t')$ from the total correlator while $(2n-1)!/2^{n-2}(n-1)!$ comes from the number of possible pairings in the remaining terms. Therefore, we can simplify the total corre-

[p] the integration variables

lator:

$$\langle \hat{\phi}_0(t)\,\hat{\phi}_0(t')\cos\hat{\phi}_0(t_1)\rangle = -1\sum_{n\geq 0}\frac{-1^n}{n!}G^{(0)}_{\phi_0}(t-t_1)G^{(0)}_{\phi_0}(t_1-t')\frac{G^{(0)}_{\phi_0}(t_1)^n}{2^n} \tag{3.208}$$

$$= -G^{(0)}_{\phi_0}(t-t_1)G^{(0)}_{\phi_0}(t_1-t')\exp\left(-\frac{G^{(0)}_{\phi_0}(0)}{2}\right) \tag{3.209}$$

Consequently the first order expansion of G_{ϕ_0} equals to:

$$G^{(1)}_{\phi_0}(t-t') = \int_{\mathbb{R}} dt_1 G^{(0)}_{\phi_0}(t-t_1)G^{(0)}_{\phi_0}(t_1-t')\left(E^\star_{\mathrm{J}} - E_{\mathrm{J}}\exp\left[-\frac{G^{(0)}_{\phi_0}(0)}{2}\right]\right) \tag{3.210}$$

Until now, $E^\star_{\mathrm{J}}$ was a free parameter. However, it can be fixed by setting:

$$E^\star_{\mathrm{J}} - E_{\mathrm{J}}\exp\left[-\frac{G^{(0)}_{\phi_0}(0)}{2}\right] = 0 \tag{3.211}$$

Thus, we recover:

$$E^\star_{\mathrm{J}} = E_{\mathrm{J}}\exp\left(-\frac{\langle\hat{\phi}_0^2\rangle}{2}\right) \tag{3.212}$$

Which is nothing less than what was obtained with the SCHA (see Eq.3.106). Hence, the latter lies on the assumption that the first order expansion of H_{int} is negligible. In other words, the quadratic Hamiltonian $\hat{H}_0$ with $E^\star_{\mathrm{J}}$ fixed by the self consistent equation 3.106 is a good approximation at first order. However, because the resulting Hamiltonian is quadratic it cannot be use to calculate the dissipation induced by the cosine term. To do so, we need to compute G_{ϕ_0} to higher orders.

Theoretical tools

The full calculation of the dissipation induced by the cosine using the second order expansion of G_{ϕ_0} is rather tedious. Therefore, only the main steps will be explained. In the previous section, we have seen that G_{ϕ_0} could be expanded in series and than each orders give a possible "story" for $\hat{\phi}_0$ to propagates from t to t'. A naive way to estimate the damping would be to expend G_{ϕ_0} to the second order and to use Eq.3.192 to compute the response function. However, it turns out that it is a too crude approximation. An intuitive way to understand it is that the second order expansion of G_{ϕ_0} give a "story" where the phase propagating between t and t' will scatter twice on the nonlinear potential. Such a simple mechanism cannot give an accurate description of the dynamics of the system since it does not account for an infinite number of ways to propagate from t to t' (the higher orders of G_{ϕ_0}). Hence, to compute the dissipation we would need to compute the full expansion of G_{ϕ_0}. However, in practice, calculating the full expansion of G_{ϕ_0} is not possible with our system. This problem can nevertheless be circumvented by using a quantity called the *self-energy*. It can be introduced by rewriting the first order expansion of G_{ϕ_0}:

$$G^{(1)}_{\phi_0}(t-t') = \int_{\mathbb{R}} dt_1 G^{(0)}_{\phi_0}(t-t_1) G^{(0)}_{\phi_0}(t_1-t') \left(E_{\mathrm{J}}^{\star} - E_{\mathrm{J}} \exp\left[-\frac{G^{(0)}_{\phi_0}(0)}{2} \right] \right) \tag{3.213}$$

$$= \int_{\mathbb{R}} \int_{\mathbb{R}} dt_1 dt_2 G^{(0)}_{\phi_0}(t-t_1) \Sigma^{(1)}(t_1-t_2) G^{(0)}_{\phi_0}(t_2-t) \tag{3.214}$$

where $\Sigma^{(1)}$ is the self-energy at first order since it is composed of interaction terms coming from the first order expansion of G_{ϕ_0}. It is defined as:

$$\Sigma^{(1)}(t_1-t_2) = \delta(t_1-t_2) \left(E_{\mathrm{J}}^{\star} - E_{\mathrm{J}} \exp\left[-\frac{G^{(0)}_{\phi_0}(0)}{2} \right] \right) \tag{3.215}$$

Now that we have introduce the concept of self-energy we will relate it to the the losses induced by the nonlinearity. These two are related via the *Dyson's equation*. In the following we will provide an hand-waving derivation for this equation (see Chapter 9 of [103] for a more rigorous proof). First, we can replace the first order expansion of the self-energy $\Sigma^{(1)}$ in Eq.3.214 by its full expression defined as:

$$\Sigma(t_1-t_2) = \Sigma^{(1)}(t_1-t_2) + \Sigma^{(2)}(t_1-t_2) + \cdots = \sum_{n\geq 1} \Sigma^{(n)}(t_1-t_2) \tag{3.216}$$

where $\Sigma^{(n)}(t_1-t_2)$ is composed of interaction terms coming from the n order expansion of G_{ϕ_0}. Second, we can replace the last $G^{(0)}_{\phi_0}(t_2-t)$ in Eq.3.214 by $G_{\phi_0}(t_2-t)$. Therefore, we have from Eq.3.196:

$$G_{\phi_0}(t-t') = G^{(0)}_{\phi_0}(t-t') + \int_{\mathbb{R}} \int_{\mathbb{R}} dt_1 dt_2 G^{(0)}_{\phi_0}(t-t_1) \Sigma(t_1-t_2) G_{\phi_0}(t_2-t) \tag{3.217}$$

The second term of the right hand side is a double convolution. Hence, the Fourier transform of this equation gives:

$$G_{\phi_0}(\omega) = G^{(0)}_{\phi_0}(\omega) + G^{(0)}_{\phi_0}(\omega) \Sigma(\omega) G_{\phi_0}(\omega) \tag{3.218}$$

which is nothing but Dyson's equation. Despite the derivation being not rigorous, this expression is exact and constitutes an alternative way to calculate the full expansion of G_{ϕ_0}. Let us see now explain how the latter can be used to compute dissipation. Since, this equation is self-consistent we have:

$$G_{\phi_0}(\omega) = G^{(0)}_{\phi_0}(\omega) + G^{(0)}_{\phi_0}(\omega) \Sigma(\omega) G^{(0)}_{\phi_0}(\omega) + \dots \tag{3.219}$$

Because of that the phase propagating from t to t' can whether not interact, or interact ones, twice, etc. (corresponding to the first, second and third term of the expansion). Hence, Dyson's equation is summing up all the contribution of the time trajectories where an excitation of frequency ω comes back to its initial state after different kinds of interactions. Then, we will show that it enables us to properly account for the decay time of the mode of frequency ω, or conversely to its broadening. Coming back to Eq.3.218 we can write:

$$G_{\phi_0}(\omega) = \frac{G^{(0)}_{\phi_0}(\omega)}{1 - G^{(0)}_{\phi_0}(\omega)\Sigma(\omega)} \tag{3.220}$$

In the vicinity of a mode ω_k, $G^{(0)}_{\phi_0}$ can be written as (a detailed calculation is given in Appendix A.10):

$$G^{(0)}_{\phi_0}(\omega) = \frac{1}{2}\frac{\xi^2_{0,k}}{\omega - \omega_k} \tag{3.221}$$

Inserting Eq.3.221 in Eq.3.220 and considering that the self-energy is constant a first order we get:

$$G_{\phi_0}(\omega) = \frac{\xi^2_{0,k}/2}{\omega - \omega_k - \Sigma(\omega_k)\xi^2_{0,k}/2} \tag{3.222}$$

Then, the self-energy can be decomposed in its real and imaginary part $\Sigma(\omega_k) = \Sigma^{'}(\omega_k) - i\Sigma^{''}(\omega_k)$ such that the dissipative part of the response function $\chi^{''}_{\phi_0}$ around ω_k is given by:

$$\chi^{''}_{\phi_0}(\omega) = \frac{\Sigma^{''}(\omega_k)\xi^2_{0,k}/2}{\left(\omega - \omega_k - \Sigma^{'}(\omega_k)\xi^2_{0,k}/2\right)^2 + \left(\Sigma^{''}(\omega_k)\xi^2_{0,k}/2\right)^2} \tag{3.223}$$

Hence, the response function is a sum of Lorentzian functions with a full width at half maximum $\Sigma^{''}(\omega_k)\,\xi^2_{0,k}$ and resonant frequency $\omega_k - \Sigma^{'}(\omega_k)\xi^2_{0,k}/2$ (see Fig.3.22). Hence, the modes are shifted as we saw in the previous section but they are also broadened. Note that these shifts come on top of the shifts obtained from the first order perturbative expansion. However it can be shown that these "new" shifts are negligible with respect to the first ones. We also see that if $\Sigma^{''}$ does not depend too much on the frequency, the brodenings are maximum around the damped frequency of the nonlinear junction $\omega^{\star}_{\mathrm{d}}$ since it depends on $\xi^2_{0,k}/2$.

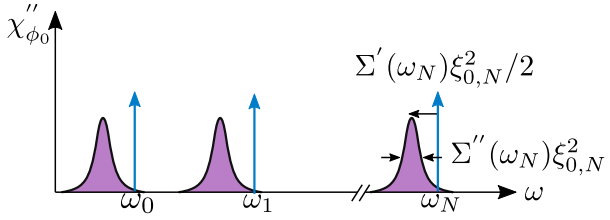

Figure 3.22 – Schematic of the dissipative part of the nonlinear junction response function in the frequency domaine. At first order it is composed of delta function since the Hamiltonian is quadratic (blue). At second order these resonant frequencies are both shifted downward by $\Sigma^{'}(\omega_k)\xi^2_{0,k}/2$ and broadened by $\Sigma^{''}(\omega_k)\xi^2_{0,k}$.

Second order perturbation

In practice obtaining an exact expression for Σ is not simpler than calculating the full expansion of G_{ϕ_0}. However, as we saw with Eq.3.216 the self-energy can also be developed in series. Since we set the first order to zero to find an expression for $E_J^\star$, we need to develop the self-energy up to the second order. In doing so, we select an infinite number of interaction terms for the losses to be estimated properly, but not all of them, so that the self-energy can be computed. The full calculation is tedious (the main steps are reported in Appendix A.9) but the result is:

$$\Sigma^{(2)}(t_1-t_2) = i\left(\frac{E_J^\star}{\hbar}\right)^2 \delta(t_1-t_2)\int_{\mathbb{R}} dt_3 \cos[G_{\phi_0}^{(0)}(t_1-t_3)] - 1 + \frac{1}{2}G_{\phi_0}^{(0)}(t_1-t_3)^2 \tag{3.224}$$

$$+\left(\frac{E_J^\star}{\hbar}\right)^2 \left[\sin[G_{\phi_0}^{(0)}(t_1-t_2)] - G_{\phi_0}^{(0)}(t_1-t_2)\right] \tag{3.225}$$

The self-energy then has to be Fourier transform numerically to obtain $\Sigma^{''}(\omega)$ and $\Sigma^{'}(\omega)$.

Interpretation of $\Sigma^{(2)}$

Now that we have an equation for the second order expansion of the self-energy we can try to interpret it. At lowest order in $G_{\phi_0}^{(0)}$, $\Sigma^{(2)}$ is given by:

$$\Sigma^{(2)}(t_1-t_2) \simeq -\frac{1}{6}\left(\frac{E_J^\star}{\hbar}\right)^2 G_{\phi_0}^{(0)}(t_1-t_2)^3 \tag{3.226}$$

By using Eq.3.205 we get:

$$\Sigma^{(2)}(t) \simeq -\frac{i}{48}\left(\frac{E_J^\star}{\hbar}\right)^2 \sum_{k_1,k_2,k_3} \xi_{0,k_1}^2 \xi_{0,k_2}^2 \xi_{0,k_3}^2 e^{-i\left(\omega_{k_1}+\omega_{k_2}+\omega_{k_3}\right)|t|} \tag{3.227}$$

We can then perform a Fourier transform and evaluate its imaginary part at ω_k (a detailed calculation is given in Appendix A.11):

$$\Sigma^{(2)}(\omega_k)^{''} = -\frac{E_J^{\star 2}}{48\hbar^3}\sum_{k_1,k_2,k_3} \xi_{0,k_1}^2 \xi_{0,k_2}^2 \xi_{0,k_3}^2 \left[\delta(\omega_k-\omega_\Sigma)+\delta(\omega_k+\omega_\Sigma)\right] \tag{3.228}$$

where $\omega_\Sigma = \omega_{k_1}+\omega_{k_2}+\omega_{k_3}$. Therefore, the dissipation induced in the modes is mainly[q] coming from the coupling between 1 and 3-photons states (but also 5, 7,... by expending the sine in Eq.3.225 at higher orders[r]). In other words, a single photon excitation can decay into multi-photon states because of the nonlinearity. Because of that in the following they will be called *photon conversion processes*. Therefore, the

[q] We did not discussed the other contributions to the Self Energy.

[r] This is one of the main difference between the Kerr approximation, which is only considering coupling between single-photon states and three-photons states

lifetime of the single-photon states is finite and translates into a broadening of the modes according to Heisenberg's principle.

In order to get a physical intuition on this lowest order expansion of $\Sigma^{(2)}$ we can simplify our circuit. First, we consider the fifth first modes only. Second, the first site is considered grounded while the nonlinear junction site is seen as an open. Finally, we consider the chain dispersion relation to be linear. With these assumptions, the dispersion relation is given by (see Section 3.1.2):

$$\omega_{k_n} = v_\varphi k_n \tag{3.229}$$

with :

$$k_n = \pi \frac{(n + \frac{1}{2})}{(N - \frac{1}{2})} \tag{3.230}$$

Hence, an excitation in the fourth mode, labeled $|k_4\rangle$, is coupled to two three-photons states (see Figure 3.23) since they are the only ones with the same energy (given by $9\pi v_\varphi/(2N-1)$): one where two photons are in the zeroth mode while one photon is in the third mode, another one were the three excitations are in the zeroth, first and second modes respectively. Hence the self-energy $\Sigma^{(2)}$ evaluated at ω_{k_4} quantify the decay rate of an excitation in states $|k_4\rangle$ resulting from the coupling with these states.

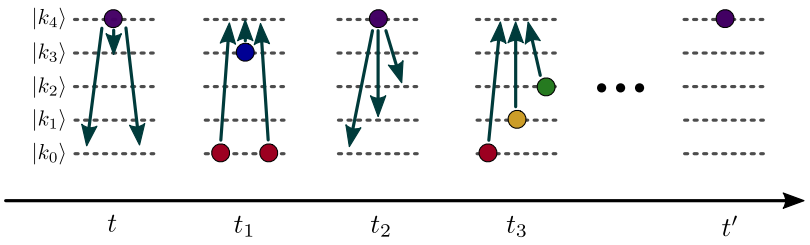

Figure 3.23 – Schematic of the processes occurring between a time t and t' included in the lowest order expansion of $\Sigma^{(2)}$. $|k_n\rangle$ is a state corresponding to one excitation in mode n. The interaction between the single-photon state and the three-photons states occurs at times t_1, t_2, t_3, ... between t and t'.

However, since the chain is a quasi-continuum, the self-energy is not a well-defined function of the frequency. As we see from see from Eq.3.228 it is composed of delta functions only. This can be arranged by taking the thermodynamic limit for the chain. Then, the self-energy is composed of an infinite number of delta functions and is therefore a continuous function of the frequency. A more physical way to understand it is that, for a perfectly isolated quasi-continuum, the interaction between the modes of the chain will only creates coherent oscillations between the single-photon states and the multi-photons states. Hence, by taking the thermodynamic limit these oscillations will destructively interfere and decays of excitations will be possible. This thermodynamic limit can be justify if the estimating damping rate is larger than the mode spacing of the final states, the multi-photon states. However, this approximation is not mandatory within our formalism. A more realistic approach can be made by realizing that our system is not perfectly isolated. The quasi-continuum is indeed coupled to other noise sources and/or to the measurement setup. Because of that, any excitation in the circuit have a finite lifetime and the mode broaden (see Appendix C.1).

This broadening does not result from the photon conversion process but will be enhance by it. Then if the number of multi-photon states is large enough, the resulting modes overlap and the self-energy become a well define function of the frequency.

In conclusion, we saw that single-photon and multi-photons states are coupled via the non-linearity of the junction. The main contributions being the coupling between single-photon states with odd-numbered photon states. To do so we had to understood the link between the SCHA and a perturbative treatment of the nonlinearity. We saw that, at first order, this theory allowed us to recover the self-consistent relation for the renormalized Josephson energy of the nonlinear junction. However, no dissipative effect could occur since the resulting Hamiltonian was well approximated by a quadratic one with eigenmodes of frequency ω_k. These modes correspond to the transition frequency between a zero-photon state (the GS) and a single-photon excited state in the mode k. Therefore, since the nonlinearity couples these single-photon states to other multi-photons states, an infinite number of processes can happen between them while going from t to t'. Consequently, they acquires a finite lifetime and they are both shifted and broadened. Finally, we have not included in this section the effects that the temperature could have on the broadening in order not to complicate the discussion. The model we used to explain the measured data will take into account these thermal effects. However, from the fact that the brodenings depend on $\xi^2_{0,k}$ we can expect that the broadenings increase with the temperature and that the relative contribution of the low frequency modes increases when heating up the sytem.

Experimental Setup and Fabrication 4

Contents

4.1 Thermalisation and Filtering 88
4.1.1 Preamble 88
4.1.2 Different kinds of attenuators 88
4.1.3 The microwave setup 92
4.1.4 Radiative and magnetic shielding 96
4.2 Temperature regulation 97
4.3 Fabrication 97
4.3.1 Bridge Free fabrication technique. 98
4.3.2 DC measurement on test structures 99

4.1 Thermalisation and Filtering

In this section we will see what are the experimental conditions required to investigate the properties of our circuits. This will allow us to approach the various filtering and thermalization techniques used during my PhD.

4.1.1 Preamble

In order for the circuits to be properly characterized, they must be in their ground state at equilibrium. If not, uncontrolled excitations could blur the measures. To this aim, two constrains have to be respected. First, the temperature should be low enough. Second, the circuits have to be decoupled from any external noise source, such as an uncontrolled magnetic field.

To estimate the required temperature, we recall that collective excitations in a microwave circuit can be seen as photons. The photon occupation number at thermal equilibrium is given by the Bose-Einstein distribution:

$$n\left(f,T\right)=\frac{1}{\exp\left(\frac{hf}{k_{\mathrm{B}}T}\right)-1} \tag{4.1}$$

A system is in its GS if n is much less than 1[a]. This sets a higher bound to the (potentially frequency dependent) temperature at which the device should be operated:

$$T_{\mathrm{eff}}\left(f\right)=\frac{hf}{k_{\mathrm{B}}\ln(2)}\simeq\frac{hf}{k_{\mathrm{B}}} \tag{4.2}$$

The typical bandwidth (BW) of our devices is 0.5 GHz to 20 GHz. This translates into a maximum temperature $T=20\,\mathrm{mK}$. Reaching such a temperature is possible using a dilution refrigerator (a detailed presentation of our fridge is given in [67]). If this latter was perfectly isolated from any source of radiation the sample would be in its GS. Nonetheless, the sample has to be measured. Since the measurement apparatus is at room temperature and $50\,\Omega$ matched, it radiates a Johnson-Nyquist noise which might excite the circuit. The solution is to filter that noise using different kind of attenuators.

4.1.2 Different kinds of attenuators

Why using attenuators ?

An attenuator is a two ports component. Since commercial attenuator are $50\,\Omega$ matched we will not consider any reflection in port 1 or 2 but only the signal being transmitted from one port to another. In addition, most of the attenuators are reciprocal medium (except for a directional attenuator). So we will just model one direction and the ports will be labelled input and output. An attenuator is a dissipative component, meaning that the incoming signal will be coupled to a bath at a temperature given by the one of the attenuator. Because of all these properties the

[a] Thus, thermal excitations can be neglected and only quantum fluctuations remain.

transmission through an attenuator can be modeled as a mirror in the input-output formalism [80].

Let a_{in} and a_{out} be the amplitude (in Volt) of incoming and outgoing signals while b_{in} and b_{out} are the noise coming from the attenuator itself and the signal absorbed by that latter respectively. These quantity are defined in the frequency domaine. We have:

$$a_{\text{out}} = \sqrt{t}a_{\text{in}} + i\sqrt{1-t}b_{\text{in}} \tag{4.3a}$$

$$b_{\text{out}} = \sqrt{t}b_{\text{in}} + i\sqrt{1-t}a_{\text{in}} \tag{4.3b}$$

with t being the power transparency. Taking the mean square value of these equations:

$$\langle |a_{\text{out}}|^2 \rangle = t\langle |a_{\text{in}}^2| \rangle + (1-t)\langle |b_{\text{in}}|^2 \rangle \tag{4.4a}$$

$$\langle |b_{\text{out}}|^2 \rangle = t\langle |b_{\text{in}}|^2 \rangle + (1-t)\langle |a_{\text{in}}|^2 \rangle \tag{4.4b}$$

using that the signal fluctuations from input and output ports are uncorrelated and taking the mean value of the signal to be zero. As we have seen in Section 3.1.2 the Johnson-Nyquist formula links these voltage fluctuations to temperature:

$$\bar{S}_V(f) = \frac{4Zhf}{\exp\left(\frac{hf}{k_{\text{B}}T}\right) - 1} = 4Zhfn(f,T) \tag{4.5}$$

with Z the impedance of the device and n a number of excitations per units of time and bandwidth. Note that we dropped the quantum part of the fluctuation since thermalization will not affect it. Moreover, we take the one-sided noise convention in this section. Let us now assume that the attenuator is thermalized at T_{att} while the incoming signal is at T_{in}. Consequently $\langle |b_{\text{in}}|^2 \rangle$ is at T_{att}, $\langle |a_{\text{in}}|^2 \rangle$ at T_{in}. Using Eq.4.5 in Eq.4.4b:

$$n_{\text{a,out}}(f, T_{\text{in}}, T_{\text{att}}) = |t|^2 n_{\text{a, in}}(f, T_{\text{in}}) + \left(1 - |t|^2\right) n_{b,in}(f, T_{\text{att}}) \tag{4.6}$$

with $n_{\text{a/b, in/out}}$ being the number of excitation carried by the waves per unit of bandwidth and time. While not being the same quantity, it has the same expression than Eq.4.1. This last equation shows that the role of an attenuator is to mix the excitations (or noise) coming from the input signal and the attenuator so that if $T_{\text{in}} > T_{\text{att}}$ then $n_{\text{a, out}} < n_{\text{a, in}}$. We can also see that the thermalization is more efficient at low transparency value.

Discrete attenuator

Discrete attenuators are based on lumped resistor circuits. A detailed analysis is given in [104]. They provide a constant attenuation over the bandwidth specified by the manufacturer. For instance, the bandwidth of the XMA cryogenic attenuator used in our fridge (Part number 2782-6051-dB- CRYO) ranges from DC to 26.5 GHz. This is

more than enough to filter excitations over the operating range of our device (from 0.5 to 20 GHz).

Nonetheless, our devices are fabricated from aluminum thin films with a superconducting gap estimated to $\Delta/e \sim 210\,\mu V$. Consequently, if photons with an energy higher than 2Δ reach our sample they will create quasi-particles such that our device will be coupled to uncontrolled degrees of freedom. That corresponds to a frequency of 100 GHz, far beyond the operating range of a discrete attenuator.

The reason why such attenuators cannot operate at higher frequencies comes from their lumped nature. A possible approach to solve that issue is to make use of distributed attenuator.

Distributed attenuator

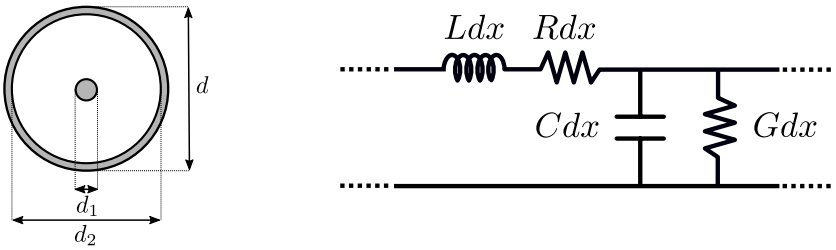

Figure 4.1 – **Left.** Sectional view of a coaxial cable. Grey parts are made out of metal while the space in between is filled with a dielectric. **Right.** Lumped element representation of dx long portion. L, R, C and G are the inductance, resistance, capacitance and conductance per meter

A distributed attenuator can be implemented using a resistive coaxial cable. The propagation constant of the TEM modes propagating along this latter is given by:

$$\gamma(\omega) = \sqrt{(G + j\omega C)\,(R + j\omega L)} \tag{4.7}$$

where G, C, R and L are respectively the conductance, capacitance, resistance and inductance per meter represented on Fig.4.1. These parameters are given by [105]:

$$R\,(\omega) = \omega^{1/2}\left(\frac{1}{\pi d_1}\left(\frac{\mu_0\rho_1}{2}\right)^{1/2} + \frac{1}{\pi d_2}\left(\frac{\mu_0\rho_2}{2}\right)^{1/2}\right) \tag{4.8}$$

$$C = \frac{2\pi\epsilon_r\epsilon_0}{\ln\,(d2/d1)} \tag{4.9}$$

$$G = \frac{2\pi\sigma}{\ln\,(d2/d1)} \tag{4.10}$$

$$L = \frac{\mu_0}{2\pi}\ln\,(d2/d1) \tag{4.11}$$

with $\rho_{1/2}$ being the resistivity of the inner and outer part of the coaxial cable while ϵ_r is the relative permittivity of the dielectric filling it and σ is its conductivity.

Eq.4.8 is valid as long as the skin depth is smaller than the thickness of the conductor. Which is the case in the Gigahertz range for such cables.

The ones I installed in the fridge are the cryogenic cables SC-040/50-CN-CN from Coax Co. The inner and outer conductors are made out of cupro-nickel with diameters $d_1 = 0.080\,\text{mm}$, $d_2 = 0.26\,\text{mm}$ and $d = 0.40\,\text{mm}$. The dielectric is a PFA polymer. Manufacturer's data-sheet for the capacitance per meter allows us to estimate the relative permittivity to be $\epsilon_\text{r} = 2.03$ (it will be taken constant with frequency). Because of the relatively low loss tangent of PFA, G can in general be neglected compared to ωC in the propagation constant. Consequently, the attenuation in decibel per meter is given by:

$$A_\text{dB}(\omega) = \frac{20}{\ln(10)}\,\text{Re}\{\gamma(\omega)\} = \frac{20}{\ln(10)}\,\text{Re}\left\{\sqrt{j\omega C\,(R + j\omega L)}\right\} \tag{4.12}$$

Using Eq.4.12 to fit the attenuation given by manufacturer at 4K we find $\rho_{\text{CN, 4K}} = 0.255\,\mu\Omega\,\text{m}$. The result of the fit is shown on Fig.4.2.

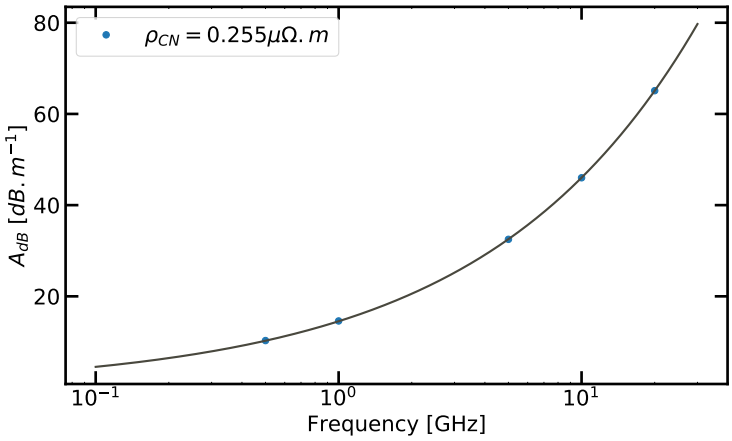

Figure 4.2 – Attenuation per meter of the coaxial cables used as distributed attenuators in this thesis. Blue dots come from manufacturer's data-sheet, grey line is the fit outcome.

These cables will be used at the coldest stage of the dilution fridge. The temperature of the latter is around 20 mK. This is way colder than 4 K. Hence, the cables resistance will be at most the one estimated from the fit. In practice, the resistance is not supposed to vary much from 4 K to 20 mK. Consequently, it will be taken as a constant.

Even though they are not lumped circuits, coaxial cables have a finite bandwidth. The manufacturer data-sheet gives a high frequency cut-off of 400 GHz. The latter correspond to the low frequency cut-off of the TE_{11} mode. Nevertheless, this mode does not change significantly the attenuation of the cable [105]. The first that will drastically reduce the attenuation of the cable is the TE_{01} mode. The cut off frequency is the first non trivial zero of:

$$J_1\left(\frac{\pi d_1}{v_\varphi f}\right) Y_1\left(\frac{\pi d_2}{v_\varphi f}\right) - J_1\left(\frac{\pi d_2}{v_\varphi f}\right) Y_1\left(\frac{\pi d_1}{v_\varphi f}\right) = 0 \tag{4.13}$$

where J_1 and Y_1 are Bessel functions and $v_\varphi = 1/\sqrt{\epsilon_0 \epsilon_r \mu_0}$ is the phase velocity. For our cable we find $f_c \sim 1\,\text{THz}$.

Directional attenuator - Isolator

The two previously presented attenuators are reciprocal medium, meaning that they attenuate equally in both directions. There are some scenarios for which we would like to attenuate the signal in only one direction. For that, time reversal symmetry has to be broken. That can be easily done using a magnetic field. A detailed study is given in Chapter 9 of [104]. The isolators used in our fridge are the CWJ0312KI from Quinstar. S_{21} and S_{12} parameters are plotted in Fig.4.3 showing a 3 to 20 GHz bandwidth. At least 10 dB of attenuation is provided over that latter.

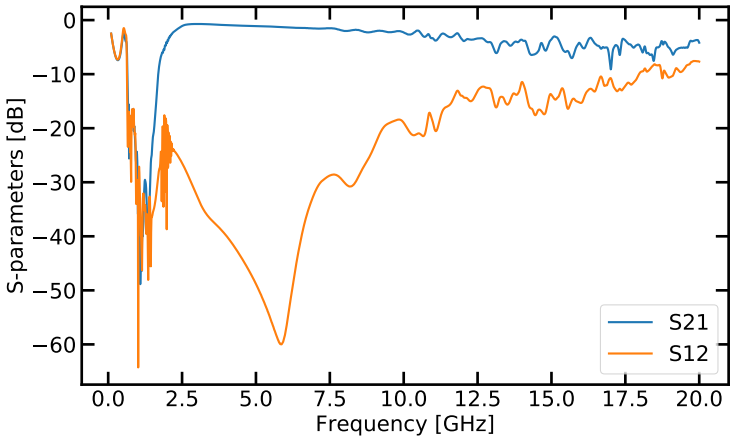

Figure 4.3 – Measured S_{21} and S_{12} parameters with respect to the frequency. S_{12} is below 10 dB from 3 to 20 GHz

4.1.3 The microwave setup

Now that the basics of thermalization using different kind of attenuators have been introduced the microwave setup will be presented.

Input line

The input line is on the left side of Fig.4.4. To thermalize the incoming flux of excitations 4 stages of attenuation are used at respectively 4 K, 200 mK, 40 mK and 20 mK. Attenuators are anchored to copper mounts such as the one in Fig.4.5. Therefore, we can estimate their temperature to be the one of the different stages. In addition the distributed attenuators (labeled IR filter on Fig.4.4) are anchored to a copper plate using a Silver epoxy paste, providing a good thermal contact along the cable. Since the space available at the last stage of our fridge is limited, the length of these cables is 5 cm.

The resulting number of excitation per unit of bandwidth and time, in the frequency range of our devices, is given on Fig.4.6.

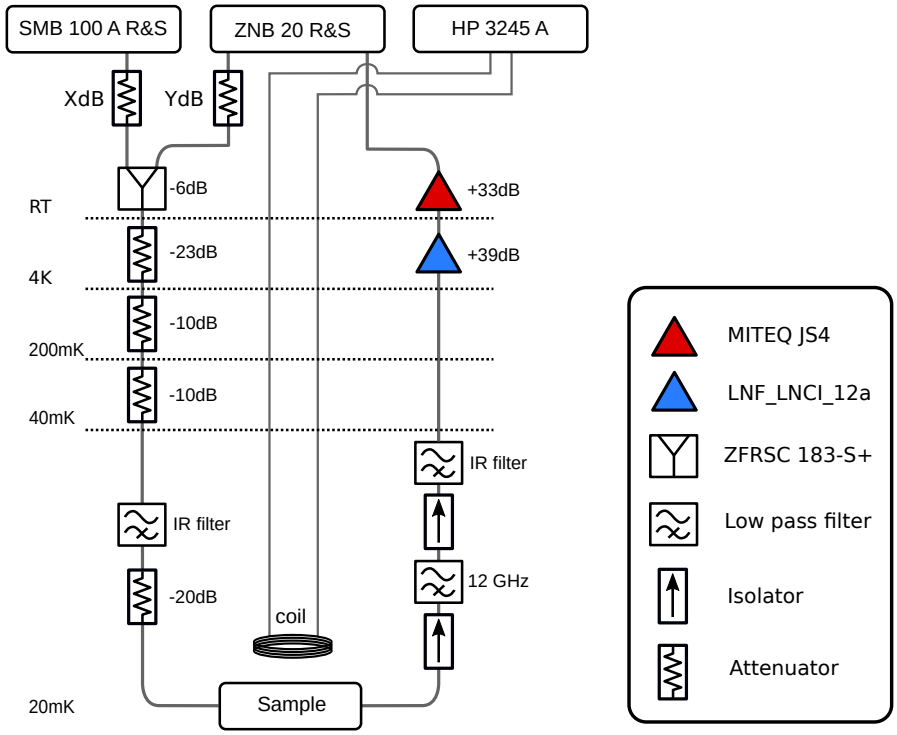

Figure 4.4 – Schematic of the microwave setup used to probe our device. SMB 100 A R&S is a microwave source. ZNB 20 R&S is a vector network analyzer. HP 3245 A is the current source used to applied magnetic flux via a superconducting coil.

The incoming number of excitation per unit of bandwidth and time coming from the input line is always lower than 1 in between 0.5 and 20 GHz.

As explained in Section 4.1.2 photons at a frequencies higher than 100 GHz can create quasiparticles in our sample. We make the hypothesis that neither the coaxial cables linking the various stages between room temperature and base temperature (they are thicker and less resistive than the continuous attenuator and their high frequency cut of is around 190 GHz) nor the discrete attenuators provide attenuation at these frequencies. Thus, we find the number of excitations shown in Fig.4.7

Despite the number of excitations being drastically reduced, these remain higher than one. Nonetheless, they could be further reduced by cascading the number of distributed attenuators on the 20 mK stage. Three of them have been mounted in case other lines of measurement would be needed.

Output line

Now that the number of excitations per units of bandwidth and time coming from the input line has been estimated we can now investigate what happens at the output. The output line is represented at the right side of Fig.4.4.

The role of this line is twofold : thermalising the excitations coming from the outside of the fridge and amplifying the signal coming from the sample. Therefore, discrete attenuators cannot be used in between the sample and the High Electron Mobility Transistor (HEMT) amplifier (LNF-LNC1-12A) located at 4K. Otherwise, it will drastically reduce the signal coming from the sample. The solution is to use isolators presented in Section 4.1.2. Nevertheless, these are not filtering correctly outside

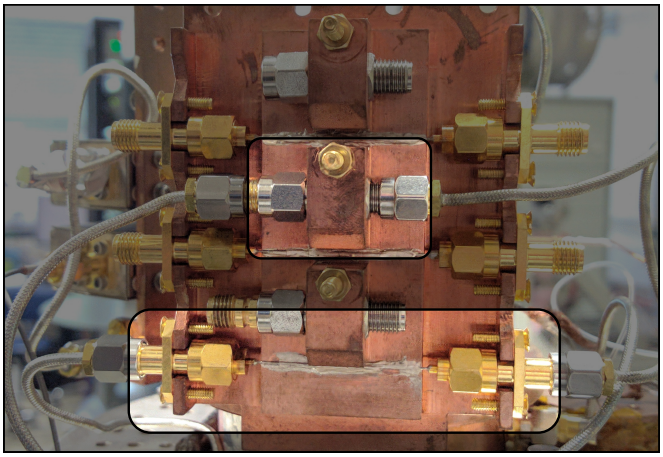

Figure 4.5 – Attenuators thermalisation on the 20 mK stage. The upper part is à -20dB discrete attenuator, the lower one is a distributed one.

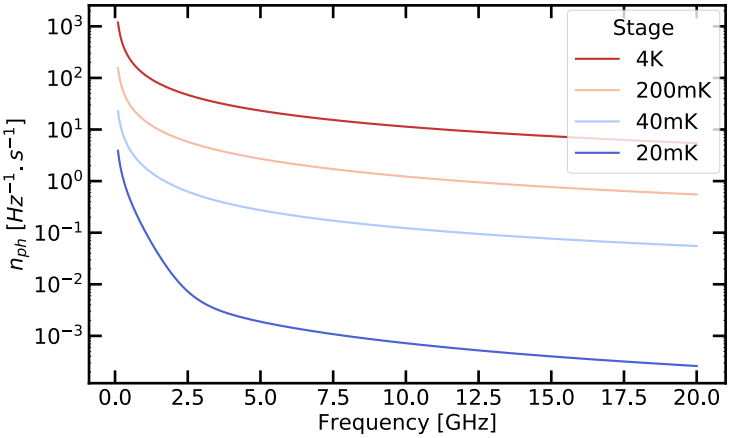

Figure 4.6 – Number of photons per unit of bandwidth and time at the output of the different thermalisation stages on the input line.

of their 3 to 12 GHz bandwidth. Consequently, a K&L 6L250-00089 low pass filter is used, it can be modeled as a perfect −50 dB attenuator between 12 and 26 GHz. In addition, a distributed attenuator is used, since its attenuation is less than 3 dB in the BW of the HEMT (2 to 12 GHz).

In the following two assumptions are made: all the noise comes from the HEMT and it can be modeled has a 5.5 K 50 Ω resistance. The last hypothesis is coming from manufacter's data-sheet indicating a noise temperature of 5.5 K. Then the number of excitations reaching the sample can be computed.

Since there is almost no filtering below 0.6 GHz the number of excitations is very high in this range. That could be a problem for the low frequency modes of our devices. However, we saw that the lower bound of the HEMT bandwidth is around 2 GHz. Outside of their bandwidth the input impedance of such amplifiers is no longer 50 Ω matched but very large. Therefore, the noise coming from the amplifier outside of its bandwidth is mostly reflected. Hence, it is likely that the number of excitations below 2 GHz is largely overestimated. A proper measurement of the input impedance

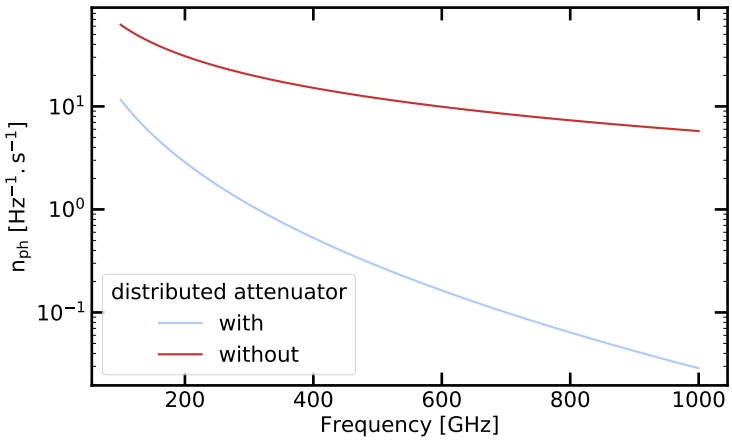

Figure 4.7 – Number of high frequency photons per unit of bandwidth and time coming from the input line with and without a distributed attenuator at the 20 mK stage.

of such amplifier at the operating temperature of the fridge would need to be carried in order to quantitatively estimate the number of excitations brought by the output line in this frequency range.

Number of photons in the device modes

The flux of photon per units of bandwidth reaching the sample being known we can compute the number of thermal excitations in our devices. Different kind of samples have been measured, however each of our system modes can be modeled as a symmetric two ports resonator. While being a toy model this will give a good order of magnitude for the number of thermal photons in the system because of the lines. Transfert function between the flux of photons per unit of bandwidth and the number of photons per hertz in our modes is :

$$|T(\omega)|^2 = \frac{\kappa_e}{\kappa_e^2 + (\omega - \omega_r)^2} \tag{4.14}$$

with κ_e and ω_r the coupling between the resonator and the transmission line and the resonant frequency of the mode.

Then the energy in the resonator in given by:

$$E = \int_{-\infty}^{+\infty} \frac{d\omega}{2\pi} |T(\omega)|^2 \hbar\omega \left(n_{in}(\omega) + n_{out}(\omega)\right) \tag{4.15}$$

with n_{in} and n_{out} being the number of photons per unit of time and bandwidth coming from the input and output ports. Because $\hbar\omega n_{in/out}$ does not vary much over k_e, typically $k_e \sim 1$ MHz, they are considered as constant. The average photon number in the mode is then:

$$n(\omega_r) = \frac{E}{\hbar\omega_r} = \frac{1}{2}\left(n_{in}(\omega_r) + n_{out}(\omega_r)\right) \tag{4.16}$$

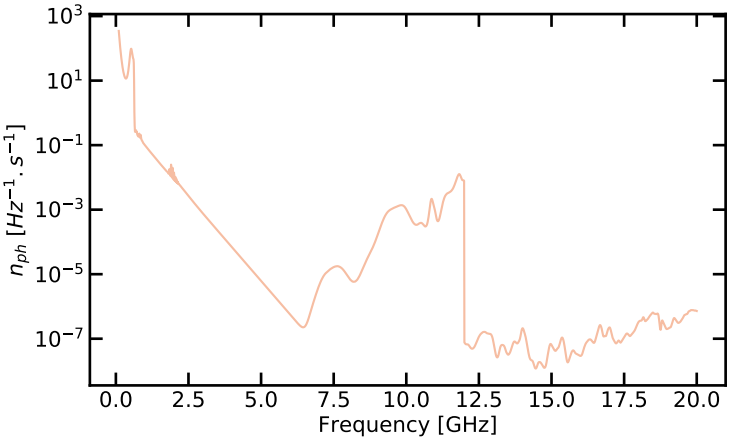

Figure 4.8 – Number of photons per unit of bandwidth coming from the output line

for a mode at 0.5 GHz, where the filtering of the output line is not very good, that would give around 40 photons. However, we saw in the previous section that this number was likely to be largely overestimated. For a mode at 4 GHz we find $1.3.10^{-3}$.

As a conclusion we could see that the study of the properties of our circuits required that the temperature of the latter should not exceed 20mK. As a result, the measuring lines used to characterize these circuits are thermalized using different types of attenuators, which ensures that only a small amount of excitation can pass over a wide frequency range.

4.1.4 Radiative and magnetic shielding

We have seen the importance of protecting the device from radiation. The coaxial cables are not the only source of it. Indeed, the fridge is placed at room temperature. Therefore, it is surrounded by thermal photons. Most of these are filtered since the different stages of the fridge are enclosed in polished aluminum screens with a plasma frequency $\sim$ 3000 THz. Nevertheless, the last screen is at 4 K and the shielding is not perfect, allowing a few photons to pass through.

Following [106, 107] a black coated copper shield is added around the sample holder and the sample in enclosed in a tight copper box. Since, the plasma frequency of copper is around 1500 THz most of the photons will be reflected. The black coating will absorb some of the ones able to pass through. Ensuring that the samples will mostly see 20 mK black body radiation. The coating is done using a Stycast epoxy loaded with silicon balls and carbon powder.

Since, SQUID are used in the devices we also need magnetic shielding. The shields described before cannot efficiently screen constant and slow varying magnetic field. The solution consists in using a high relative permeability metal, called μ-metal. This material confines the magnetic field such that it is attenuated by a factor μ_r at the sample position (discarding prefactors depending on the geometry [108]). The μ-metal screen used in the setup are 1.5mm thick CryoShield cylinder from Magnetic shield Ltd with a typical relative permeability of 70000 at 4K.

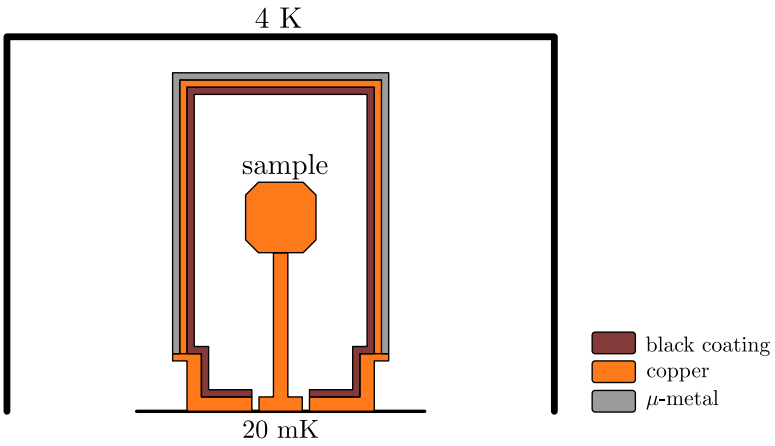

Figure 4.9 – Sectional view of the different shields used at 20mK

4.2 Temperature regulation

A temperature regulation of the mixing chamber has been implemented in order to study the effect of temperature on our devices . The control electronics I used is developed in house. It consists in a Proportional–Integral–Derivative (PID) controller called MGC3. The feedback is done on the current sent to a 1 kΩ heater anchored to the mixing chamber. The control parameter is the temperature given by a thermometer called MMR3. A schematic of the working principle is displayed on Fig.4.10. The MMR3 measures the sensor thermalised at the mixing chamber using 4 probe technique. The 4 probes measurement is done using AC squared pulses, enabling the cancellation of possible offset in voltage coming from thermo-electric currents, current source bias, etc. Typical precision in temperature measurement is about 10% from 20mK to 300K.

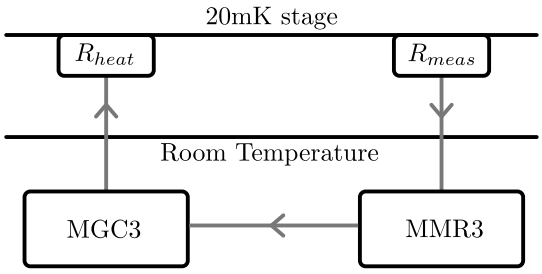

Figure 4.10 – Schematic of the PID working principle.

The PID is controlled via a Transmission Control Protocol (TCP) enabling automated temperature sweep in parallel to microwave measurement. Such a sweep is shown in Fig.4.11.

4.3 Fabrication

The fabrication techniques used during my PhD do not differ from [67]. Consequently, we will focus on the key points of the devices design. In a first part the Bridge Free Fabrication Bridge (BFF) technique used to fabricate Josephson Junction (JJ) will be

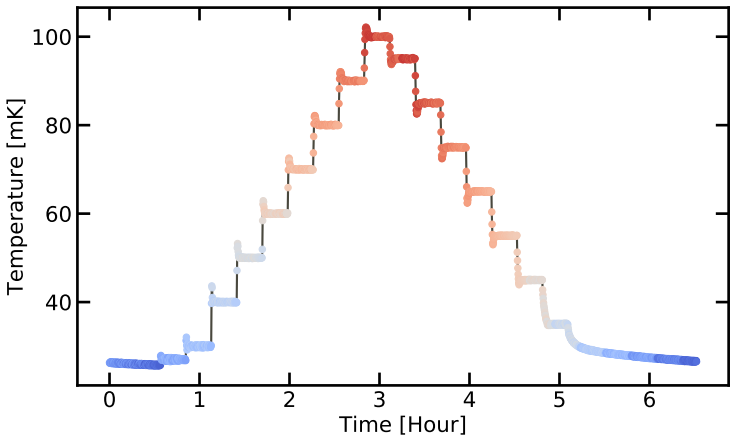

Figure 4.11 – Typical temperature sweep generated by the MGC3 and measured by the MMR3.

explained. Then, an explanation of the room temperature junction characterization will be given.

4.3.1 Bridge Free fabrication technique.

Among the different components designed on our chips JJ is the most important and delicate one. This difficulty comes from the fact that Josephson energy, or conversely critical current, of such junction is inversely proportional to the exponential of tunnel barrier thickness. This means that the oxide layer should be created in a controlled environment to have a reproducible process. That can be done by oxidizing the aluminum in situ between the two metallic layer depositions. To do so, a two angle evaporation with bi-layered mask is well suited. The mostly used one in the field is known as the Niemeyer-Dolan technique [109].

Nonetheless, that last suffers from several drawbacks. The size range for the junctions is limited because too long junctions can cause a bridge collapse and the cleaning of the area beneath that latter is difficult. Since, most of the problems caused by that technique is coming from the use of a bridge another technique called BFF has been used here. It has been developed in Neel Institut by F.Lecocq [110] and perfected by J. Puertas-Martínez [67]. The main difference between the two is the replacement of a bridge by a controlled undercut as shown by Fig.4.12

As for the Niemeyer-Dolan Bridge technique the steps are:

1. Deposition of a first layer a PMMA-MAA 9% and a second layer of PMMA 4% resist.

2. E-beam exposure of the resist. The first layer if more sensitive to electrons than the second. Enabling us to carve an undercut.

3. Development of the exposed resist.

4. Double angle evaporation. An oxide layer is created in between the two depositions.

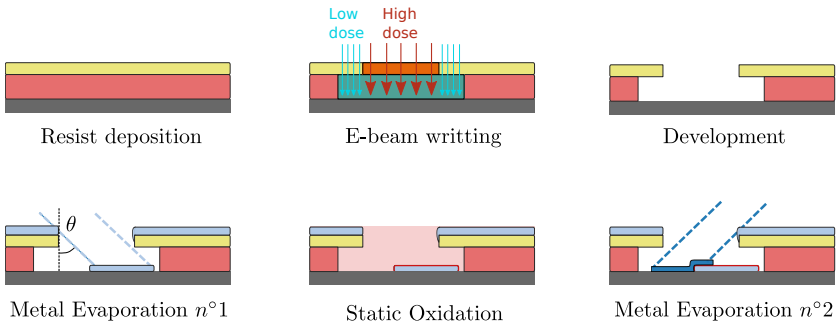

Figure 4.12 – **Steps of the BFF from top left to bottom right. Resist deposition:** The double layer resist is spin coated. **E-beam writing**: Exposition of the resist, the second layer is more sensitive than the second. **Development**: the exposed resist is removed. **First deposition:** the first layer of aluminum is deposited with a θ angle. **Static Oxidation:** the aluminum layer is oxidized in a controlled environment. **Second deposition:** the second layer of aluminum is deposited with a $-\theta$ angle. Schematic courtesy of Luca Planat.

5. Lift-off of the metal sitting on the resist.

Fig.4.13 shows one type of junction that can be fabricated using the BFF technique. Detailed recipes and patterns used for different designs of junctions are discussed in Appendices B.1 and B.2.

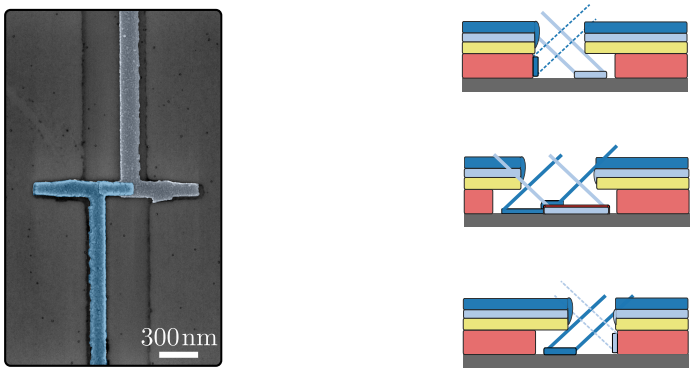

Figure 4.13 – **Left.** Scanning electron microscope (SEM) picture of a Josephson Junction. Colors correspond to the two layers of aluminum. **Right.** The corresponding kind of undercuts used to fabricate the junction.

4.3.2 DC measurement on test structures

After fabricating our device DC measurement of test structures are performed. It consists in measuring the room temperature resistance of the designed Josephson junctions. Aims of this step are twofold. First, it is a sanity check for the reproducibility of the process. Second, it enables us to estimate the parameters of our devices.

The resistance of a JJ is linked to its critical superconducting current via the Ambegaokar-Baratoff formula [111]:

$$I_{\mathrm{C}}(T) = \frac{\pi \Delta_{\mathrm{Al}}}{2eR_{\mathrm{n}}} \tanh\left(\frac{\Delta_{\mathrm{Al}}}{2k_{\mathrm{B}}T}\right) \tag{4.17}$$

with Δ_{Al} the superconducting gap of aluminum and R_{n} the normal resistance of the junction. Since $\Delta_{\mathrm{Al}} = 210\,\mu\mathrm{eV}$ and our devices will be characterized at $T \sim 20\mathrm{mK}$ that formula can be taken as its zero temperature version:

$$I_C = \frac{\pi \Delta_{\mathrm{Al}}}{2eR_{\mathrm{n}}} \tag{4.18}$$

Finally, the resistance of a tunnel junction at room temperature is an underestimation of its normal resistance. The conversion factor is $R_n = \beta_{\mathrm{f}} R_{\mathrm{RT}}$ with $\beta_{\mathrm{f}} = 1.2$ [112].

Now that the relationship between the RT resistance and the critical current of the junction at very low temperature is known we will explain the measurement protocol. On every device, arrays of test structures are dispatched. Each array contains one of the designs used on the chip, as shown on Fig.4.14. Within an array the number of junctions varies with a given step. By measuring the resistance of the test structures within an array we will have a relation between the junctions number and the measured resistance.

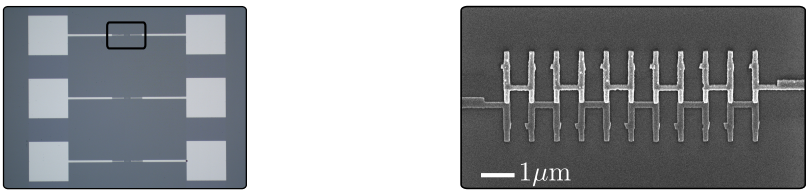

Figure 4.14 – **Left.** Portion of an array of test structures for a given junction design. The black squared is the magnified region. **Right.** SEM picture of a test structure within the array.

The slope is the resistance of one junction while the intercept is the residual resistance coming from the setup (we are using 2 points measurement). A typical DC test for two arrays containing the same design of junction is shown on Fig.4.15

From the knowledge of that latter the reproducibility of the process can be monitored. If the quality and thickness of the tunnel barrier is reproducible we expect its critical current density to be the same from one batch to another and from one junction to another. The current density can be simply estimated by dividing the current by the area of the junction. For junction bigger than $\sim 0.15\,\mu\mathrm{m}^2$ the expected value is 15 to $16.5\,\mathrm{A\,cm^{-1}}$ with the parameter of the recipe[b]. For small junctions the expected value is lower since the edge of the interface start to play a role. In addition we can also estimate the Josephson energy and the charging energy of those junction. The first by using the relation between the critical current density and the Josephson

[b]For smaller junctions we saw that the critical current density was decreasing with the junction area

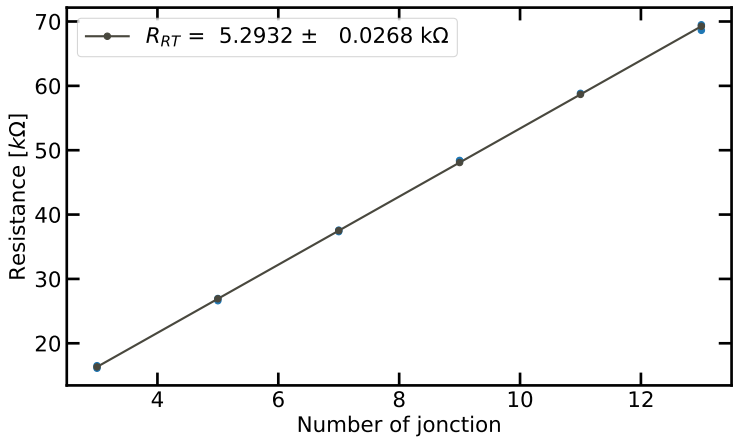

Figure 4.15 – Resistance of the test structures as a function of the number of junctions for two arrays containing the same design. Blue dots are experimental data while the grey line and dots are the outcome of the linear fit.

energy. The second by using the relation between the area of a tunnel junction and its capacitance, estimated to be $45\,\mathrm{fF\,\mu m^{-2}}$ with this recipe.

For instance, the junctions of Fig.4.15 have a $0.32\,\mu\mathrm{m}^2$ area and a resistance of $(5.29 \pm 0.03)\,\mathrm{k\Omega}$. Using Eq.4.18 we find a critical current density of $(16.20 \pm 0.01)\,\mathrm{A\,cm^{-1}}$, a Josephson energy of $(25.8 \pm 0.2)\,\mathrm{GHz}$ and a charging energy of $5.4\,\mathrm{GHz}$.

Renormalization of the nonlinear junction

5

Contents

5.1 Fixed nonlinearity 104
5.1.1 Sample presentation 104
5.1.2 Transmission measurement 105
5.1.3 Dispersion Relation 107
5.1.4 Phase shifts 112
5.1.5 Renormalization as a function of temperature 115
5.1.6 How many modes contribute ? 117
5.2 Tunable nonlinearity 120
5.2.1 Sample presentation 121
5.2.2 Flux tunability 122
5.2.3 Dispersion relation 122
5.2.4 Josephson relative phase shift 124
5.2.5 Renormalization with respect to the nonlinearity 127

In this section, the effect of the environment induced fluctuations on the plasma frequency of the nonlinear junction will be presented. In a first part, we will see how it evolves with temperature. Then, the effect of the junction nonlinearity, or conversely its E_J/E_C ratio, will be discussed.

5.1 Fixed nonlinearity

The first effect I will discuss in this thesis is the junction frequency renormalization. To observe it, we designed and fabricated the circuit presented in Section 3.2. Then, the spectroscopy of this circuit was performed using the measurement setup discussed in 4.1.3. Finally, we repeated that measurement for different temperatures to check if the SCHA could accurately describe the ground state of our circuit. This procedure has been performed on three samples, denoted A, B and C. These three are made of nominally identical chain (same junction size and number of junctions) but of three different nonlinear junction sizes (and consequently three different regimes of nonlinearity). The nonlinearity of the junctions decreases from sample A to C.

5.1.1 Sample presentation

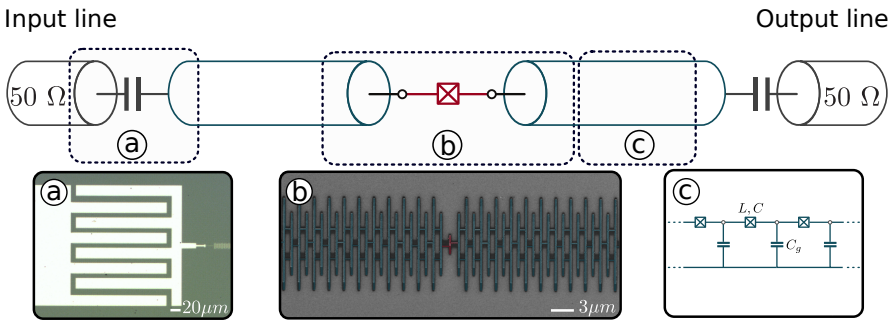

Figure 5.1 – Schematic of the measured circuit. The SQUID chains, depicted as blue transmission lines, are capacitively coupled to the input and output 50 Ω coaxial cables and galvanically coupled to the nonlinear Josephson junction (in red). **a** Optical picture of the input and output capacitive coupling pads. **b** SEM picture of a few of the SQUIDs (1500 in total for each chain) that are coupled to the nonlinear Josephson junction (in red). **c** Equivalence between the transmission line effective picture and the SQUID chain characterized by three microscopic parameters L and C the inductance and capacitance per SQUID respectively and C_g the ground capacitance.

The sample consists of a nonlinear Josephson junction of characteristic impedance on the order of Z_q ($E_J/E_C \lesssim 1$), which is embedded in the middle of two SQUID chains, each consisting of 1500 unit cells (Figure 5.1). The reason why chains are made up of SQUIDs and not single junctions is detailed in Appendix E. Nevertheless, the magnetic flux control of these SQUIDs has not been used. Therefore, they will be considered as junctions. The chains are capacitively coupled to the measurement setup to suppress DC noise which could affect the nonlinear junction.

5.1.2 Transmission measurement

In order to measure the nonlinear junction renormalization we performed a broadband spectroscopy of the device. This is done by measuring its transmission defined as:

$$S_{21}(\omega) = \frac{V_{\text{out}}(\omega)}{V_{\text{in}}(\omega)} \tag{5.1}$$

where S_{21} is the complex transmission coefficient and $V_{\text{out/in}}$ are respectively the complex amplitude of signal (in Volt for instance) at the input and output of the sample. Whenever we are close to one of the circuit resonances we expect the signal to interfere constructively such that the transmission will be given by (see Appendix C.1.1):

$$S_{21}(\omega) = \frac{\gamma_{\text{ext}}}{\gamma_{\text{int}} + \gamma_{\text{ext}} + 2i(\omega - \omega_{\text{r}})} \tag{5.2}$$

where γ_{ext}, γ_{int} are the broadenings caused by external and internal losses while ω_{r} is the resonant frequency. It is important to note that ω_{r} corresponds to one of the modes k (see Section 3.2.2) of our circuits only if the average number of photons in the circuit is low enough so that the transmission measurement probes only the transitions between the zero-photon state (the ground state) and single-photon states. This condition is all the more strict as the measured circuits are nonlinear.

We see that the transmitted power, which is given by the modulus square of Eq.5.2, is a Lorentzian function of width given by the dissipation. Therefore, this quantity is closely related to the response function in phase χ_ϕ of the RLC oscillator that we discussed in Section 3.3.2. This link is developed in Appendix C.1.

Because of the symmetry of our system there exists two kinds of resonant modes: the so-called odd and even modes (see Section 3.2.1). Because of that the resonant modes come in pair (Fig.5.2). Thus, the transmission is an array of double peaks whose shapes are almost Lorentzian. We recall that only the odd modes couple to the nonlinear junction since they are the only ones to induce a phase difference across it (Section 3.2).

To find an analytical formula for such double peaks we use the effective circuit presented in the lower right part of Fig.5.2. The nonlinear junction is replaced by an effective RLC circuit of parameters $L_{\text{J}}^{\star}$, C_{J} and R_{J}. This is valid under the assumption that the probe drive lets the circuit close to its ground state. If not, the SCHA is not valid since it is giving an expression for $L_{\text{J}}^{\star}$ when the circuit it at thermal equilibrium. The resistance R_{J} is an effective parameter used to account for the losses generated by the junction[a]. The chain modes are also modeled by RLC circuits around their resonant frequency, as is common practice [104]. Since the circuit is measured in transmission a mode of our chains can be modeled as an out-of-line RLC circuit of effective parameters $L_{\text{r}}, C_{\text{r}}$ and R_{r}. For a given mode the two chains are modeled with the same parameters because they are supposed to be identical. The impedance of the measurement lines is labelled Z_{tl}. To find the scattering parameters of such a circuit we can use ABCD matrices [104], by doing so we end up with:

[a]This is of course valid only if the broadening induced by the junction is not frequency dependent in the vicinity of the resonances, see Section 3.6.2

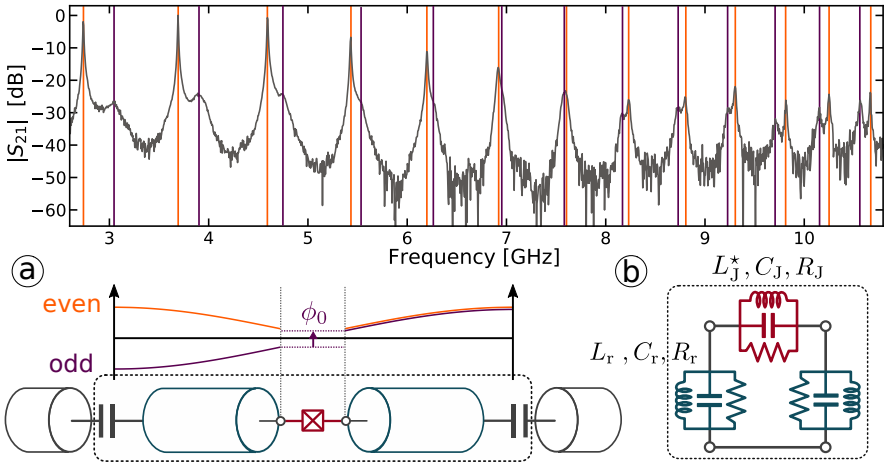

Figure 5.2 – **Upper part.** Transmission $|S_{21}|$ as a function of the frequency for sample A. The orange and violet lines indicate the position of the even and odd modes. **Lower part. a** The double peaks come from the symmetry of our circuit: even (orange) and odd modes (violet) are both resonant and therefore each correspond to a maximum of transmission. **b** Effective circuit for frequencies close to a double peak. The nonlinear junction is modeled as an in line RLC circuit where $L_J^\star$, C_J are respectively the renormalized inductance and capacitance while R_J is a resistance accounting for losses. The chain modes are modeled as two out-of-line RLC circuits where L_r, C_r and R_r are the effective parameters of the mode.

$$S_{21}(\omega) = \frac{2}{A + B/Z_{tl} + CZ_{tl} + D} \tag{5.3}$$

with:

$$A = 1 + \frac{Y_r}{Y_J} \tag{5.4}$$

$$B = \frac{1}{Y_J} \tag{5.5}$$

$$C = 2Y_r + \frac{Y_r^2}{Y_J} \tag{5.6}$$

$$D = 1 + \frac{Y_r}{Y_J} \tag{5.7}$$

where Y_r and Y_J are respectively the admittance of the out-of-line and in-line RLC circuits. Now that we have a model for the even-odd modes we need to link the effective circuit parameters to the resonant frequencies and broadenings of theses peaks. When neglecting the losses coming from R, R_J and Z_{tl} we find the following resonant modes:

$$\omega_{\text{even}} = \frac{1}{\sqrt{LC}} \tag{5.8}$$

$$\omega_{\text{odd}} = \frac{1}{\sqrt{L_\Sigma C_\Sigma}} \tag{5.9}$$

with $1/L_\Sigma = 1/2L_\text{r} + 1/L_\text{J}$ and $C_\Sigma = C_\text{r}/2 + C_\text{J}$. Therefore, by analogy with Appendix C.1.1 we define the following quantities:

$$\gamma_{\text{even}} = \frac{1}{R_\text{r} C_\text{r}} \tag{5.10}$$

$$\gamma_{\text{ext,even}} = \frac{2}{Z_\text{tl} C_\text{r}} \tag{5.11}$$

$$\gamma_{\text{odd}} = \frac{1}{R_\Sigma C_\Sigma} \tag{5.12}$$

$$\gamma_{\text{ext, odd}} = \frac{2}{Z_\text{tl} C_\Sigma} \tag{5.13}$$

where $1/R_\Sigma = 1/2R_\text{r} + 1/R_\text{J}$. Hence, we have an effective model for the transmission which enables us to access to the resonant frequencies and broadenings in our circuit. While in section 1.5 we used arguments based on response functions (see Section 3.5) to explain why the Even-Odd relative phase shift changes sign at the nonlinear junction renormalized frequency, we will now show that the same result can be obtained using this simple circuit model (this is because the impedance and the phase response function are closely related, as we showed in A.8). For modes at frequencies such that $\omega_{\text{odd}}, \omega_{\text{even}} \ll \omega_\text{J}^\star$, the capacitance of the nonlinear junction can be neglected since C_r is much bigger leading to $\omega_{\text{odd}} > \omega_{\text{even}}$. In the opposite case ($\omega_{\text{odd}}, \omega_{\text{even}} \gg \omega_\text{J}^\star$) the inductance can be neglected, giving $\omega_{\text{odd}} < \omega_{\text{even}}$. The most interesting regime is when the system is probed close to $\omega_\text{J}^\star$. In that case, the impedance of the nonlinear junction diverges and consequently the two effective oscillators are uncoupled leading to $\omega_{\text{odd}} = \omega_{\text{even}}$. From these simple arguments we can assign to each peaks the family it belongs to (even or odd, see upper part of Fig.5.2). Note that, in theory, it would be possible to access directly to $L_\text{J}^\star$ and C_J from the fit of the double peaks and, therefore, and directly measure the Even-Odd relative phase shift. Nonetheless, in practice, this fitting procedure was not accurate enough to do so and the phase shift measurement had been used. An example of a measured double peak fitted using our effective model is given in Fig.5.3.

5.1.3 Dispersion Relation

In Section 3.1.2 we have seen that the dispersion relation links the frequency of the resonant modes to their wave vectors. The even modes do not couple to the nonlinear junction. Therefore, the dispersion relation depends only on the chain parameters and the coupling capacitances.

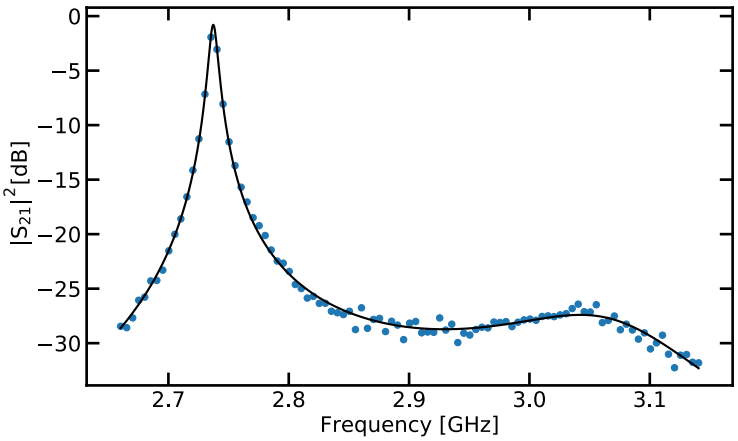

Figure 5.3 – Transmission $|S_{21}|^2$ as a function of the frequency for a given double peak. Blue dots are experimental data while the black line is resulting from the fit using our effective model.

Two-tones measurement

A transmission measurement gives the frequency of these modes only in the measurement bandwidth of the readout setup. This bandwidth is limited by the HEMT and the filtering used in the output line, which is from 2.5 GHz to 12 GHz in our case. However, this limitation can be overcome by using the so-called two-tones measurement [90]. This technique takes advantage of the fact that a chain remains weakly nonlinear even in the high $E_{\mathrm{J,ch}}/E_{\mathrm{C}}$ regime. Therefore, the chain modes are coupled via a cross-kerr interaction [48, 113]. In other words, if the number of excitations in one mode increases, this will result in a frequency shift of the other chain modes[b].

The two-tones measurement then consists in probing the transmission of a mode which is within the measurement bandwidth while performing a frequency sweep with an auxiliary microwave source. When the frequency of the auxiliary signal corresponds to a mode of the circuit it will shift the frequency of the probed mode, resulting in a drastic transmission change. Because of that, the only limitation is now the bandwidth of the microwave source. The result of such a measurement is given in Fig.5.4

We have seen that thanks to the two-tones measurement the chain resonant modes could be measured on a wide frequency range. However, to measure the dispersion relation we need to relate these frequencies to their wave vectors.

Coupling capacitance

The wave vectors depend on the boundary conditions. Figure 5.5 shows the effective circuit for the even modes taking into account the capacitive pad on the last site. C_{c}, $C_{\mathrm{c,i}}$ and $C_{\mathrm{c,o}}$ being respectively the in-line capacitance, the capacitance to ground on the chain side and the one on the measurement line side. In addition, there is

[b]Note that the Kerr interaction we are discussing here comes from the remaining nonlinearity of the modes. It is in addition to the one coming from the nonlinear junction (see Section 3.6.1). However the junction nonlinearity can be ignored here since we are probing the even modes

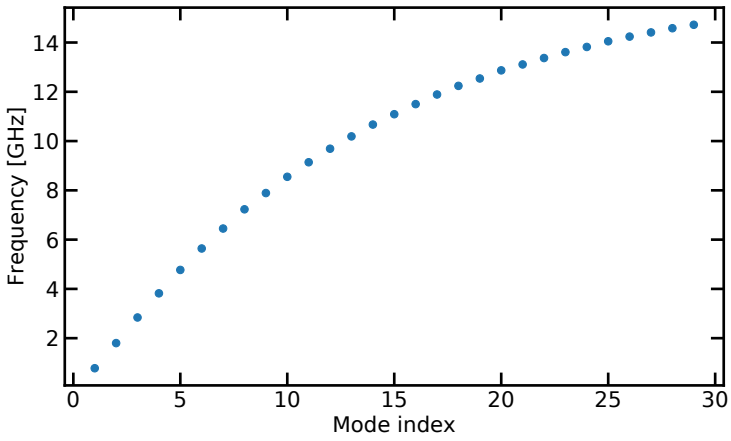

Figure 5.4 – Chain resonant frequencies as a function of the mode index resulting from the two-tones measurement of sample B.

also a capacitance $\tilde{C}_\mathrm{g}$ at first site[c]. Since, the two boundary conditions are frequency dependent we cannot use the phase shift formalism developed in Chapter 3. A possible way is then to do a numerical diagonalization of the circuit to fit the dispersion relation but that is inefficient because of the large number of sites. Moreover, it would add 3 fitting parameters.

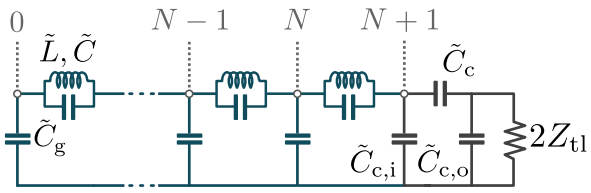

Figure 5.5 – Effective circuit for the even modes. The first site is grounded via a capacitance $\tilde{C}_\mathrm{g}$. The last site has a more complex boundary condition because of the coupling capacitances. $\tilde{C}_\mathrm{c}$, $C_\mathrm{c,i}$ and $C_\mathrm{c,o}$ are respectively the in-line capacitance, the ground capacitance on the chain side and ground capacitance in parallel with the load modeling the measurement setup. $Z_\mathrm{tl} = 50\,\Omega$ is the impedance of the line used to measure the circuit.

Instead, we estimated the coupling capacitances using a microwave simulation software. The recipe we used is given in Appendix D. The estimated capacitances are respectively $C_\mathrm{c} = (102 \pm 1)\,\mathrm{fF}$, $C_\mathrm{c,i} = (58 \pm 1)\,\mathrm{fF}$ and $C_\mathrm{c,o} = (101 \pm 1)\,\mathrm{fF}$. Then, the complex reflection coefficient induced by the pads can be estimated using:

$$r(\omega) = \frac{Z(\omega) - Z_\mathrm{C}}{Z(\omega) + Z_\mathrm{C}} \tag{5.14}$$

[c]We recall that the circuit parameters are effective, the tilde means that the capacitance and the inductance are respectively divided and multiplied by two compared to the real parameters, see Section 3.2.1

Since $Z_{\mathrm{tl}} \ll 1/\omega C_{\mathrm{c,o}}$ and $1/\omega C_{\mathrm{c}}$ for all the measured resonant modes we have:

$$Z(\omega) \simeq \frac{1}{i\omega\left(C_{\mathrm{c,i}} + C_{\mathrm{c}}\right)} \tag{5.15}$$

Therefore, the dissipation induced by the measurement line is neglected and the modulus of the reflection coefficient is unitary. However the capacitances induce a phase shift, taking the imaginary and real part of Eq.5.14 yields:

$$\theta(\omega) = -\arctan\left(\frac{2\omega Z_{\mathrm{C}}\left(C_{\mathrm{c}} + C_{\mathrm{c,i}}\right)}{1 - \left[Z_{\mathrm{C}}\left(C_{\mathrm{c}} + C_{\mathrm{c,i}}\right)\right]^2}\right) \tag{5.16}$$

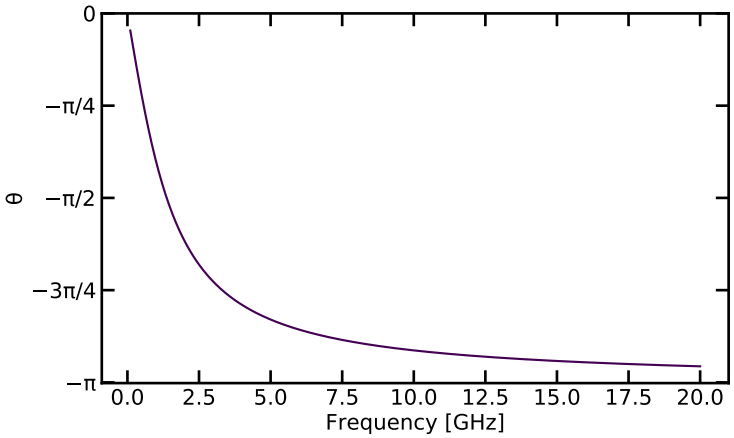

Figure 5.6 – Phase shift induced by the capacitive pad. At low frequency the phase goes to zero since Z diverges. In the opposite case the phase goes to $-\pi$ since Z goes to zero.

To estimate how the phase varies with frequency we make the hypothesis that the chain impedance is about $2\,\mathrm{k}\Omega$ (this will be verified by the dispersion relation fit). In addition, the frequency dependance of the chain impedance is neglected. With these assumptions the phase goes to zero at low frequency and tends to $-\pi$ for frequencies higher that $5\,\mathrm{GHz}$ (Fig.5.6). This can be explained by the fact that at low frequency the capacitances behave as an open while it is a shunt at high frequency. Because of that, it is hard to find a simple expression for the wave vectors. However, we verified that the dispersion relation fit was more accurate when considering the last site as an open. It may seem paradoxical since the phase goes rapidly to $-\pi$, corresponding to a shunt to the ground. This is probably because the slope of the dispersion relation is bigger at low frequency. Hence, the low frequency modes are more affected by the boundary conditions (the frequency shift is larger).

In addition, the first site capacitance $\tilde{C}_{\mathrm{g}}$ has to be small for the characteristic impedance of the chain to be in the kilo ohm range. Therefore, this site can also be seen as an open. By using 3.39 for the first and last site we end up with:

$$k_n = \frac{\pi}{N} n \tag{5.17}$$

Chain parameters

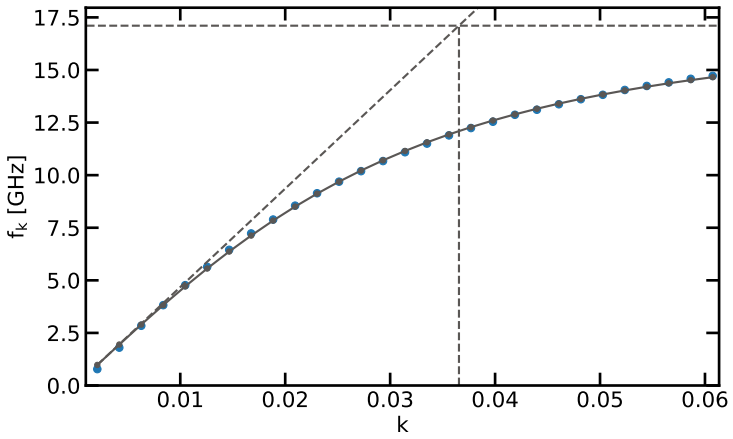

Figure 5.7 – Dispersion relation for sample B. Blue dots are data, gray dots results from the fit. The horizontal dashed line is the plasma frequency, the vertical one is $1/l_c$ and the linear one shows where the modes are TEM.

Now that the mode indexes have been linked to their wave vectors we can fit the dispersion relation of the chain using Eq.3.34. The result of the fit performed on the data of Fig.5.4 is shown in Fig.5.7. From that last we estimated $v_\varphi = (468 \pm 4)\,\mathrm{GHz}$ and $l_c = (27.4 \pm 0.2)$. Thus, modes having a wavelength shorter than 27 sites will suffer from the inter-sites Coulomb screening. The size of a site is $a = 2\,\mu\mathrm{m}$, which gives a phase velocity of $v_\varphi a = 0.02c$, where c is the speed of light in vacuum. The phase velocity is two orders of magnitude smaller than this latter. This is because of the large inductance of the chain.

To find the circuit parameters we need to fix one of them since the fit gives access to two parameters (the slope of the curve at small k and the value of the plasma frequency) and that three are needed to describe the circuit. The one we choose is the junction capacitance. This capacitance can be accurately estimated from the junction area. As when have seen in Section 4.3.2, these two are related via $C = 45\,\mathrm{fF}\,\mu\mathrm{m}^{-2}$. Since the area of the chain junctions is $3.2\,\mu\mathrm{m}^2$ we find $\tilde{C} = 72\,\mathrm{fF}$. Therefore the two other circuit parameters are $\tilde{C}_g = (96 \pm 2)\,\mathrm{aF}$ and $\tilde{L} = (1.2 \pm 0.1)\,\mathrm{nH}$. From these three circuit parameters we estimate the plasma frequency to be $\omega_p = (17 \pm 1)\,\mathrm{GHz}$ and the characteristic impedance in the TEM regime $\tilde{Z}_C = (3.5 \pm 0.1)\,\mathrm{k}\Omega$.

It is worth noting than the E_J/E_c ratio of the chain is above 450 for all the measured chains. Therefore, they are, indeed, almost linear [114]. Moreover, the circuit parameters estimations enable us to validate the assumptions we did to find the link between the wave vectors and the mode indexes since $\tilde{Z}_C$ is in the kilo ohms range. The chain parameters of sample A, B and C can be found in 5.1.From this table we can note that the chain fabrication process is reproducible since the scatter in the parameters is low.

Table 5.1 – Chain parameters for sample A, B and C.

Sample	A	B	C
av_φ/c [%]	(1.89 ± 0.02)	(1.96 ± 0.01)	(2.01 ± 0.03)
l_c	(27.7 ± 0.3)	(27.3 ± 0.2)	(28.3 ± 0.4)
$\tilde{C}$ [fF]	72	72	72
$\tilde{C}_g$ [aF]	(94 ± 2)	(96 ± 2)	(91 ± 2)
$\tilde{L}$ [nH]	(1.3 ± 0.1)	(1.2 ± 0.1)	(1.2 ± 0.1)
ω_p [GHz]	(16 ± 1)	(17 ± 1)	(17 ± 1)
$\tilde{Z}_c$ [kΩ]	(3.7 ± 0.1)	(3.5 ± 0.1)	(3.7 ± 0.1)

5.1.4 Phase shifts

Now that the chain parameters are known we will estimate those of the nonlinear junctions. For that, two kinds of relative phase shifts will be measured. The first one is the Capacitance relative phase shift that will be used to measure the nonlinear junction capacitance. Once this is done the Even-Odd relative phase shift will be measured to estimate the nonlinear junction renormalized inductance. We recall that these notions are introduced in Section 3.5.

Estimation of the nonlinear junction capacitance

The capacitance relative phase shift $\delta\theta^C$ is the phase shift introduced by a capacitance at one extremity of the chain while the other is grounded. However, the boundary condition induced by the capacitive pads is more complex than a shunt to ground. Nevertheless, this pad will have a negligible influence on $\delta\theta^C$. This can be proven using numerical diagonalization (see Appendix F.1).

To obtain $\delta\theta^C$ the nonlinear junction should behave as a capacitance. That can be done using a very high power drive to probe the system. Despite the lack of a theoretical model in such a regime it can be understood from hand-waving arguments. An increase in the probe power will lead to an increase in the effective population (the system is out of equilibrium) of the circuit modes. Thus, phase fluctuations will also increase. If the fluctuations are such that phase jumps at the nonlinear junction level become non-negligible then $\langle \cos \hat{\phi}_0 \rangle \sim 0$ and the effective inductance will be infinite. Therefore, in such a regime the nonlinear junction behaves as a capacitance. This effect has also been measured in the case of a Transmon qubit coupled to a cavity mode [115].

Figure 5.8 shows the evolution of microwave transmission for several different probe powers. At low power, we recover the transmission shown in Fig.5.2. When the probe power increases the even mode frequencies do not change. On the other hand, the odd modes shift to lower frequencies. At high power all the frequencies of the odd modes are lower than the even ones. Therefore, the relative phase shift is a negative function of the frequency. This is signaling that the nonlinear junction behaves as

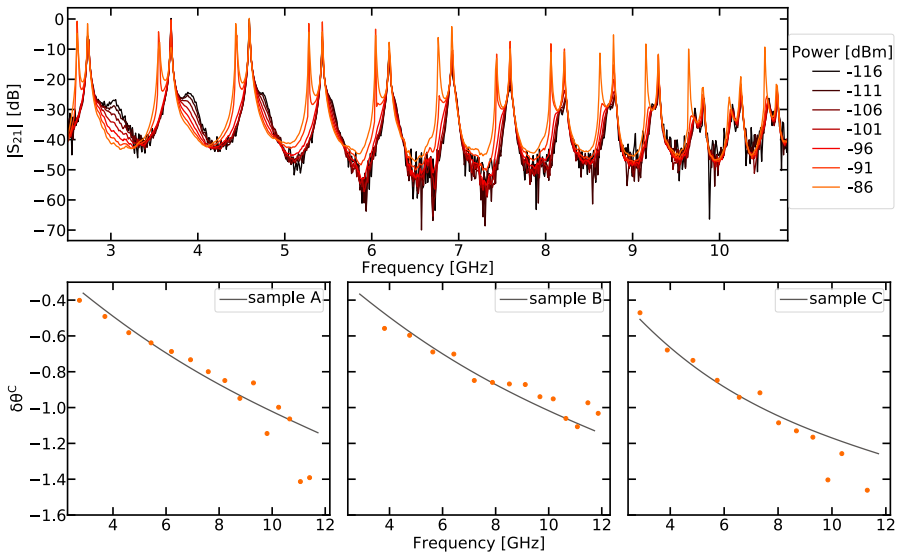

Figure 5.8 – **Upper part**. Transmission $|S_{21}|$ as a function of the frequency and of the probe power for sample A. The even modes are not affected while the odd modes shifts to lower frequency, signaling that the nonlinear junction behaves as a capacitance. **Lower part.** Capacitance relative phase shifts as a function of the frequency for the three samples. The dots are extracted from the positions of the resonance peaks while the gray lines are the result from the fits.

a capacitance when probed at high power (see the discussion on the effective model in Section 5.1.2). The resonant peaks are then fitted using Eq.5.3. From the fit we can extract the even and odd mode resonant frequencies and compute the capacitance relative splitting using Eq.3.144. This relative phase shift is then fitted using the result of Section 3.2.3:

$$\delta\theta^{\mathrm{C}}(\omega) = \arctan\left(\frac{\lambda^{\mathrm{C}}(\omega)-1}{\lambda^{\mathrm{C}}(\omega)+1}\sqrt{\left[\frac{4\tilde{C}}{\tilde{C}_g}+1\right]\left[\left(\frac{\omega_{\mathrm{p}}}{\omega}\right)^2-1\right]}\right) \tag{5.18}$$

$$\lambda^{\mathrm{C}}(\omega) = 1 - \frac{\omega^2\tilde{L}\left(C_{\mathrm{J}}+\tilde{C}_{\mathrm{g}}\right)}{1-\omega^2\tilde{L}\tilde{C}} \tag{5.19}$$

Where the chain parameters are taken from the dispersion relation fit and C_{J} is the nonlinear junction capacitance. From the fit we estimate this latter to be (5.8 ± 0.5) fF, (5.7 ± 0.5) fF and (8.2 ± 0.4) fF for sample A, B and C.

Estimation of the renormalized Josephson Energy

Once the non linear junction capacitance is estimated, only the renormalized inductance remains unknown. It can be estimated using the same recipe that for the capacitance but in a different regime of phase fluctuations. Because we want to measure the renormalization of the nonlinear junction in its ground state we probe the circuit in the low power regime. In other word, we probe the circuit at a power for which the resonant frequencies are not power dependent. Then the resonant peaks are fitted using Equation 5.3. The results of the fit is shown in Figure 5.9 for three double peaks

of sample A.

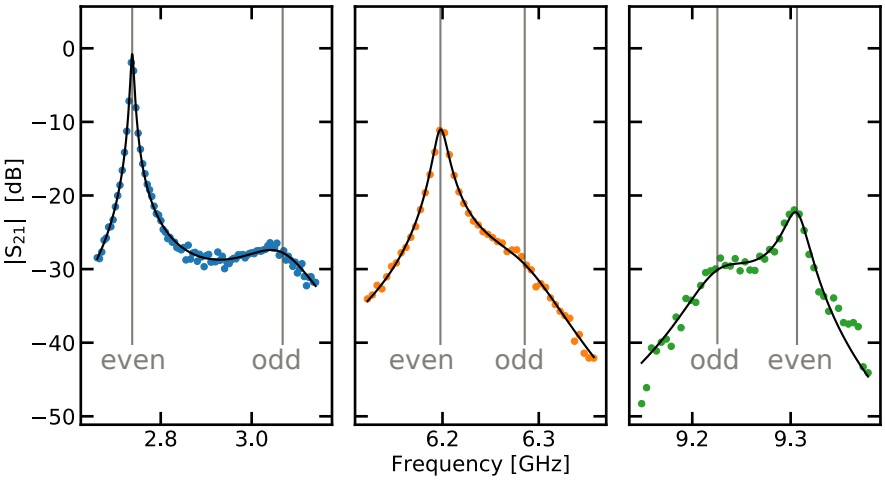

Figure 5.9 – Transmission $|S_{21}|$ as a function of the frequency for three even-odd modes. The dots are the measured data while the black lines are the results of the fit. From the fit we estimate the frequency of the even and odd modes.

From these fits the even and odd frequencies can be estimated and we can compute the Even-Odd relative phase shift. This relative phase shift is then fitted using Equation 5.18, replacing λ^{C} by $\lambda^{\mathrm{e/o}}$:

$$\lambda^{\mathrm{e/o}}(\omega) = 1 + \frac{\tilde{L}}{L_{\mathrm{J}}^{\star}} \frac{1 - \omega^2 L_{\mathrm{J}}^{\star}\left(C_{\mathrm{J}} + \tilde{C}_{\mathrm{g}}\right)}{1 - \omega^2 \tilde{L}\tilde{C}} \tag{5.20}$$

The result of the fit is shown in Figure 5.10 for sample A, the only fitting parameter is the renormalized inductance. From the fit we can directly infer the nonlinear junction renormalized frequency. This is given by the frequency at which the relative phase shift is equal to zero (see Section 3.5.2). For instance, this is about 7 GHz for this sample.

For sample A, B and C we find the renormalized inductance to be (92.9 ± 7.4), (55.0 ± 2.4) and (29.5 ± 1.3) nH. It translates to a Josephson energy of (1.76 ± 0.14), (2.97 ± 0.13) and (5.54 ± 0.24) GHz.

To see the effect of vacuum fluctuations, we compare $E_{\mathrm{J}}^{\star}$ to the bare Josephson energy of the nonlinear junction, which was obtained as follows. We fabricated many nominally identical Josephson junctions on the same chip and measured their room temperature resistances. The expected bare Josephson energy of the nonlinear Josephson junction $E_{\mathrm{J,AB}}$ was then inferred using the Ambegaokar-Baratoff law (see Section 4.3.2). We find respectively (3.7 ± 0.2), (5.8 ± 0.3) and (6.8 ± 0.5) GHz for sample A, B and C. Therefore, a systematic shift is observed between this energy and the renormalized one we inferred from $|S_{21}|$ measurements, a shift that is more pronounced for sample A that shows a high nonlinearity (it has the smallest $E_{\mathrm{J,AB}}/E_{\mathrm{C}}$ ratio). This points towards a large renormalization induced by the strong zero-point phase fluctuations.

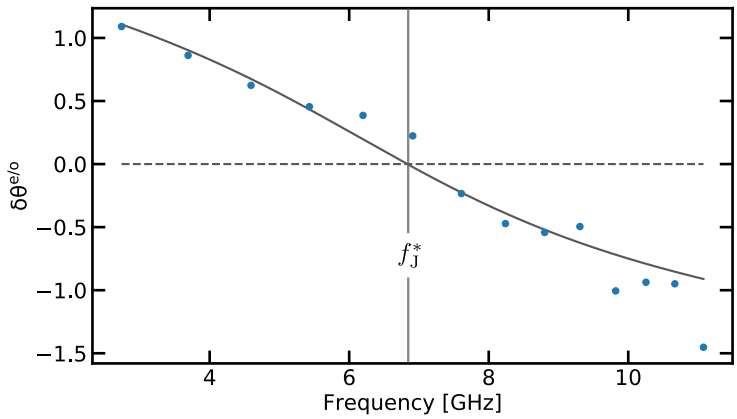

Figure 5.10 – Even-Odd relative phase shift as a function of the frequency for sample A. The dots result from the double peaks fits while the gray line is the Even-Odd relative phase shift fit. It is equal to zero at the nonlinear junction renormalized frequency $f_J^\star$.

5.1.5 Renormalization as a function of temperature

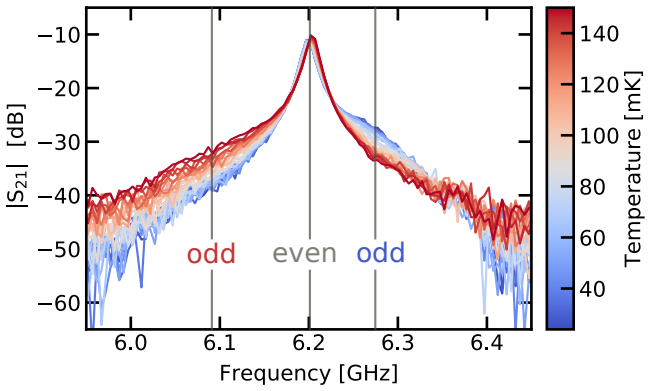

Figure 5.11 – Zoom on an even–odd pair of transmission peaks for sample A at temperature ranging from 24 to 150 mK. The even mode (gray) does not move while the odd mode (blue is at 25 mK, red at 130 mK) shifts down in frequency when warming up, showing a downward renormalization of the junction frequency.

The designed circuits seems to exhibit strong zero-point fluctuation. We will now see how these fluctuations evolve with temperature. Then we will check if the SCHA can quantitatively explain the magnitude of these fluctuations.

The temperature of the circuit is regulated via the control electronics presented in Section 4.2. To illustrate how the renormalized frequency evolves with temperature we plotted an even-odd transmission peaks for sample A for temperatures ranging from 24 to 150mK (Figure 5.11). At low temperature the Even-Odd relative phase shift is positive. Therefore, the renormalized frequency is higher than this peaks. When warming up the even mode does not move while the odd mode shifts to lower frequency, signaling that the frequency renormalization is increasing. This is expected since the

modes population, and hence the phase fluctuations, increases with temperature. This is reminiscent of what was happening when the probe power was increased.

In order to be more quantitative we applied the same recipe than before for different temperatures and for the three samples (extra Figures can be found in Appendix F.2 and F.3). After that we fitted the renormalized frequency as a function of the temperature letting the nonlinear junction Josephson energy, labeled $E_{\mathrm{J,\,th}}$ as a fitting parameter. We recall that the renormalized frequency is given by:

$$f^{\star}_{\mathrm{J,exp/th}}\left(T\right) = \sqrt{2E^{\star}_{\mathrm{J,exp/th}}\left(T\right)E_{\mathrm{C}}} \tag{5.21}$$

where $E^{\star}_{\mathrm{J,exp}}$ is given by the relative phase shift, $E^{\star}_{\mathrm{J,th}}$ results from Eq.3.106 using $E_{\mathrm{J,\,th}}$ as a free parameter and E_{C} as been measured in Section 5.1.4. The resulting plots are shown in Fig.5.12.

As expected, the renormalized frequencies are decreasing when warming up since the population of the modes and therefore the nonlinear junction fluctuations increase. This is clear in right panel of Fig.5.12 where we plotted these fluctuations using:

$$\langle\hat{\phi}_0^2\rangle\left(T\right)_{\mathrm{exp/th}} = 2\ln\left(\frac{E^{\star}_{\mathrm{J,\,exp/th}}\left(T\right)}{E_{\mathrm{J,\,th}}}\right) \tag{5.22}$$

This increase is more important for sample A since its frequency is lower. Hence, the nonlinear junction is coupled to the lower modes which are more sensitive to the temperature (see Section 3.4.4 and especially Figure 3.18). In order to show more clearly the influence of the ZPF we also plotted what would be the temperature evolution of the renormalized frequency without the quantum part of the fluctuations. To do so, we computed the junction fluctuations using:

$$\langle\hat{\phi}_0^2\rangle\left(T\right)_{\mathrm{no\ ZPF}} = \sum_{k=0}^{N}\frac{|\xi_{0,k}|^2}{2}n_k \tag{5.23}$$

This expression is the same than the one used to compute the SCHA but without the $\frac{1}{2}$ factor accounting for quantum fluctuations. They are then inserted in Eq.3.106 to compute the renormalized Josephson energy and in Eq.5.21 to estimate the renormalized frequency. The resulting frequencies are the dashed lines of Fig.5.12 We can see that the purely quantum part of the frequency renormalization is about 3 GHz for sample A.

All the nonlinear junction estimated parameters are shown in Tab.5.2. The agreement between the theoretical Josephson energy and the one inferred from Ambegaokar–Baratoff law is good for sample A and B. This is not the case for sample C. This is likely to be because the resonant frequency of this junction is outside of the measurement bandwidth. Therefore the estimation of the frequency seems to suffer from a systematic error. The SCHA can describe the evolution of the frequency with respect to temperature. Nevertheless, we should keep in mind that above 80mK (plus or minus 10mK) this comparison suffers from several limitations. First, when warming up the odd modes broadenings drastically increase (an explanation will be given in Chapter 6). Therefore, the fit of the peaks starts to become difficult and so does the accuracy of the extracted even-odd frequencies. Second, in this temperature range the phase fluctuations increase sharply (at least for sample A and B, see the right panel of Fig.5.12). Hence, the SCHA reaches its limit of validity since $\langle\phi_0^2\rangle$ goes way beyond

Table 5.2 – Junction parameters for sample A, B and C. C_J is the capacitance. E_C is the corresponding charging energy. $E^\star_{J,exp}$ is the renormalized Josephson energy measured from the transmited power. $E_{J,AB}$ is the Josephson energy inferred from the Ambegaokar–Baratoff law. $E_{J,th}$ is the one estimated from the renormalised frequency fits.

Sample	A	B	C
C_J [fF]	(5.8 ± 0.5)	(5.7 ± 0.5)	(8.2 ± 0.4)
E_C[GHz]	(13 ± 2)	(13 ± 2)	(9 ± 1)
$E^\star_{J,exp}$ [GHz]	(1.8 ± 0.2)	(3.0 ± 0.2)	(5.5 ± 0.3)
$E_{J,AB}$ [GHz]	(3.7 ± 0.2)	(5.8 ± 0.3)	(6.8 ± 0.5)
$E_{J,th}$ [GHz]	3.6	5.3	8.0
$Z^\star_J$ [kΩ]	2.8	2.3	1.5
Nonlinearity $E_{J,th}/E_C$	0.28	0.41	0.89
Renormalization $E^\star_{J,exp}/E_{J,th}$	0.50	0.57	0.69

unity (Section 3.1.1). Moreover, until now we considered that the circuit was at the temperature indicated by the control electronics. However, the measured circuits are also coupled to external radiations due to an imperfect noise filtering. Therefore, the temperature of the circuit is most likely higher than the measured one [116–119]. In the current state of our knowledge our model does not allow us to extract this extra contribution since a clear disagreement appears between the experimental data and the theoretical model (see Appendix F.4).

5.1.6 How many modes contribute ?

The SCHA can explain the renormalization of the nonlinear junction. We will now use the result from the previous sections to study the nonlinear junction response function. From this response function we can extract both the damped frequency $\omega^\star_d$ of the nonlinear junction and its full width half maximum (FWHM). Using this approach we will be able to see how many modes contribute to the renormalization and how much the junction is damped by its environment.

In Section 3.5.2 we have seen that the derivative of the Even-Odd relative phase shift is linked to the dissipative part of the nonlinear junction response function via Eq.3.164. To obtain the response function, or equivalently the antisymmetric part of the noise spectral density since the two are equal up to $\hbar$ (see Eq.3.123), we can take the result of the Even-Odd relative phase shift fit at the lowest fridge temperature. Then, we apply the transformation given by Eq.3.164 to the numerical derivative of the fit. The result is shown in the left part of Fig.5.13 (plain line). Because we extracted all the circuits parameters we can also directly compute the nonlinear junction response function using Eq.3.124 in the thermodynamic limit (we take 10000 sites). The resulting response functions are plotted in dashed lines. These two quantities

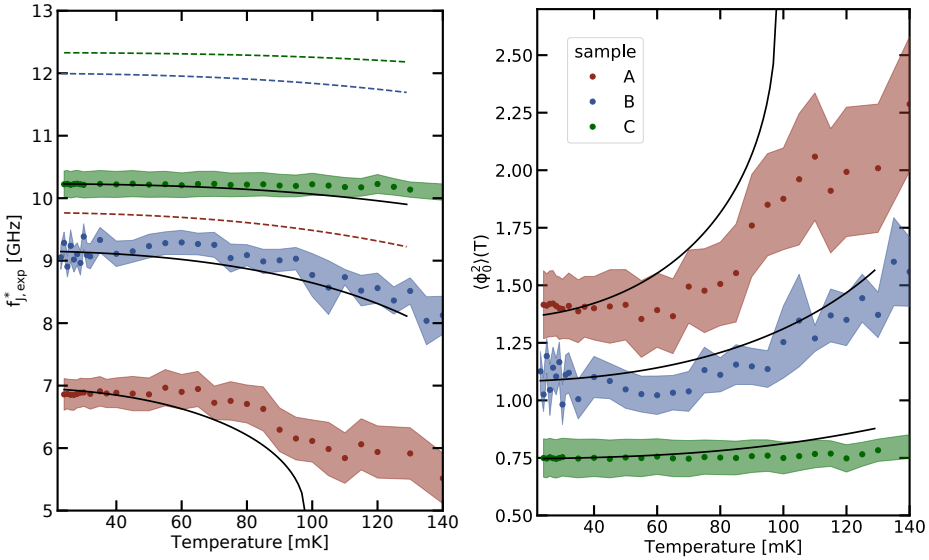

Figure 5.12 – **Left.**Renormalized frequency of the nonlinear junction as a function of the temperature for sample A (red), B (blue) and C (green). The dots are the values extracted from the transmission measurements, the shaded areas are the corresponding error bars. The black lines are the result from the fit using the SCHA while the dashed lines represent what would be the temperature evolution of these frequencies if ZPF were omitted from $\langle\phi_0^2\rangle$, using the same values of $E_{\mathrm{J,th}}$. **Right.** The corresponding phase fluctuations. The latter are stronger in sample A, which is associated to a smaller ratio $E_{\mathrm{J,th}}/E_{\mathrm{c}}$ (larger nonlinearity).

have the same qualitative behavior, the main discrepancies appear at higher frequencies since relation 3.164 is valid for frequencies well below the chain plasma frequency. Both the damped frequency of the nonlinear junction and the FWHM are extracted from the relative phase shift derivative and the response function. They are labeled respectively $\omega^{\star}_{\mathrm{r},\delta\theta}$, $\omega^{\star}_{\mathrm{r},\phi}$, $\gamma_{\delta\theta}$ and γ_{ϕ} and their estimations are reported in Tab.5.3. The order of magnitude of these two parameters estimated from the two techniques are the same.

In addition, we also plotted the response function of the nonlinear junction for the actual number of junctions (meaning 1500), the result is the dots in the left panel of Fig.5.13. We can see that it does not completely match the response function obtained in the thermodynamic regime. This is showing that the number of junction in the chain is too low so that it acts strictly as a dissipative (thermodynamic) bath.

The shift between the renormalized frequency estimated from the SCHA $\omega^{\star}_{\mathrm{J}}$ (vertical lines in the left panel of Fig.5.13) and the damped frequency $\omega^{\star}_{\mathrm{d}}$ (maximum of the response function) increases from sample C to A. This can be explain from the fact that the damping increases from sample C to A (see Tab.5.3). Hence, from our formalism we can distinguish the renormalization coming from the ZPF, given by $\omega_{\mathrm{J}} - \omega^{\star}_{\mathrm{J}}$, and the one coming from the coupling to a thermodynamic bath, given by $\omega^{\star}_{\mathrm{d}} - \omega^{\star}_{\mathrm{J}}$. To my knowledge, such a distinction has never been made before in the field, except in the context of the mode splitting between a Transmon and a resonator mode [120].

In Tab.5.3 we also reported the damping rate resulting from the RLC toy model, meaning $\gamma_{RC} = 1/\tilde{Z}_{\mathrm{C}}C_{\mathrm{J}}$. This formula overestimates the actual damping. This is coming from the fact that the actual characteristic impedance of the chain increases with

frequency (Eq.3.38). As a result, the nonlinear junction "sees" an effective impedance bigger than $\tilde{Z}_C$ and therefore the damping rate is lower. From the value of FWHM and damped frequencies extracted we can see that the nonlinear junctions are in the so-called deep strong coupling regime since the ratio between the two is about one [52, 53] for the three samples. Note that this regime has been defined in the context of the spin boson model and very little is known about such a regime for the BSG model. Nevertheless, a recent paper shows that a mapping exists between the two systems [70]. Therefore, we can safely say that reaching such a regime is an important step toward the observation of phenomena analoguous to the predictions made in such a regime for the spin boson Hamiltonian [55, 72–75]

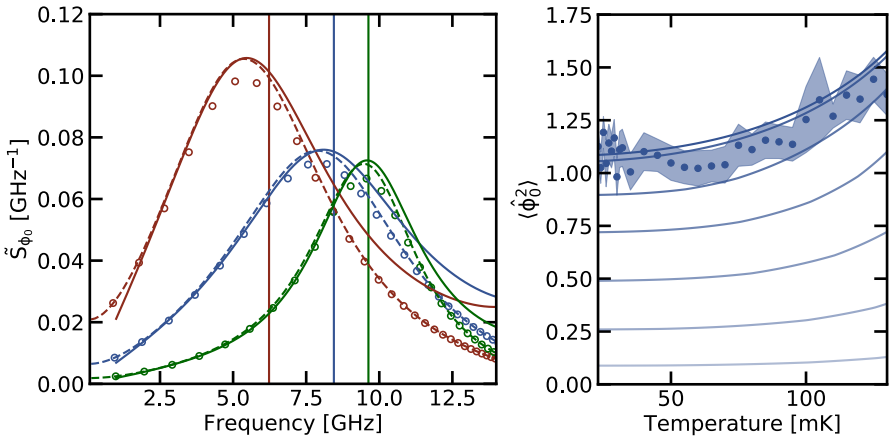

Figure 5.13 – **Left.** Antisymmetric part of the noise spectral density as a function of the frequency. The color code is the same than for Fig.5.12. The plain lines are the result of the Even-Odd relative phase shift fit at the lowest fridge temperature after applying the transformation given by Eq.3.164 and 3.165. The dashed line is the response function given by Eq.3.124 in the thermodynamic limit. The dot are the result of the same equation but for the actual number of junctions. The vertical line denote the position of $\omega_J^\star$. The shift of the damped frequency $\omega_d^\star$ with respect to $\omega_J^\star$ increases from almost zero to 1 GHz from sample C to A. **Right.** Total phase fluctuations across the nonlinear Josephson junction in sample B (blue dots), taking into account in our model the largest contributions, ranging from one mode (light blue) to all the modes (dark blue).

Finally we will see how many modes have to be considered in order to properly account for the fluctuations across the junction for sample B. The left panel of Fig.3.18 shows than only the modes close to the damped frequency $\omega_d^\star$ contribute. From this observation we can plot again the result of Fig.5.12 but with the main contributions to the total fluctuations only. That has been done in the right panel of Fig.5.13. When increasing the number of contributing modes, the total phase fluctuations converge to the result obtained while considering all the modes (it corresponds to the highest one in the graph). From this plot we see that the result obtained with the 30 largest contributions does not differ so much from the total contributions. That will be our criteria to say that about 30 modes are involved in the renormalization of the nonlinear junction.

Consequently, the designed circuits constitute a complex many body problem displaying a non perturbative renormalization of the Josephson Energy, and therefore

Table 5.3 – $Z_{\mathrm{J}}^{\star}$ is the characteristic impedance of the nonlinear junction within the SCHA. $\gamma_{\delta\theta}$ is the FWHM extracted from the relative phase shift. γ_{ϕ} is the one given by the response function. γ_{RC} is given by $1/\tilde{Z}_{\mathrm{C}}C_{\mathrm{J}}$. $\omega_{J}^{\star}$ is the renormalized frequency of the nonlinear junction at the lowest fridge temperature. $\omega_{\mathrm{d}}^{\star}$ is the damped one.

Sample	A	B	C
Damping regime $Z_{\mathrm{J}}^{\star}/\tilde{Z}_{\mathrm{C}}$	0.75	0.65	0.41
$\gamma_{\delta\theta}$ [GHz]	6.8	7.7	4.6
γ_{ϕ} [GHz]	6.3	6.9	4.3
γ_{RC} [GHz]	7.4	7.9	5.3
$\omega_{\mathrm{d},\phi}^{\star}$ [GHz]	5.33	7.91	9.46
$\omega_{\mathrm{d},\delta\theta}^{\star}$ [GHz]	5.46	8.10	9.58
$\omega_{\mathrm{J}}^{\star}$ [GHz]	6.23	8.45	9.63
$\gamma_{\phi}/\omega_{\mathrm{d},\phi}^{\star}$	1.2	0.9	0.45

of its resonant frequency. The largest renormalization was obtained for sample A for which the $E_{\mathrm{J}}^{\star}/E_{\mathrm{J}}$ ratio was about 0.5. Regarding the resonant frequency it converts to a 0.7 renormalization (neglecting the one coming from the damping). A renormalization with a similar order of magnitude was obtained in other experiments using different circuits. In 2016, P.Forn Diaz and coworkers [50] measured a frequency renormalization for a flux qubit coupled to a waveguide of the order of 0.8. The same year Yoshihara [42] and coworkers reported a renormalization of the first excited state of a flux qubit coupled to a resonator of the order of 0.3. There are two main differences between our work and these other realizations. First they use qubits or two level systems. Their circuits then belong to the spin-boson category. Second they use very different environments. In the first case, it was a $50\,\Omega$ matched waveguide. Because of that the environment modes are not resolved and its properties are hard to extract (for example the cut off frequency). In the second case, the environment was only one resonator mode and is therefore a rather different problem. Moreover this work reports a coupling between a quantum system (the nonlinear junction) and many modes since the ratio between the characteristic impedance of the nonlinear junction and the one of the chain is about unity (see Tab.5.3). Because of that the nonlinear junctions are close to the overdamped regime. As a consequence, 30 modes are non negligibly contributing to the nonlinear junction renormalization of sample B. This is a drastic increase compared to what was previously reported [59, 68, 93].

5.2 Tunable nonlinearity

In the previous section we have seen than the SCHA could explain the behavior of the Boundary Sine Gordon circuit in its ground state. Nevertheless, because we used a junction and not a SQUID we had to measure different samples to study how the

nonlinearity of the junction was impacting the circuit properties.

The reason why we did so comes from the fact that at this stage of my PhD we did not have a theoretical model to estimate phase fluctuations. Because of that we were concerned about the fact that a SQUID always contain an additional capacitance coming from the interaction between its two arms (see Section 4.3.2 of [67]). Such a parasitic capacitance would decrease the charging energy and therefore the nonlinearity of the junction. However, a large renormalization could be achieved even for moderate capacitance (see sample C).

Moreover, we observed that the odd modes broadening was much larger than the one of the even ones (see Fig.5.2), indicating that the nonlinear junction was inducing losses in these modes. Nevertheless, because of the chosen circuit geometry a careful calibration of the background transmission coming for the measurement setup is needed to accurately estimate theses losses (this is discussed in C.1).

Finally, the even-odd modes circuit was useful to access the nonlinear junction response function via the Even-Odd relative phase shift and also to understand how it was affecting the environment via the comparison of the odd and even modes quality factors (It will be discussed in more details in Chapter 6). However, the fit of the double peaks was quite challenging. In order to overcome these limitations we designed and measured a different sample

5.2.1 Sample presentation

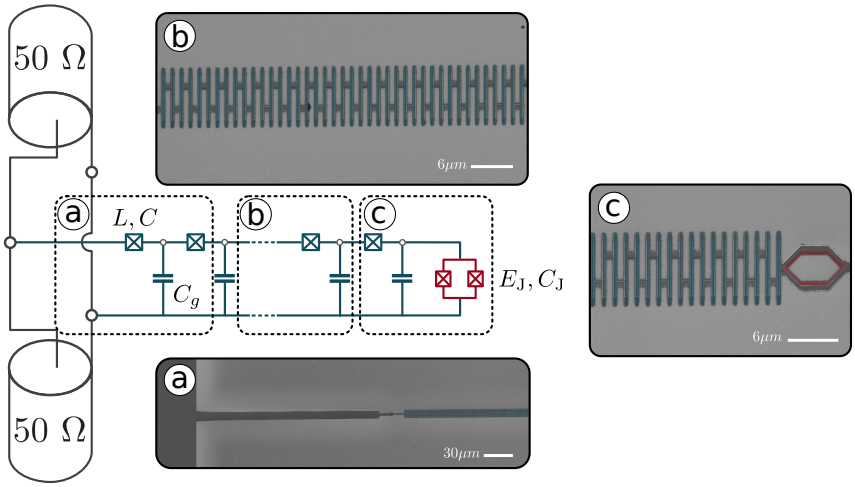

Figure 5.14 – Schematic of the measured circuit. The Josephson junction chain, depicted in blue, is characterized by its three parameters L, C and C_g. The chain is terminated by a nonlinear SQUID, depicted in red and characterized by its two parameters E_J and E_C. **a** SEM picture of the galvanic coupling between the JJ chain and the 50 Ω micro-strip feed-line. The two are coupled such that the circuit forms a hanging resonator. **b** SEM picture of the JJ chain composed of 4250 sites. **c** SEM picture of the galvanic coupling between the JJ chain and the nonlinear SQUID. The junction is grounded at its right.

The sample consists in a nonlinear SQUID that can be tuned in situ via a magnetic

flux. The relation between the Josephson energy and the magnetic flux is:

$$E_{\mathrm{J}}\left(\Phi_{\mathrm{B}}\right) = E_{\mathrm{J}}\left(0\right)\left|\cos(\pi\Phi_{\mathrm{B}}/\Phi_{\mathrm{q}})\right| \tag{5.24}$$

Therefore, at magnetic flux close to half a quantum, or equivalently for $\Phi_{\mathrm{B}}/\Phi_{\mathrm{q}}$ close to 0.5, the SQUID Josephson energy drastically decreases while the charging energy stays put. Therefore, the SQUID nonlinearity can be changed thanks to a magnetic flux. The SQUID is galvanically coupled to a Josephson junction chain, made of 4250 cells. The chain is galvanically coupled at its left to a 50 Ω micro-strip feed-line while the nonlinear SQUID is grounded at its right. Because of that the circuit can be seen as a hanging resonator, enabling us to measure in-situ the transmission background coming from the measurement setup (see Section C.1).

5.2.2 Flux tunability

In order to study the nonlinear junction we measured the transmitted power of the sample in the same way as above. However, because the latter is a SQUID we have an extra knob. Since the circuit is a hanging resonator we can use the formula C.15 of Appendix C.1.2 to fit the resonant modes of our circuit:

$$S_{21}\left(\omega\right) = \frac{Z_{\mathrm{tl}}}{Z_{\mathrm{tl}} + iX_{\mathrm{e}}} \frac{\gamma_{\mathrm{int}} + 2i\left(\omega - \omega_{\mathrm{d}}\right)}{\gamma_{\mathrm{ext}} + \gamma_{\mathrm{int}}\frac{Z_{\mathrm{tl}}+iX_{\mathrm{e}}}{Z_{\mathrm{tl}}} + 2i\left(\omega - \omega_{\mathrm{d}}\right)} \tag{5.25}$$

where Z_{tl} is the impedance of the feed-line, X_{e} is here to take care of a possible impedance mismatch between the feed-line and the measurement setup (see Appendix B of [121]), ω_{d} is the resonant frequency of the mode, γ_{int} is the internal broadening and γ_{ext} is the external one. The impedance of the designed chain is in the kilo Ohm range and the nonlinear junction is inducing loss in the modes. Hence, the ratio $\gamma_{\mathrm{ext}}/\gamma_{\mathrm{int}}$ is rather low in our circuit, especially at magnetic fluxes close to 0.5 where the SQUID is highly nonlinear. Therefore, the amplitude of the dip of transmitted power can be less than a decibel (see the lower left panel of Fig.5.15). Since the background is not flat it can be very hard to find these dips and even harder, if not impossible, to fit them. To overcome this issue we developed an original background extraction method using the flux tunability of the SQUID (Appendix C.2). Two examples of transmitted power resulting from this calibration as a function of the frequency are shown in the left part of Fig.5.15.

From the fit of these transmission dips we can extract the resonant frequencies of the circuit over a period of magnetic flux in the SQUID. The result is shown in the right panel Fig.5.15. The resonant frequencies are accurately resolved over an entire magnetic flux period and for frequencies ranging from 2 to 10 GHz despite the large internal broadening at magnetic flux close to 0.5.

5.2.3 Dispersion relation

In order to study the renormalization we need again to access the circuit parameters. As we did for the previous circuits, we will start with those of the chain. For this circuit we do not have access to even modes. Consequently, the modes, and therefore the dispersion relation is always affected by the junction. To simplify the problem we

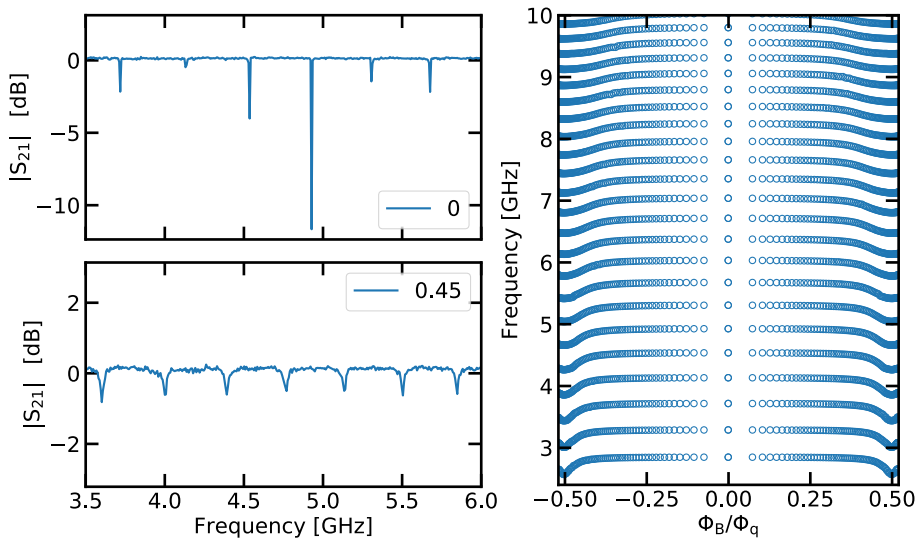

Figure 5.15 – **Upper Left**. Transmission $|S_{21}|$ as a function of the frequency at $\Phi_B/\Phi_q = 0$.**Lower Left.** Same at $\Phi_B/\Phi_q = 0.45$ **Right.** Resonant modes frequencies as a function of Φ_B/Φ_q resulting from the fit of the transmitted power.

will study the dispersion relation of the chain at $\Phi_B/\Phi_q = 0.5$. At this flux value the Josephson energy of the SQUID goes to zero (see Eq.5.24). Thus, the right boundary condition only depends on the capacitance of the nonlinear SQUID. Whatever the applied magnetic flux, the left boundary condition is a shunt to ground because of the large impedance mismatch between the micro-strip feed-line and the chain. The most accurate way to fit the dispersion relation would be to account for the wave vector shift induced by the SQUID capacitance using the following self consistent set of equations (see Section 3.2.3):

$$k_n = k_n^0 + \frac{\delta\theta_n^C}{N - \frac{1}{2}} \tag{5.26}$$

$$\omega_n = v_\varphi \sqrt{\frac{2\left(1 - \cos k_n\right)}{1 + 2\left(1 - \cos k_n\right) l_c^2}} \tag{5.27}$$

$$\delta\theta_n^C = \arctan\left(\frac{\lambda_n^C - 1}{\lambda_n^C + 1}\sqrt{\left[\frac{4C}{C_g} + 1\right]\left[\left(\frac{\omega_p}{\omega_n}\right)^2 - 1\right]}\right) \tag{5.28}$$

$$\lambda_n^C = 1 - \frac{\omega_n^2 L\left(C_J + C_g\right)}{1 - \omega_n^2 LC} \tag{5.29}$$

where k_n^0 is the bare wave vector of mode n, given by $k_n^0 = (n + \frac{1}{2})/(N - \frac{1}{2})$. However, when doing so we found that the SQUID capacitance uncertainty was bigger than its estimated value. Therefore, the SQUID capacitance is not a relevant parameter for the dispersion relation. The best fit, shown in Fig.5.16, was obtained while considering that the SQUID was shorted, and thus, that the wave-vectors were given by $k_n = \frac{n}{N}$. Nevertheless, by assuming the SQUID to be an open we found the same estimated

parameters with a deviation of the order on the percent. The extracted parameters are reported in Tab.5.4. The characteristic impedance of the chain is about half of the previous one. This is expected since the junction size is the same. The one half factor comes from the fact that the chain coupled to the SQUID is the physical one and not the one coming from the even-odd decoupling. We chose this impedance value so that the external broadening, and thus the $\gamma_{\text{ext}}/\gamma_{\text{int}}$ ratio, is not too small while keeping the phase fluctuations strong.

The external broadening can indeed be inferred from the Fabry-Pérot model. The amplitude of the phase waves in the circuit is exponentially decaying with a characteristic time τ_{D} because of the coupling with to measurement setup[d]. Hence after a round trip the cavity energy decreases by a factor [122]:

$$e^{-T_{\text{r}}/\tau_{\text{D}}} = R = \left|\frac{Z_{\text{tl}} - Z_{\text{C}}}{Z_{\text{tl}} + Z_{\text{C}}}\right|^2 \tag{5.30}$$

where T_{r} is the round trip time defined in Section 3.1.2 and Z_{C} is the chain impedance far from its plasma frequency. Hence, the external broadening is given by:

$$\gamma_{\text{ext}} = \frac{1}{\tau_{\text{D}}} = \frac{2}{T_{\text{r}}} \ln\left|\frac{Z_{\text{tl}} + Z_{\text{C}}}{Z_{\text{tl}} - Z_{\text{C}}}\right| \tag{5.31}$$

This equation can be easily interpreted: if the round trip time increases the circuit excitations will take a more time to come back to the coupling point, and hence, the decay time will increase. When increasing the chain impedance, the phase velocity decreases[e], therefore, the round trip time increases (see Eq.3.44). Moreover, if the chain impedance increases, the circuit is less coupled to the measurement setup (R is lowered) and the decay probability decreases. In conclusion, γ_{ext} grows inversely with the chain impedance. On the other hand, we saw that the phase fluctuations of the nonlinear junction, and hence the losses induced by the latter, increase with the chain impedance. Hence, the ratio $\gamma_{\text{ext}}/\gamma_{\text{int}}$ drops with the chain impedance. As this ratio gives the depth of the transmission dips we had to chose a impedance value where nonlinear effects where maximized while keeping $\gamma_{\text{ext}}/\gamma_{\text{int}}$ not to low so that the dips could be measured.

5.2.4 Josephson relative phase shift

The chain parameters being known we are going to estimate those of the SQUID. The technique used is again to measure a relative phase shift. However, due to the design chosen, we will not be able to measure the one between the even and odd modes but what we called the Josephson relative phase shift. As seen in Section 3.5 this quantity is defined as:

$$\delta\theta^{\text{J}}(\omega) = \theta^{\text{JC}}(\omega) - \theta^{\text{C}}(\omega) \tag{5.32}$$

Where θ^{JC} and θ^{C} are respectively the phase shift induced by a Josephson junction, or a SQUID in our case, and the one induced by a capacitance. This quantity is easily

[d] We can neglect the losses induced by the nonlinear junction for the estimation of the external broadening.

[e] We recall that the phase velocity is given by $v_\varphi = 1/\sqrt{LC_{\text{g}}}$, therefore, to increase the chain impedance we saw that we have to boost L. Hence, the phase velocity diminishes.

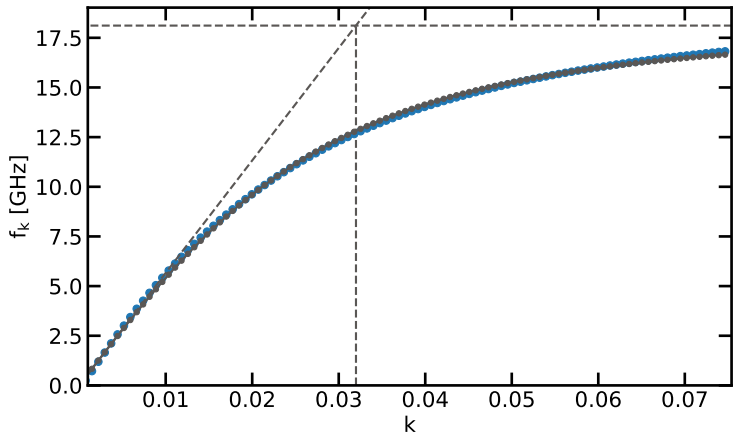

Figure 5.16 – Dispersion relation. Blue dots are data, grey dots results from the fit. The horizontal dashed line is the plasma frequency, the vertical one is $1/l_c$ and the linear one shows where the modes are TEM.

Table 5.4 – Chain parameters for the hanging resonator. C, C_g, L and Z_C stand for the actual chain parameters since with this design there is no more even and odd modes.

av_φ/c [%]	(4.74 ± 0.023533)
l_c	(31.3 ± 0.2)
C [fF]	144
C_g [aF]	(147 ± 2)
L [nH]	(0.536 ± 0.002)
ω_p [GHz]	(18.12 ± 0.04)
Z_c [kΩ]	(1.914 ± 0.001)

accessible since θ^C corresponds to the case of the SQUID at half a flux quantum as we have seen in the previous Section.

Estimation of the capacitance

The problem of using directly that relative phase shift is that it will depend on both the SQUID capacitance and Josephson energy. Therefore, the fit can be rather inaccurate. To overcome this limitation we can use the fact that the Josephson relative phase shifts measured for magnetic fluxes close to zero are almost monotonous functions of the frequency (see experimental data in Fig.5.17). To understand what does it means we need to recall that, using the definitions introduced in Section 3.5, $\delta\theta^J$ can be decomposed as:

$$\delta\theta^J(\omega) = \delta\theta^{e/o}(\omega) - \delta\theta^C(\omega) \tag{5.33}$$

where $\delta\theta^{e/o}$ is the Even-Odd relative phase shift. Fig.3.19 shows that $\delta\theta^{e/o}$ is almost constant way below or above the resonant frequency of the nonlinear junction, or SQUID (especially at $E_J^\star / E_C \sim 10$, which is the order of magnitude for our SQUID at low magnetic flux as we will see). Therefore if we make the hypothesis that at low magnetic fluxes the SQUID frequency is above the measurement bandwidth we have:

$$\delta\theta^J(\omega) = -\delta\theta^C(\omega) \tag{5.34}$$

up to a constant. This quantity is a monotonous, increasing function of the frequency as we saw in Section 5.1.4. This is explaining why the experimental relative phase shifts are also a monotonous, increasing function of the frequency in the largest part of the measurement bandwidth. Hence, the relative phase shift mostly depends on the SQUID capacitance.

Therefore this capacitance will be estimatd with a good accuracy[f]. Magnetic fluxes used for the capacitance estimation are the one between -0.3 and 0.3. The result is given in Fig.5.17.

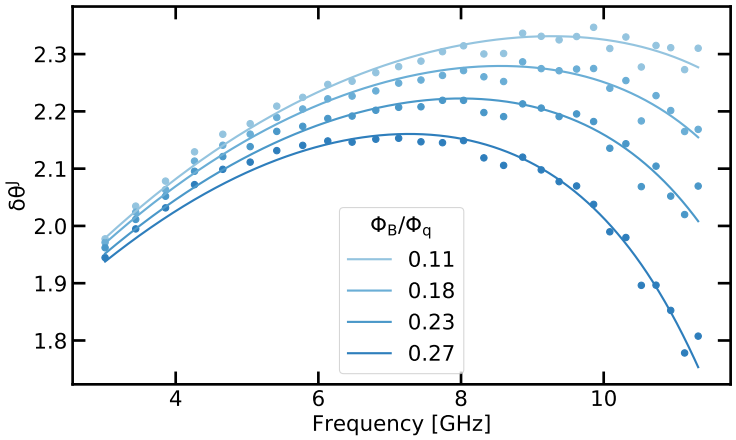

Figure 5.17 – Josephson Relative phase shift $\delta\theta^J$ versus frequency for four magnetic fluxes between 0 and 0.3. It is a positive, almost monotonously growing function of the frequency and therefore behaves as $-\delta\theta^C$ for the magnetic fluxes considered (see Fig 5.8 for comparison). Blue dots are the experimental data extracted from Fig.5.15, the plain lines are the resulting fits.

By doing so we estimated C_J for 35 flux points. The extracted value is then $C_J = (14.5 \pm 0.2)\,\text{fF}$, or conversely $E_C = (5.35 \pm 0.05)\,\text{GHz}$ where the uncertainty is given by the standard deviation of the data set. This can be compared to the capacitance expected from the area of the junctions composing the SQUID. From SEM pictures we measured a total area of $0.24\,\mu\text{m}^2$. Therefore, using the relation between the size area and the capacitance (see Section 4.3.2) we get $C_J = 11\,\text{fF}$. It is slightly lower than the value estimated from the relative phase shift measurement. This is probably because of a spurious capacitance coming from the electromagnetic environment of the SQUID.

[f]Note that the SQUID inductance is also let as a free parameter. It means that we are fitting the relative phase shift using $\delta\theta^J$ and not $\delta\theta^C$. However, since the SQUID frequency is outside the measurement bandwidth its estimation is rather inaccurate, and therefore discarded.

Estimation of the Josephson Energy

Now that the SQUID capacitance is known we can use it to fit the Josephson relative phase shift for $|\Phi_B/\Phi_q| \in [0.3, 0.5]$ with only $E_J^\star(\Phi_B)$ as a free parameter. Some examples of the resulting fits are shown in Fig.5.18. Both the SQUID capacitance and renormalized Josephson energy as a function of the magnetic flux have been estimated. Therefore, we can now study how the renormalization evolves with the magnetic flux or equivalently with the SQUID nonlinearity.

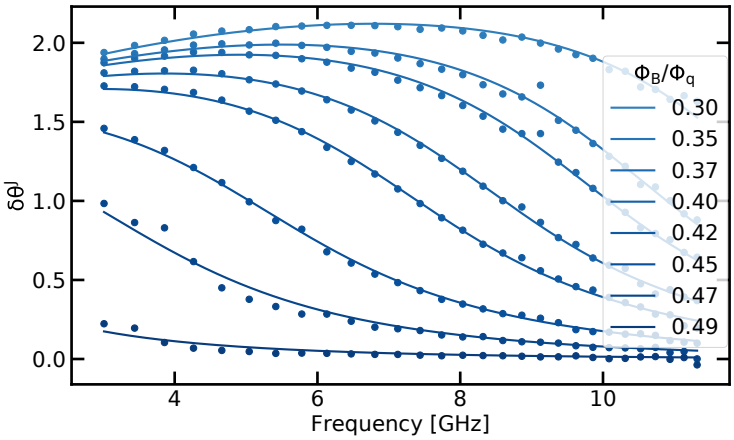

Figure 5.18 – Josephson Relative phase shift $\delta\theta^J$ versus frequency for eight magnetic fluxes between 0.3 and 0.5. They are used to estimate the nonlinear SQUID Josephson energy, and therefore its resonant frequency, as a function of the magnetic flux. Blue dots are the experimental data extracted from Fig.5.15, the plain lines are the resulting fits.

5.2.5 Renormalization with respect to the nonlinearity

We recall that using a SQUID enables us to tune the Josephson energy at fixed charging energy. The ratio of these two energies decreases, or equivalently its non linearity increases, when the magnetic flux is close to half a flux quanta. From the estimation of these two energies we can compute the renormalized frequency as:

$$f_J^\star(\Phi_B) = \sqrt{2E_J^\star(\Phi_B)\,E_C} \tag{5.35}$$

This quantity can be fitted with $E_J(\Phi_B = 0)$ as the only fitting parameter by using SCHA. The result is shown in Fig.5.19 for a temperature of 23 mK, corresponding to the one of the mixing chamber for this experiment. From the fit we estimate $E_J(\Phi_B = 0) = (27.8 \pm 0.2)$ GHz. That can be compared to the value estimated from Ambegaokar-Baratoff $E_J^{AB} = (25.8 \pm 0.5)$ GHz (the procedure is the same than for the previous samples) even if these two values are not strictly equal the SCHA gives the good order of magnitude. On Fig.5.19 we also plotted in dashed line the frequency

corresponding to:

$$f_{\mathrm{J,lin}}\left(\Phi_{\mathrm{B}}\right) = \sqrt{2E_{\mathrm{J}}^{\star}\left(\Phi_{B}\right)E_{\mathrm{C}}} \tag{5.36}$$

$$E_{\mathrm{J}}^{\star}\left(\Phi_{B}\right) = E_{\mathrm{J}}^{\star}\left(0\right)\left|\cos(\pi\Phi_{\mathrm{B}}/\Phi_{\mathrm{q}})\right| \tag{5.37}$$

This would correspond to a linear SQUID assumption and thus that no renormalization would occur. In such a case the frequency would be a linear function of the square root of the cosine of the magnetic flux. Note that in Eq.5.36 we refer to the Josephson energy as $E_{\mathrm{J}}^{\star}$. This is just to say that we take the Josephson energy at zero flux inferred from the relative phase shift. Nevertheless, for that equation we do not use the SCHA to compute the Josephson energy. As expected the data show a deviation from a linear behavior. This deviation increases with the nonlinearity.

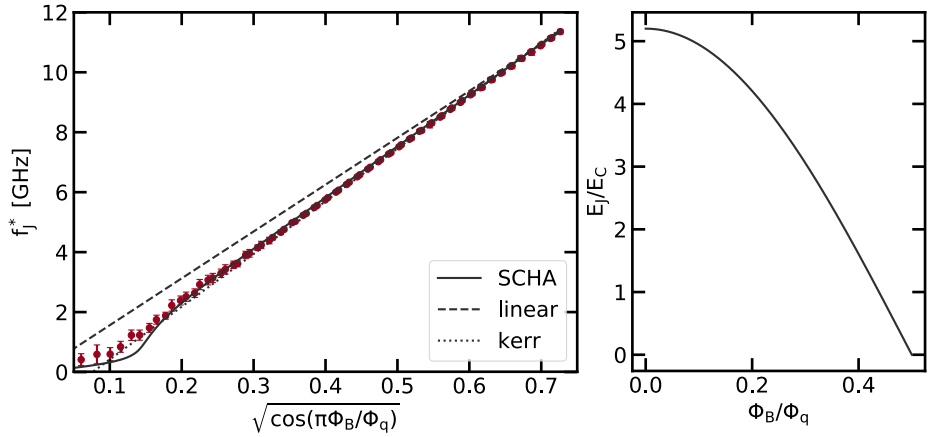

Figure 5.19 – **Left.** SQUID renormalized frequency as a function of the square root of the cosine of the magnetic flux. If the SQUID was linear its frequency would be a linear function of the latter. Red dots are the experimental data extracted from the relative phase shifts. The dashed line indicates what would be the junction frequency if it was linear. The dotted line is the result of the fit using the Kerr approximation. The plain line is the result from the fit using the SCHA. **Right.** Bare nonlinearity $E_{\mathrm{J}}/E_{\mathrm{C}}$ resulting from the fit as a function of the magnetic flux $\Phi_{\mathrm{B}}/\Phi_{\mathrm{q}}$.

In order to see if a simpler theory could describe the renormalized frequency flux dependence we also tried to fit it with a simpler model:

$$f_{\mathrm{J,kerr}} = \sqrt{2E_{\mathrm{J,kerr}}E_{\mathrm{C}}} - \frac{E_{\mathrm{C}}}{4} \tag{5.38}$$

This is the so-called Kerr shift commonly used for the Transmon qubit (see Section 3.1.1 or [30]). The resulting fit is also plotted in the left panel of Fig.5.19. We can see that the Kerr approximation seems to reproduce the SQUID frequency behavior at least as well as the SCHA. The Josephson energy extracted is $E_{\mathrm{J,kerr}} = (28.9 \pm 0.1)$ GHz. We see that the estimated energy is higher than with the SCHA and consequently the agreement with $E_{\mathrm{J,AB}}$ is worst. We can think that this is coming from a poor estimation of $E_{\mathrm{J,AB}}$. Nevertheless, the fact that $E_{\mathrm{J,kerr}}$ is larger than with the SCHA means than the renormalization estimated from the Kerr approximation is bigger than the one estimated from the SCHA. This is surprising for two

reasons: first the Kerr approximation is cruder than the SCHA since it result from the fourth order expansion of the non linearity (see Section 3.1.1) , second the Kerr approximation does not account for thermal fluctuations contrary to the SCHA and we know that the temperature boosts fluctuations.

To solve this paradox we have to recall that the Kerr approximation does not consider the damping from the chain (see 3.4.2 Fig.3.16). This damping decreases of the fluctuations. Hence, despite being intuitive [68, 93] such an approximation is not accurate for nonlinear junctions, even for Transmon, close to or in, the over-damped regime. This can be clearly seen on the right panel of Fig.5.20. On this figure we plotted the estimated phase fluctuations using:

$$\langle \hat{\phi}_0^2 \rangle = 2 \ln\left(\frac{E_\mathrm{J}}{E_\mathrm{J}^\star}\right) \tag{5.39}$$

where E_J is the value estimated from the SCHA and $E_\mathrm{J}^\star$ the values extracted either from the relative phase shift (red dots) or from a SCHA estimate (plain line). We see that both agree until the renormalization becomes to strong. This is coming from the fact that for these values the experimental data accuracy decreases and the SCHA is expected to breakdown since the fluctuations are larger than one. On this graph we also plotted the fluctuations expected for an isolated junction at T=0:

$$\langle \hat{\phi}_0^2 \rangle = \pi \frac{Z_\mathrm{J}^\star}{Z_\mathrm{q}} \tag{5.40}$$

where $Z_\mathrm{J}^\star$ is the renormalized characteristic impedance coming from the SCHA estimation. We see that it is always overestimating the nonlinear SQUID fluctuations, explaining why the Kerr approximation is overestimating the renormalization.

As a conclusion, this SQUID can be tuned from a weakly nonlinear oscillator to a highly nonlinear oscillator where the SCHA breaks down. This is very clear from the left panel of Fig.5.20. This panel displays the renormalized Josephson energy as a function of the bare one in logarithmic scale showing the increase of renormalization when the Josephson energy is decreased. We see that for the smallest values of E_J the ratio $E_\mathrm{J}^\star/E_\mathrm{J}$ is between 0.2 and 0.1 (for exemple at $E_\mathrm{J} = 1\,\mathrm{GHz}$ we have $E_\mathrm{J}^\star = 0.2\,\mathrm{GHz}$). Hence, the renormalization is strong enough to almost suppress the Cooper pair tunneling across the nonlinear SQUID. At the same time the SQUID transitions from highly underdamped to overdamped as the right panel of 5.20 shows (see also Appendix F.5 for the evolution of $\gamma_\mathrm{R}/\omega_\mathrm{d}^\star$ versus the magnetic flux.). In addition, because the circuit we designed contains only one chain the mode density is increased such that the free spectral range is around 400 MHz while it was about a gigahertz in the previous sample.

Thus, this circuit is a very good platform to study the BSG problem both in trivial regimes, where the nonlinearity is weak and underdamped, and in highly non-trivial regimes where the nonlinearity is such that phase fluctuations induce measurable effects such as a nonperturbative renormalization of its resonant frequency. Moreover, we can induce large enough damping such that tens of modes are affected by the nonlinearity. We have also been able to place the circuit in a regime where the theoretical tools we have developed no longer work, thus highlighting the richness of this problem. In what follows we will take advantage of the fact that the nonlinearity is coupled to a quasi-continuum (and not to a true continuum) to study the impact that

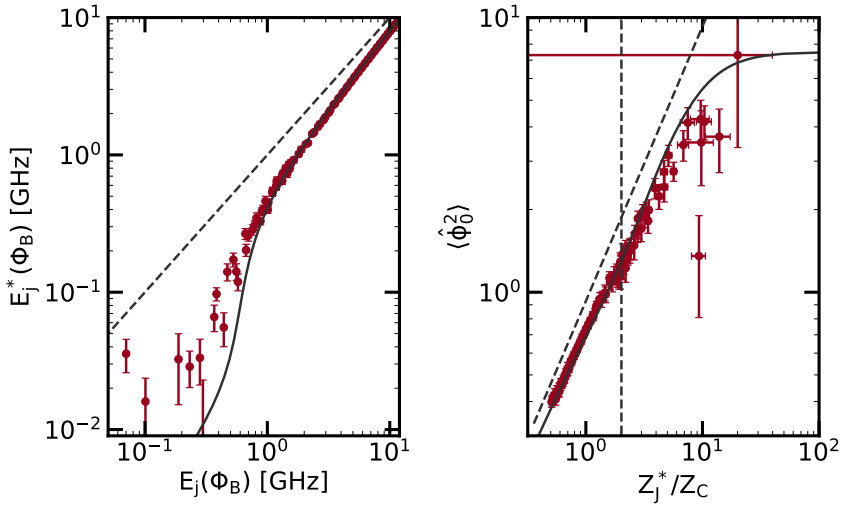

Figure 5.20 – **Left.** Renormalized Josephson energy $E_J^\star$ as a function of the bare Josephson Energy obtained from the fit of the nonlinear SQUID frequency. The red dots are the data extracted from the phase shifts. The dashed line indicates the bare Josephson energy. The plain line is the renormalized one given by the SCHA. **Right.** Phase fluctuations of the junction as a function of the ratio of its renormalized characteristic impedance and the one of the chain. Red dots are the data. The plain line is the estimation from the SCHA. The vertical dashed line separates the overdamped regime from the underdamped one, which means that $2Z_J^\star = Z_C$. The other line indicates what would be the fluctuations if the junction was isolated using Eq.5.40 at T=0.

the latter has on its environment.

Dissipation induced by the nonlinear junction

6

Contents

6.1 Dissipation with respect to various parameters 132

6.1.1 Dissipation with respect to the magnetic flux 132

6.1.2 Dissipation with respect to the input power 132

6.1.3 Dissipation with respect to frequency 135

6.2 Theory-Data agreement 137

6.2.1 Photon conversion broadening 138

6.2.2 Other loss mechanisms 139

In this section the dissipation induced by the nonlinear SQUID on the chain modes will be studied with respect to various parameters. Then, we will compare the experimental data with the model presented in Section 3.6. The data presented in this chapter come from the spectroscopy of the sample presented in Section 5.2

6.1 Dissipation with respect to various parameters

In Section 5.1 we saw that the odd modes were much broader than the even ones (see Fig.5.2). The only difference between these two families of modes is that the odd modes are coupled to the nonlinear junction while the even ones are not. This suggests that the dissipation is induced by the SQUID itself. A possible mechanism for that is that the SQUID can frequency-convert the photons sent in the system thanks to its nonlinearity (see Section 3.6.2).

6.1.1 Dissipation with respect to the magnetic flux

There is no Even-Odd symmetry in the circuit studied in Section 5.2. However, we can tune the nonlinear SQUID frequency via the magnetic flux. If the losses are related to the SQUID they should be related to its resonant frequency. To investigate this effect, we can simply use the data resulting from the circuit spectroscopy with respect to frequency and magnetic flux presented in Fig.5.15. We recall that in this study we extracted the resonant dips of the circuit (using Eq.5.25) as a function of the frequency and the magnetic flux. It is therefore possible to associate an internal broadening[a] to each of these resonances, the result is shown in Fig.6.1.

From this, we can see that the internal broadening of the modes increases by three orders of magnitude from $\Phi_B/\Phi_q \sim 0$ compared to $\Phi_B/\Phi_q \sim 0.5$. On the other hand, when Φ_B/Φ_q is approaching 0.5, the SQUID frequency decreases, or conversely its nonlinearity increases (see Fig.5.19), drastically ($\omega_J^\star$ corresponds to the black dashed line). Thus, this result suggests that the mode losses are related to the nonlinearity of the SQUID.

6.1.2 Dissipation with respect to the input power

We saw that the losses in the chain modes seem to be related to the SQUID nonlinearity. In this section we will report on the power dependence of the circuit resonances. This will be useful to ensure that the power we send in the circuit is low enough so that the losses we measure are not power dependent. Or said differently, the circuit is close enough to equilibrium so that the formalism we derived in Section 3.6.2 can be applied. This will also be interesting to see how the system behaves far from equilibrium despite the lack of a theoretical model. The results of this study are shown in Fig.6.2. The left panels display the measured transmission for various input power. The upper panel shows a resonance for a magnetic flux close to half a flux quantum while the lower panel is measured at zero magnetic flux. From that, we can see

[a] We recall that two kinds of broadening can be extracted from the spectroscopy. The internal one, labeled $\gamma_{\text{int},k}$ describes the dissipation occuring within the circuit. The external one, labeled $\gamma_{\text{ext},k}$, describes the brodening coming from the measurement setup connections. See Appendix C.1 for a more detailed explanation.

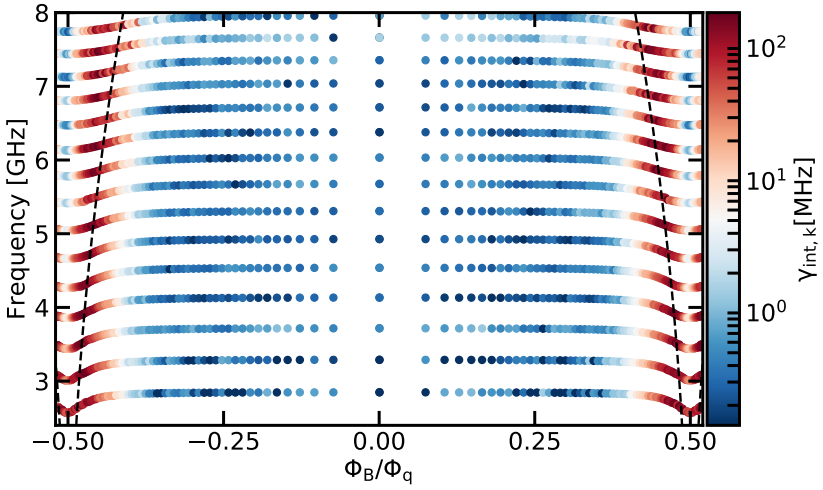

Figure 6.1 – Internal broadening $\gamma_{\mathrm{int},k}$ of the modes with respect to the frequency and magnetic flux $\Phi_\mathrm{B}/\Phi_\mathrm{q}$. The smallest broadening are in blue while the largest are in red. The dashed black line indicates the junction renormalized frequency $\omega_\mathrm{J}^\star$

that the resonances behavior with respect to the input power is completely different. For the dip corresponding to $\Phi_\mathrm{B}/\Phi_\mathrm{q} = 0.46$, the resonance is shifted down a few tens of megahertz when the input power is increased. For the one corresponding to $\Phi_\mathrm{B}/\Phi_\mathrm{q} = 0$, the shift is one order of magnitude lower. In Section 5.1.4, we saw that when the input power is increased the modes population increases and hence the Josephson energy tends to average to zero. Therefore, the modes are less affected at $\Phi_\mathrm{B}/\Phi_\mathrm{q} = 0$ for two reasons. First, the SQUID frequency is about 16 GHz while it is 5 GHz at $\Phi_\mathrm{B}/\Phi_\mathrm{q} = 0.46$. Hence the mode at 6 GHz is a less affected than the one at 6.5 GHz by the downward renormalization of the SQUID frequency. However, the main reason why the mode at $\Phi_\mathrm{B}/\Phi_\mathrm{q} = 0.46$ is more affected is because at this magnetic flux the SQUID is more nonlinear and therefore more sensitive to the input power.

This analysis is supported by the evolution of internal broadening that can be seen on the right panels of Fig.6.2. In the upper panel, the internal broadening as a function of the mode frequency shift is reported for 5 resonances corresponding to magnetic flux close to half a flux quantum. The same was done close to zero flux in the lower panel. The internal broadening is estimated from the fit of the dip for input power ranging from -129dBm to -100dBm (using Eq.5.25). For higher powers, the peaks are distorted by nonlinear effects, as expected for a nonlinear oscillator [123]. The internal broadening of the resonances corresponding to $\Phi_\mathrm{B}/\Phi_\mathrm{q} = 0.46$ increases with power and then starts to decrease before a sharp transition corresponding most likely to the Josephson energy of the SQUID going to zero. On the other hand, the internal broadening of the modes corresponding to $\Phi_\mathrm{B}/\Phi_\mathrm{q} = 0$ slightly decreases with input power and then increases. This two observations can be understood if we state that the losses are given by the nonlinear SQUID at $\Phi_\mathrm{B}/\Phi_\mathrm{q} = 0.46$ and not for $\Phi_\mathrm{B}/\Phi_\mathrm{q} = 0$. Then at $\Phi_\mathrm{B}/\Phi_\mathrm{q} = 0.46$, the modes population increases with the power. Therefore, the SQUID becomes more nonlinear and generate more losses. However, when the Josephson energy averages to zero this losses contribution vanishes

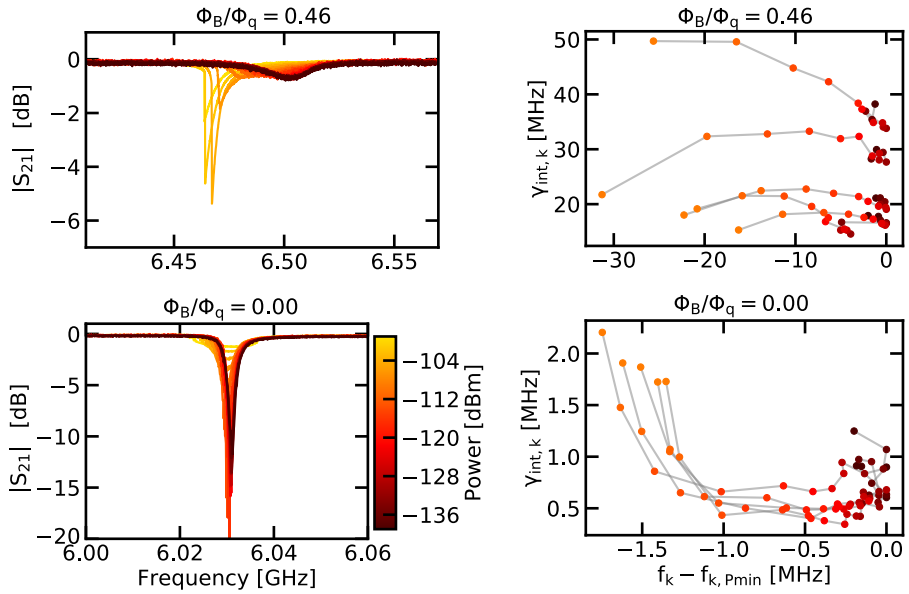

Figure 6.2 – **Upper left.** Transmission versus frequency for a dip at $\Phi_B/\Phi_q = 0.46$ with respect to various input power. **Lower left.** Transmission versus frequency for a dip at $\Phi_B/\Phi_q = 0$ with respect to various input Power. **Upper right.** Estimated internal broadening $\gamma_{int,k}$ as a function of $f_k - f_{k,P_{min}}$ the frequency difference between the resonant frequency at a given power and the one at the lowest input power for five resonances (corresponding to 5.82, 6.16, 6.50, 6.83 and 7.14 GHz) at $\Phi_B/\Phi_q = 0.46$ (using Eq.5.25). The displayed data correspond to the input powers below -110 dBm where the resonance is not distorted by nonlinear effects. The data corresponding to the same resonance are linked via a grey line. The color code is the same than for the left panels. **Lower right.** Same at $\Phi_B/\Phi_q = 0$ and for resonances at 5.30, 5.67, 6.03, 6.37 and 6.71 GHz

and the resonances are the ones of a chain of slightly nonlinear oscillators, explaining the Duffing-oscillator-like response. On the other hand, at $\Phi_B/\Phi_q = 0$, the SQUID nonlinearity is smaller. In addition, the SQUID resonant frequency is higher and we saw in Section 3.6.2 that the modes are more affected by the nonlinearity when they are close to its frequency. Hence, the dominant loss mechanism probably does not come from the SQUID at this magnetic flux. There is evidence that the losses in Josephson chains come mainly from the dielectric forming the tunnel barriers (see Section 6.1.3). For this dissipation mechanism we expect the internal broadenings to decrease with increasing power because of the saturation of the two level systems contained in the dielectric [124]. It could explain why the internal broadening seems to decrease with power at this flux. However, there is a power threshold for which the internal losses increase again. This is most probably because above this power nonlinear losses coming either from the SQUID or the junction of the chain start to dominate. Nevertheless, since we do not have a model for the strongly driven circuit the precise origin of theses nonlinear losses is unclear.

Finally, this study shows that by probing the circuit with an input power of -139 dBm, neither the resonant frequencies nor the broadenings change. Therefore, at this power the circuit is close enough to equilibrium for our formalism to be applied. However, this power corresponds to a radically different number of photons in the

modes. From these fits, we can indeed estimate the average number of photons injected into the modes by the probing power. For -139 dBm, the average photon number is the modes is about unity at $\Phi_B/\Phi_q = 0.46$ while is it about 100 at $\Phi_B/\Phi_q = 0$ (see Appendix G.2), pointing out that at magnetic fluxes close to zero, the circuit is almost linear while it is strongly nonlinear for those close to half a flux quantum.

6.1.3 Dissipation with respect to frequency

Now that we calibrated the input power, we can study the frequency dependence of these nonlinear losses for various magnetic fluxes. The result of this study is shown in Fig.6.3. We can see that, the internal losses do not vary between 0 and 0.3, signaling that in this region the losses do not come from the SQUID nonlinearity as we explained in the previous section. For Φ_B/Φ_q from 0.35 to 0.48, the losses go through a maximum. Finally at $\Phi_B/\Phi_q = 0.5$, the losses decrease with frequency until they are low enough to follow the baseline observed at magnetic fluxes close to zero.

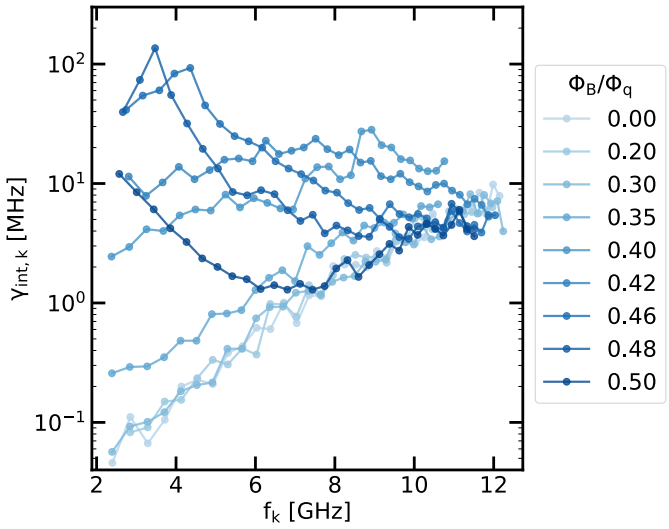

Figure 6.3 – Internal broadening $\gamma_{\text{int},k}$ as a function of the frequency f_k for various magnetic fluxes Φ_B/Φ_q.

These observations suggest that for magnetic fluxes between 0.3 and 0.5 the SQUID is nonlinear enough for the losses it generates to dominate. This observation is supported by the fact that the frequency at which the losses are maximal decreases when Φ_B/Φ_q approaches 0.5. We know from section 3.6.2 that if the losses comes from the photon-conversion, the broadening in a mode k is given by $\gamma_{\text{int},k} = \xi_{0,k}^2 \Sigma''(\omega_k)$. Therefore, if the frequency dependence of Σ'' can be neglected with respect to the one of $\xi_{0,k}^2$ [b] then the losses should be maximal when the latter is maximal, meaning at $\omega_d^\star$ (see Section 6.2 for an in-depth study). Hence, the losses increase with the SQUID nonlinearity and their maxima follow the same trend as $\omega_d^\star$, pointing again towards nonlinear losses generated by the SQUID.

[b] It is the case in practice

Contribution of the junction dielectric

In the previous section we saw that losses at fluxes close to zero seem not to be dominated by the SQUID nonlinearity. Because of the frequency dependence of these losses we think that the dielectric composing the tunnel barrier of the junction chain is the main source of dissipation. We can model the capacitance of the junction chain as:

$$C = \epsilon d \tag{6.1}$$

where ϵ is the permittivity of the dielectric and d is a parameter proportional to a length which depends on the capacitance geometry. If the dielectric is lossy then:

$$C = \left(\epsilon' - i\epsilon''\right) d \tag{6.2}$$

where ϵ' and ϵ'' are respectively the real and imaginary part of the permittivity. Hence, the capacitance admittance is given by:

$$Y_{\mathrm{C}}(\omega) = i\omega \,\mathrm{Re}(C) + \omega \,\mathrm{Im}(C) \tag{6.3}$$

$$= i\omega C + \frac{1}{R_{\mathrm{C}}(\omega)} \tag{6.4}$$

where we assimilated C to its real part while its imaginary part is included in R_{C}. Since the admittance has a real part the junctions of the chain can be replaced by parallel RLC resonators as Fig.6.4 shows. In this case it can be shown, by adding a

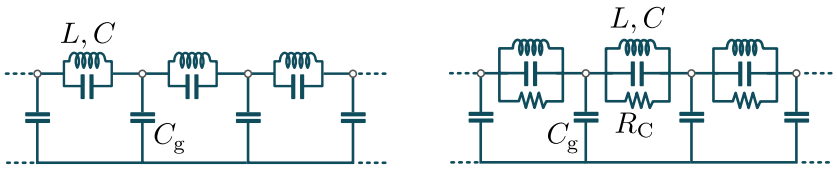

Figure 6.4 – **Left.** Circuit representation of a chain in the linear regime with L and C being respectively the inductance and capacitance of a junction. Each node is grounded via a capacitance C_{g}. **Right.** Equivalently representation while accounting for the dielectric loss of the junction tunnel barrier. These losses can be modeled as a frequency dependent resistance R_{C}

complex part in the chain wave-vectors modes, that the losses are given by[c] (a detailed calculation is provided in [125]):

$$\gamma_{\mathrm{C}}(\omega) = \frac{\omega \tan\delta}{2} \left(\frac{\omega}{\omega_{\mathrm{p}}}\right)^2 \tag{6.5}$$

[c]Note that here we neglected the nonlinear SQUID. This is not a strong approximation since the losses do not show flux dependence close to zero magnetic flux. Therefore the junction can be considered as a dissipationless component. Hence, the only influence of the SQUID is to shift the modes frequency. Since we want to model the chain losses these frequency shifts are irrelevant

with $\tan\delta$ is defined as:

$$\tan\delta = \frac{\mathrm{Im}\, C}{\mathrm{Re}\, C} = A\omega^b \tag{6.6}$$

where A is the constant part of $\tan\delta$ with respect to frequency while b is introduced to handle a possible frequency dependence. We fitted the data corresponding to Φ_B/Φ_q between 0 and 0.3 using Eq.6.5, the result is displayed in Fig.6.5. The estimated parameters are $A = (6.8 \pm 2.9).10^{-4}$ and $b = (0.5 \pm 0.2)$ which agrees with what was reported for similar chains (see the Supplementary Material of [92])

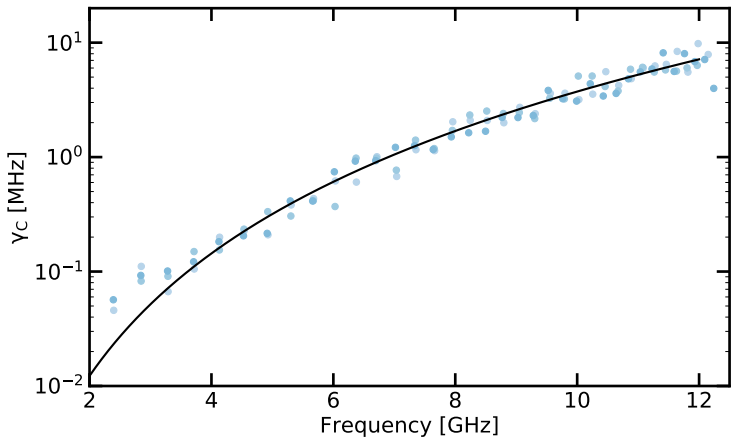

Figure 6.5 – Internal broadening γ_C versus frequency for three values of Φ_B/Φ_q corresponding to 0, 0.2 and 0.3. The black line is the estimation from Eq.6.5. The color code is the same than for Fig.6.3

6.2 Theory-Data agreement

We could estimate the internal loss coming from the dielectric of the junction chain. Hence, the losses coming from the nonlinear SQUID can be estimated from:

$$\gamma_{J,k} = \gamma_{\mathrm{int},k} - \gamma_{C,k} \tag{6.7}$$

where $\gamma_{J,k}$, $\gamma_{\mathrm{int},k}$ and $\gamma_{C,k}$ are respectively the broadening coming from the nonlinear SQUID, the total internal broadening and the chain contribution in the mode k. $\gamma_{J,k}$ can then be normalized by $\Delta\omega_{\mathrm{FSR},k}$, the free spectral range for the mode k evaluated from Eq.3.43. This quantity can be interpreted as the probability per round trip for a photon to decay. Indeed, if for example $\gamma_{J,k}/\Delta\omega_{\mathrm{FSR},k} = 1$, the resonances are no more defined since any photon emitted in the system would decay after a round trip. This decay probability can be plotted as a function of $f_k - f_d^\star$, where $f_d^\star$ is the damped renormalized frequency of the SQUID estimated from the toy model formula $f_d^\star = \sqrt{f_J^{\star 2} - \gamma_{RC}^2/4}$ with $2\pi\gamma_{RC} = 1/C_J Z_C$. The results is given in Fig.6.6. We see that the decay probability is maximal at the damped SQUID frequency. This is compatible with the model of photon conversion developed in Section 3.6.2 since it

predicts a decay probability given by:

$$\frac{\gamma_{\mathrm{J},k}}{\Delta_{\mathrm{FSR},k}} = \Sigma''(\omega_k)\frac{\xi^2_{0,k}}{\Delta_{\mathrm{FSR},k}} = \frac{2\hbar}{\pi}\Sigma''(\omega_k)\chi''_{\phi_0}(\omega_k) \tag{6.8}$$

which is maximal when the dissipative part of the response function χ''_{ϕ_0} is maximal if the self-energy Σ'' is almost constant with frequency.

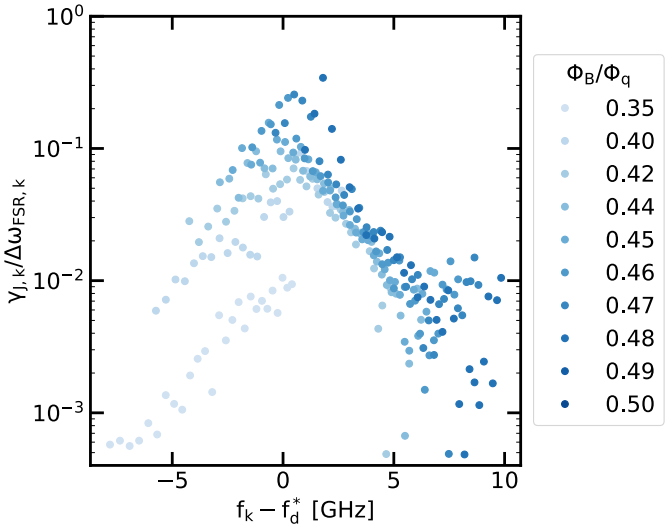

Figure 6.6 – The decay probability per round trip $\gamma_{\mathrm{J,k}}/\Delta\omega_{\mathrm{FSR},k}$ as a function of $f_k - f_\mathrm{d}^\star$ for various magnetic fluxes $\Phi_\mathrm{B}/\Phi_\mathrm{q}$ between 0.35 and 0.5

6.2.1 Photon conversion broadening

Since we can access which part of the internal loss comes from the nonlinear SQUID and which part comes from the chain we can use the model developed in section 3.6.2 to see if the photon conversion can explain the losses attributed to the SQUID. To do so, we use the loss coming from the chain such that the circuit is not a quasi-continuum composed of a discrete set of modes (or, in other words, a sum of Dirac functions) but rather a continuum composed of resonances whose width are given by $\gamma_{\mathrm{C},k}$ (or a sum of Lorentzian curves whose widths are $\gamma_{\mathrm{C},k}$). Therefore, the self-energy derived in Section 3.6.2 is a well-defined function of the frequency. As we previously said, another solution would have been to consider that the chain is infinite, or in other words, to take the thermodynamic limit. However, since the formalism used allows for a microscopic modeling of the circuit there is no need to do so. Now that the spectral distribution of the chain without the nonlinearity effects is known we can directly use our model to estimate γ_J. The results is given for six magnetic fluxes $\Phi_\mathrm{B}/\Phi_\mathrm{q}$ between 0.35 and 0.5 and for four circuit temperature between 0 and 120 mK in Fig.6.7. We see that for a circuit temperature equal to zero, the photon conversion processes are negligible and hence cannot explain the SQUID induced losses. However, when increasing the circuit temperature up to 120 mK we see that the photon conversion process can fairly reproduce the observed losses with respect to both the frequency and magnetic flux lower that 0.46 since the perturbative treatment breakdown for

higher flux (see the last panel of 6.7) It is important to note that, beside temperature, there is not fitting parameter in our theory.

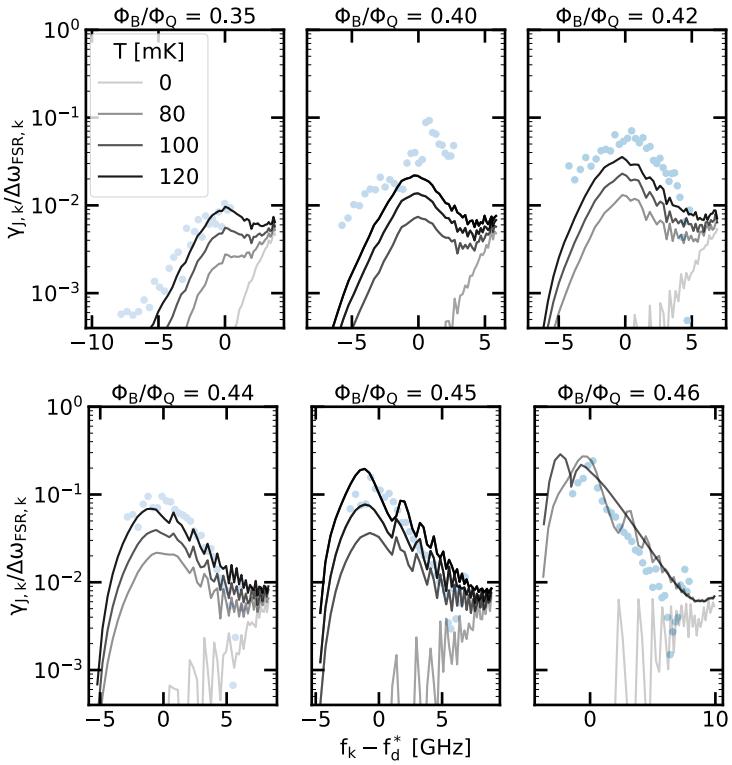

Figure 6.7 – The decay probability per round trip $\gamma_{J,k}/\Delta\omega_{FSR,k}$ as a function of $f_k - f_d^\star$ for six magnetic fluxes Φ_B/Φ_q between 0.35 and 0.46. The dots correspond to the experimental data while the plain line result from the theory using four circuit temperature ranging from 0 mK (light grey) to 120 mK (black).

The drastic increase of the photon conversion losses with temperature can be understood since at $T = 0$ only the processes involving the decay of a probing photon into an odd number of photons[d] can generate losses. However, at non-zero temperature the mode population increases and is no longer equal to zero. Hence, processes where one photon inserted in the circuit interacts with, for example, a thermal photon and both are converted at different frequencies can occurs. Moreover, when the temperature increases the phase fluctuations also increase and processes involving 5,7,... photons become more likely. Therefore, the number of processes involving a photon conversion, and hence the associated losses, explodes at higher temperature.

6.2.2 Other loss mechanisms

We saw that the photon conversion process seems to be a good candidate to explain the observed losses. However, other processes could explain the frequency dependence of γ_J. In the following we will investigate what other kind of processes could be involved.

[d] with the decay into three photon being the most probable one since it is proportional to $\langle\phi_0^4\rangle$ while the others are proportional to higher orders

Toy model for the losses induced by dissipation at the SQUID level

Since the losses are maximal at the damped SQUID frequency the simplest model we could think about is to add a resistance R_J in parallel to the SQUID. This corresponds to the famous Resistively and Capacitively Shunted Junction (RCSJ) model. Then we can consider that the SCHA is applied to our nonlinear SQUID such that it can be modeled by a parallel RLC. Finally the chain is taken in its thermodynamic limit and we neglect its plasma frequency. Hence the model circuit is the one of an RLC circuit at the end of a an infinite transmission line of characteristic impedance Z_C. This circuit is displayed in Fig.6.8.

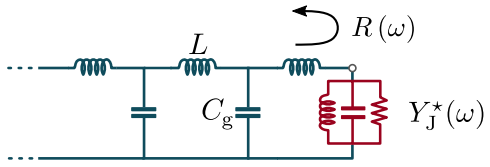

Figure 6.8 – Toy model circuit used to estimate γ_J for a transmission line of characteristic impedance $Z_\mathrm{C} = \sqrt{L/C_\mathrm{g}}$ coupled to a SQUID modeled as a parallel RLC circuit of impedance $Y_\mathrm{J}^\star$. The reflection coefficient in amplitude at the SQUID site is labeled R.

Because of that we can use the formula we derived from the Fabri-Perot model (Eq.5.31) to compute the losses generated by R_J:

$$\gamma_\mathrm{J}(\omega) = \frac{\Delta\omega_\mathrm{FSR}}{\pi} \ln\left|\frac{1}{R(\omega)}\right| \tag{6.9}$$

where R is the reflection coefficient in amplitude at the nonlinear SQUID site. Hence, from the reflection coefficent between a parallel RLC circuit and a transmission line we find:

$$\gamma_\mathrm{J}\,(\omega) = \frac{\Delta\omega_\mathrm{FSR}}{\pi} \ln\left|\frac{1 + Z_\mathrm{C} Y_\mathrm{J}^\star(\omega)}{1 - Z_\mathrm{C} Y_\mathrm{J}^\star(\omega)}\right| \tag{6.10}$$

where $Y_\mathrm{J}^\star(\omega)$ is the RLC circuit admittance, given by:

$$Y_\mathrm{J}^\star(\omega) = \frac{1}{R_\mathrm{J}} + \frac{1 - (\omega/\omega_\mathrm{J}^\star)^2}{i\omega L_\mathrm{J}^\star} \tag{6.11}$$

Hence, this situation is equivalent to a RLC resonator probed by a transmission line of impedance Z_C. Therefore, two types of broadening occurs (see Appendix C for more details). The one coming from the transmission line, labeled $\gamma_\mathrm{RC} = 1/C_\mathrm{J} Z_\mathrm{C}$, and the one coming from the resistance R_J ,labeled $\gamma_{\mathrm{R_JC}} = 1/C_\mathrm{J} R_\mathrm{J}$. Neglecting the frequency shift induced by the damping on $\omega_\mathrm{J}^\star$, considering only the frequencies around the latter and for $\gamma_{\mathrm{R_JC}} \ll \gamma_\mathrm{RC}$[e] we find (see Appendix G.1):

$$\gamma_\mathrm{J}\,(\omega) = \frac{2\Delta\omega_\mathrm{FSR}}{\pi} \frac{\gamma_\mathrm{RC}\gamma_{\mathrm{R_JC}}}{\left(\gamma_{\mathrm{R_JC}} + \gamma_\mathrm{RC}\right)^2 + \left(\omega^2 - \omega_\mathrm{J}^{\star 2}\right)^2} \tag{6.12}$$

[e] It is not a strong approximation for realistic parameters.

Hence, the FWHM of γ_J is given by γ_{RC} and the maximal losses occurs at $\omega_J^\star$ where they are equal to:

$$\gamma_J\left(\omega_J^\star\right) = \frac{2\Delta\omega_{FSR}}{\pi}\frac{\gamma_{R_JC}}{\gamma_{RC}} \tag{6.13}$$

Therefore, if we find a source of dissipation that can be modeled by a parallel resistance R_J it would mimic the frequency behavior of the photon-conversion one. Thus, we will now discuss what sources of dissipation can be described by this model.

Dielectric losses

We saw that the losses in the chain could be explained by the dielectric losses of the oxide barrier composing its junctions. We can then try to see if the same phenomenon is responsible for γ_J. We recall that the dielectric losses can be modeled by a resistance, given by:

$$R_J(\omega) = \frac{1}{\omega C \tan\delta} \tag{6.14}$$

Hence, the resistance decreases when the frequency increase. Therefore, using Eq.6.13, we see that the maximum of the dielectric induced loss should increase when the frequency increases. This is the opposite of what we observe in Fig.6.7. However, we can still check what would be the order of magnitude we could obtain. The result is displayed in Fig.6.9 for a SQUID frequency corresponding to $\Phi_B/\Phi_q = 0.44$.

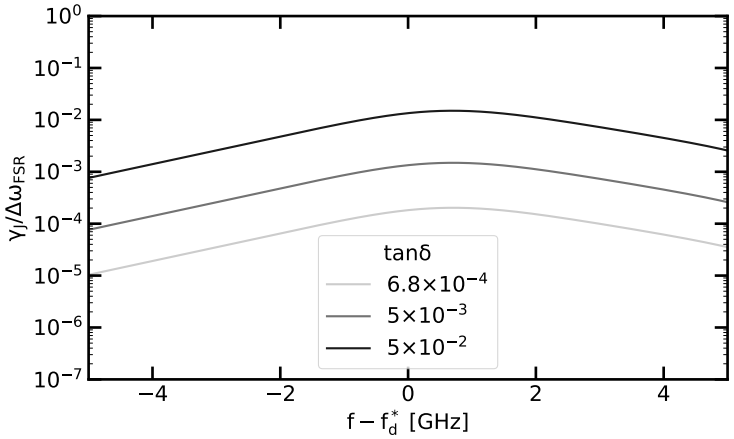

Figure 6.9 – The decay probability per round trip $\gamma_{J,k}/\Delta\omega_{FSR,k}$ as a function of $f_k - f_d^\star$ for a $\tan\delta$ between $0.68.10^{-4}$ (light gray) and 5.10^{-2} (black).

We see that, by taking the same $\tan\delta$ than for the chain junctions (we neglect its frequency dependence) the maximal decay probability per round trip of about 10^{-2}. Even tacking an unrealistically large $\tan\delta$ of 5.10^{-2} is not enough to explain the measured γ_J. It could have been inferred from the dielectric loss of the chain: the losses generated by 4500 junction was orders of magnitude below the SQUID dependent losses. Hence, the dielectric losses caused by the SQUID alone has to be negligible compared to the chain ones and hence to γ_J.

Quasiparticle losses

Another phenomenon that can be modeled by a parallel resistance is the quasiparticle induced losses. For quasiparticles in the high frequency regime we have [126][f]:

$$R_{\mathrm{qp}}(\omega) = \frac{\pi\omega L_{\mathrm{J}}^{\star}}{x_{\mathrm{qp}}}\sqrt{\frac{2\Delta}{\hbar\omega}} \tag{6.15}$$

where x_{qp} and Δ are respectively the quasiparticles density normalized to the Cooper pair density and the superconducting gap of our superconductor. In this modeling we do not need to make hypothesis on the quasiparticle distribution, they are considered out of equilibrium. The measured values range from 10^{-5} to 10^{-8} ([127] provides a good set of articles). We see that since the losses comes from the inductive part of the junction, the resistance increases with frequency. Hence, this could be a good candidate to explain the SQUID induced losses. In Fig.6.10, we plotted the estimated losses for various x_{qp} and for a SQUID frequency corresponding to $\Phi_{\mathrm{B}}/\Phi_{\mathrm{q}} = 0.44$.

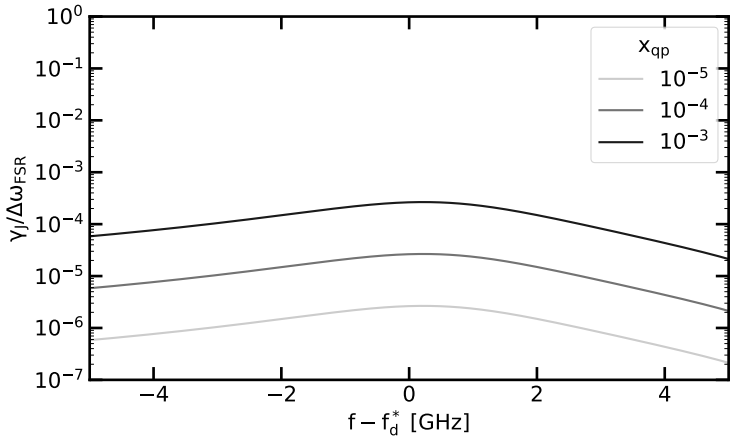

Figure 6.10 – The decay probability per round trip $\gamma_{\mathrm{J,k}}/\Delta\omega_{\mathrm{FSR},k}$ as a function of $f_k - f_{\mathrm{d}}^{\star}$ for quasiparticles density x_{qp} between 10^{-5} (light gray) and 10^{-3} (black).

We see that even for quasiparticles densities several orders of magnitude larger than what was reported the maximal losses are still several orders of magnitude smaller than the ones measured.

Quantum phase slip losses

During the writing of this manuscript R. Kuzmin and coworkers reported similar results than ours [128]. They were able to explain the losses induced by the SQUID by quantum phase slips across the latter. These phase slips can be explained as follows: the nonlinearity can be seen as a particle of kinetic energy E_{C} in a periodic potential given by $E_{\mathrm{J}}\left(1-\cos\hat{\phi}_0\right)$. Then, the phase fluctuations coming from the interaction between the nonlinearity and the high impedance environment can trigger quantum tunneling between the potential energy minima. In other words, the phase can slip

[f] In the following we neglect the thermal quasiparticles since we checked they were negligeable even at temperature about 100 mK

by 2π. Because of that, the nonlinearity can be seen as a phase slip junction with a potential energy $\nu\cos(2\pi\hat{n})$ where $\hat{n}$ is the dynamical charge variable divided by the Cooper pair charge and ν is the phase slip amplitude [129]. Finally, because $\hat{n}$ is coupled to the environment modes it creates a nonlinear interaction between them. This nonlinear interaction is the dual of the one derived to explain the photon conversion processes and generates therefore the same kind of losses.

However, the samples that could be described by this model are in the highly underdamped regime since $\gamma_{\mathrm{RC}}/\omega_{\mathrm{d}}^{\star} \ll 1$ while our circuit is close to the overdamped regime (and even overdamped for $\Phi_{\mathrm{B}}/\Phi_{\mathrm{q}}$ larger than 0.47). This is because the chain impedance is much higher that in our circuits. In addition, the model they used is supposed to be valid only for SQUID with $E_{\mathrm{J}}/E_{\mathrm{C}} \gg 1$ while our SQUID is in a regime where $E_{\mathrm{J}}/E_{\mathrm{C}} \sim 1$. Moreover, they state that the quantum phase slips are "relevant" only for a chain impedance Z_{C} higher than the quantum of resistance Z_{q}. This is the so-called insulating regime, using the wording of the superconductor-isolator transition (see Introduction). However, they have data for a sample which is in the superconducting regime ($Z_{\mathrm{C}} < Z_{\mathrm{q}}$) and the model they rely on seems to make no assumption on the chain impedance [130]. Moreover, whether the superconducting-insulating transition applies to such systems remains unclear since a clear phase diagram was never produced and that circuits predicted to be in the insulating regime showed superconducting properties [18, 92]. In addition, we showed that the impedance of junction chains is not simply given by Z_{C} contrary to what is commonly done in these models[g]. On the contrary, it is very different from the latter in the low frequency regime (see Appendix A.1) and close to the chain plasma frequency (see Section 3.1.2). However it is true that the model derived in this paper predicts a drastic decrease of quantum phase slip when the impedance decreases. It is expected since the phase fluctuations decrease with the impedance. Therefore, the tunneling probability is drastically reduced with the latter. However, it seems to be compensated by a higher sensitivity to the circuit temperature, in other words at lower impedance the nonlinearity is less sensitive to quantum phase slips and more to thermal ones. Thus, we are currently investigating whether this model could explain our observed losses.

Discussion

In conclusion, we saw that our circuit exhibits losses that could be attributed to the SQUID thanks to its magnetic flux, frequency and power dependencies. These losses could be explained by the photon conversion induced by the SQUID nonlinearity. However, this model quantitatively estimates the losses at the expense of an effective circuit temperature around 100 mK. This temperature does not seems to contradict what can can found in the literature. Nevertheless, in Section 5.2.5, we could reproduce the SQUID Josephson energy renormalization with a circuit temperature of 24 mK and the SCHA has convergences issues for this temperature range at $\Phi_{\mathrm{B}}/\Phi_{\mathrm{q}}$ close to 0.5. This signals the limit of validity of this approximation. This is similar to what we observed when adding an effective temperature in our circuit in Appendix F.4.

This points toward two possibilities. First, the current model may need to be refined. For example, by developing the SCHA to higher orders. Second, other phenomena could be responsible for the observed losses. Because of that, we used a toy

[g] This approximation amounts to considering that the environment seen by nonlinearity is purely ohmic.

model to estimate the losses that could be generated by either dielectric losses or quasiparticles at the SQUID level. However none of those mechanisms gives a good estimation of the SQUID induced losses. We saw that another team could explain similar losses by quantum phase slips. While the samples they could describe by that model are in an opposite regime than ours (their nonlinearities are weak and deep in the underdamped regime) we are currently investigating if that mechanism can apply to our system.

Conclusion and Perspectives 7

7.1 Conclusion

In this work, we studied the interaction between a nonlinear oscillator and a strongly dissipative environment formed by a Josephson junction chain. To do so, we designed, fabricated and characterized two types of circuits. The first one was a nonlinear Josephson junction embedded in the middle of two Josephson junction chains, each consisting of 1500 cells. The second one was a nonlinear SQUID galvanically coupled to a 4250 junction chain. We saw that these circuits could be describe by the Boundary Sine Gordon (BSG) model.

The first striking effect of the interplay between the nonlinearity and the high impedance of the chain was a large downward shift of its Josephson energy E_J to a renormalized value $E_\mathrm{J}^\star$. The ratio of these two quantities reached 0.1 in the most nonlinear regime we could measure, this convert to 0.3 for $\omega_\mathrm{J}^\star/\omega_\mathrm{J}$. Hence, the obtained renormalization was strong enough to almost suppress the Cooper pair tunneling across the nonlinear junction. Making this system a possible platform for the study of the superconductor-isolator transition described in the introduction. To my knowledge, two experiments were able to measure a renormalization of such an amplitude in c-QED. Nevertheless, in these two experiments it is the quantum phase slip amplitude $\nu^\star$ that was renormalized, and not $E_\mathrm{J}^\star$[a]. Moreover, but the environment used was either a single mode [42] or a true continuum [50].

In addition to this strong renormalization, phase fluctuations also induce losses in vertu of the fluctuation dissipation theorem. This losses could be explained by photon conversion processes where a single incoming photon can decay into multiple ones. The maximal decay probability per round trip was about 0.1. It is known that photon conversion in c-QED system can be orders of magnitude more efficient than in other experimental platforms because of the strong nonlinearity in such system. However, in most applications in this field, photon conversion relies on significant pumping to compensate for the relatively low conversion probability of these photons. We emphasis that our circuits exhibit these losses at the single photon level. We saw that another team could explains this losses by quantum phase slip of the nonlinearity [128, 130]. Although the sample that can be described by this model is in an opposite regime to ours, we are currently investigating whether this mechanism can be applied to our system as well.

Finally, the use of a quasi-continuum instead of a continuum allows us to question how dissipation is generated by an environment. We have seen, first, that despite the absence of a true continuum, our chain behaves like one for the nonlinearity since

[a]This is why they used a low impedance environment. The phase slip amplitude is reduced if the charge is delocalized. It is the case in low impedance environments.

the measured response functions correspond to those obtained in the thermodynamic limit. Thus, the renormalization of the nonlinearity can be explained even without having a true dissipative environment. However, in order to quantify the dissipation (the photon loss discussed in the last chapter), we need to consider the coupling of our system with the measurement setup and with other dissipative channels. If this is not taken into account no dissipation is expected in the model.

7.2 Perspectives

Finally, in what follows we will discuss what remains to be understood and the different perspectives opened by this work.

7.2.1 Conclude on the SCHA temperature problem

The SCHA can be used to infer the main properties of our system, meaning the renormalization of the Josephson energy and the losses induced by the latter. However, this model could quantitatively estimates the losses at the expense of an effective circuit temperature around 100 mK. This temperature does not seem to contradict what can be found in the literature [116–119] but we saw that the SCHA has convergences issues for this temperature range while estimating the renormalization. Hence, in order to be consistent, these two phenomena would have to be explained by the same circuit temperature. As we said, this issue might be cured by an higher order perturbative expansion of the SCHA. Nevertheless, this approximation may not be precise enough. A possible limitation of the SCHA could be that it does not take into account possible quantum (or thermal) phase slips. The study of the superconductor-insulator (or equivalently Schmid-Bulgadaev) transition discussed in the last section could gives us information on the relevance of these phase slips.

7.2.2 Measuring direct evidence of photon conversion

We saw that the losses induced by the nonlinearity could be coming from photon conversion processes. For example, one probe photon could decay into an odd number of photons after interacting with the nonlinearity. Nevertheless, the measurement of these losses is an indirect observation of this underlying effect. We think that two types of measures could be more convincing.

First, if the photon conversion processes are responsible for the losses its because they couple single-photon states with multi-photon states. Since, the nonlinearity is coupled to a quasi-continuum the number of single-photon states to which it is coupled is finite. Hence, since the number of multi-photon states are also finite we should be able to observe them, in particular their anti-crossing with single-photon states in the circuit spectroscopy. However, we could not observe any of these effects in our circuit. The reasons why we could not observe these effects are twofold. First, the number of multi-photon states grows way faster than the number of single-photon states. For instance, we saw in Section 3.6.2 that one single-photon state could be decomposed into two three-photon states but it can also be decompose in higher number of photon states. Thus, multi-photon states form a dense set of modes. It turns out that by setting the temperature to a value other than zero, the number of accessible multi-photon states explodes. In addition, the temperature decreases the life-time of these

states, and hence broaden the associated modes, such that the multi-photon spectrum losses its frequency structure and becomes a smooth function of it, making these multi-photon states hard to observe in practice. A possible way to circumvent this problem is to decrease the chain junction number such that only few modes remain in the linear part of the spectrum. Then, the number of multi-photon states is drastically reduced and anticrossing between the single-photon and multi-photon states should be accessible. This idea is currently investigated in our team.

Second, we could, directly try to observe the photons resulting from the decay of the single-photon states. Even if the probability of decay per round trip we measured was on the order of 0.1, this experiment looks harder to implement. The reason why is that a photon inserted in the circuit can decay in a random combination of multi-photon states[b]. Moreover, this multi-photon states can then decay multiple times before a photon escapes from the circuit. Hence, we can estimate for the sake of simplicity that the frequency bandwidth we have to monitor ranges from 0 to the probe photon frequency. The amplitude of the expected signal is a portion of the input signal, say 10% maximum, which is equally distributed over this bandwidth. If we are looking, for example, for the photons who decayed from the mode number ten then the portion of signal per mode is about 1%[c]. Therefore, since we want the input signal to be small enough for the system to be close to equilibrium, the signal we want to measure is then extremely small.

7.2.3 Investigating the superconductor-insulator transition

We saw that the fluctuations induced by the interaction between the nonlinearity and the high impedance environment was able to strongly reduce the tunneling of Cooper pair across the nonlinear junction. Hence, our circuit could be a good platform to study the superconductor-insulator transition. The main limitation here is the bandwidth of our setup. We saw that below the gigahertz the measurement of $E_\mathrm{J}^\star$ was quite inaccurate. A possible way to overcome this is to measure in parallel the response function of the nonlinear junction in the quasi DC regime by current biasing it. If the nonlinear junction becomes insulating we expect to see a resistance peak at zero bias corresponding to the impedance of our high impedance environment since $d\phi/dt \neq 0$. However our chain is superconducting and has a finite length. Hence it is not clear that this is what will be observed.

Nevertheless, if we are able to establish the DC phase diagram of the nonlinearity we could then correlate it to the losses measured in the gigahertz regime. If the losses are coming from the nonlinearity we saw that they are parametrized by $E_\mathrm{J}^\star$ and Z_C mainly. On the other hand, the quantum phase slip interpretation relies also on the coupling between single-photon states and multi-photon states. To understand that we need to express the Hamiltonian of this circuit in this framework[d]:

$$\hat{H} = \sum_k \hbar\omega_k \hat{a}_k^\dagger \hat{a}_k + \nu \cos(2\pi\hat{n}_0) \tag{7.1}$$

where $\hat{n}_0$ is the dynamical charge on the nonlinear junction site divided by the Cooper pair charge, introduced in Section 3.1.2. Therefore by analogy with the photon con-

[b] As long as it respect the energy conservation and the distribution of the decay probability.
[c] If the signal is equally distributed over the ten modes we have to divide 10% by 10.
[d] This Hamiltonian can describe the circuit only in the limit $E_\mathrm{J}/E_\mathrm{C} \gg 1$ [129, 131]

version losses generated by the junction nonlinearity we expect the losses generated by the quantum phase slip to be mainly parametrized by $\nu^\star$ and Z_C where $\nu^\star$ is the renormalized quantum phase slip amplitude given by:

$$\nu^\star = \nu e^{-\langle \hat{n}_0^2 \rangle / 2} \tag{7.2}$$

Hence, if we are able to find a model to quantitatively extract $E_\mathrm{J}^\star$ and $\nu^\star$ we could establish the relative contribution of the nonlinearity and the quantum phase slip in the measured losses. This would constitute a kind of high frequency phase diagram that would depend on $E_\mathrm{J}/E_\mathrm{C}$ and Z_C and that could be correlated to the DC response of the nonlinearity.

Appendices

Calculation

A

A.1 Charge offset

In Section 3.1.1 we stated that the charge offset on the Josephson junction could be discarded. In our experiment two kind of junctions are used: those used in the chain and the nonlinear one. In the first case, we have seen that because they are in the $E_{\mathrm{J}} \gg E_{\mathrm{C}}$ limit the cosine terme could be developed at second order:

$$\hat{H} = E_{\mathrm{C}} \left(\hat{n} - n_{\mathrm{g}}\right)^2 + \frac{E_{\mathrm{J}}}{2}\hat{\phi}^2 \tag{A.1}$$

Because of that, it is easy to discard the charge offset via the usual unitary transformation:

$$U = e^{-in_{\mathrm{g}}\hat{\phi}} \tag{A.2}$$

In other words, the charge offset has no influence on the eigenenergies. The second case is a bit more subtle. If the nonlinear junction was isolated it should be sensitive to the offset charge. Nevertheless, in our circuit the latter is galvanically coupled to a chain of junction. Then the chain can either be capacitively (first designed circuit) or galvanically (second designed circuit) coupled to the measurement setup. The measurement setup can be modeled as a $50\,\Omega$ impedance Z_{tl}[a]. Then, for the capacitive coupling, the impedance to the ground at site $N+1$, making the connection with the measurement setup, is (see Fig.A.1):

$$Z_{N+1}\left(\omega\right) \simeq L\omega i + \frac{1}{\left(C_{\mathrm{c,i}} + C_{\mathrm{c}}\right)\omega i} \tag{A.3}$$

where we neglected the capacitance C since we are interested in the low frequency regime. Moreover we assumed that $Z_{\mathrm{tl}} \ll 1/\omega C_{\mathrm{c,o}}$ and $1/\omega C_{\mathrm{c}}$ since these are the parameters used for the circuit design. Then, Z_{N+1} can be compared to the inductance on last site. When the frequency goes to zero Z_{N+1} goes to infinite while the inductance impedance goes to zero. Therefore, we neglected the inductance and Z_{N+1} is in parallel to the capacitance to ground on site N. Hence the last site impedance to ground is now $Z_N = 1/\left(\left[C_{\mathrm{c,i}} + C_{\mathrm{c}} + C_{\mathrm{g}}\right)\omega i\right])$. Repeating, this procedure we find that the nonlinear junction has a parallel capacitance equal to $C_{\mathrm{c,i}} + C_{\mathrm{c}} + NC_{\mathrm{g}}$ in the low frequency regime. This capacitance is equal to few hundreds of femto Farad with

[a] It should be $2Z_{\mathrm{tl}}$ for the first designed circuit because of the Even-Odd symmetry and $Z_{\mathrm{tl}}/2$ for the second designed circuit because of the coupling scheme. However, it does not change the discussion.

the samples parameters. Therefore, at low frequency, the circuit can be mapped to a single Josephson junction with $E_J \gg E_C$ and the charge noise can be neglected [30].

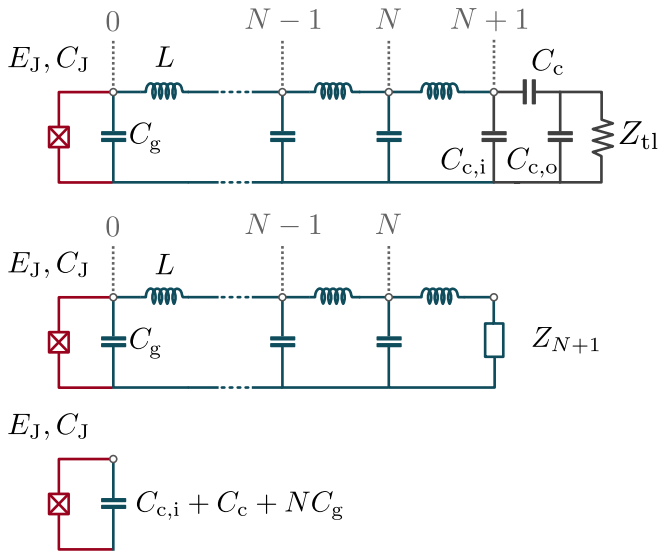

Figure A.1 – **Upper panel.** Effective circuit for the odd modes of the first designed circuit. The nonlinear junction parameters are E_J and E_C. The chain junction inductance is L, its capacitance is neglected since we want to describe the low frequency regime. C_c, $C_{c,i}$ and $C_{c,o}$ are respectively the in-line capacitance, the ground capacitance on the chain side and ground capacitance in parallel with the load modeling the measurement setup. $Z_{tl} = 50\,\Omega$ is the impedance of the line used to measure the circuit. **Middle panel.** Same circuit where Z_{N+1} is the impedance to the ground of site $N+1$ at low frequency. **Lower panel.** Effective circuit in the low frequency regime.

For the galvanic coupling the procedure is the same but the protection from the charge noise lies on a different reason. The admittance to ground on the last site is:

$$Y_N(\omega) = C_g \omega i + \frac{1}{Z_{lt} + L\omega i} \tag{A.4}$$

Hence, in the low frequency regime we have $Y_N \simeq 1/\left(Z_{lt} + L\omega i\right)$ This admittance can be added to the inductance going from site N to $N-1$. Then the admittance to the ground is $Y_{N-1} = 1/(2L\omega i + Z_{tl})$. By repeating this until the nonlinear junction site we end up with a parallel impedance equal to $NL\omega i + Z_{tl}$. Therefore in the low frequency regime the capacitance is shunted by Z_{tl} and no charge noise can take place.

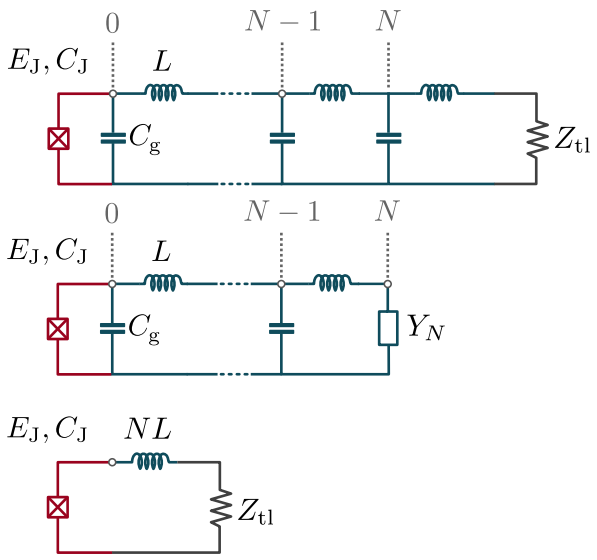

Figure A.2 – **Upper panel.** Circuit corresponding to a galvanic coupling to the measurement setup. It describes the second designed circuit. The nonlinear junction parameters are E_J and E_C. The chain junction inductance is L, its capacitance is neglected since we want to describe the low frequency regime. $Z_\mathrm{tl} = 50\,\Omega$ is the impedance of the line used to measure the circuit. **Middle panel.** Same circuit where Y_N is the admittance to the ground of site N at low frequency. **Lower panel.** Effective circuit in the low frequency regime

A.2 SCHA for the nonlinear oscillator

In this section we derive the expression of the renormalized Josephson energy (Eq.3.18) given in Section 3.1.1. By inserting Eq.3.16 in 3.17 we find:

$$\partial_{E_\mathrm{J}^\star} \langle\psi_\mathrm{t}|\, \hat{H}\, |\psi_\mathrm{t}\rangle = \partial_{E_\mathrm{J}^\star} \langle\psi_\mathrm{t}|\, \hat{H}_\mathrm{t}\, |\psi_\mathrm{t}\rangle - E_\mathrm{J}\partial_{E_\mathrm{J}^\star} \langle\psi_\mathrm{t}|\cos\hat{\phi}\, |\psi_\mathrm{t}\rangle - \frac{1}{2}\langle\psi_\mathrm{t}|\, \hat{\phi}^2\, |\psi_\mathrm{t}\rangle$$

$$- \frac{E_\mathrm{J}^\star}{2}\partial_{E_\mathrm{J}^\star} \langle\psi_\mathrm{t}|\, \hat{\phi}^2\, |\psi_\mathrm{t}\rangle \tag{A.5}$$

Since $|\psi_\mathrm{t}\rangle$ is an eigenvector of $\hat{H}_\mathrm{t}$ of energy E_GS we have:

$$\partial_{E_\mathrm{J}^\star} \langle\psi_\mathrm{t}|\, \hat{H}_\mathrm{t}\, |\psi_\mathrm{t}\rangle = E_\mathrm{GS}\partial_{E_\mathrm{J}^\star} \langle\psi_\mathrm{t}|\psi_\mathrm{t}\rangle + \langle\psi_\mathrm{t}|\, \partial_{E_\mathrm{J}^\star}\hat{H}_\mathrm{t}\, |\psi_\mathrm{t}\rangle \tag{A.6}$$

$$= \frac{1}{2}\langle\psi_\mathrm{t}|\, \hat{\phi}^2\, |\psi_\mathrm{t}\rangle \tag{A.7}$$

$$= \frac{\langle\hat{\phi}^2\rangle_\mathrm{t}}{2} \tag{A.8}$$

Moreover, because $\hat{H}_\mathrm{t}$ is harmonic $|\psi_\mathrm{t}\rangle$ is a Gaussian state (see [82] Chapter 3). Therefore:

$$\langle\psi_\mathrm{t}|\cos\hat{\phi}\,|\psi_\mathrm{t}\rangle = \int_{\mathbb{R}^2} d\phi d\phi'\,\langle\psi_\mathrm{t}|\phi\rangle\,\langle\phi|\cos\hat{\phi}\,\left|\phi'\right\rangle\left\langle\psi_\mathrm{t}\right|\phi'\rangle \tag{A.9}$$

$$= \int_{\mathbb{R}} d\phi\cos\phi|\psi_\mathrm{t}\,(\phi)\,|^2 \tag{A.10}$$

$$= \left(\frac{1}{2\pi\langle\hat{\phi}^2\rangle_\mathrm{t}}\right)^{1/2}\int_{\mathbb{R}} d\phi e^{-\frac{\phi^2}{2\langle\hat{\phi}^2\rangle_\mathrm{t}}}\left(\frac{e^{i\phi}+e^{-i\phi}}{2}\right) \tag{A.11}$$

$$= \frac{1}{2}\left(\frac{1}{2\pi\langle\hat{\phi}^2\rangle_\mathrm{t}}\right)^{1/2} e^{-\langle\hat{\phi}^2\rangle_\mathrm{t}/2}\int_{\mathbb{R}} d\phi\exp\left(-\left[\frac{\phi}{2\sqrt{\langle\hat{\phi}^2\rangle_\mathrm{t}}}-i\frac{\sqrt{\langle\hat{\phi}^2\rangle_\mathrm{t}}}{\sqrt{2}}\right]^2\right)$$

$$+\exp\left(-\left[\frac{\phi}{2\sqrt{\langle\hat{\phi}^2\rangle_\mathrm{t}}}+i\frac{\sqrt{\langle\hat{\phi}^2\rangle_\mathrm{t}}}{\sqrt{2}}\right]^2\right) \tag{A.12}$$

$$= e^{-\langle\hat{\phi}^2\rangle_\mathrm{t}/2} \tag{A.13}$$

A.3 Mode Envelope Normalization

In this section we present the detail of the sum calculation used to find the phase mode amplitude in Section 3.1.2 and 3.2.3

$$\sum_{l=1}^{N}{\xi_{l,k}}^2 = \sum_{l=1}^{N}\cos\left(k\left[l-\frac{1}{2}\right]-\theta_k\right)^2 \tag{A.14}$$

$$= \sum_{l=0}^{N-1}\frac{1}{2}+\cos\left(2k\left[l+\frac{1}{2}\right]-2\theta_k\right) \tag{A.15}$$

$$= \frac{N}{2}+\frac{1}{2}\,\mathrm{Re}\left\{e^{i(k-2\theta_k)}\sum_{l=0}^{N-1}e^{2ikl}\right\} \tag{A.16}$$

$$= \frac{N}{2}+\frac{\sin(kN)}{2\sin k}\cos(kN-2\theta_k) \tag{A.17}$$

where for the last equality we used the well known formula for a geometrical sum. Then by using the grounded boundary condition at site N we have:

$$k_n\left(N-\frac{1}{2}\right)-\theta_k = \pi\left(n+\frac{1}{2}\right) \tag{A.18}$$

By inserting it in Eq.A.17:

$$\sum_{l=1}^{N} {\xi_{l,k}}^2 = \frac{N}{2} + \frac{1}{2\sin k_n} \cos\left(\frac{k_n}{2} + \theta_k\right) \sin\left(\theta_k - \frac{k_n}{2}\right) \tag{A.19}$$

which is the expression used in Section 3.2.3. Then by setting $\theta_k = 0$ we end up with:

$$\sum_{l=1}^{N} {\xi_{l,k}}^2 = \frac{1}{2}\left(N - \frac{1}{2}\right) \tag{A.20}$$

which is the one used in Section 3.1.2

A.4 Self Consistent Harmonic Approximation

For the sake of clarity we replace $\xi_{0,k}/\sqrt{2}$ by ϕ_k. Then using Eq.3.94 and the Baker-Campbell-Hausdorff formula:

$$\langle e^{i\hat{\phi}_0} \rangle_{\mathrm{t}} = \langle \exp\left(i \sum_{k=0}^{N} \phi_k (\hat{a}_k^\dagger + \hat{a}_k)\right) \rangle_{\mathrm{t}} \tag{A.21}$$

$$= \langle \exp\left(i \sum_{k=0}^{N} \phi_k \hat{a}_k^\dagger\right) \exp\left(i \sum_{k=0}^{N} \phi_k \hat{a}_k\right) \rangle_{\mathrm{t}} \exp\left(-\frac{1}{2} \sum_{k=0}^{N} \phi_k^2\right) \tag{A.22}$$

$$= \langle \sum_{n\geq 0} \sum_{m\geq 0} \frac{i^n i^m}{n!m!} \left(\sum_{k=0}^{N} \phi_k \hat{a}_k\right)^n \left(\sum_{k=0}^{N} \phi_k \hat{a}_k\right)^m \rangle_t \exp\left(-\frac{1}{2} \sum_{k=0}^{N} \phi_k^2\right). \tag{A.23}$$

The terms where $n = m$ are the only one different from 0 :

$$\langle e^{i\hat{\phi}_0}\rangle_{\mathrm{t}} = \sum_{m\geq 0}\frac{(-1)^n}{n!^2}\sum_{k_1\ldots k_n}\phi_{k_1}\ldots\phi_{k_n}\sum_{k'_1\ldots k'_n}\phi_{k'_1}\ldots\phi_{k'_n}\langle a^\dagger_{k_1}\ldots a^\dagger_{k_n}a_{k'_1}\ldots a_{k'_n}\rangle_t \tag{A.24}$$

$$= \sum_{n\geq 0}\frac{(-1)^n}{n!^2}n!\sum_{k_1\ldots k_n}\phi^2_{k_1}\ldots\phi^2_{k_n}\langle a^\dagger_{k_1}a_{k_1}\rangle_t\ldots\langle a^\dagger_{k_n}a_{k_n}\rangle_t\exp\left(-\frac{1}{2}\sum_{k=0}^{N}\phi^2_k\right) \tag{A.25}$$

$$= \sum_{n\geq 0}\frac{1}{n!}\left(-\sum_{k=0}^{N}\left(n_k\phi^2_k\right)\right)^n\exp\left(-\frac{1}{2}\sum_{k=0}^{N}\phi^2_k\right) \tag{A.26}$$

$$= \exp\left(-\sum_{k=0}^{N}(n_k+\frac{1}{2})\phi^2_k\right) \tag{A.27}$$

$$= \exp\left(-\frac{1}{2}\sum_{k=0}^{N}(n_k+\frac{1}{2})\xi^2_{0,k}\right) \tag{A.28}$$

$$= \exp\Big(-\langle\hat{\phi}^2_0\rangle_{\mathrm{t}}/2\Big). \tag{A.29}$$

Wick's theorem has been used between Eq. (A.24) and Eq. (A.25), and $n_k = 1/[\exp(\hbar\omega_k/k_{\mathrm{B}}T) - 1]$ is the Bose factor. One verifies easily that $\langle e^{-i\hat{\phi}_0}\rangle_{\mathrm{t}} = \langle e^{i\hat{\phi}_0}\rangle_{\mathrm{t}}$.

A.5 Response function and noise spectral density

In this section we derive the link between the Fourier transform of the dissipative part of the response function and the anti-symmetric part of the noise spectral density. The latter is by definition:

$$\tilde{\chi}_{\phi_0}(t) = \frac{1}{2}\left[\chi_{\phi_0}(t) - \chi_{\phi_0}(-t)\right] \tag{A.30}$$

Its Fourier transform is given by:

$$\tilde{\chi}_{\phi_0}(\omega) = \frac{1}{2}\int_{\mathbb{R}}dt\left[\chi_{\phi_0}(t) - \chi_{\phi_0}(-t)\right]e^{i\omega t} \tag{A.31}$$

$$= i\int_0^\infty dt\chi_{\phi_0}(t)\sin\omega t \tag{A.32}$$

where we used the causality of the reponse function. Therefore, the Fourier transform of $\tilde{\chi}$ is linked to the Fourier transform of dissipative part of the response function via:

$$\tilde{\chi}_{\phi_0}(\omega) = i\,\mathrm{Im}\,\chi_{\phi_0}(\omega) \tag{A.33}$$

$$= i\chi''_{\phi_0}(\omega) \tag{A.34}$$

Kubo formula gives:

$$\chi_{\phi_0}(t) = \frac{i}{\hbar}\Theta(t)\,\langle[\hat{\phi}_0(t), \hat{\phi}_0]\rangle \tag{A.35}$$

Inserting the latter in Eq.A.31 and using Eq.A.34:

$$\chi''_{\phi_0}(\omega) = \int_{\mathbb{R}} \frac{dt}{2\hbar}\Theta(t)\,\langle[\hat{\phi}_0(t), \hat{\phi}_0]\rangle e^{i\omega t} - \int_{\mathbb{R}} \frac{dt}{2\hbar}\Theta(-t)\,\langle[\hat{\phi}_0(-t), \hat{\phi}_0]\rangle e^{i\omega t} \tag{A.36}$$

$$= \int_{\mathbb{R}} \frac{dt}{2\hbar}\langle[\hat{\phi}_0(t), \hat{\phi}_0]\rangle e^{i\omega t} \tag{A.37}$$

$$= \frac{1}{\hbar}\tilde{S}_{\phi_0}(\omega) \tag{A.38}$$

A.6 Response function and toy model

In this section we will see under which approximations the response fonction of the nonlinear junction matches the one of the toy model. The noise spectral density is:

$$S_{\phi_0}(\omega) = \frac{2\hbar}{\phi_{\mathrm{q}}^2\omega}\frac{Z(\omega)}{1-e^{-\hbar\omega/k_{\mathrm{B}}T}}\cos^2\left(\frac{k(\omega)}{2} + \theta(\omega)\right) \tag{A.39}$$

In the continuum limit we have $k \ll 1$. Therefore, at first order in k:

$$S_{\phi_0}(\omega) = \frac{2\hbar}{\phi_{\mathrm{q}}^2\omega}\frac{Z(\omega)}{1-e^{-\hbar\omega/k_{\mathrm{B}}T}}\cos^2(\theta(\omega)) \tag{A.40}$$

From Eq.3.148, 3.149 and 3.113:

$$\cos^2(\theta(\omega)) = \frac{1}{1+[f(\omega)\,X(\omega)]^2} \tag{A.41}$$

In the experiments $L/L_{\mathrm{J}}^{\star}$ is always way below unity. Consequently up to the second order in the latter:

$$f^2(\omega) = \frac{[\lambda(\omega)-1]^2}{4} \tag{A.42}$$

Hence, the cosine reads:

$$\cos^2(\theta(\omega)) = \frac{\gamma_{RC}^2(\omega)\,\omega^2}{\gamma_{RC}^2(\omega)\,\omega^2 + \left(\omega_{\mathrm{J}}^{\star 2} - \omega^2\right)^2} \tag{A.43}$$

where $\gamma_{RC}(\omega) = 1/Z_{\mathrm{C}}(\omega)C_{\mathrm{J}}$. Finally by rewriting X we end up with:

$$X^2(\omega) = \frac{4}{LC_{\mathrm{g}}\omega^2}\left(1-\left(\frac{\omega}{\omega_{\mathrm{p}}}\right)^2\right) \tag{A.44}$$

So that the response function is the one we found for the toy model:

$$\chi''_{\phi_0}(\omega) = \frac{1}{\phi_{\mathrm{q}}^2 C_{\mathrm{J}}} \frac{\omega \gamma_{RC}(\omega)}{\gamma_{RC}^2(\omega)\,\omega^2 + \left(\omega_{\mathrm{J}}^{\star 2} - \omega^2\right)^2} \tag{A.45}$$

The only difference being that the damping rate γ_{RC} is frequency dependent since no assumption has been made on the chain plasma frequency ω_{p}. By considering the limit where it is infinite we find back the imaginary part of Eq.3.130.

A.7 Link between the total impedance and the response function

In this section we explain the link between the total circuit impedance and the phase response function of the nonlinear junction. The total impedance of the toy model is:

$$Z_{\mathrm{t}}(\omega) = \frac{1}{\frac{1}{i\omega L_{\mathrm{J}}^{\star}} + i\omega C_{\mathrm{J}} + \frac{1}{Z_{\mathrm{C}}}} \tag{A.46}$$

where $L_{\mathrm{J}}^{\star}$ is the renormalized effective inductance given by the SCHA. The impedance can then be rewritten as:

$$Z_{\mathrm{t}}(\omega) = \frac{i\omega}{C_{\mathrm{J}}} \frac{1}{\omega_{\mathrm{J}}^{\star 2} - \omega^2 + i\omega\gamma_{RC}} \tag{A.47}$$

Consequently the dissipative part of the response function and the real part of the total impedance are related via

$$\mathrm{Re}\{Z_{\mathrm{t}}(\omega)\} = \omega \phi_{\mathrm{q}}^2 \chi''_{\phi_0}(\omega) \tag{A.48}$$

It give then an alternative way to study the noise spectral density.

A.8 Link between $\mathrm{Im}\, G_{\phi_0}(\omega)$ and $\chi''_{\phi_0}(\omega)$

In this section we will derive the relation 3.192. The first step is to find the link between $\mathrm{Im}\, G_{\phi_0}(\omega)$ and $\bar{S}_{\phi_0}(\omega)$. Using Eq.3.191 in $G_{\phi_0}(t)$ and taking its Fourier transform yields:

$$G_{\phi_0}(\omega) = -i \int_0^{+\infty} dt \langle \hat{\phi}_0(t)\hat{\phi}_0 \rangle e^{i\omega t} - i \int_{-\infty}^{0} dt \langle \hat{\phi}_0(-t)\hat{\phi}_0 \rangle e^{i\omega t} \tag{A.49}$$

$$= -i \int_0^{+\infty} dt \langle \hat{\phi}_0(t)\hat{\phi}_0 \rangle e^{i\omega t} - i \int_0^{+\infty} dt \langle \hat{\phi}_0(t)\hat{\phi}_0 \rangle e^{-i\omega t} \tag{A.50}$$

$$= -2i \int_0^{+\infty} dt \langle \hat{\phi}_0(t)\hat{\phi}_0 \rangle \cos \omega t \tag{A.51}$$

Then the imaginary part of $G_{\phi_0}(\omega)$ is given by:

$$\mathrm{Im}\, G_{\phi_0}(\omega) = -2\int_0^{+\infty} dt\, \mathrm{Re}\langle\hat{\phi}_0(t)\hat{\phi}_0\rangle \cos\omega t \tag{A.52}$$

We saw in Section 3.1.2 that in the classical case the correlator is symmetric in time and real. Therefore $\mathrm{Re}\langle\hat{\phi}_0(t)\hat{\phi}_0\rangle = \bar{S}_{\phi_0}(t)$ and:

$$\mathrm{Im}\, G_{\phi_0}(\omega) = 2\int_0^{+\infty} dt \bar{S}_{\phi_0}(t) \cos\omega t \tag{A.53}$$

On the other hand, from Eq.3.75 we can compute $\bar{S}_{\phi_0}(\omega)$:

$$\bar{S}_{\phi_0}(\omega) = \frac{1}{2}\int_{\mathbb{R}} dt S_{\phi_0}(t)\left(e^{i\omega t} + e^{-i\omega t}\right) \tag{A.54}$$

$$= \int_{\mathbb{R}} dt S_{\phi_0}(t) \cos\omega t \tag{A.55}$$

Using the time symmetry of S_{ϕ_0} we have:

$$\bar{S}_{\phi_0}(\omega) = 2\int_0^{\infty} dt \bar{S}_{\phi_0}(t) \cos\omega t \tag{A.56}$$

$$= -\,\mathrm{Im}\, G_{\phi_0}(\omega) \tag{A.57}$$

Now that we have a relation between $\mathrm{Im}\, G_{\phi_0}(\omega)$ and $\bar{S}_{\phi_0}(\omega)$ we need to find the link between the latter and $\tilde{S}_{\phi_0}(\omega)$. For that we can use the detailed balance [132].

It states that for a system at thermal equilibrium $S_{\phi_0}(\omega) = S_{\phi_0}(-\omega)e^{-\hbar\omega/k_\mathrm{B}T}$. Hence, by using it in Eq.3.75 and 3.76 :

$$\bar{S}_{\phi_0}(\omega) = \coth\left(\frac{\hbar\omega}{2k_\mathrm{B}T}\right)\tilde{S}_{\phi_0}(\omega) \tag{A.58}$$

Finally, at $T = 0$ and using Eq.A.57 and A.38 we have:

$$\hbar\chi''_{\phi_0}(\omega) = -\mathrm{sign}(\omega)\,\mathrm{Im}\, G_{\phi_0}(\omega) \tag{A.59}$$

A.9 Derivation of $\Sigma^{(2)}$

In this section we will derive Eq.3.225. To do so, we will briefly introduce the Feynman diagram technique that is known to greatly simplify the calculation.

Feynman diagram for the first order expansion of G_{ϕ_0}

Feynman diagrams are a graphical representation of the interaction terms generated while computing G_{ϕ_0}. We saw that every order of G_{ϕ_0} could be written as functions of $G^{(0)}_{\phi_0}$. The Feynman representation of such functions is as follow:

— Every correlator $G^{(0)}_{\phi_0}$ evaluated between a time t and t' is represented as a line connecting two dots (they are called vertex in the literature) corresponding to the time t and t' (see the top left graph of Fig.A.3)

— While developing G_{ϕ_0} at order higher than zero, dummy time variables are generated (t_1 at first order, t_2 at second order, ...). These time variables are also represented as dots. The interaction can then be expressed as functions of $G^{(0)}_{\phi_0}$ thanks to Wick's theorem. This converts into lines lines connecting different dots. For example, if a term like $G^{(0)}_{\phi_0}(t_1 - t_2)^2$ is generated we draw two lines connecting the dots corresponding to t_1 and t_2 while a term like $G^{(0)}_{\phi_0}(t_1 - t_1)$ gives a loop on the dot corresponding to t_1. Theses intermediate times are represented as tilted squares symbolizing every possible interaction terms that can be generated on the left panel of Fig.A.3.

By applying this to the first order expansion of G_{ϕ_0} we find the diagrams represented on the right panel of Fig.A.3. To distinguish the interaction terms with E_J or $E^\star_\mathrm{J}$ as a prefactor we use respectively a white dot or a star. The upper left diagram is the product of two disconnected diagram since its a product of $G^{(0)}_{\phi_0}$ evaluated on different variable ($t - t'$ for the upper part and t_1 for the second, see Eq.3.199). We saw that these diagrams are not accounted since they cancel with the denominator of Eq.3.193. Therefore, this is another rules: the disconnected diagrams can be neglected. The lower left diagram corresponds to Eq.3.200 while the diagrams at the right are the ones generated by the cosine, where the disconnected diagrams are not represented. Since these diagrams are a sum of loops ranging from one to infinity they generate the exponential of $G^{(0)}_{\phi_0}$ that we saw with Eq.3.209.

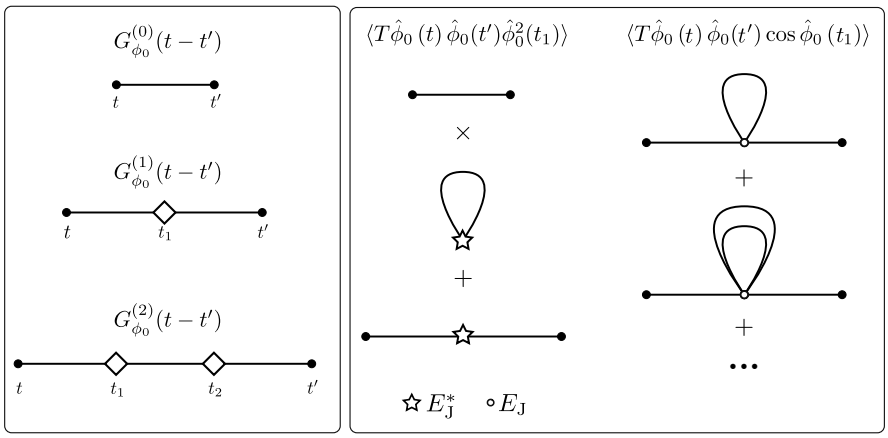

Figure A.3 – **Left panel.** Feynman diagrams for the correlator G_{ϕ_0}. Every $G^{(0)}_{\phi_0}(t - t')$ is represented as a line linking two dots corresponding to t and t'. The dummy variables generated by the order expansion of G_{ϕ_0} introduce new dots and lines. They are here represented as tilted square to stay general. **Right panel.** Feynman diagram corresponding to the first order expansion of G_{ϕ_0}. The interaction terms with E_J or $E^\star_\mathrm{J}$ as a prefactor are represented respectively with a white dot or a star. The upper left diagram correspond to Eq. 3.199, the lower left to Eq.3.200 and and right ones to Eq.3.209

The use of Feynman diagram for the self energy calculation

Now that we have seen how to draw Feynman diagrams from the interaction terms we will use it to calculate the second order expansion of the self energy $\Sigma^{(2)}$. We could see from Eq.3.214 and 3.215 that the self energy at order n is nothing but the interaction terms generated from the nth order expansion of G_{ϕ_0} where the correlator $G^{(0)}_{\phi_0}$ including the starting and stopping times t' and t are removed. In terms of Feynman diagrams it means that the self energy consists in all the diagrams where the two external lines are removed. Another rules that could not be saw from the first order expansion of G_{ϕ_0} is that the self energy is only including the diagrams that cannot be cut in two by removing a simple line, these are called *Irreductible diagrams*. If not some diagrams would be counted twice while applying Dyson's equation. This can be seen by using the Feynman diagrams representation of this equation (lower panel of Fig.A.4). The third term could be consider as a fourth order term of the self energy $\Sigma^{(4)}$ since it contains four nodes (we recall that we should not count the external lines for the self energy so it is 6 minus 2 nodes). However, it can be cut in two by removing the line connecting the two Σ and is therefore a term contained in a lower order expansion of Σ. Hence, will applying Dyson's equation such a term would be counted twice.

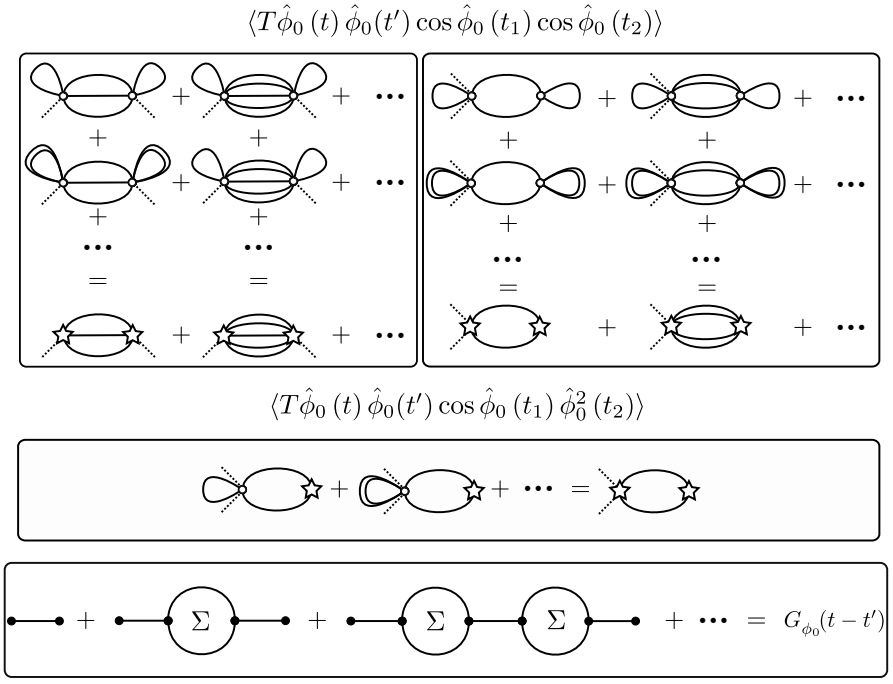

Figure A.4 – **Upper left panel.** Irreducible diagram generated by the double cosine term.**Upper right panel.** Irreducible diagram generated by the crossing term **Lower panel.** Feynman diagrams representation of the Dyson's equation. The dashed line represent where the self energy diagrams are connected to t and t'.

Let us now develop the second order expansion of $G^{(2)}_{\phi_0}$:

$$G^{(2)}_{\phi_0}(t-t') = \frac{i}{\hbar^2}\int_{\mathbb{R}^2} dt_1 dt_2 \langle T\hat{\phi}_0(t)\hat{\phi}_0(t')\hat{H}_{\rm int}(t_1)\hat{H}_{\rm int}(t_2)\rangle \tag{A.60}$$

$$= \frac{i}{\hbar^2}\int_{\mathbb{R}^2} [dt_1 dt_2 \langle T\hat{\phi}_0(t)\hat{\phi}_0(t')\cos\hat{\phi}_0(t_1)\cos\hat{\phi}_0(t_2)\rangle \tag{A.61}$$

$$+ E_{\rm J}E^{\star}_{\rm J}\langle T\hat{\phi}_0(t)\hat{\phi}_0(t')\hat{\phi}_0(t_1)^2\cos\hat{\phi}_0(t_2)\rangle \tag{A.62}$$

$$+ \frac{E^{\star 2}_{\rm J}}{4}\langle T\hat{\phi}_0(t)\hat{\phi}_0(t')\hat{\phi}_0(t_1)^2\hat{\phi}_0(t_2)^2\rangle] \tag{A.63}$$

$$\tag{A.64}$$

The last term at the right hand sight is only generating unconnected or reducible diagrams and is therefore neglected. The first term is generating the two families of diagrams reported in the upper panel of Fig.A.4. The second term is generating the family of diagrams generated at in the medium panel of Fig.A.4. We recall that we stated that the second order expansion of the self energy was:

$$\Sigma^{(2)}(t_1-t_2) = -i\left(\frac{E^{\star}_{\rm J}}{\hbar}\right)^2 \delta(t-t')\int_{\mathbb{R}} dt_3 \cos G^{(0)}_{\phi_0}(t_1-t_3) - 1 + \frac{1}{2}G^{(0)}_{\phi_0}(t_1-t_3)^2$$

$$+ \left(\frac{E^{\star}_{\rm J}}{\hbar}\right)^2 \left[\sin G^{(0)}_{\phi_0}(t_1-t_2) - G^{(0)}_{\phi_0}(t_1-t_2)\right] \tag{A.65}$$

We will now prove it using the Feynman diagrams. In the upper left panel we see that each row is a sum of diagrams where only the number of loops at each nodes increases. Such sums gave the exponential function of $G^{(0)}_{\phi_0}$ while calculating the first order expansion of G_{ϕ_0}. This quantity was set equal to the effective quadratic potential of amplitude $E^{\star}_{\rm J}$. Therefore, they can be replaced by stars (see the previous Section). Moreover, the external line connecting the self energy to t and t' (the dashed line in Fig.A.4) are on two different nodes. Consequently, the parity of the cosine enforces that these two nodes (stars) are linked by an odd number of lines. These graphs are responsible for the sine function of $G^{(0)}_{\phi_0}$ in Eq.3.225 (minus $G^{(0)}_{\phi_0}$ since a simple line would be a reducible diagram). In the upper right part we can also replace each rows by an equivalent diagram where each node is a star. Moreover, the external lines are on the same node. Therefore the parity of the cosine enforces that an even number of lines link these two nodes. These graphs are responsible for the cosine function of $G^{(0)}_{\phi_0}$ (minus one). Following the same reasoning, we find that the middle panel is responsible for the $G^{(0)2}_{\phi_0}$ in Eq.3.225.

A.10 $G^{(0)}_{\phi_0}$ in the vicinity of a mode

In this section we will derive the expression for $G^{(0)}_{\phi_0}$ in the vicinity of a mode used in Eq.3.221. To do so, we use Eq.3.205 and 3.67 at $T = 0$:

$$G^{(0)}_{\phi_0}(t) = -i \sum_k \frac{\xi^2_{0,k}}{2} e^{-i\omega_k |t|} \tag{A.66}$$

Therefore the Fourier transform is given by:

$$G^{(0)}_{\phi_0}(\omega) = -i \sum_k \frac{\xi^2_{0,k}}{2} \lim_{\eta \to 0^+} \left[\int_0^\infty dt e^{i(\omega-\omega_k)t} e^{-\eta t} + \int_{-\infty}^0 dt e^{i(\omega+\omega_k)t} e^{\eta t} \right] \tag{A.67}$$

where $e^{\pm \eta t}$ is added to insure convergence of the integrals. Hence:

$$G^{(0)}_{\phi_0}(\omega) = -i \sum_k \frac{\xi^2_{0,k}}{2} \lim_{\eta \to 0^+} \left[\frac{-1}{i\left(\omega - \omega_k\right) - \eta} + \frac{1}{i\left(\omega + \omega_k\right) + \eta} \right] \tag{A.68}$$

$$= \sum_k \frac{\xi^2_{0,k}}{2} \frac{2\omega_k}{\omega^2 - \omega_k^2} \tag{A.69}$$

At the vicinity of ω_k, at first order in $\omega - \omega_k$ we get:

$$G^{(0)}_{\phi_0}(\omega) = \frac{1}{2} \frac{\xi^2_{0,k}}{\omega - \omega_k} \tag{A.70}$$

which is nothing but Eq.3.221.

A.11 Fourier transform of the approximate formula for $\Sigma^{(2)}$

In this section we will calculate the Fourier transform of the approximate formula for $\Sigma^{(2)}$ (see Eq.3.227) that was derived in Section 3.6.2. We recall that it was given by:

$$\Sigma^{(2)}(t) \simeq -\frac{i}{48} \left(\frac{E^\star_\mathrm{J}}{\hbar} \right)^2 \sum_{k_1,k_2,k_3} \xi^2_{0,k_1} \xi^2_{0,k_2} \xi^2_{0,k_3} e^{-i\omega_\Sigma |t|} \tag{A.71}$$

where ω_Σ is defined as $\omega_\Sigma = \omega_{k_1} + \omega_{k_2} + \omega_{k_3}$. To calculate the Fourier transform of Eq.A.71 we need to calculate the one of $e^{-i\omega_\Sigma |t|}$:

$$\int_\mathbb{R} dt e^{-i\omega_\Sigma |t|} e^{i\omega t} = \lim_{\eta \to 0^+} \int_0^{+\infty} e^{i(\omega-\omega_\Sigma)t} e^{-\eta t} + \int_{-\infty}^0 e^{i(\omega+\omega_\Sigma)t} e^{\eta t} \tag{A.72}$$

$$= \lim_{\eta \to 0^+} \frac{i}{(\omega - \omega_\Sigma) + i\eta} - \frac{i}{(\omega + \omega_\Sigma) - i\eta} \tag{A.73}$$

where $e^{\pm\eta t}$ is added to insure convergence of the integrals. Therefore, the Fourier transform of the self-energy is given by:

$$\Sigma^{(2)}(\omega) \simeq \frac{1}{48}\left(\frac{E_{\mathrm{J}}^{\star}}{\hbar}\right)^{2} \sum_{k_1,k_2,k_3} \xi_{0,k_1}^{2}\xi_{0,k_2}^{2}\xi_{0,k_3}^{2}\left[\lim_{\eta\to 0^{+}} \frac{1}{(\omega-\omega_{\Sigma})+i\eta} - \frac{1}{(\omega+\omega_{\Sigma})-i\eta}\right] \tag{A.74}$$

Hence, using the Sokhotski–Plemelj theorem [b] we get for the imaginary part of the self energy Fourier transform at ω_k:

$$\Sigma^{(2)}(\omega_k)'' = -\frac{\pi}{48}\left(\frac{E_{\mathrm{J}}^{\star}}{\hbar}\right)^{2} \sum_{k_1,k_2,k_3} \xi_{0,k_1}^{2}\xi_{0,k_2}^{2}\xi_{0,k_3}^{2}\left[\delta(\omega_k-\omega_{\Sigma})+\delta(\omega_k+\omega_{\Sigma})\right] \tag{A.75}$$

[b] $\lim_{\eta\to 0^{+}} \frac{1}{\omega\pm i\eta} = \mp i\pi\delta(\omega) + \mathcal{P}(\frac{1}{\omega})$ where $\mathcal{P}$ is the Cauchy principal value

Fabrications

B

B.1 Recipe

In this section we put the recipe used for the sample nanofabrication. The areas corresponding to *Junction*, *Undercut* and *Chain inner part* in the second step are explained in B.2

Step	Parameters
0. Wafer cleaning	RIE O_2 at 20 W and 0.07 mbar for 20 min
1. Resist spin coating	First resist: PMMA-MMA 9% Spin Coater Parameters: 30 sec / 4000 rpm / 4000 rpm.s^{-1} Baking: 200 °C for 10 min Deposited thickness : between 700 and 800 nm Second resist: PMMA 4% Spin Coater Parameters: 30 sec / 5000 rpm / 5000 rpm.s^{-1} Baking: 150 °C for 5 min Deposited thickness : 200 nm
2. Exposure	Junction: 11 Cm^{-2} Undercut: 3 Cm^{-2} Chain inner part: 8 Cm^{-2}
3. Development	First solvent: MIBK-IPA 1:3 for 60 sec Second solvent: IPA for 30 sec
4. Undercut cleaning	RIE O_2 at 10 W and 0.07 mbar for 15 sec
5. Evaporation	First deposition: 20 nm of aluminum at 0.1 nm sec^{-1} Static Oxidation: 4 Torr for 5 min Second deposition: 50 nm of aluminum at 0.1 nm sec^{-1}
6. Lift-off	NMP at 80 °C for 6 h + Ultrasonic Bath for 60 sec Rince with: Acetone Ethanol and IPA

B.2 Different designs of junction

In this section we will present different junction models I used to design my samples. In the upper panel of Fig.B.1 we represented the exposure patterns in the second step of the recipe. The two designs at the left are used because of the low footprint in the chain axis. The two at the right are most suited to design small, and therefore nonlinear, junctions since they are not sensitive to errors in the rotation axis. The lower panel shows SEM picture of the designed junctions.

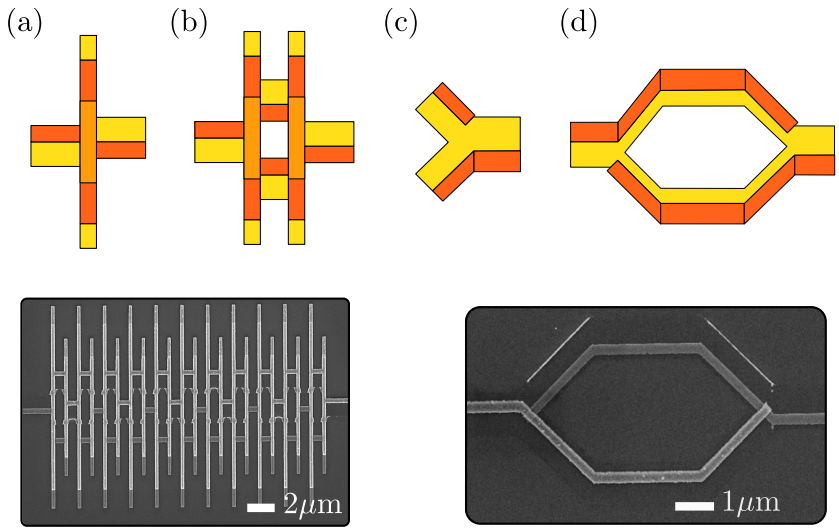

Figure B.1 – **Upper panel** Schematic of the exposure patterns used in the second step of the recipe for various junction and SQUIDs designed. The rotation axis is horizontal. The yellow correspond to was is called the Undercut, the dark orange to the Junction and the light orange to the Chain inner part. **a** and **b** are respectively the junction and SQUIDs used in the chain. **c** and **d** are the respectively the junctions and SQUID design that are more suited for the nonlinear junction design. **Lower left panel** SEM picture of few SQUIDs resulting from design **b**.**Lower right panel** SEM picture of a SQUID resulting from design **a**

Spectroscopy

C

C.1 Spectroscopy of a resonator

C.1.1 In line resonator

The first kind on sample that was probed can be simplified as a in-line resonator. In the vicinity of one of its resonance it can be modeled as an effective out-of line RLC circuit of admittance Y as shown in Fig.C.1 Then, the transmission S_{21}^{res} is given by:

$$S_{21}^{\text{res}}(\omega) = \frac{V_{\text{out}}^{\text{res}}}{V_{\text{in}}^{\text{res}}} = \frac{1}{1 + Z_{\text{tl}} Y(\omega)/2} \tag{C.1}$$

where $V_{\text{in}}^{\text{res}}$ and $V_{\text{out}}^{\text{res}}$ are respectively the voltage sent at the input of the resonator and the one received at its output while Z_{tl} are the input and output impedance of the measurement apparatus (a Vector Network Analyzer in our case).

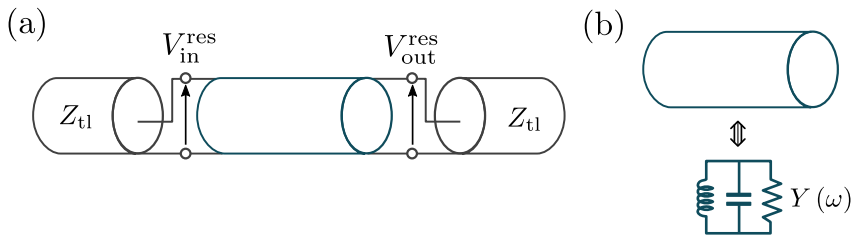

Figure C.1 – **(a)** Transmission measurement of an in-line resonator (blue) by a Vector Network Analyzer of characteristic input and output impedance Z_{tl}. It can probe S_{21}^{res}, the ratio between $V_{\text{out}}^{\text{res}}$ and $V_{\text{in}}^{\text{res}}$ as a function of the frequency. **(b)** Equivalence between the in-line resonator and an out-of-line admittance Y in the vicinity of a mode.

The admittance of the effective circuit is:

$$Y(\omega) = \frac{1}{L\omega i} + C\omega i + \frac{1}{R} \tag{C.2}$$

where R accounts for possible losses in the resonator. Eq.C.2 can by simplified since the effective circuit representation is only valid near the resonance:

$$Y(\omega) \simeq \frac{1}{R} + 2iC(\omega - \omega_{\text{r}}) \tag{C.3}$$

That approximation is refereed as the rotating wave approximation in quantum optics. Then, inserting Eq.C.3 in C.1 yields:

$$S_{21}^{\text{res}}(\omega) = \frac{2R/Z_{\text{tl}}}{1 + 2R/Z_{\text{tl}} + 2iRC(\omega - \omega_r)} \tag{C.4}$$

Where $\omega_{\text{r}} = 1/LC$ is the resonant frequency of the resonator (without taking into account the shift due to the resistance). In the same fashion than in Section 3.3.2 we define the damping rates:

$$\gamma_{\text{int}} = \frac{1}{RC} \tag{C.5}$$

$$\gamma_{\text{ext}} = \frac{2}{Z_{\text{tl}}C} \tag{C.6}$$

Where the factor 2 in γ_{ext} comes from the fact that the resonator is wired to two impedance Z_{tl}, one at the input and the other at the output. Therefore, the ports are acting as a $Z_{\text{tl}}/2$ impedance. By using these damping rates, S_{21}^{res} can be recast as:

$$S_{21}^{\text{res}}(\omega) = \frac{\gamma_{\text{ext}}}{\gamma_{\text{int}} + \gamma_{\text{ext}} + 2i(\omega - \omega_{\text{r}})} \tag{C.7}$$

From this expression we see that probing our resonator induces dissipation via γ_{ext}. This dissipation comes on top of an possible internal loss. Nevertheless, these two contributions can be estimated separately as we will see. First we can define the transmission amplitude and the phase accumulated by the signal:

$$|S_{21}(\omega)|^2 = \frac{\gamma_{\text{ext}}^2}{(\gamma_{\text{int}} + \gamma_{\text{ext}})^2 + 4(\omega - \omega_{\text{r}})^2} \tag{C.8}$$

$$\varphi_{21}(\omega) = \arctan\frac{\text{Im}\{S_{21}\}}{\text{Re}\{S_{21}\}} = -\arctan\left(\frac{2(\omega - \omega_{\text{r}})}{\gamma_{\text{ext}} + \gamma_{\text{int}}}\right) \tag{C.9}$$

From Eq.C.8 we can see that the maximum of transmission is at ω_{r} and is equal to $\gamma_{\text{ext}}^2/\left(\gamma_{\text{int}}^2 + \gamma_{\text{ext}}^2\right)$ while the full width half maxima gives $\left(\gamma_{\text{int}}^2 + \gamma_{\text{ext}}^2\right)$. Consequently, from the fit of the transmission we can access to both γ_{ext}, γ_{int} and ω_{r} separately.

Nevertheless, as we have seen in Section 4.1.3 that the transmission of our sample cannot be measured directly since the signal sent by the VNA must pass through the input and output lines. Hence the measured transmission will be:

$$S_{21}^{\text{tot}}(\omega) = S_{21}^{\text{IL}}(\omega) S_{21}^{\text{res}}(\omega) S_{21}^{\text{OL}}(\omega) \tag{C.10}$$

$$= A(\omega) e^{i\varphi(\omega)} S_{21}^{\text{res}}(\omega) \tag{C.11}$$

Where S_{21}^{IL} and S_{21}^{OL} are the transmission of the input and output lines while A and φ are the amplitude and phase accumlated along these lines. Therefore, a careful calibration of these two is needed to remove their contributions. If not, ω_{r} and the

total broadening can still be measured but we will not be able to distinguish the internal and external broadening.

C.1.2 Hanging resonator

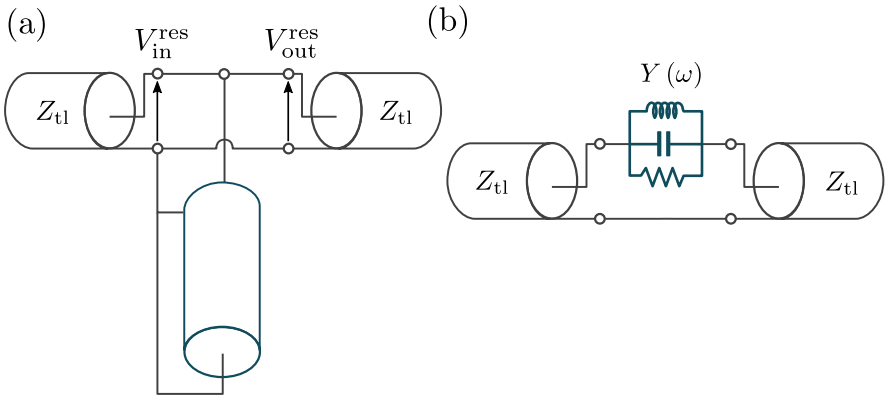

Figure C.2 – **(a)** Transmission measurement of an hanging resonator (blue) by a Vector Network Analyzer of characteristic input and output impedance Z_{tl}. **(b)** Equivalence between the resonator and an in-line admittance Y in the vicinity of a given resonant frequency.

One possible way to circumvent the need of a calibration is to probe the resonator in a hanging geometry. In the vicinity of one of its resonance the resonator can be model as an in-line parallel RLC of admittance Y as shown in Fig.C.2. Thus, the transmission is given by:

$$S_{21}^{\text{res}}(\omega) = \frac{1}{1 + 1/(2Z_{tl}Y(\omega))} \tag{C.12}$$

$$= 1 - \frac{1}{1 + 2Y(\omega) Z_{\text{tl}}} \tag{C.13}$$

Therefore, the analysis carried in the previous section can be applied here by replacing $\gamma_{\text{ext}} = 2/Z_{\text{tl}}C$ with $\gamma_{\text{ext}} = 1/2Z_{\text{tl}}C$ since the resonator "sees" two impedances Z_{tl} in series. The transmission is then given by:

$$S_{21}(\omega) = 1 - \frac{\gamma_{\text{ext}}}{\gamma_{\text{int}} + \gamma_{\text{ext}} + 2i(\omega - \omega_{\text{r}})} \tag{C.14}$$

It is clear from this expression that the factor 1 gives a baseline for the transmission, so no calibration will be necessary. Finally, this expression can be generalized in case of an impedance mismatch between the devices and the measurement setup (see Appendix of [121]):

$$S_{21}(\omega) = \frac{Z_{\text{tl}}}{Z_{\text{tl}} + iX_{\text{e}}} \frac{\gamma_{\text{int}} + 2i(\omega - \omega_{\text{r}})}{\gamma_{\text{ext}} + \gamma_{\text{int}} \frac{Z_{\text{tl}} + iX_{\text{e}}}{Z_{\text{tl}}} + 2i(\omega - \omega_{\text{r}})} \tag{C.15}$$

C.2 Calibration of the background for the hanging resonator.

In this section we present the calibration technique used to remove the measurement setup contribution to the transmitted signal for the hanging resonator. To remove the background we used the flux tunability of the nonlinear SQUID. Because of that the chain modes can shift in frequency (see Fig.5.15). The order in magnitude for this shift is the free spectral range (FSR) of the chain. Although it is large, the broadening of the modes remains smaller than the FSR. Therefore, regardless of the frequency point we look at their will be always a magnetic flux point for which the transmission will not be affected by any mode. Hence, there will always be a flux point for which we will be able to measure the measurement background.

Knowing this, we measured the transmission with a very high resolution in both frequency and magnetic flux. Then, for each frequency we took the median value of measured transmission for the flux datasets. The result of this procedure is shown in Fig.C.3 for the amplitude and phase transmitted.

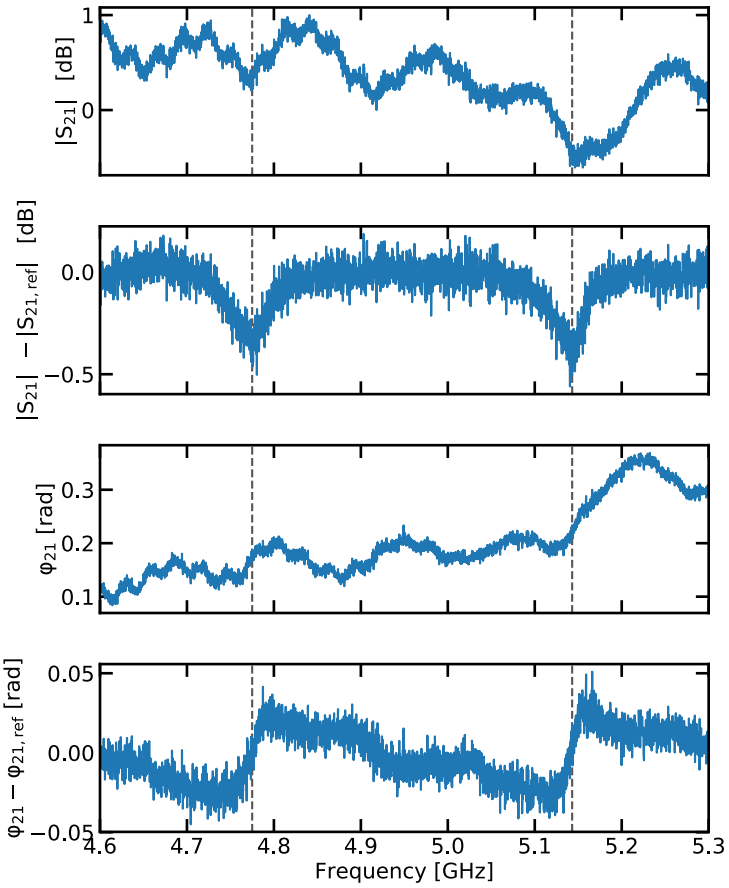

Figure C.3 – From top to bottom: Transmitted power as a function the frequency without the calibration. Same with the calibration. Signal phase without calibration. Same with the calibration. The dashed lines indicate the position of the resonances.

Microwave simulation - Capacitance estimation

D

D.1 Circuit modeling

In this section we will expain the procedure used to estimate the coupling capacitance of sample A, B and C (see Section 5.1.3). The capacitive coupling geometry is sketched in Fig.D.1.a. The left part is connected to the measurement setup (the input or output line) while the right one is galvanitically coupled to the circuit. This coupling element can be modeled with three capacitances: C_c the in-plan coupling capacitance, $C_\mathrm{c,o}$ the capacitance to ground on the measurement line side while $C_\mathrm{c,i}$ the one on the chain side. This circuit representation is shown in Fig.D.1.b.

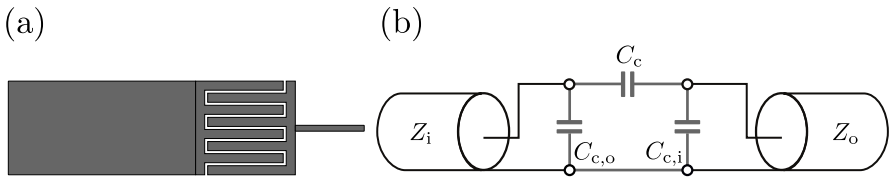

Figure D.1 – **(a)**. Schematic representation of the coupling capacitance. The left part is connected to the measurement line while the right part is connected to the circuit. **(b)** Equivalent circuit representation where Z_i and Z_o would be the characteristic impedance of the measurement line and the circuit respectively. C_c is the in-plan coupling capacitance, $C_\mathrm{c,o}$ the capacitance to ground on the measurement line side while $C_\mathrm{c,i}$ the one on the chain side

We model the measurement line as a transmission line of characteristic impedance Z_i while the circuit is modeled as a transmission line of characteristic impedance Z_o.

D.2 Microwave simulation

To find the capacitances previously introduced we use a finite element microwave simulation software called Sonnet. In the latter, we connected the two part of the coupling element with an lumped inductance $L = 10\,\mathrm{nH}$. Therefore, the resulting circuit has resonances that will depend on the capacitances. We can then simulate the transmission of such an element using Sonnet and fit the result using the formula [104]:

$$S_{21}(\omega) = \frac{(Z_\mathrm{i} Z_\mathrm{o})^{1/2}}{(Z_\mathrm{i} + Z_\mathrm{o})/2 + Y(\omega) Z_\mathrm{i} Z_\mathrm{o}/2} \tag{D.1}$$

Where Y is the admittance of the coupling element shown in Fig.D.2. Note that if $Z_\mathrm{i} = Z_\mathrm{o}$ we recover formula C.1

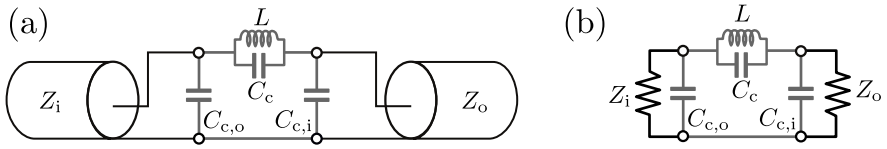

Figure D.2 – **(a)**. Circuit representation of the coupling element where we added an inductance in parallel to C_c such that we have now a resonant circuit. **(b)** Equivalent representation where the transmission lines have been replaced by their characteristic impedances.

Then we will distinguish three cases for the characteristic impedances Z_i and Z_o:

— at $Z_\mathrm{i} = Z_\mathrm{o} = 50\,\Omega$ we expect the two capacitances to the ground to be shunted. This is because the expected capacitance is about 10 fF and the frequency of interest is the gigahertz. Therefore, the susceptance of these capacitances will be around 0.1 mS while the admittance of the ports is 20 mS. Thus, we should only see a dip of transmission at $\omega_\mathrm{r} = 1/\sqrt{LC_\mathrm{c}}$.

— at $Z_\mathrm{i} = 50\,\Omega$ and $Z_\mathrm{o} = 50\,\mathrm{k}\Omega$ the right capacitance to the ground is not shorted. Therefore, the deep of transmission will still be here but in addition there will be a peak of transmission around $\omega_{\mathrm{r,\,i}} = 1/\sqrt{L\,(C_\mathrm{c} + C_\mathrm{c,i})}$

— at $Z_\mathrm{i} = 50\,\mathrm{k}\Omega$ and $Z_\mathrm{o} = 50\,\Omega$ the left capacitance to the ground is not shunted such that a peak of transmission will appear at $\omega_{\mathrm{r,\,o}} = 1/\sqrt{L\,(C_\mathrm{c} + C_\mathrm{c,o})}$

The result of the simulation in these three scenarios in shown in Fig.D.3. Because we have three different resonances we can estimate the three capacitances of the coupling element. From the fit we estimate $C_\mathrm{c} = (102 \pm 1)$ fF, $C_\mathrm{c,i} = (58 \pm 1)$ fF and $C_\mathrm{c,o} = (100 \pm 1)$ fF.

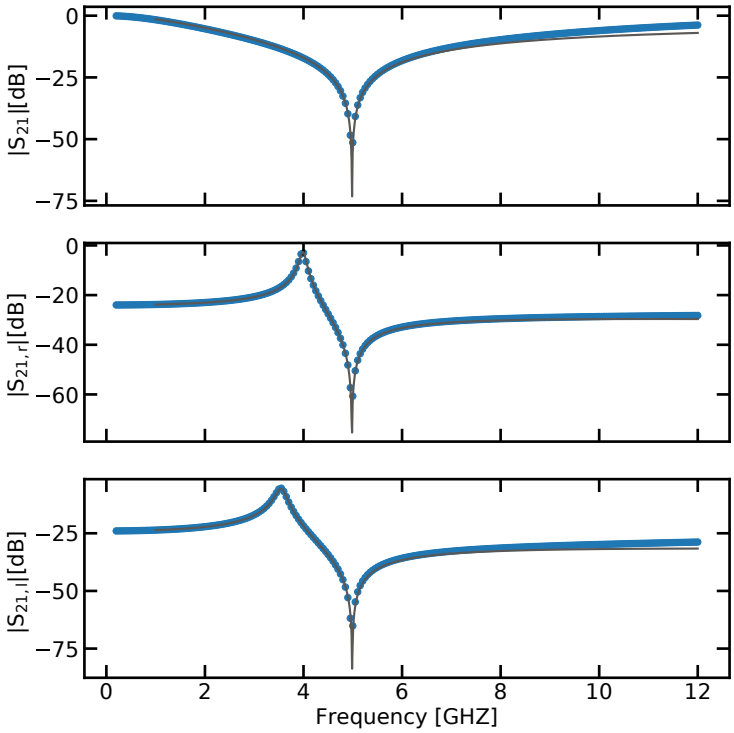

Figure D.3 – Transmission of the coupling element as a function of the frequency for the three cases. The blue dots are the simulated data while the grey lines are the estimations from the fit. The upper part is the case for which $Z_\mathrm{i} = Z_\mathrm{o} = 50\,\Omega$. The middle part is for $Z_\mathrm{i} = 50\,\Omega$ and $Z_\mathrm{o} = 50\,\mathrm{k}\Omega$. The lower part is for $Z_\mathrm{i} = 50\,\mathrm{k}\Omega$ and $Z_\mathrm{o} = 50\,\Omega$.

SQUID chain

E

In this section we will develop the reason why the flux tunability of the SQUID chain of sample A, B and C was not used. The SQUID of the chains are asymmetric. Therefore the SQUID inductance is given by:

$$L\left(\Phi_B\right) = \frac{L}{\sqrt{\cos^2\left(\pi\frac{\Phi_\mathrm{B}}{\Phi_\mathrm{q}}\right) + d^2\sin^2\left(\pi\frac{\Phi_\mathrm{B}}{\Phi_\mathrm{q}}\right)}} \tag{E.1}$$

where d is the asymmetry factor defined in [30] and Φ_B is the magnetic flux in the SQUID loop. The use of asymmetric SQUID creates a sweet-spot at half a quantum of flux. This is convenient to study the properties of a circuit at such a point since it will be less sensitive to flux drifts. The very interesting feature of a SQUID chain is that the characteristic impedance of such a chain is given by:

$$Z_\mathrm{C}\left(\Phi_B\right) = \sqrt{\frac{L\left(\Phi_B\right)}{C_\mathrm{g}}} \tag{E.2}$$

Where C_g is the capacitance to the ground per site. Therefore, the characteristic impedance of such a chain is flux tunable. It can then be useful to study the renormalization of the nonlinear junction as a function of the environment impedance. To see how the nonlinear junction frequency should evolve with this flux we computed it using the parameters of sample A. The result is in Fig.E.1.

The deviation of the nonlinear junction frequency with respect to its value at zero magnetic flux is quite small. It is at maximum 4% which is below what can be measured experimentally (see the error-bars on Fig.5.12). The reason why the shift is small lies on the fact that by tuning the SQUID inductance we also tune the chain plasma frequency:

$$\omega_\mathrm{p}\left(\Phi_\mathrm{B}\right) = \frac{1}{\sqrt{L\left(\Phi_B\right)\left(C + C_\mathrm{g}/4\right)}} \tag{E.3}$$

When the flux is tuned close to the sweet-spot the plasma frequency of the chain decreases. Hence, the renormalization of the junction is smaller that what it would have been if this effect had been neglected. (see Fig.3.17). To make it clearer we also plotted what would be the renormalized frequency as a function of the magnetic flux by neglecting the chain plasma frequency (i.e. only the chain characteristic impedance matters). To do so we computed the nonlinear junction renormalization with the SQUIDs capacitance sets at 0. The renormalization is then twice the one previously

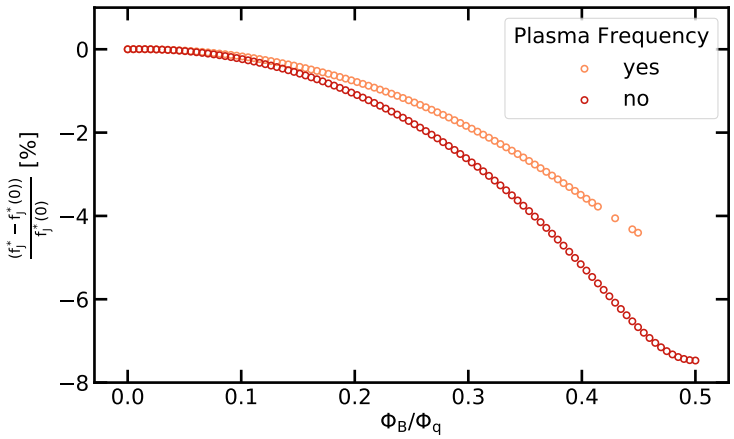

Figure E.1 – Nonlinear junction renormalized frequency as a funtion of the magnetic flux in the SQUID chain. The y-axis is the deviation of the frequency from its value at zero magnetic flux in percent. The x-axis is the magnetic flux Φ_B/Φ_q. The orange dots corresponds to the parameters of sample A. The red dots correspond also to sample A but where the SQUIDs plasma frequency is taken to infinite.

computed confirming that the chain plasma frequency is reducing the renormalization. This is what we explained in Section 3.4.3.

Supplementary information for the Renormalization

F

F.1 Does the capacitive pads affect the relative phase shifts ?

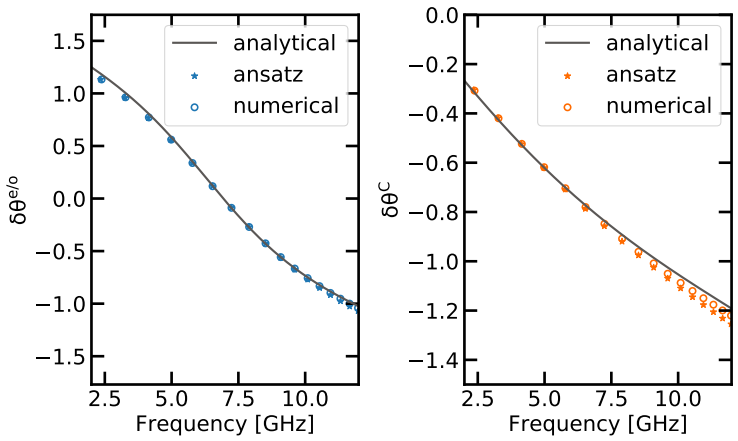

Figure F.1 – **Left.** Even-Odd relative phase shift computed with sample A parameters. The plain line is the analytical formula valid in the thermodynamic limit. The dots result from the numerical diagonalization. The stars are the data obtained from the ansatz. **Right.** Capacitance relative phase shift computed with sample A parameters.

In Section 5.1.4 we stated that the capacitive pads at the chain extremities could be neglected for the Capacitive relative phase shift. That assumption was also used for the Even-Odd relative phase shift. To see if this was justified or not, we computed the even mode, the odd mode and the ones corresponding to the case of a chain terminated by a capacitance using Eq.3.120. From these three families of modes we computed the two relative phase shifts. Then we did the same using the ansatz developed in Section 3.2.3. Finally we compared the results obtained from these two methods with the analytical expression for the relative phase shifts obtained in the thermodynamic limit (Eq.3.113). The result for sample A parameters with the capacitances estimated in Appendix D is shown in Fig.F.1.

The agreement between the numerical diagonalization and the result using the ansatz is quite good for the two relative phase shifts. The discrepancy grows with frequency. However, the maximal relative error found for a given frequency point was below 4%. Note that the two methods are not reproducing exactly the analytical formula. This is because the number of sites is not big enough to be deep in the

thermodynamic limit as we explained in Section 3.5.3. However, it should not be a problem regarding the nonlinear junction parameters extraction since the scatter over the experimental data is greater than these discrepancies (see Fig.5.8). This is also justifying the use of the ansatz instead of the numerical diagonalization for the frequency renormalization fit done in Section 5.1.5.

F.2 Even and odd modes fits

In Fig.F.2 we show double peaks and their fit for sample A, B and C and various temperature.

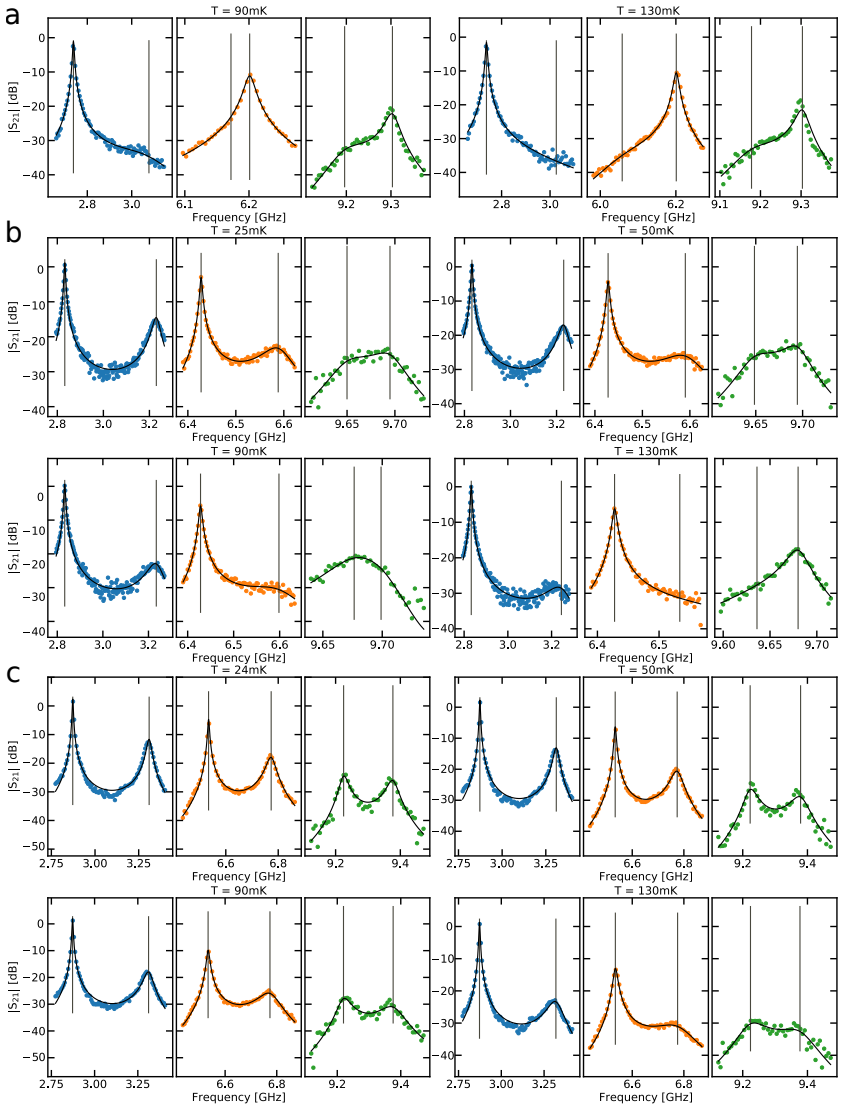

Figure F.2 – Fitting of various double peaks. Panel **a** is for sample A, panel **b** is for sample B and panel **c** is for sample C. Various temperature choices are indicated, and for each case, three frequencies ranges are indicated (in blue, orange and green respectively). Vertical grey lines are the positions of the resonance pairs found by the regression (black lines).

F.3 Splitting fits

In Fig.F.3 we show Even Odd relative phase shift and their fit for sample A, B and C and various temperature.

F.4 Effective Temperature

In Section 5.1.5 we saw that the SCHA could explain the renormalization of the nonlinear junction with respect to the temperature. However, we considered so far that

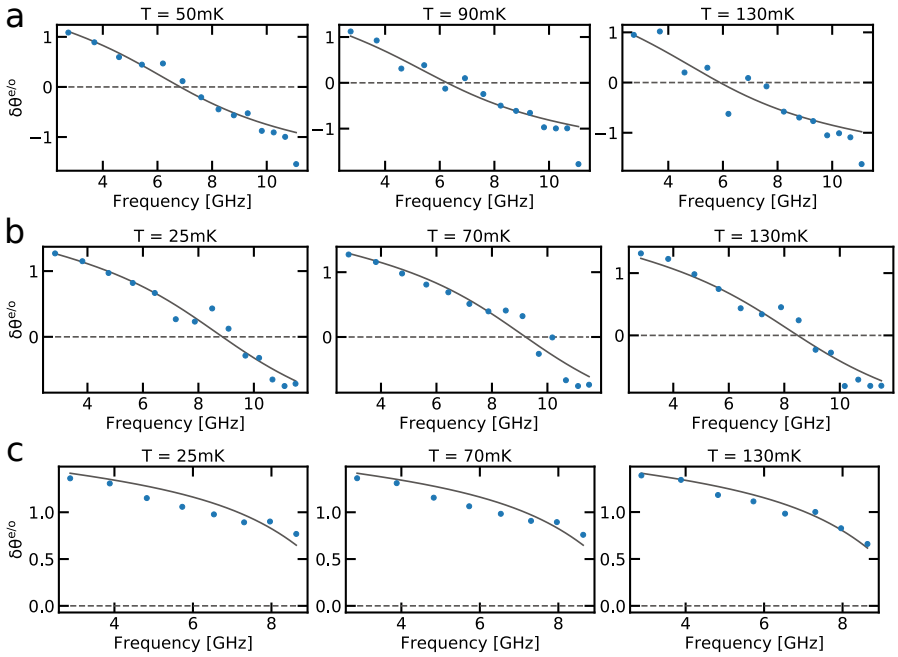

Figure F.3 – Analysis of the experimental Even Odd relative phase shift. The extracted experimental relative phase shifts are shown as dots for our three samples (**a** is for sample A, **b** is for sample B and **c** is for sample C) and various temperatures as indicated. Gray line is the result from the fit.

the circuit temperature was the one indicated by the control electronics. In doing so, we neglected the contribution of external radiations coming from an imperfect filtering. Such radiations can be accounted by considering that the actual temperature is given by:

$$T_{\text{circ}} = T_{\text{mes}} + T_{\text{eff}} \tag{F.1}$$

where T_{circ}, T_{mes} and T_{eff} are respectively the circuit temperature, the measured temperature and the contribution coming from the radiations. To quantity the effect of such an effective temperature on the renormalization we fitted the nonlinear junction frequency as a function of the temperature according to the method use in Section 5.1.5 by replacing T_{mes} with T_{circ}. This has been done for T_{eff} equal to 0, 50 and 100 mK. The results are shown for sample B and C in Fig.F.4. We could not apply this procedure for sample A because the SCHA was at the limit of its validity and therefore did not converge.

When increasing the effective temperature the renormalization increases as expected. The estimated bare Josephson energies are reported in Tab.F.1. The variation of the latter is at most around 10% for sample B and less for sample C. This has to be compared to the relative difference between the renormalized energy and it bare value which is about 50% for sample B.

However, the introduction of an effective temperature changes drastically the temperature dependence of the renormalized frequencyoduce the measured values. This can be a problem since T_{eff} is probably not equal to zero. A possible explanation is that while warming up the fluctuations are boosted and the SCHA is no longer a good approximation. We are currently investigating a way to solve this issue.

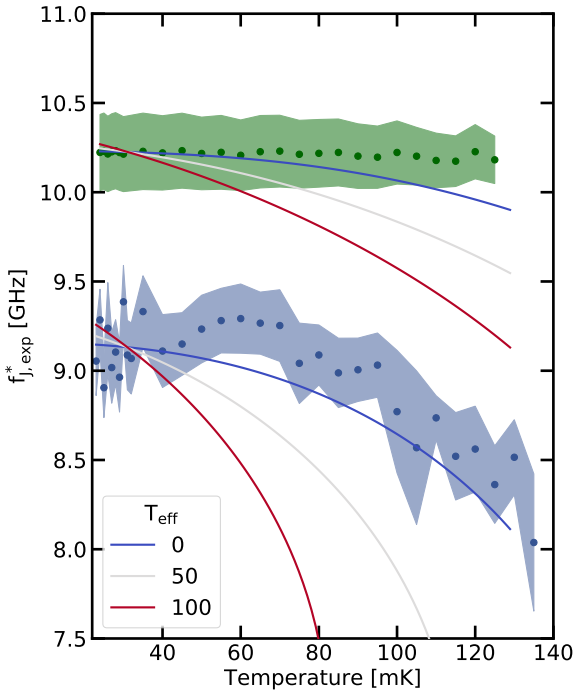

Figure F.4 – Renormalized frequency of the nonlinear junctions as a function of the temperature for sample B (red) and C (green). The plain lines are the the result for the fit using the SCHA with three differents effective temperatures.

As a conclusion, the introduction of an effective temperature is not changing qualitatively the SCHA estimation of E_J and therefore the renormalization amplitude at low temperature. However, while warming up a clear disagreement appears between the experimental data and the theoretical model. Hence, it is not possible to estimate what would be the effective temperature of our circuit from this experiment. However, the fact that we could not apply this procedure to sample A shows that the SCHA was pushed to the limit. Thus, these estimates of the effective temperature, at least for sample A, should be taken with caution.

Table F.1 – $E_{J,th}$ in gigahertz resulting from the regression for sample B and C and three different effective temperatures. The renormalization increases with the effective temperature as expected. However, the variation of the bare Josephson energy is at most around 10%.

T_{eff} [mK]	B	C
0	5.30	8.04
50	5.51	8.16
100	6.00	8.45

F.5 Response function for the second circuit design

In this section we explain how the nonlinear SQUID response function can be inferred from the Josephson relative phase shift. In section 5.2.4 we saw that because of the choice of using one chain instead of two only, the Josephson relative phase shift induced by the SQUID could be measured. However, we could estimate the SQUID capacitance C_{J} from the fit of the relative phase independently to the SQUID inductance (see Section 5.2.4). Therefore the Capacitance relative phase shift can be estimated from the estimation of C_{J}. Then, using the relation between the Even-Odd $\delta\theta^{\mathrm{e/o}}$, the Capacitance $\delta\theta^{\mathrm{C}}$ and the Josephson phase shift $\delta\theta^{\mathrm{J}}$:

$$\delta\theta^{\mathrm{e/o}}(\omega) = \delta\theta^{\mathrm{J}}(\omega) + \delta\theta^{\mathrm{C}}(\omega) \tag{F.2}$$

we can infer the Even-Odd relative phase shift by adding $\delta\theta^{\mathrm{C}}$ to the measured $\delta\theta^{\mathrm{J}}$. The result is shown in Fig.F.5 for various magnetic fluxes. We see from the latter that the experimental data and the modeling agrees well for all the flux between $\Phi_{\mathrm{B}}/\Phi_{\mathrm{q}} = 0.35$ to 0.49.

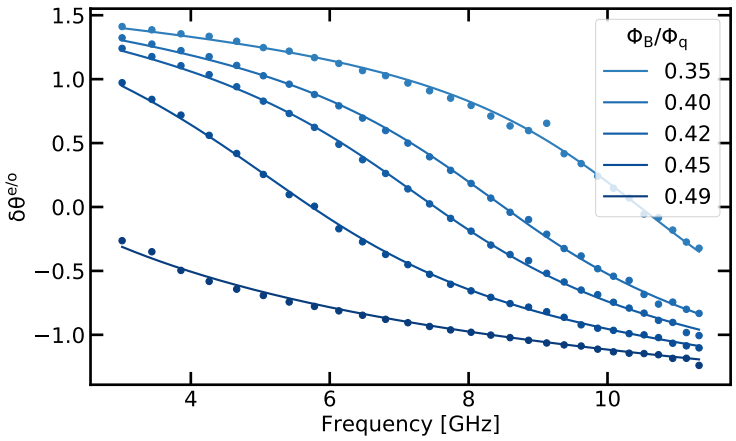

Figure F.5 – Even-Odd relative phase shift as a function of the frequency for various magnetic fluxes. They were extracted from the measurement of Josephson relative phase shift where the Capacitance relative phase shift was subtracted

From the latter we can use the same method that in Section 5.1.6 to estimate the nonlinear SQUID response function. The results are shown in Fig.F.6. From that, we see that the chain can be safely considered in the thermodynamic limit since the discrepancy between the response function computed in the thermodynamic limit (dashed line) and the one with the actual number of junctions (empty dots, for both we used Eq.3.124) is very small. The two match the derivative of the Even-Odd relative phase shift apart at higher frequencies since relation 3.164 is valid for frequencies well below the chain plasma frequency.

Finally, from this we can study the behavior of the renormalized SQUID frequency $\omega_{\mathrm{J}}^{\star}$ (the zero of $\delta\theta^{\mathrm{e/o}}$) and the damped SQUID frequency $\omega_{\mathrm{d}}^{\star}$ (the maximum of the derivative of $\delta\theta^{\mathrm{e/o}}$). Moreover, the FWHM of the SQUID response function can be extracted from the derivative of $\delta\theta^{\mathrm{e/o}}$ and is labeled γ_{RC}.

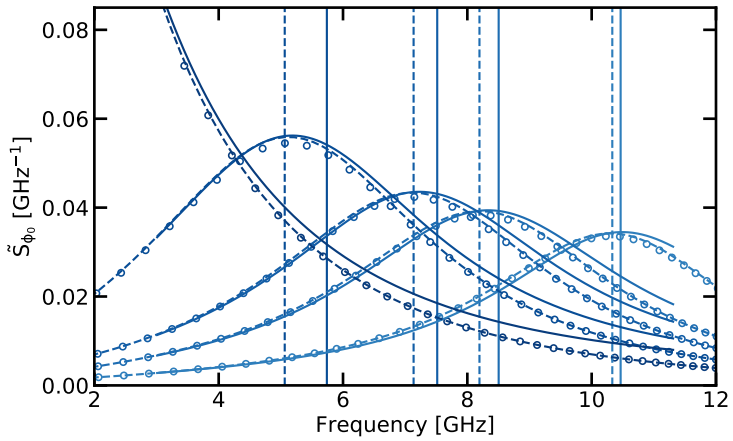

Figure F.6 – Antisymmetric part of the noise spectral density as a function of the frequency. The color code is the same than for Fig.F.5. The plain lines are the result of the Even-Odd relative phase shift fit after applying the transformation given by Eq.3.164 and 3.165. The dashed line is the response function given from Eq.3.124 is the thermodynamic limit. The dot are the result of the same equation but for the actual number of junctions. The vertical line denote the position of $\omega_{\mathrm{J}}^{\star}$. The shift of the damped frequency $\omega_{\mathrm{d}}^{\star}$ with respect to $\omega_{\mathrm{J}}^{\star}$ increases from almost zero to 1 GHz from $\Phi_{\mathrm{B}}/\Phi_{\mathrm{q}} = 0.35$ to 0.49.

We see that the frequency shift between $\omega_{\mathrm{J}}^{\star}$ and $\omega_{\mathrm{d}}^{\star}$ increases from $\Phi_{\mathrm{B}}/\Phi_{\mathrm{q}} = 0.35$ where it is almost equal to zero to $\Phi_{\mathrm{B}}/\Phi_{\mathrm{q}} = 0.47$ where it is about 1 GHz. At the same time, we see that both the FWHM and damped renormalized frequency are well reproduced using the formula developed in Section 3.3.2 in the underdamped regime. It shows that despite being complex our system can be explained using simple formulas since we are in the thermodynamic limit. The broadening of the response function start to be larger than $\omega_{\mathrm{d}}^{\star}$ for magnetic fluxes above 0.45 and the SQUID is even overdamped for magnetic flux above 0.47.

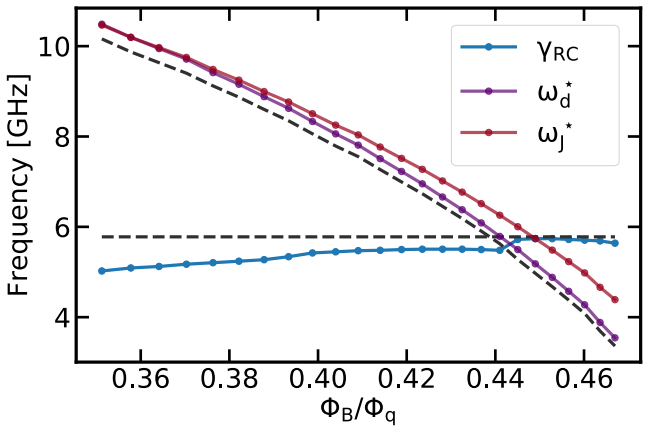

Figure F.7 – FWHM estimated from the Even-Odd relative phase shift γ_{RC}, renormalized and damped SQUID frequency $\omega_{\mathrm{J}}^{\star}$ and $\omega_{\mathrm{d}}^{\star}$ versus $\Phi_{\mathrm{B}}/\Phi_{\mathrm{q}}$. The dashed lines correspond to the damping rate and damped renormalized frequency estimated using the results derived in Section 3.3.2 for the underdamped case.

Supplementary information for the mode damping

G

G.1 Toy model for the losses induced by the junction γ_J

In this section we will derive Eq.6.12. To do that we start with the reflection coefficient:

$$R(\omega) = \frac{1 - Z_C Y_J^\star}{1 + Z_C Y_J^\star} \tag{G.1}$$

$$= \frac{1 - Z_C/R_J + iC_J\left(\omega_J^{\star 2} - \omega^2\right)^2/\omega}{1 + Z_C/R_J - iC_J\left(\omega_J^{\star 2} - \omega^2\right)^2/\omega} \tag{G.2}$$

Then we define $\gamma_{RC} = 1/C_J Z_C$ and $\gamma_{R_J C} = 1/C_J R_J$ and we take the modulus square of R:

$$|R(\omega)|^2 = 1 - 4\frac{\gamma_{RC}\gamma_{R_J C}\omega^2}{\left(\gamma_{R_J C} + \gamma_{RC}\right)^2\omega^2 + \left(\omega^2 - \omega_J^{\star 2}\right)^2} \tag{G.3}$$

If we consider only frequency close to $\omega_J^\star$ and consider $\gamma_{R_J C} \ll \gamma_{RC} = 1/C_J Z_C$ then $|R|^2$ is close to one and we can get Eq.6.12 from 6.9 by taking the first order expansion around one.

G.2 Internal broadening versus the photon number.

In this section we display the internal broadening of the mode versus the average photon number. This number can be inferred using the fact that the average power lost P_{diss} in a mode in related to the energy lost in this mode E and its internal broadening via[a]:

$$E = \frac{P_{\text{diss}}}{\gamma_{\text{int}}} \tag{G.4}$$

Then the conservation of energy impose that:

$$P_{\text{diss}} = P_{\text{in}} \left(1 - |S_{21}|^2 - |S_{11}|^2\right) \tag{G.5}$$

Therefore, using Eq.5.25 where we neglect X_{e} and the conservation of amplitude $S_{11} + S_{21} = 1$ we obtain at ω_{r}, the resonant frequency of the mode being probed:

$$P_{\text{diss}} = P_{\text{in}} \frac{2\gamma_{\text{int}}\gamma_{\text{ext}}}{\left(\gamma_{\text{int}} + \gamma_{\text{ext}}\right)^2} \tag{G.6}$$

Hence, using that $E = n_{\text{ph}}\,\hbar\omega_{\text{r}}$ we find:

$$n_{\text{ph}} = \frac{2P_{\text{in}}}{\hbar\omega_{\text{r}}} \frac{\gamma_{\text{ext}}}{\left(\gamma_{\text{int}} + \gamma_{\text{ext}}\right)^2} \tag{G.7}$$

Using Eq.G.7 we can plot the panel of Fig.6.2 versus the photon number. From that we see that the lowest number of photons at $\Phi_{\text{B}}/\Phi_{\text{q}} = 0.46$ is about one while it is around 100 for $\Phi_{\text{B}}/\Phi_{\text{q}} = 0$.

[a] This derivation is closely following the supplementary material [87]

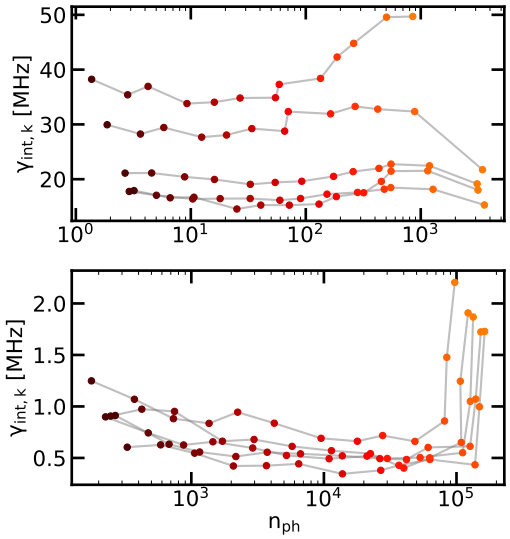

Figure G.1 – **Upper right.** Estimated internal broadening $\gamma_{\mathrm{int},k}$ as a function of n_{ph} the average photon number in the modes for five resonances at $\Phi_{\mathrm{B}}/\Phi_{\mathrm{q}} = 0.46$ (using Eq.5.25). The displayed data correspond to the input powers below -110 dBm where the resonance is not distorted by nonlinear effects. The data corresponding to the same resonance are linked via a grey line. The color code is the same than for the left panels. **Lower right.** Same at $\Phi_{\mathrm{B}}/\Phi_{\mathrm{q}} = 0$

Bibliography

[1] B. Josephson, "Possible new effects in superconductive tunnelling," *Physics Letters*, vol. 1, pp. 251–253, July 1962.
(Cited on pages 1 and 17.)

[2] B. Josephson, "Supercurrents through barriers," *Advances in Physics*, vol. 14, pp. 419–451, Oct. 1965.
(Cited on pages 1 and 17.)

[3] J. Clarke, A. N. Cleland, M. H. Devoret, D. Esteve, and J. M. Martinis, "Quantum Mechanics of a Macroscopic Variable: The Phase Difference of a Josephson Junction," *Science*, vol. 239, pp. 992–997, Feb. 1988. Publisher: American Association for the Advancement of Science Section: Articles.
(Cited on pages 2 and 18.)

[4] D. B. Schwartz, B. Sen, C. N. Archie, and J. E. Lukens, "Quantitative Study of the Effect of the Environment on Macroscopic Quantum Tunneling," *Physical Review Letters*, vol. 55, pp. 1547–1550, Oct. 1985.
(Cited on pages 2 and 18.)

[5] R. F. Voss and R. A. Webb, "Macroscopic Quantum Tunneling in 1-μm Nb Josephson Junctions," *Physical Review Letters*, vol. 47, pp. 265–268, July 1981.
(Cited on pages 2 and 18.)

[6] A. Blais, A. L. Grimsmo, S. M. Girvin, and A. Wallraff, "Circuit Quantum Electrodynamics," *arXiv:2005.12667 [quant-ph]*, May 2020. arXiv: 2005.12667.
(Cited on pages 2 and 18.)

[7] A. O. Caldeira and A. J. Leggett, "Quantum Tunnelling in a Dissipative System," *Annals of Physics*, vol. 149, p. 83, Dec. 1983.
(Cited on pages 2 and 18.)

[8] A. I. Larkin and Y. N. Ovchinnikov, "Damping of a superconducting current in tunnel junctions," *Zh. Eksp. Teor. Fiz.*, vol. 85, pp. 1510–1520, 1983.
(Cited on pages 2 and 18.)

[9] V. Ambegaokar, U. Eckern, and G. Schön, "Quantum Dynamics of Tunneling between Superconductors," *Physical Review Letters*, vol. 48, pp. 1745–1748, June 1982.
(Cited on pages 2 and 18.)

[10] A. D. Zaikin and S. V. Panyukov, "Quantum decay of metastable current states at superconducting junctions," *Zh. Eksp. Teor. Fiz.*, vol. 89, pp. 242–257, 1985.
(Cited on pages 2 and 18.)

[11] A. Schmid, "Diffusion and Localization in a Dissipative Quantum System," *Physical Review Letters*, vol. 51, pp. 1506–1509, Oct. 1983.
(Cited on pages 2 and 19.)

[12] S. A. Bulgadaev, "Phase Diagram of a Dissipative Quantum System," *JETP Letters*, vol. 39, pp. 264–267, 1984.
(Cited on pages 2 and 19.)

[13] G. Schön and A. Zaikin, "Quantum coherent effects, phase transitions, and the dissipative dynamics of ultra small tunnel junctions," *Physics Reports*, vol. 198, pp. 237–412, Dec. 1990.
(Cited on pages 3, 19, and 52.)

[14] J. S. Penttilä, P. J. Hakonen, E. B. Sonin, and M. A. Paalanen, "Experiments on Dissipative Dynamics of Single Josephson Junctions," *Journal of Low Temperature Physics*, vol. 125, pp. 89–114, Nov. 2001.
(Cited on pages 3 and 19.)

[15] R. Yagi, S.-i. Kobayashi, and Y. Ootuka, "Phase Diagram for Superconductor-Insolator Transistion in Single Small Josephson Junctions with Shunt Resistor," *Journal of the Physical Society of Japan*, 1997.
(Cited on pages 3 and 19.)

[16] L. Kuzmin and D. Haviland, "Observation of the Bloch oscillations in an ultrasmall Josephson junction," *Physical Review Letters*, vol. 67, pp. 2890–2893, Nov. 1991.
(Cited on pages 3 and 19.)

[17] D. V. Averin, A. B. Zorin, and K. K. Likharev, "Bloch oscillations in small Josephson junctions," *Zh. Eksp. Teor. Fiz.*, vol. 88, pp. 692–703, 1985.
(Cited on pages 3 and 19.)

[18] A. Murani, N. Bourlet, H. le Sueur, F. Portier, C. Altimiras, D. Esteve, H. Grabert, J. Stockburger, J. Ankerhold, and P. Joyez, "Absence of a Dissipative Quantum Phase Transition in Josephson Junctions," *Physical Review X*, vol. 10, p. 021003, Apr. 2020.
(Cited on pages 3, 19, and 143.)

[19] Y. Nakamura, Y. A. Pashkin, and J. S. Tsai, "Coherent control of macroscopic quantum states in a single-Cooper-pair box," *Nature*, vol. 398, pp. 786–788, Apr. 1999. Number: 6730 Publisher: Nature Publishing Group.
(Cited on pages 3 and 19.)

[20] V. Bouchiat, D. Vion, P. Joyez, D. Esteve, and M. H. Devoret, "Quantum coherence with a single Cooper pair," *Physica Scripta*, vol. 1998, p. 165, Jan. 1998. Publisher: IOP Publishing.
(Cited on pages 3 and 19.)

[21] M. Büttiker, "Zero-current persistent potential drop across small-capacitance Josephson junctions," *Physical Review B*, vol. 36, pp. 3548–3555, Sept. 1987.
(Cited on pages 3 and 19.)

[22] D. Vion, A. Aassime, A. Cottet, P. Joyez, H. Pothier, C. Urbina, D. Esteve, and M. H. Devoret, "Manipulating the Quantum State of an Electrical Circuit," *Science*, vol. 296, pp. 886–889, May 2002. Publisher: American Association for the Advancement of Science Section: Report.
(Cited on pages 3 and 20.)

[23] J. R. Friedman, V. Patel, W. Chen, S. K. Tolpygo, and J. E. Lukens, "Quantum superposition of distinct macroscopic states," *Nature*, vol. 406, pp. 43–46, July 2000. Number: 6791 Publisher: Nature Publishing Group.
(Cited on pages 3 and 20.)

[24] J. E. Mooij, T. P. Orlando, L. Levitov, L. Tian, C. H. v. d. Wal, and S. Lloyd, "Josephson Persistent-Current Qubit," *Science*, vol. 285, pp. 1036–1039, Aug. 1999. Publisher: American Association for the Advancement of Science Section: Report.
(Not cited.)

[25] C. H. v. d. Wal, A. C. J. t. Haar, F. K. Wilhelm, R. N. Schouten, C. J. P. M. Harmans, T. P. Orlando, S. Lloyd, and J. E. Mooij, "Quantum Superposition of Macroscopic Persistent-Current States," *Science*, vol. 290, pp. 773–777, Oct. 2000. Publisher: American Association for the Advancement of Science Section: Research Article.
(Not cited.)

[26] I. Chiorescu, Y. Nakamura, C. J. P. M. Harmans, and J. E. Mooij, "Coherent Quantum Dynamics of a Superconducting Flux Qubit," *Science*, vol. 299, pp. 1869–1871, Mar. 2003. Publisher: American Association for the Advancement of Science Section: Report.
(Cited on pages 3 and 20.)

[27] V. E. Manucharyan, J. Koch, L. I. Glazman, and M. H. Devoret, "Fluxonium: Single Cooper-Pair Circuit Free of Charge Offsets," *Science*, vol. 326, pp. 113–116, Oct. 2009. Publisher: American Association for the Advancement of Science Section: Report.
(Cited on pages 3 and 20.)

[28] J. M. Martinis, S. Nam, J. Aumentado, and C. Urbina, "Rabi Oscillations in a Large Josephson-Junction Qubit," *Physical Review Letters*, vol. 89, p. 117901, Aug. 2002.
(Cited on pages 3 and 20.)

[29] J. M. Martinis, "Superconducting phase qubits," *Quantum Information Processing*, vol. 8, pp. 81–103, June 2009.
(Cited on page 3.)

[30] J. Koch, T. M. Yu, J. Gambetta, A. A. Houck, D. I. Schuster, J. Majer, A. Blais, M. H. Devoret, S. M. Girvin, and R. J. Schoelkopf, "Charge insensitive qubit

design derived from the Cooper pair box," *arXiv:cond-mat/0703002*, Sept. 2007. arXiv: cond-mat/0703002.
(Cited on pages 3, 20, 35, 128, 152, and 177.)

[31] O. Buisson and F. W. J. Hekking, "Entangled states in a Josephson charge qubit coupled to a superconducting resonator," *arXiv:cond-mat/0008275*, Aug. 2000. arXiv: cond-mat/0008275.
(Cited on pages 3 and 20.)

[32] A. Blais, R.-S. Huang, A. Wallraff, S. M. Girvin, and R. J. Schoelkopf, "Cavity quantum electrodynamics for superconducting electrical circuits: An architecture for quantum computation," *Physical Review A*, vol. 69, p. 062320, June 2004.
(Cited on pages 3 and 20.)

[33] A. Wallraff, D. I. Schuster, A. Blais, L. Frunzio, R.-S. Huang, J. Majer, S. Kumar, S. M. Girvin, and R. J. Schoelkopf, "Strong coupling of a single photon to a superconducting qubit using circuit quantum electrodynamics," *Nature*, vol. 431, pp. 162–167, Sept. 2004. Number: 7005 Publisher: Nature Publishing Group.
(Cited on pages 3 and 20.)

[34] I. Chiorescu, P. Bertet, K. Semba, Y. Nakamura, C. J. P. M. Harmans, and J. E. Mooij, "Coherent dynamics of a flux qubit coupled to a harmonic oscillator," *Nature*, vol. 431, pp. 159–162, Sept. 2004. Number: 7005 Publisher: Nature Publishing Group.
(Not cited.)

[35] A. Wallraff, D. I. Schuster, A. Blais, L. Frunzio, J. Majer, M. H. Devoret, S. M. Girvin, and R. J. Schoelkopf, "Approaching Unit Visibility for Control of a Superconducting Qubit with Dispersive Readout," *Physical Review Letters*, vol. 95, p. 060501, Aug. 2005. Publisher: American Physical Society.
(Not cited.)

[36] D. I. Schuster, A. Wallraff, A. Blais, L. Frunzio, R.-S. Huang, J. Majer, S. M. Girvin, and R. J. Schoelkopf, "ac Stark Shift and Dephasing of a Superconducting Qubit Strongly Coupled to a Cavity Field," *Physical Review Letters*, vol. 94, p. 123602, Mar. 2005. Publisher: American Physical Society.
(Not cited.)

[37] J. A. Schreier, A. A. Houck, J. Koch, D. I. Schuster, B. R. Johnson, J. M. Chow, J. M. Gambetta, J. Majer, L. Frunzio, M. H. Devoret, S. M. Girvin, and R. J. Schoelkopf, "Suppressing charge noise decoherence in superconducting charge qubits," *Physical Review B*, vol. 77, p. 180502, May 2008. Publisher: American Physical Society.
(Cited on pages 3 and 20.)

[38] M. H. Devoret, S. Girvin, and R. Schoelkopf, "Circuit-QED: How strong can the coupling between a Josephson junction atom and a transmission line resonator be?," *Annalen der Physik*, vol. 16, no. 10-11, pp. 767–779, 2007. _eprint: https://onlinelibrary.wiley.com/doi/pdf/10.1002/andp.200710261.
(Cited on pages 3, 5, 20, and 21.)

[39] V. E. Manucharyan, A. Baksic, and C. Ciuti, "Resilience of the quantum Rabi model in circuit QED," *Journal of Physics A: Mathematical and Theoretical*, vol. 50, p. 294001, July 2017.
(Cited on pages 3 and 20.)

[40] P. Forn-Díaz, J. Lisenfeld, D. Marcos, J. J. García-Ripoll, E. Solano, C. J. P. M. Harmans, and J. E. Mooij, "Observation of the Bloch-Siegert Shift in a Qubit-Oscillator System in the Ultrastrong Coupling Regime," *Physical Review Letters*, vol. 105, p. 237001, Nov. 2010.
(Cited on pages 4 and 20.)

[41] T. Niemczyk, F. Deppe, H. Huebl, E. P. Menzel, F. Hocke, M. J. Schwarz, J. J. Garcia-Ripoll, D. Zueco, T. Hümmer, E. Solano, A. Marx, and R. Gross, "Circuit quantum electrodynamics in the ultrastrong-coupling regime," *Nature Physics*, vol. 6, pp. 772–776, Oct. 2010. Number: 10 Publisher: Nature Publishing Group.
(Cited on pages 4 and 20.)

[42] F. Yoshihara, T. Fuse, S. Ashhab, K. Kakuyanagi, S. Saito, and K. Semba, "Superconducting qubit–oscillator circuit beyond the ultrastrong-coupling regime," *Nature Physics*, vol. 13, pp. 44–47, Jan. 2017.
(Cited on pages 4, 20, 120, and 145.)

[43] O. Astafiev, A. M. Zagoskin, A. A. Abdumalikov, Y. A. Pashkin, T. Yamamoto, K. Inomata, Y. Nakamura, and J. S. Tsai, "Resonance Fluorescence of a Single Artificial Atom," *Science*, vol. 327, pp. 840–843, Feb. 2010. Publisher: American Association for the Advancement of Science Section: Report.
(Cited on pages 4 and 20.)

[44] A. A. Abdumalikov, O. Astafiev, A. M. Zagoskin, Y. A. Pashkin, Y. Nakamura, and J. S. Tsai, "Electromagnetically Induced Transparency on a Single Artificial Atom," *Physical Review Letters*, vol. 104, p. 193601, May 2010.
(Cited on pages 4 and 20.)

[45] A. J. Leggett, S. Chakravarty, A. T. Dorsey, M. P. A. Fisher, A. Garg, and W. Zwerger, "Dynamics of the dissipative two-state system," *Rev. Mod. Phys.*, vol. 59, no. 1, p. 85, 1987.
(Cited on pages 4 and 20.)

[46] U. Weiss, *Quantum Dissipative Systems*. WORLD SCIENTIFIC, 4 ed., Mar. 2012.
(Cited on pages 4, 5, 20, and 22.)

[47] S. E. Nigg, H. Paik, B. Vlastakis, G. Kirchmair, S. Shankar, L. Frunzio, M. H. Devoret, R. J. Schoelkopf, and S. M. Girvin, "Black-Box Superconducting Circuit Quantization," *Physical Review Letters*, vol. 108, p. 240502, June 2012.
(Cited on pages 4 and 20.)

[48] J. Bourassa, F. Beaudoin, J. M. Gambetta, and A. Blais, "Josephson-junction-embedded transmission-line resonators: From Kerr medium to in-line transmon," *Physical Review A*, vol. 86, p. 013814, July 2012.
(Cited on page 108.)

[49] T. Weißl, B. Küng, E. Dumur, A. K. Feofanov, I. Matei, C. Naud, O. Buisson, F. W. J. Hekking, and W. Guichard, "Kerr coefficients of plasma resonances in Josephson junction chains," *Physical Review B*, vol. 92, p. 104508, Sept. 2015.
(Cited on pages 4, 5, 20, 21, 74, and 75.)

[50] P. Forn-Díaz, J. J. García-Ripoll, B. Peropadre, J.-L. Orgiazzi, M. A. Yurtalan, R. Belyansky, C. M. Wilson, and A. Lupascu, "Ultrastrong coupling of a single artificial atom to an electromagnetic continuum in the nonperturbative regime," *Nature Physics*, vol. 13, pp. 39–43, Jan. 2017. Number: 1 Publisher: Nature Publishing Group.
(Cited on pages 4, 20, 120, and 145.)

[51] L. Magazzù, P. Forn-Díaz, R. Belyansky, J.-L. Orgiazzi, M. A. Yurtalan, M. R. Otto, A. Lupascu, C. M. Wilson, and M. Grifoni, "Probing the strongly driven spin-boson model in a superconducting quantum circuit," *Nature Communications*, vol. 9, p. 1403, Dec. 2018.
(Cited on pages 4 and 20.)

[52] P. Forn-Díaz, L. Lamata, E. Rico, J. Kono, and E. Solano, "Ultrastrong coupling regimes of light-matter interaction," *Reviews of Modern Physics*, vol. 91, p. 025005, June 2019.
(Cited on pages 4, 10, 20, 27, and 119.)

[53] A. Frisk Kockum, A. Miranowicz, S. De Liberato, S. Savasta, and F. Nori, "Ultrastrong coupling between light and matter," *Nature Reviews Physics*, vol. 1, pp. 19–40, Jan. 2019. Number: 1 Publisher: Nature Publishing Group.
(Cited on pages 4, 10, 20, 27, and 119.)

[54] K. Le Hur, "Kondo resonance of a microwave photon," *Physical Review B*, vol. 85, p. 140506, Apr. 2012.
(Cited on pages 4 and 20.)

[55] I. Snyman and S. Florens, "Robust Josephson-Kondo screening cloud in circuit quantum electrodynamics," *Physical Review B*, vol. 92, p. 085131, Aug. 2015.
(Cited on pages 10, 27, 45, and 119.)

[56] M. Goldstein, M. H. Devoret, M. Houzet, and L. I. Glazman, "Inelastic Microwave Photon Scattering off a Quantum Impurity in a Josephson-Junction Array," *Physical Review Letters*, vol. 110, p. 017002, Jan. 2013.
(Cited on pages 4 and 20.)

[57] I.-C. Hoi, C. M. Wilson, G. Johansson, J. Lindkvist, B. Peropadre, T. Palomaki, and P. Delsing, "Microwave quantum optics with an artificial atom in one-dimensional open space," *New Journal of Physics*, vol. 15, p. 025011, Feb. 2013.
(Cited on pages 4 and 20.)

[58] I.-C. Hoi, C. M. Wilson, G. Johansson, T. Palomaki, B. Peropadre, and P. Delsing, "Demonstration of a Single-Photon Router in the Microwave Regime," *Physical Review Letters*, vol. 107, p. 073601, Aug. 2011.
(Cited on pages 4 and 20.)

[59] N. M. Sundaresan, Y. Liu, D. Sadri, L. J. Szőcs, D. L. Underwood, M. Malekakhlagh, H. E. Türeci, and A. A. Houck, "Beyond Strong Coupling in a Multimode Cavity," *Physical Review X*, vol. 5, p. 021035, June 2015.
(Cited on pages 4, 20, and 120.)

[60] S. Haroche and J.-M. Raimond, *Exploring the quantum: atoms, cavities and photons*. Oxford graduate texts, Oxford ; New York: Oxford University Press, 2006. OCLC: ocm68770236.
(Cited on pages 4 and 21.)

[61] S. Chakram, A. E. Oriani, R. K. Naik, A. V. Dixit, K. He, A. Agrawal, H. Kwon, and D. I. Schuster, "Seamless high-Q microwave cavities for multimode circuit QED," *arXiv:2010.16382 [cond-mat, physics:quant-ph]*, Nov. 2020. arXiv: 2010.16382.
(Cited on pages 4 and 21.)

[62] S. J. Bosman, M. F. Gely, V. Singh, A. Bruno, D. Bothner, and G. A. Steele, "Multi-mode ultra-strong coupling in circuit quantum electrodynamics," *npj Quantum Information*, vol. 3, pp. 1–6, Oct. 2017. Number: 1 Publisher: Nature Publishing Group.
(Cited on pages 5 and 21.)

[63] V. E. Manucharyan, N. A. Masluk, A. Kamal, J. Koch, L. I. Glazman, and M. H. Devoret, "Evidence for coherent quantum phase slips across a Josephson junction array," *Physical Review B*, vol. 85, p. 024521, Jan. 2012.
(Cited on pages 5 and 21.)

[64] A. Ergül, T. Weißl, J. Johansson, J. Lidmar, and D. B. Haviland, "Spatial and temporal distribution of phase slips in Josephson junction chains," *Scientific Reports*, vol. 7, p. 11447, Sept. 2017. Number: 1 Publisher: Nature Publishing Group.
(Not cited.)

[65] I. M. Pop, I. Protopopov, F. Lecocq, Z. Peng, B. Pannetier, O. Buisson, and W. Guichard, "Measurement of the effect of quantum phase slips in a Josephson junction chain," *Nature Physics*, vol. 6, pp. 589–592, Aug. 2010. Number: 8 Publisher: Nature Publishing Group.
(Cited on pages 5 and 21.)

[66] C. Altimiras, O. Parlavecchio, P. Joyez, D. Vion, P. Roche, D. Esteve, and F. Portier, "Tunable microwave impedance matching to a high impedance source using a Josephson metamaterial," *Applied Physics Letters*, vol. 103, p. 212601, Nov. 2013.
(Cited on pages 5 and 21.)

[67] J. P. Martínez, *Probing light-matter interaction in the many-body regime of superconducting quantum circuits*. phdthesis, Université Grenoble - Alpes, June 2018.
(Cited on pages 5, 21, 45, 88, 97, 98, and 121.)

[68] R. Kuzmin, N. Mehta, N. Grabon, R. Mencia, and V. E. Manucharyan, "Superstrong coupling in circuit quantum electrodynamics," *npj Quantum Information*, vol. 5, pp. 1–6, Feb. 2019. Number: 1 Publisher: Nature Publishing Group.
(Cited on pages 5, 21, 39, 120, and 129.)

[69] D. O. Krimer, M. Liertzer, S. Rotter, and H. E. Türeci, "Route from spontaneous decay to complex multimode dynamics in cavity QED," *Physical Review A*, vol. 89, p. 033820, Mar. 2014.
(Cited on pages 5 and 21.)

[70] K. Kaur, T. Sépulcre, N. Roch, I. Snyman, S. Florens, and S. Bera, "Absence of spin-boson quantum phase transition for transmon qubits," *arXiv:2010.01016 [cond-mat, physics:quant-ph]*, Oct. 2020. arXiv: 2010.01016.
(Cited on pages 5, 10, 22, 27, and 119.)

[71] A. O. Gogolin, A. A. Nersesyan, and A. M. Tsvelik, *Bosonization and strongly correlated systems*. Cambridge: Cambridge Univ. Press, 1. paperback ed ed., 2004. OCLC: 254843165.
(Cited on pages 5 and 22.)

[72] N. Gheeraert, X. H. H. Zhang, T. Sépulcre, S. Bera, N. Roch, H. U. Baranger, and S. Florens, "Particle production in ultrastrong-coupling waveguide QED," *Physical Review A*, vol. 98, p. 043816, Oct. 2018.
(Cited on pages 10, 27, and 119.)

[73] N. Gheeraert, S. Bera, and S. Florens, "Spontaneous emission of Schrödinger cats in a waveguide at ultrastrong coupling," *New Journal of Physics*, vol. 19, p. 023036, Feb. 2017.
(Not cited.)

[74] M. Goldstein, M. H. Devoret, M. Houzet, and L. I. Glazman, "Inelastic Microwave Photon Scattering off a Quantum Impurity in a Josephson-Junction Array," *Physical Review Letters*, vol. 110, p. 017002, Jan. 2013.
(Not cited.)

[75] B. Peropadre, D. Zueco, D. Porras, and J. J. García-Ripoll, "Nonequilibrium and Nonperturbative Dynamics of Ultrastrong Coupling in Open Lines," *Physical Review Letters*, vol. 111, p. 243602, Dec. 2013.
(Cited on pages 10, 27, and 119.)

[76] R. Dassonneville, *Qubit readouts using a transmon molecule in a 3D circuit quantum electrodynamics architecture*. phdthesis, Université Grenoble Alpes, Jan. 2019.
(Cited on page 14.)

[77] U. Vool and M. Devoret, "Introduction to quantum electromagnetic circuits: Introduction to quantum electromagnetic circuits," *International Journal of Circuit Theory and Applications*, vol. 45, pp. 897–934, July 2017.
(Cited on pages 32 and 38.)

[78] H. B. Callen and T. A. Welton, "Irreversibility and Generalized Noise," *Physical Review*, vol. 83, pp. 34–40, July 1951.
(Cited on page 34.)

[79] R. Kubo, "The fluctuation-dissipation theorem," *Reports on Progress in Physics*, vol. 29, pp. 255–284, Jan. 1966.
(Cited on pages 34 and 58.)

[80] A. A. Clerk, M. H. Devoret, S. M. Girvin, F. Marquardt, and R. J. Schoelkopf, "Introduction to quantum noise, measurement, and amplification," *Reviews of Modern Physics*, vol. 82, pp. 1155–1208, Apr. 2010.
(Cited on pages 34, 47, and 89.)

[81] B. Diu, C. Cohen-Tannoudji, F. Laloe, N. Ostrowsky, and D. Ostrowsky, *Quantum Mechanics Volume II: Angular Momentum, Spin, and Approximation Methods*. 2020. OCLC: 1199700306.
(Cited on page 35.)

[82] M. H. Devoret, B. Huard, R. Schoelkopf, and L. F. Cugliandolo, eds., *Quantum machines: measurement and control of engineered quantum systems*. Oxford, United Kingdom: Oxford University Press, first edition ed., 2014. Meeting Name: Ecole d'été de physique théorique (Les Houches, Haute-Savoie, France) OCLC: ocn876285697.
(Cited on pages 35, 36, and 154.)

[83] P. Bocchieri and A. Loinger, "Quantum Recurrence Theorem," *Physical Review*, vol. 107, pp. 337–338, July 1957.
(Cited on page 38.)

[84] L. Grünhaupt, M. Spiecker, D. Gusenkova, N. Maleeva, S. T. Skacel, I. Takmakov, F. Valenti, P. Winkel, H. Rotzinger, W. Wernsdorfer, A. V. Ustinov, and I. M. Pop, "Granular aluminium as a superconducting material for high-impedance quantum circuits," *Nature Materials*, vol. 18, pp. 816–819, Aug. 2019.
(Cited on page 38.)

[85] N. Maleeva, L. Grünhaupt, T. Klein, F. Levy-Bertrand, O. Dupre, M. Calvo, F. Valenti, P. Winkel, F. Friedrich, W. Wernsdorfer, A. V. Ustinov, H. Rotzinger, A. Monfardini, M. V. Fistul, and I. M. Pop, "Circuit quantum electrodynamics of granular aluminum resonators," *Nature Communications*, vol. 9, p. 3889, Dec. 2018.
(Cited on page 38.)

[86] D. Niepce, J. Burnett, and J. Bylander, "High Kinetic Inductance Nb N Nanowire Superinductors," *Physical Review Applied*, vol. 11, p. 044014, Apr. 2019.
(Cited on page 38.)

[87] N. Samkharadze, A. Bruno, P. Scarlino, G. Zheng, D. DiVincenzo, L. DiCarlo, and L. Vandersypen, "High-Kinetic-Inductance Superconducting Nanowire Resonators for Circuit QED in a Magnetic Field," *Physical Review Applied*, vol. 5,

p. 044004, Apr. 2016.
(Cited on pages 38 and 188.)

[88] A. Shearrow, G. Koolstra, S. J. Whiteley, N. Earnest, P. S. Barry, F. J. Heremans, D. D. Awschalom, E. Shirokoff, and D. I. Schuster, "Atomic layer deposition of titanium nitride for quantum circuits," *Applied Physics Letters*, vol. 113, p. 212601, Nov. 2018.
(Cited on page 38.)

[89] S. Corlevi, W. Guichard, F. W. J. Hekking, and D. B. Haviland, "Phase-Charge Duality of a Josephson Junction in a Fluctuating Electromagnetic Environment," *Physical Review Letters*, vol. 97, p. 096802, Aug. 2006.
(Cited on page 38.)

[90] N. A. Masluk, I. M. Pop, A. Kamal, Z. K. Minev, and M. H. Devoret, "Microwave Characterization of Josephson Junction Arrays: Implementing a Low Loss Superinductance," *Physical Review Letters*, vol. 109, p. 137002, Sept. 2012.
(Cited on page 108.)

[91] M. T. Bell, I. A. Sadovskyy, L. B. Ioffe, A. Y. Kitaev, and M. E. Gershenson, "Quantum Superinductor with Tunable Nonlinearity," *Physical Review Letters*, vol. 109, p. 137003, Sept. 2012.
(Cited on page 38.)

[92] R. Kuzmin, R. Mencia, N. Grabon, N. Mehta, Y.-H. Lin, and V. E. Manucharyan, "Quantum electrodynamics of a superconductor–insulator phase transition," *Nature Physics*, vol. 15, pp. 930–934, Sept. 2019.
(Cited on pages 39, 137, and 143.)

[93] J. Puertas Martínez, S. Léger, N. Gheeraert, R. Dassonneville, L. Planat, F. Foroughi, Y. Krupko, O. Buisson, C. Naud, W. Hasch-Guichard, S. Florens, I. Snyman, and N. Roch, "A tunable Josephson platform to explore many-body quantum optics in circuit-QED," *npj Quantum Information*, vol. 5, p. 19, Dec. 2019.
(Cited on pages 52, 120, and 129.)

[94] S. Léger, J. Puertas-Martínez, K. Bharadwaj, R. Dassonneville, J. Delaforce, F. Foroughi, V. Milchakov, L. Planat, O. Buisson, C. Naud, W. Hasch-Guichard, S. Florens, I. Snyman, and N. Roch, "Observation of quantum many-body effects due to zero point fluctuations in superconducting circuits," *Nature Communications*, vol. 10, p. 5259, Dec. 2019.
(Cited on pages 39 and 52.)

[95] D. M. Basko, "Superconductor-insulator transition in Josephson junction chains by quantum Monte Carlo calculations," *PHYSICAL REVIEW B*, p. 11, 2020.
(Cited on page 40.)

[96] R. P. Feynman, R. B. Leighton, M. L. Sands, and R. P. Feynman, *Mainly electromagnetism and matter*. No. Feynman, Leighton, Sands ; volume 2 in The Feynman lectures on physics, New York: Basic Books, new millenium edition ed., 2010. OCLC: 838503554.
(Cited on page 41.)

[97] H. Nyquist, "Thermal Agitation of Electric Charge in Conductors," *Physical Review*, vol. 32, pp. 110–113, July 1928.
(Cited on page 48.)

[98] P. Joyez, "Self-Consistent Dynamics of a Josephson Junction in the Presence of an Arbitrary Environment," *Physical Review Letters*, vol. 110, p. 217003, May 2013.
(Cited on page 52.)

[99] A. Huber, "Variational Principles in Quantum Statistical Mechanics," in *Mathematical Methods in Solid State and Superfluid Theory* (R. C. Clark and G. H. Derrick, eds.), pp. 364–392, Boston, MA: Springer US, 1968.
(Cited on page 52.)

[100] T. Weissl, *Quantum phase and charge in Josephson junction chains*. These de doctorat, Grenoble, Oct. 2014.
(Cited on page 57.)

[101] P. Coleman, *Introduction to many body physics*. New York, NY: Cambridge University Press, 2015.
(Cited on pages 77 and 79.)

[102] H. Bruus and K. Flensberg, *Many-body quantum theory in condensed matter physics: an introduction*. Oxford graduate texts, Oxford ; New York: Oxford University Press, 2004. OCLC: ocm56694794.
(Cited on page 78.)

[103] A. L. Fetter and J. D. Walecka, *Quantum theory of many-particle systems*. International series in pure and applied physics, New York, NY: McGraw-Hill, 1971. OCLC: 108056.
(Cited on page 81.)

[104] D. Pozar, *Microwave Engineering*. John Wiley and Sons, 4th ed ed., 2005.
(Cited on pages 89, 92, 105, and 173.)

[105] A. B. Zorin, "The thermocoax cable as the microwave frequency filter for single electron circuits," *Review of Scientific Instruments*, vol. 66, pp. 4296–4300, Aug. 1995.
(Cited on pages 90 and 91.)

[106] R. Barends, J. Wenner, M. Lenander, Y. Chen, R. C. Bialczak, J. Kelly, E. Lucero, P. O'Malley, M. Mariantoni, D. Sank, H. Wang, T. C. White, Y. Yin, J. Zhao, A. N. Cleland, J. M. Martinis, and J. J. A. Baselmans, "Minimizing quasiparticle generation from stray infrared light in superconducting quantum circuits," *Applied Physics Letters*, vol. 99, p. 113507, Sept. 2011.
(Cited on page 96.)

[107] J. J. A. Baselmans, S. J. C. Yates, B. Young, B. Cabrera, and A. Miller, "Long quasiparticle lifetime in Aluminum Microwave Kinetic Inductance Detectors using coaxial stray light filters," (Stanford (California)), pp. 160–163, 2009.
(Cited on page 96.)

[108] S. Celozzi, R. Araneo, and G. Lovat, "Appendix B: Magnetic Shielding," in *Electromagnetic Shielding*, pp. 282–316, John Wiley & Sons, Ltd, 2008. _eprint: https://onlinelibrary.wiley.com/doi/pdf/10.1002/9780470268483.app2.
(Cited on page 96.)

[109] G. J. Dolan, "Offset masks for lift-off photoprocessing," *Applied Physics Letters*, vol. 31, pp. 337–339, Sept. 1977.
(Cited on page 98.)

[110] F. Lecocq, *Dynamique quantique dans un dcSQUID : du qubit de phase à l'oscillateur quantique bidimensionnel*. phdthesis, Université de Grenoble, May 2011.
(Cited on page 98.)

[111] V. Ambegaokar and A. Baratoff, "Tunneling Between Superconductors," *Physical Review Letters*, vol. 10, pp. 486–489, June 1963.
(Cited on page 100.)

[112] J. Claudon, *Oscillations cohérentes dans un circuit quantique supraconducteur : le SQUID dc*. phdthesis, Université Joseph-Fourier - Grenoble I, Sept. 2005.
(Cited on page 100.)

[113] T. Weißl, G. Rastelli, I. Matei, I. M. Pop, O. Buisson, F. W. J. Hekking, and W. Guichard, "Bloch band dynamics of a Josephson junction in an inductive environment," *Physical Review B*, vol. 91, p. 014507, Jan. 2015.
(Cited on page 108.)

[114] Y. Krupko, V. D. Nguyen, T. Weißl, Dumur, J. Puertas, C. Naud, F. W. J. Hekking, D. M. Basko, O. Buisson, N. Roch, and W. Hasch-Guichard, "Kerr non-linearity in a superconducting Josephson metamaterial," *Physical Review B*, vol. 98, p. 094516, Sept. 2018. arXiv: 1807.01499.
(Cited on page 111.)

[115] R. Lescanne, L. Verney, Q. Ficheux, M. H. Devoret, B. Huard, M. Mirrahimi, and Z. Leghtas, "Escape of a Driven Quantum Josephson Circuit into Unconfined States," *Physical Review Applied*, vol. 11, p. 014030, Jan. 2019.
(Cited on page 112.)

[116] J.-H. Yeh, J. LeFebvre, S. Premaratne, F. C. Wellstood, and B. S. Palmer, "Microwave attenuators for use with quantum devices below 100 mK," *Journal of Applied Physics*, vol. 121, p. 224501, June 2017.
(Cited on pages 117 and 146.)

[117] Z. Wang, S. Shankar, Z. Minev, P. Campagne-Ibarcq, A. Narla, and M. Devoret, "Cavity Attenuators for Superconducting Qubits," *Physical Review Applied*, vol. 11, p. 014031, Jan. 2019.
(Not cited.)

[118] F. Yan, S. Gustavsson, A. Kamal, J. Birenbaum, A. P. Sears, D. Hover, T. J. Gudmundsen, D. Rosenberg, G. Samach, S. Weber, J. L. Yoder, T. P. Orlando, J. Clarke, A. J. Kerman, and W. D. Oliver, "The flux qubit revisited to enhance coherence and reproducibility," *Nature Communications*, vol. 7, p. 12964, Nov.

2016. Number: 1 Publisher: Nature Publishing Group.
(Not cited.)

[119] A. D. Córcoles, J. M. Chow, J. M. Gambetta, C. Rigetti, J. R. Rozen, G. A. Keefe, M. Beth Rothwell, M. B. Ketchen, and M. Steffen, "Protecting superconducting qubits from radiation," *Applied Physics Letters*, vol. 99, p. 181906, Oct. 2011.
(Cited on pages 117 and 146.)

[120] M. F. Gely, G. A. Steele, and D. Bothner, "Nature of the Lamb shift in weakly anharmonic atoms: From normal-mode splitting to quantum fluctuations," *Physical Review A*, vol. 98, p. 053808, Nov. 2018.
(Cited on page 118.)

[121] E. Dumur, *A V-shape superconducting artificial atom for circuit quantum electrodynamics*. phdthesis, Université Grenoble Alpes, Feb. 2015.
(Cited on pages 122 and 171.)

[122] N. Ismail, C. C. Kores, D. Geskus, and M. Pollnau, "Fabry-Pérot resonator: spectral line shapes, generic and related Airy distributions, linewidths, finesses, and performance at low or frequency-dependent reflectivity," *Optics Express*, vol. 24, p. 16366, July 2016.
(Cited on page 124.)

[123] V. E. Manucharyan, E. Boaknin, M. Metcalfe, R. Vijay, I. Siddiqi, and M. Devoret, "Microwave bifurcation of a Josephson junction: Embedding-circuit requirements," *Physical Review B*, vol. 76, p. 014524, July 2007.
(Cited on page 133.)

[124] C. R. H. McRae, H. Wang, J. Gao, M. Vissers, T. Brecht, A. Dunsworth, D. Pappas, and J. Mutus, "Materials loss measurements using superconducting microwave resonators," *arXiv:2006.04718 [physics, physics:quant-ph]*, Sept. 2020. arXiv: 2006.04718.
(Cited on page 134.)

[125] D. M. Basko and F. W. J. Hekking, "Disordered Josephson junction chains: Anderson localization of normal modes and impedance fluctuations," *Physical Review B*, vol. 88, p. 094507, Sept. 2013.
(Cited on page 136.)

[126] G. Catelani, R. J. Schoelkopf, M. H. Devoret, and L. I. Glazman, "Relaxation and frequency shifts induced by quasiparticles in superconducting qubits," *Physical Review B*, vol. 84, p. 064517, Aug. 2011.
(Cited on page 142.)

[127] K. Serniak, S. Diamond, M. Hays, V. Fatemi, S. Shankar, L. Frunzio, R. Schoelkopf, and M. Devoret, "Direct Dispersive Monitoring of Charge Parity in Offset-Charge-Sensitive Transmons," *Physical Review Applied*, vol. 12, p. 014052, July 2019.
(Cited on page 142.)

[128] R. Kuzmin, N. Grabon, N. Mehta, A. Burshtein, M. Goldstein, M. Houzet, L. I. Glazman, and V. E. Manucharyan, "Photon decay in circuit quantum electrodynamics," *arXiv:2010.02099 [cond-mat, physics:quant-ph]*, Oct. 2020. arXiv: 2010.02099.
(Cited on pages 142 and 145.)

[129] J. E. Mooij and Y. V. Nazarov, "Superconducting nanowires as quantum phase-slip junctions," *Nature Physics*, vol. 2, pp. 169–172, Mar. 2006.
(Cited on pages 143 and 147.)

[130] A. Burshtein, R. Kuzmin, V. E. Manucharyan, and M. Goldstein, "Photon-instanton collider implemented by a superconducting circuit," *arXiv:2010.02630 [cond-mat, physics:hep-th, physics:quant-ph]*, Jan. 2021. arXiv: 2010.02630.
(Cited on pages 143 and 145.)

[131] M. Houzet and L. I. Glazman, "Critical fluorescence of a transmon at the Schmid transition," *Physical Review Letters*, vol. 125, p. 267701, Dec. 2020. arXiv: 2012.02233.
(Cited on page 147.)

[132] L. Van Hove, "Correlations in Space and Time and Born Approximation Scattering in Systems of Interacting Particles," *Physical Review*, vol. 95, pp. 249–262, July 1954.
(Cited on page 159.)